UNIVERSITY OF SOUTHAMPTON

Faculty of Engineering and the Environment

Fluid Structure Interactions Research Group

Analysis of Human Underwater Undulatory Swimming Using Musculoskeletal Modelling

by

Christopher W.G. Phillips

Thesis for the degree of
Doctor of Philosophy

June 2013

UNIVERSITY OF SOUTHAMPTON

Abstract

Faculty of Engineering and the Environment
Fluid Structure Interactions Research Group

Doctor of Philosophy

Analysis of Human Underwater Undulatory Swimming Using Musculoskeletal Modelling

by Christopher W.G. Phillips

Elite swimming is a highly competitive sport. At this professional level, the difference between a podium finish or not, is measured in fractions of a second. While improvements in specific performance metrics may deliver a marginal improvement, it is through the accumulation of marginal gains that the winning margins are created. Quantifying performance in elite sport is therefore fundamental in identifying and implementing improvements.

The trade-off between energy expenditure, thrust generated and attained velocity are identified as key aspects to performance. From a review of previous swimming research it was identified that there was a lack of suitable methods for simultaneously quantifying the energy expenditure, thrust and velocity for a particular swimming technique.

The aim of this thesis is to analyse the performance of human underwater undulatory swimming (UUS) —a significant proportion of a race for multiple events. This encompasses experimentally gathered data and computational musculoskeletal modelling in the analysis and evaluation of UUS technique.

This thesis has developed a novel, fully functional musculoskeletal model with which detailed analysis of human UUS can be performed. The experimental and processing methods for two methods of acquiring the athlete's kinematics have also been developed. A model based upon fish locomotion is coupled with the musculoskeletal model to provide the fluid loadings for the simulation. Detailed analysis of two techniques of an elite athlete has demonstrated this process in a case study. Energy expended by the simulated muscles is estimated. Combined with the measured velocity and predicted thrust, the propulsive efficiency for each technique is determined.

Contents

List of Figures

List of Tables

Nomenclature

A	Kick amplitude	m
$\bar{A}_{LL}$	Mean left leg activity per second	s^{-1}
$\bar{A}_{L:T}$	Ratio of leg to trunk activity per second	s^{-1}
$\bar{A}_{Tot}$	Mean total activity per second	s^{-1}
$\bar{A}_{Tr}$	Mean trunk activity per second	s^{-1}
a	Parametric distance along body	m
B	Breadth at pelvis	m
B_{seg}	Segment buoyancy	N
C_D	Drag coefficient	
C_S	Energy cost of locomotion	$kJ\,m^{-1}$
D	Drag	N
$\dot{E}$	Metabolic power in	W
F_m	Force in contractile element of muscle	N
F_0	Muscle force at neutral fibre length	N
f	Kick frequency	Hz
g	Acceleration due to gravity	$m\,s^{-2}$
J	Advance ratio	
k	Kinematic multiplication factor (Ch.5), Number of parameters (Ch.7)	
$\bar{L}_f$	Neutral fibre length	m
$\dot{L}_m$	Contractile velocity of muscle	$m\,s^{-1}$
l_f	Muscle fibre length	m
M	Total number of muscles	
$\bar{M}_{max}$	Mean maximum muscle activity	
m	Mass per unit length	kg m
m_{seg}	Mass of segment	kg
n	Number of strips along the body (Ch.5), Number of sample points (Ch.7)	
$PCSA$	Physiological cross-sectional area	m^2
P_D	Delivered power	W

P_E	Effective power	W
P_I	Installed power	W
Q	Side force on body segment	N
R_T	Total resistance	N
R_{Wave}	Wave resistance	N
R_{VP}	Viscous pressure resistance	N
R_F	Frictional resistance	N
S	Frontal area	m^2
St	Strouhal number	
T	Thrust	N
t	Time	s
V	Velocity	$\mathrm{m\,s}^{-1}$
V_{disp}	Volume of displaced fluid	m^3
$\dot{V}O_2$	Rate of oxygen consumption	$\mathrm{ml\,kg}^{-1}\,\mathrm{min}^{-1}$
v	Water velocity component parallel to body	$\mathrm{m\,s}^{-1}$
v_m	Muscle volume	m^3
W_M	Muscle work done	N m
W_O	Work out	N m
w	Water velocity perpendicular to body	$\mathrm{m\,s}^{-1}$
x_i	Muscle activity for the ith muscle	
γ	Pennation angle	$^\circ$
η_D	Delivered efficiency or quasi propulsive efficiency	
η_M	Metabolic efficiency	
η_O	Overall efficiency	
η_P	Propulsive efficiency	
η_T	Transition efficiency	
ρ_f	Density of water	$\mathrm{kg\,m}^{-2}$
ρ_{seg}	Density of segment	$\mathrm{kg\,m}^{-2}$
ξ	Area bounding motion	
Π	Reference plane orthogonal to body at tip	

Abbreviations

AMMR AnyBody managed model repository.

AMS AnyBody Modelling System.

ATP adenosine triphosphate.

BS British Swimming.

BSN body sensor network.

CFC Chelsea Football Club.

CFD computational fluid dynamics.

CMAS Comité des Sports Sous-Marins.

DOF degree of freedom.

EKF extended Kalman filter.

EMG Electromyography.

FINA Fédération Internationale de Natation.

fps frames per second.

GB Great Britain.

GPS global positioning system.

GUI graphical user interface.

IMUs inertial measurement units.

ISB International Society of Biomechanics.

ITC Intensive Training Centre.

MEMS MicroElectroMechanical systems.

MS musculoskeletal.

PCSA physiological cross-sectional area.

PSEL Performance Sports Engineering Laboratory.

SPH smooth particle hydrodynamics.

UUS underwater undulatory swimming.

VPM velocity perturbation method.

Declaration of Authorship

I, Christopher Phillips, declare that this thesis titled, 'Analysis of Human Underwater Undulatory Swimming Using Musculoskeletal Modelling' and the work presented in it are my own and have been generated by me as the result of my own original research. I confirm that:

1. This work was done wholly or mainly while in candidature for a research degree at this University;
2. Where any part of this thesis has previously been submitted for a degree or any other qualification at this University or any other institution, this has been clearly stated;
3. Where I have consulted the published work of others, this is always clearly attributed;
4. Where I have quoted from the work of others, the source is always given. With the exception of such quotations, this thesis is entirely my own work;
5. I have acknowledged all main sources of help;
6. Where the thesis is based on work done by myself jointly with others, I have made clear exactly what was done by others and what I have contributed myself;
7. Either none of this work has been published before submission, or parts of this work have been published as: [please list references below]:

Signed: _____

Date: _____

Statement of Ethics

The studies contained within this thesis were given ethical approval. The approval was granted by the Faculty of Health Sciences Ethics Committee and is in accordance with the document SoHS-ETHICS-2010-027. A copy of this document may be found in Appendix A.

This thesis is dedicated to my parents and brother.

Preface

The background of the work within this thesis has its origins in a sandpit-meeting at Chelsea Football Club (CFC) 2009. The sport, swimming, was facing a ban on the *super-suits*, which were instrumental in the setting of so many Olympic and World records at the 2008 Beijing Olympic Games. It was thought that the full-body polyurethane suits were providing a 3% performance gain which was to be subsequently lost following the ban. British Swimming (BS) and UK Sport, therefore, set about to mitigate against this loss.

The benefits of sports collaborating with science - in particular engineering - are exemplified by the success of British Cycling at the last two Olympic Games (Beijing 2008 and London 2012) and British Skeleton in the 2009 Vancouver Winter Olympics; the latter of which two postgraduate research students of this research group played a fundamental part in securing Great Britain's only gold medal.

Following the CFC sandpit meeting, funding for three postgraduate studentships was made available by UK Sport and the Engineering and Physical Sciences Research Council (EPSRC) for research to be undertaken at the University of Southampton under the Performance Sports Engineering Laboratory (PSEL). The quality and success of work undertaken by the PSEL was recognised in 2011 with the awarding of the Queen's Anniversary Prize for services to Higher Education.

The research to be conducted would investigate how the 3% performance loss due to the banning of the suits could be regained, or even surpassed. The subsequent work, therefore, fell into two categories; poolside assessment with immediate feedback and longer-term research projects investigating performance gains in swimming, with both in partnership with and deliverable to BS.

The poolside feedback comprised of various items of hardware to acquire data which could be processed into performance metrics. These would be displayed in a feedback centre poolside for immediate analysis and discussion with athletes and coaches. The systems were such that they could be transported anywhere, which included; the University of Southampton, Loughborough and Bath Intensive Training Centres (ITCs) and the BS Olympic squad camp at the Aquatics Centre, Stratford.

The longer-term research was split between the three studentships with focus on three different aspects; propelled resistance of freestyle swimming computational fluid dynamics (CFD), swimming race-time simulator and musculoskeletal model of underwater undulatory swimming (UUS). It is the last then, which this thesis will describe.

Acknowledgements

I would like to thank my PhD supervisors Prof. Stephen Turnock, Dr. Alexander Forrester and Dr. Dominic Hudson for their guidance and support, without whom this work would have been an unrealised aspiration.

I am grateful to UK Sport, EPSRC and the University of Southampton for the sponsorship of this PhD.

Joe Banks and Angus Webb, fellow SwimSIM research students. Together we surpassed expectations of our involvement in the sport and by no accident. Through hard graft and mutual encouragement our research has lead us to Olympic training camps and attracted attention from international media. You have both been instrumental in the culmination of this work.

My thanks to Jonty Skinner for providing invaluable insight into swimming and for his tremendous enthusiasm —manifested particularly in his high-fives.

I would like to thank Dr. Chris Brooks for his defiant perseverance in creating a usable sensor system.

Other members of the University and UK Sport have contributed to this work and in particular I would like to thank Dr. Dominic Taunton, Prof. Maria Stokes, Dr. Martyn Prince and Dr. Martin Warner, as well as Dr. Scott Drawer, Naomi Stenhouse and Gavin Atkins.

I would like to thank the staff of British Swimming, particularly Andrew Logan, Jodi Cossor and Clare Lobb, and all the coaches and athletes we have worked, and continue to work with.

My gratitude to Prof. John Rasmussen and the AnyBody team for their hospitality when visiting, and the support and guidance in the development of the musculoskeletal model.

Ceaseless enthusiasm and hot beverages from George Crammond has made the harder days, easier.

I am sincerely grateful for the support and understanding from my girlfriend, Susie Hunt —I am particularly appreciative of the hours spent proofreading.

My final thanks are to my parents, Sue and Mike Phillips, who have been unwavering in their support and encouragement.

Chapter 1

Introduction

1.1 Motivation of the Work

In Great Britain (GB) many people partake in swimming for recreational enjoyment, keeping fit or rehabilitation purposes. As such as widely popular, mass participation sport there is perhaps a heightened expectation when athletes perform on the World stage. In recognition of this, the national governing body British Swimming (BS) received the fourth largest funding award of all sports from the National Lottery and Government funding (£ 25.14 M) via UK Sport in the years prior to the London 2012 Olympic Games.[1]

Following the 2008 Beijing Olympic Games the international governing body for swimming, Fédération Internationale de Natation (FINA), outlawed the use of 100% polyurethane swimming suits [FINA 2010], popularly dubbed the *super-suits*. At the time it was thought that this ban would lead to a 3% reduction in performance and would consequently see the records set by athletes wearing the *super-suits* remain intact for many years to come.

In recognition of this potential loss of performance and the population's expectations at their home Games, BS sought to invest the awarded money so as to attain the best from the Olympians-to-be and to try to realise the nation's hopes.

[1] UK Sport: Sport by Sport - London 2012
http://www.uksport.gov.uk/sport/summer *Date Accessed:* 29/01/2013

One such investment was committing to scientific involvement in swimming; from the inclusion of psychology and nutrition, to biomechanics and principles of naval architecture. It is in these commitments that this thesis has its origins.

The intentions of this research collaboration were twofold: firstly, to provide engineering support to BS in an everyday poolside coaching environment, providing quantitative performance analysis that could be immediately fed-back to the athletes and coaches, initiating a cognitive learning feedback loop; secondly, to conduct detailed scientific research into the sport of swimming with the aspiration that this new knowledge would generate opportunities for increasing performance.

This thesis seeks to fulfil these intentions by conducting in-depth analysis of underwater undulatory swimming (UUS). A fusion of experimental and computational methods explores the interactions between the human body, its motion and the fluid in which it moves. In so doing, a greater understanding of these interactions is sought and in-turn provides the opportunity for evidence-based analysis supplementing the analytical tools and processes available to both coaches and athletes.

1.2 Underwater Undulatory Swimming (UUS)

Research into the sport of swimming has the ability to encompass a vast number of aspects and potential areas in which to seek improvements. In appreciation of this, the subsequent chapters will focus on the underwater phase of a competitive swimming race, or more specifically the UUS aspect of freestyle, backstroke or butterfly events. Analysis of UUS will be made possible through the acquisition of athlete motion and development of bespoke musculoskeletal models.

1.2.1 Description of UUS

As airborne creatures have evolved to thrive in the atmosphere, so too have aquatic dwelling creatures evolved to excel at life in water, each with an aptitude for moving in their respective medium. When one attempts to inhabit the other's environment, success is not always easily achieved. Humans are well suited to locomotion on land but as Schmidt-Nielsen [1972] observed, *man is a clumsy and ineffective swimmer* where

streamlining is regrettably absent. It is perhaps in light of these observations that in traversing through water humans have attempted to learn from nature's experts, striving to mimic their motion and UUS the result of these endeavours. In recognition of this and in homage to the aquatic-dwelling mammal which achieves locomotion so gracefully, it is more commonly referred to as the *dolphin kick* (as well as *fly kick* and also *the fifth stroke*).

As alluded to by its name, in UUS the body is submerged and an undulatory pattern of motion is generated by the body through the articulation of one's joints. Propulsion in UUS results from the undulations of the submerged body, streamlined (where possible), with arms raised and the hands leading. The sub-figures of Figure 1.1 storyboard an example of one kick cycle of the UUS technique by an elite athlete - arguably one of the World's fastest at UUS. In this example she is swimming on her front, however, there are no restrictions as to the orientation of this stroke. It should that in this example the athlete is not swimming at a sufficient depth where wave resistance can be assumed to be negligible. Similarly, the interaction of with the free-surface is apparent from frame *j*. Swimming at a sufficient depth were the wave resistance is negligible and where there are no interactions with the free-surface are two principle assumptions in this work. These frames are therefore provided as an illustrative example of the stroke kinematics alone.

Each kick cycle may be subdivided into a *down*-kick and an *up*-kick, where the down-kick is defined as the anterior motion of the feet relative to the athlete and conversely the up-kick the posterior motion of the feet relative to the athlete. Frames *a*-*e* are therefore the down-kick - where majority of propulsion originates - and *f*-*j* are the up-kick. In frame *a* the knee joint is at maximum flexion and the hip joint has already begun to flex. In the subsequent four frames the knee then extends; note the relative image-elevation of the pelvis during this phase. The knee is fully extended by frame *e* and subsequently the hip begins to extend, while the knee joint remains constant, rotating the leg vertically as a whole. In frame *h* the knee is beginning to flex again in preparation for the down-kick. The hip joint has also reached its maximum extension at this point and it too begins to flex. Frame *j* then marks the end of the cycle where the feet are once again at their most vertical position and the knee is at its greatest angle of flexion, both in preparation for the down-kick of the following cycle.

It is apparent from this sequence of images that the lower limbs of the body travel

through a greater range of motion than the upper-body. The pelvis-thorax extension is in phase with the knee flexion, but its amplitude is less. Similarly the magnitude of range of motion of the shoulder is less than that of the pelvis-thorax.

It is also interesting to observe in frame *e* the hyper-extension exhibited at the knee joint. This degree of hyper-extension is not typically observed in elite athletes and is perhaps a reason as to why this athlete is reported to be one of the fastest at this stroke.

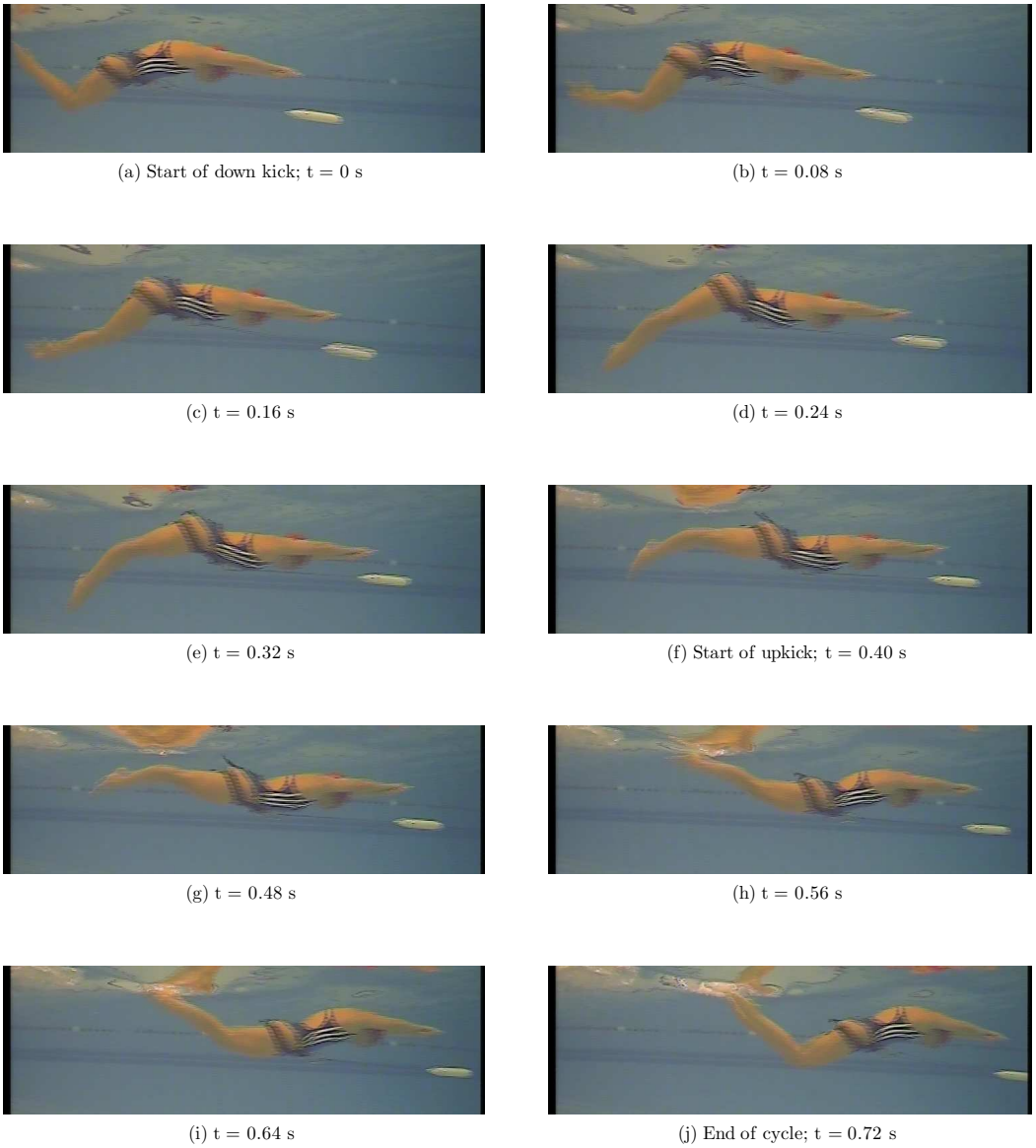

(a) Start of down kick; t = 0 s

(b) t = 0.08 s

(c) t = 0.16 s

(d) t = 0.24 s

(e) t = 0.32 s

(f) Start of upkick; t = 0.40 s

(g) t = 0.48 s

(h) t = 0.56 s

(i) t = 0.64 s

(j) End of cycle; t = 0.72 s

FIGURE 1.1: A sequence of images of an elite athlete performing UUS with a 0.08 s interval between each frame.

The extent of body undulation is used to characterise fish motion. These fall into three forms; anguilliform, carangiform and thunniform, as depicted in Figure 1.2. These

characteristic based classifications are equally transferable to human UUS - Collard *et al.* [2011]; Hochstein and Blickhan [2011] for example, refer to these classifications when discussing UUS. Anguilliform is exemplified as the characteristic motion of an eel where a body wave of almost equal amplitude is initiated just behind the head and travels along the body. Carangiform and thunniform are equally exemplified as the characteristic motion of a trout and a tuna, respectively. The oscillations for each of these occurs further along the length of the body compared to anguilliform; for carangiform it is the latter one third of the body which oscillates and for thunniform it is only the lunate tail section [Vogel 1994]. The athlete depicted in Figure 1.1 exhibits characteristics simlilar to carangiform, where the lower limbs oscillate significantly more than the torso and upper limbs.

While propulsion in anguilliform motion is in the form of resistance based propulsion, the propulsion mechanism in thunniform motion is primarily due to the shedding of vortices from the lunate tail.

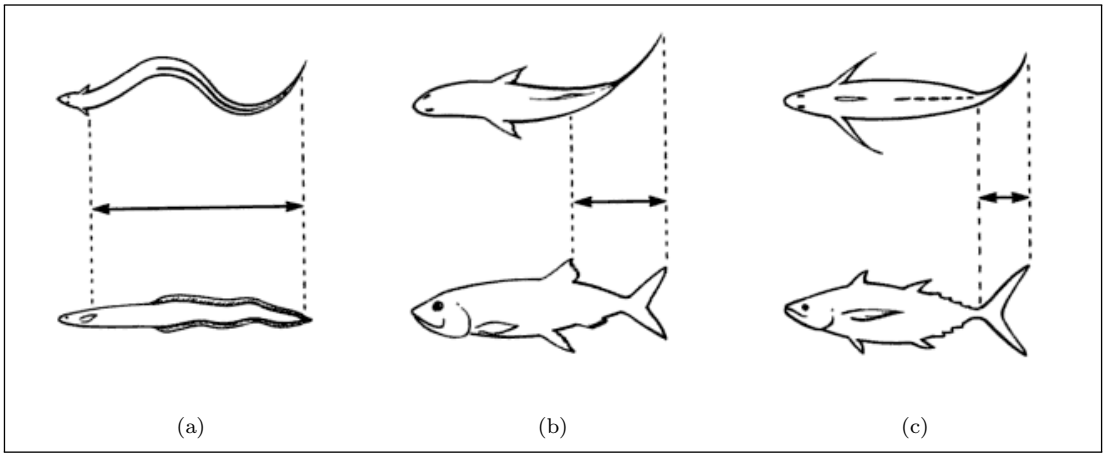

FIGURE 1.2: Illustrations of three types of fish motion; anguilliform (a), carangiform (b) and thunniform (c) [Vogel 1994].

Vogel [1994] also describes the trunk muscle of a thunniform fish to be arranged primarily to power the tail beat rather than to bend the body. As this is its main propulsive mechanism, this would be a logical expectation. It is also described as the mode which appears to be the most force- and power-efficient system for high-speed swimming, with many of the fish included in this group demonstrating both fast anaerobic burst speeds and sustainable aerobic speeds; for example, the sailfish (*Istiophorus*) is able to reach a maximum velocity of close to $30\,\mathrm{m\,s^{-1}}$ [Sagong *et al.* 2008].

1.2.2 Justification of Focus on UUS

UUS is a fundamental aspect of elite swimming, accounting for up to 30% of the total distance in long-course freestyle, backstroke and butterfly races. Through communications with GB coaches, it is also not perceived to be a particularly strong aspect of their athletes and therefore provides good scope for improvement.

Furthermore, UUS is arguably the fastest method of covering the allotted distance. In fact, it is often faster that surface swimming as demonstrated by Denis Pankratov in the 1996 Atlanta Olympic Games. In the 100 m butterfly event, Pankratov swam over half of the first length and 15m of the second underwater, breaking both Olympic and World records [Forman 1996].

Following Pankratov's achievements, however, FINA placed a 15 m limit on the distance an athlete may travel underwater following a start or turn, by which point the athlete's head must have broken the surface (see SW5.3, 6.3, 8.5 in FINA [2013*a*])

Many more examples of the effectiveness of UUS can be found online; for example, Squilacci111 [2009] shows a competitor at a United States college meeting, swim the entire distance of the 50 m butterfly event underwater and finish in 23.10 s, 4.85 s ahead of his fellow competitors. For context, 24.40 s was the world record at the time and 22.43 s the current world record [FINA 2013*b*]. Although he was disqualified for violating the 15 m underwater limit, it is a clear demonstration as to the effectiveness of UUS. Despite this and many other examples in both literature and social media, it was noticeable and perhaps surprising that many athletes in the Olympic Games held in Beijing (2008) and London (2012) failed to take full advantage of the allocated distance.

Anecdotal evidence through direct communication with individual elite athletes and coaches alludes to the fact many simply do not feel they are *good* at UUS and hence do not pursue it [e.g. J. Skinner, personal communications, 11th June 2011]. While the speed advantage has been demonstrated above as being beneficial, the energy cost associated with this type of swimming is significantly detrimental to the remaining 70% of the race and therefore potentially outweighs any advantages.

Consequently, it would be desirable to be able to analyse an athlete's UUS technique and assess their energy expenditure. By doing this, one can modify the athlete's technique

so as to *either* increase velocity for their existing energy expenditure, *or* maintain the same velocity for reduced energy output.

1.2.3 Clarification of Competition Restrictions of UUS

The UUS stroke is transferable between disciplines of swimming and is allowed in freestyle, backstroke and butterfly events. It is however, only permitted for the first 15 m following a start or turn and within this distance the athlete's head must break the surface of the water (SW5.3, 6.3, 8.5 [FINA 2013*a*]). In breaststroke, there is greater limitation with only one kick permissible during the first arm stroke following a start or turn (SW7.1 [FINA 2013*a*]).

The technique of UUS is permitted in finswimming, but in accordance with regulations as set-out by finswimming's governing body, Comité des Sports Sous-Marins (CMAS). Similarly to swimming, in surface finswimming disciplines, the athlete must break the surface within 15 m following a start or turn (Sections 2.2.1.2-3 [CMAS 2012]), allowing for the utilisation of UUS up to this distance. For immersion disciplines however, there are no such restrictions and the rules clearly state *the athlete must progress with a monofin or two fins by means of the swimmer's muscular force only and without the force of a mechanism, not even muscle-powered* (Section 1 [CMAS 2012]).

1.2.4 Overview of Musculoskeletal Modelling

Human musculoskeletal models seek to computationally replicate the function and anatomy of an individual's musculoskeletal system. The skeletal components are assumed to be rigid body segments and connected together with hinging or articulating joints. These joints are spanned by computational interpretation of muscles to recreate the motion and the forces required. External forces —for example, gravity— also act upon these segments, either helping or hindering the motion with regards to the muscle forces necessary to reproduce this motion. There are two principles for solving a musculoskeletal system, either employing inverse dynamics or forward dynamics [Pandy 2001]. Both methods require the geometries of the model to be defined (for example, femur length), as well as the key muscle properties —for example, maximum force the muscle can produce—

and external forces —for example, hydrodynamic forces. They differ in that inverse dynamics solvers require the model kinematics to be explicitly defined and determine the instantaneous muscle forces, while forwards dynamics requires the muscle activations to be defined and solves the equations of motion and hence the model kinematics.

These models are employed in a variety of contexts, for example: the propensity to rupture ligaments in the knee due to a range of defined activities [Schmidt 2008]; determination of muscle forces for finite-element analysis for femoral-fracture fixation plates [Grujicic *et al.* 2010]; optimising the ergonomics of a product design [Rasmussen *et al.* 2012], and vehicle egress and ingress [Schwirtz *et al.* 2009].

Obtaining the muscle activities experimentally is invasive, only providing detail on the exact motion that is performed. These models, however, offer a computational and non-invasive method for estimating muscle activities of a simulated task for any given input motion. Described in this thesis is the development and implementation of such a model for use in determining the required muscle forces in UUS and hence for estimation of overall and propulsive efficiencies.

The content of this thesis provides a logical first step in creating an holistic model for this purpose. The focus of development is upon a creation of a fully functional model representative of human UUS, capable of evaluating comparative differences and discerning between techniques. Validation of musculoskeletal models is a significantly challenging undertaking, particularly of a submerged body. In recognition of such, and in the interest of developing a fully functional model, validation of the musculoskeletal properties is precluded from the scope of this thesis.

1.3 Aims and Objectives

The aim of this thesis is to analyse the performance of human UUS. This will encompass experimentally gathered data and computational musculoskeletal modelling in the analysis and evaluation of UUS technique.

The aims will be realised by:

1. creating methods for acquiring and storing experimental data;

2. developing a fully functional musculoskeletal model representative of UUS;
3. implement methods for acquiring the joint kinematics and fluid load required by the musculoskeletal model;
4. quantifying the useful work produced and the work done by the muscles and hence the propulsive efficiency;
5. demonstrating the capacity of the developed models and methods to evaluate UUS techniques;
6. obtaining theoretically optimal techniques for the trade-off between thrust and energy expenditure.

1.4 Structure of the Thesis

This introductory chapter has detailed the motivation for this research and created the context for the subsequent chapters. Here, UUS has been identified as a fundamental aspect of a competitive swimming race, but with scope for improvement. Its pattern of motion has been described as well as the competition restrictions.

Investigations to determine performance gains are made possible through the quantification of the energy required by the body to perform a particular technique, the thrust and velocity attained. Musculoskeletal models, also summarised here, offer a non-invasive method for quantifying the energy cost associated with the simulated motion and restricted by the force loadings.

A review of previous research is conducted in Chapter 2. It identifies previous methods, both experimental and computational, employed for quantifying performance. A description of methods to quantify energy expenditure during swimming is presented, with examples of specific values observed. Further details of musculoskeletal modelling is then assessed, detailing the specifics of such a model. Following this is a review of methods for capturing human kinematics.

The development of specific tools, detailed in Chapter 3, enabled the acquisition of the experimental data used in the later chapters, including video, velocity and force data.

The development of a fully functional musculoskeletal model representative of UUS is described in Chapter 4. This encompasses specific details of the musculoskeletal model, as well as the methodology for acquiring the kinematics. Using these prescribed kinematics, a method for obtaining the fluid forces acting on body —required by the musculoskeletal model— and the total thrust is presented. A method for quantifying the energy expended by the muscles from the simulation is then determined.

Having detailed the development of a musculoskeletal model for UUS, it is then implemented in a case study in Chapter 5. This chapter compares two UUS techniques of an elite athlete and seeks to identify which technique, or variant thereof, is most suited to their event and discipline (50m and 100m backstroke).

The errors associated with the determination of the joint kinematics, from a manual digitisation process, are studied in Chapter 6. The influence of these errors on the resultant thrust and muscle activities are investigated.

In order to use this model as a tool for performance investigation, an example of how it could be utilised in a multi-objective optimisation of the joint kinematics is described in Chapter 7.

Having presented a fully functioning musculoskeletal model of UUS, the penultimate chapter acknowledges the importance of the determination of the joint kinematics and the significant operator time required by the manual digitisation process. Chapter 8 trials alternative methods to improve upon the identified shortcomings, presenting computer vision and inertial measurement units (IMUs) as potential alternatives and directly comparing the latter with the results from the manual digitisation process.

1.5 Research Contributions

This thesis provides a detailed approach to in-depth analysis of human UUS not previously demonstrated. Research publications which support the work in this thesis and other relevant previous research include:

Christopher W.G. Phillips, Alexander I.J. Forrester, Dominic A. Hudson, Stephen R. Turnock, Propulsive efficiency of alternative underwater flykick techniques for swimmers, (in preparation), 2013. [Appendix B.1]

Christopher W.G. Phillips, Alexander A. Purdue, Alexander I.J. Forrester, Maria J. Stokes, Optimisation of a bicycle chainring to aid in rehabilitation of athletes suffering from patellofemoral pain syndrome (PFPS), *Procedia Engineering*, **2**:3151-3156, March 2010. [Appendix B.2]

Angus P. Webb, Christopher W.G. Phillips, Dominic A. Hudson, and Stephen R. Turnock. Can Lighthill's Elongated Body Theory Predict Hydrodynamic Forces in Underwater Undulatory Swimming? *Procedia Engineering*, **34**:724-729, 2012.
DOI: doi:10.1016/j.proeng.2011.05.063.

Angus P. Webb, Joseph Banks, Christopher W.G. Phillips, Dominic A. Hudson, Dominic J. Taunton, and Stephen R. Turnock. Prediction of passive and active drag in swimming. *Procedia Engineering*, **13**:133-140, January 2011. DOI: 10.1016/j.proeng.2011.05.063.

Chapter 2

Literature Review

2.1 Methods to Quantify Performance

Analysis of swimming styles and techniques has been undertaken for decades. Even during the Second World War, Karpovich and Millman [1944] - citing articles back to 1919 - investigated energy expenditure in swimming so as to better assign it in exercise programs. While the technologies used for these assessments have been modernised, many of the fundamental principles have typically remained unchanged. This section explores the different methods that have been employed to investigate swimming performance.

In order to improve performance of a swimmer, it is important to understand the system under observation, its component parts and their interactions. Similarities maybe drawn between the energy flow in human swimming to that of a ship (Figure 2.1) for which there is a plethora of knowledge.

For a ship, a Diesel engine burns fuel, generates rotary motion which is transmitted through a gearbox and shafting to a propeller. This generates a propulsive thrust and overcomes the ship's resistance to motion. All the stages need to be matched to achieve a maximum overall efficiency [Molland *et al.* 2011].

Similarly, a swimmer processes oxygen and nutrients to release energy available to the body [Feher 2012]. The energy is converted into appropriate muscular contractions, which in underwater undulatory swimming (UUS) develop into a rearward wave-like motion travelling along the body. This causes a displacement of the water which, by

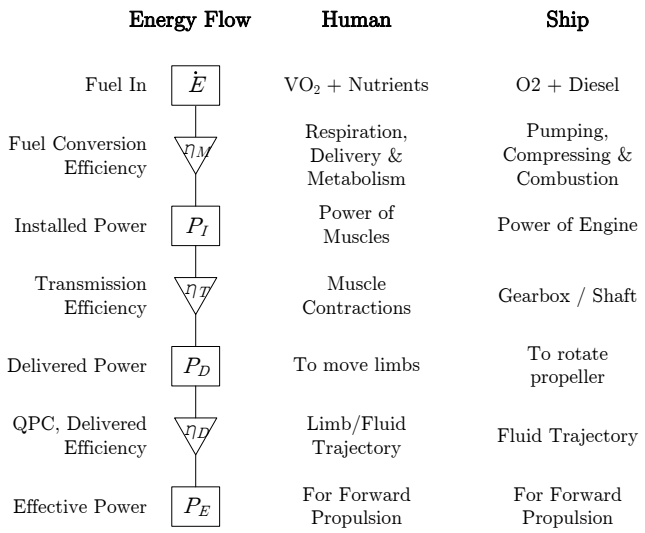

FIGURE 2.1: Similarities in the energy flow in a human and a ship.

conservation of momentum, produces a reactive force on the swimmer which the muscle contraction must work against. The components of the reactive force in the direction of travel, thrust component, contribute to forward velocity. Those which are in the opposite direction oppose forward motion and contribute to the drag. The swimmer's speed will therefore be determined by the balance of the thrust generated during the cycle and the resistive forces on the body.

Improvements in performance may be found in each of these stages of energy transfer. A biologist might be concerned with the physiological processes by which the body releases energy. The engineer by contrast, is potentially more experienced with addressing the physical elements of the system; the mechanical processes of moving bodies, the propulsive and resistive forces and associated mechanical energy required. It is in addressing these elements that an engineer may seek to improve a swimmer's performance.

Human UUS is often characterised in terms of Strouhal number (St) [e.g. Boitel *et al.* 2010; Cohen *et al.* 2012; Hochstein and Blickhan 2011; Nicolas *et al.* 2007; von Loebbecke *et al.* 2009]. The Strouhal number relates the oscillatory speed of the feet to the mean forward speed through the water[Rohr and Fish 2004], such that,

$$St = \frac{Af}{V}, \tag{2.1}$$

where A is the kick amplitude, f the kick frequency and V the mean kick-cycle velocity. Nicolas *et al.* [2007] demonstrated a positive correlation between Strouhal number and a swimmer's drag and an inverse correlation between Strouhal number and velocity. This relationship maybe explained by assuming drag is proportional to the area presented to the flow of water and therefore, an increase in kick amplitude would increase passive drag. If this relative increase in amplitude does not yield the same relative increase in velocity then by inspecting Equation 2.1, Strouhal number would therefore increase. Similarly, by inspecting the same equation it can be seen that should velocity increase for a given amplitude and frequency multiple, then Strouhal number will reduce. This is analogous to the advance ratio (J) used for a ship propeller [Molland *et al.* 2011] that relates translational speed to propeller tip speed.

2.1.1 Experimental Force-Based Methods

A swimmer propels themselves through the water by movement of their body and/or limbs. Simultaneously, the swimmer experiences hydrodynamic restive forces which hinder this progression. The total passive resistance (R_T) of a swimmer can be broken down into three constituent parts such that,

$$R_T = R_{Wave} + R_{ViscousPressure} + R_{Friction}, \tag{2.2}$$

where the subscript denotes the component part; wave, viscous-pressure and frictional resistance respectively and typically account for 59%, 33% and 8% of the total resistance, respectively [Webb *et al.* 2011]. The wave resistance component, however, diminishes until it becomes negligible as the swimmer increases distance from the water-air interface as is typical with UUS [Lyttle 1999] and may therefore be ignored for this underwater phase.

The remaining components of resistance hold a key influence on the resultant performance of a swimmer as forward propulsion is hindered by R_T. Consequently, much research has been undertaken to quantify it.

The term *passive drag* is attributed to the drag experienced by a swimmer when not actively swimming, akin to the naked hull resistance of a ship [Molland *et al.* 2011]. Logically, *active drag* is then the drag experienced by a swimmer while actively moving.

Holmér [1974] measured the passive drag and the perturbed active drag of three swimmers while also measuring their $\dot{V}O_2$. The swimmer was in a flume and holding onto a handle. The passive drag was measured using a strain gauge which was attached to the handle via a line and pulley system. The perturbed forces in the active drag scenario were achieved by hanging a mass from the same pulley system, either in-front or behind the swimmer, and attaching the line to a strap around the swimmer's waist. Using these measurements they were then able to infer each swimmer's propulsive efficiency for freestyle and breaststroke, defining propulsive efficiency as

$$\eta_P = \frac{D_{SW} \times v \times 60}{(\dot{V}O_2 - \text{SMR}) \times 4.9 \times 427} \tag{2.3}$$

where D_{SW} is the swimmer's active drag, v the swimming velocity, $\dot{V}O_2$ the rate of oxygen update during swimming, 4.9 the calorific value of oxygen and SMR the standard metabolic rate ($\dot{V}O_2$) at rest in the flume.

Subsequently there have been many other instances of publications measuring passive and active drag in swimming [e.g. Formosa *et al.* 2011; Hollander *et al.* 1986; Kolmogorov and Duplishcheva 1992; Webb *et al.* 2011]. Hollander *et al.* [1986] developed a system for *measuring active drag* known as the MAD-system and has been frequently cited in the literature. This system measures the force produced by the arms during freestyle swimming using pads positioned below the surface of the water. As the swimmer traverses the pool, they propel themselves forwards with their hands in contact with pre-positioned underwater pads. Each pad is connected to a common rod which in turn is connected to a force transducer and as the swimmer exerts a force on the pads it is measured in the transducer. It is assumed that when the swimmer is at a constant velocity, the mean push-off force is equal and opposite to the mean drag force [Toussaint and Truijens 2005]. The system, however, only measures the force produced by the arms. Even though majority of the propulsive force is produced by the arms [Holmér 1974], there is still some propulsion produced by the legs which this system fails to account for. This method of submerged pads from which to push-off, works well for freestyle where the pads may be easily seen and swimming at a near-constant depth and attitude. This, however, is less-well suited to other strokes such as breaststroke and backstroke, for example.

A simple, velocity perturbation method (VPM) was demonstrated by Kolmogorov and Duplishcheva [1992]. Here it required a swimmer to swim two lengths of a pool and

determine their velocity for each length. The first length would be swimming freely while the second would be towing an object to increase resistance. By swimming both lengths at maximal effort it is assumed that the power out is equally maximal and constant, and from which active drag can be determined. However, as demonstrated by Webb *et al.* [2011] this method of active drag measurement demonstrates high levels of uncertainty attributed to the experimental procedure and assumptions of constant power.

Another method to measure active drag are shown in [Formosa *et al.* 2011] and in [Webb *et al.* 2011]. These methods —more akin to those employed in naval architecture— use a tow-system and dynamometer arrangement. During active swimming, a swimmer is towed 5% faster than their normal free-swimming speed by a line attached to a belt around their waist. By towing above their normal swimming speed, the line remains in tension. Over-speeding the swimmer too much risks altering their kinematics from their free-swim technique. Conversely, by not towing the swimmer fast enough, the propulsion they generate means that momentarily they exceed the tow velocity, hence lose the tension in the line resulting in nothing to measure.

The base plate of the dynamometer is secured to the ground and the top aspect connected to the winch system. As the swimmer's drag varies the tension in the line varies and so the upper part of the dynamometer is displaced relative to its base. This displacement is thus proportional to the swimmer's net drag and so in measuring the displacement it is possible to measure a swimmer's passive and active net drag. In active drag scenarios where it is assumed the swimmer is generating propulsion as they move, the measured force is in fact their active drag less their propulsion ($R_T - T$).

While all of these methods provide a metric of performance, it is an overall metric of the stroke which does not necessarily identify the effects of individual components within the stroke. Holmér [1974] broke his study into arms only and legs only tests, however, it is unclear what impact this would have on the technique. While they showed the legs do not contribute much propulsion individually, in freestyle they have shown to enhance forward velocity by influencing the trajectory of the wrist during arm pull [Deschodt *et al.* 1999]. Consequently it is argued that neglecting them from the test would produce kinematics which are not truly representative.

Formosa *et al.* [2011] observed the advantages of synchronising video data with measure velocity or force data, concluding that this quantitative feedback provided a better source of knowledge from which the coach could plan intervention strategies. Similarly Thow *et al.* [2012] found that the data from their synchronous video and velocity method proved more effective in improving glide performance than other traditional methods. While beneficial utilities, it is not clear that the data from these methods are immediately discussed with coach or athlete. It is known that in the first example the information is often disseminated back to the coach and athlete upto a week following testing [private communication, British Swimming (BS) staff member, November 2010]. While a clearly presented report following testing is considered a useful resource for cataloguing trials and interventions, as well as for future reflection, it is considered immediate poolside feedback would have further and significant benefits. This would help the athlete to strengthen the connection between the task and completed action. Furthermore, the trials undertaken maybe adapted based on the quantified data thus allowing for more efficient and effective testing.

To improve an athlete's performance, directly comparing drag values between different athletes may not provide useful information. For example, to improve a triathlete's performance by simply comparing mean drag data to that of an elite swimmer might not generate any useful findings. Interrogating the differences in trajectories of the hands, for example, may prove more beneficial. The previously mentioned methods of quantifying drag measurements, however, do not facilitate such analysis. To investigate these skill differences, therefore, Bottoni *et al.* [2011] measured the pressure (using the KZ system by APLabs) at the hand of top level triathlon athletes and top level swimmers. Using this system they were able to visualise the intra-stroke pressure profile of the swimmers. They found that compared to the triathletes, the top level swimmers had higher mean pressure but not necessarily higher maximum pressure. They then intended to use these findings to attempt to improve triathlete's technique.

Although they demonstrated this system to produce insightful analysis of the kinematics comparisons between the test groups, its main drawback is its size. To measure the force at two small areas on each hand Figure 2.2 depicts the additional ancillary equipment necessary[1]. It is suggested that for bespoke testing this apparatus maybe acceptable. For more frequent and habitual testing, however, it is suggested that this would be

[1]Image from: `http://www.aplab.it/en/projects/kz.html` *Date Accessed: 06/03/2013*

deemed unacceptable by both athletes and coaches. Furthermore, if for example one were interested in taking pressure measurements at multiple locations on the body, it is apparent that a system based on this would be wholly impractical.

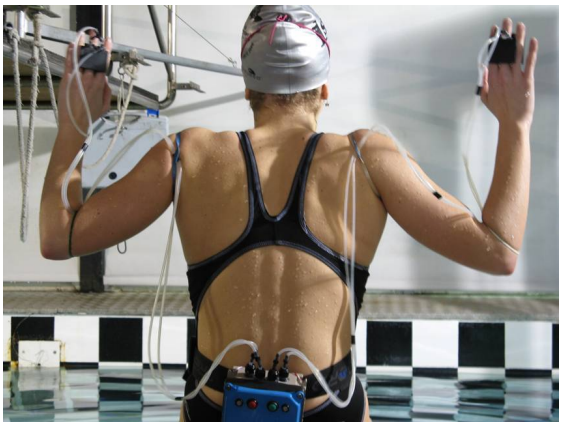

FIGURE 2.2: APLab's KZ system for measuring pressure on swimmer's hands[1].

Instead of measuring athlete's performance in the water, Zamparo and Swaine [2012] created a laboratory-based whole-body swimming ergometer (Figure 2.3). Attempting to replicate the hydrodynamic resistance to the motion, resistance to motion is applied by four air-dynes. These air-dynes are connected to hand and feet paddles by pulleys and ropes and provide resistance when pulled upon. The swimmer is suspended in a cradle supported at the torso, with their hands and feet strapped into the paddles.

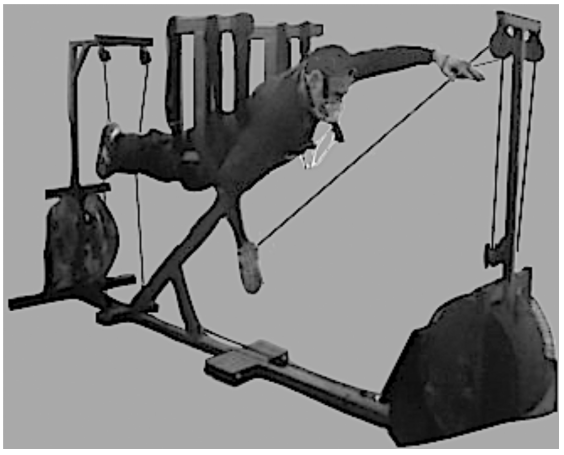

FIGURE 2.3: The laboratory-based whole-body swimming ergometer from Zamparo and Swaine [2012].

They consider their new ergometer to be an improvement upon previous methods of laboratory-based swimming benches. They describe how previously, swimming benches have contributed to knowledge and understanding of swimming in areas such as the influence of muscle power in freestyle performance and cardiopulmonary responses in

swimming exercise. However, they also suggest that previous instances have been constrictive on the motion permitted, particularly of the torso. They state that with the addition of the cradle, the erogmeter increases its capacity for the torso to flex laterally as well as enabling body roll. They describe the importance of body roll in freestyle swimming and therefore by facilitating it better replicates the real kinematics, however, to what extent remains to be established. They also acknowledge the limitations in how the hands and feet are resisted, with forces in the transverse plane unaccounted for. In addition to these, the effects due to buoyancy, the distributed load and interactions of the fluid are also neglected. It would also be impractical for strokes such as underwater flykick, for example.

Nevertheless, with this ergometer they were able to obtain estimates for the power produced for freestyle and examine the relative contribution of the legs compared to the arms. Furthermore, they conclude that in using this ergometer, while acknowledging its limitations, it is suggested that previously published values of the overall efficiency of freestyle swimming are likely to have been underestimated and conversely, propulsive efficiency to have been overestimated. They attribute this to the difficulty and incomplete quantification of all mechanical factors that contribute to the total mechanical power out.

2.1.2 Computational Methods

Many computational methods for assessing swimming performance are primarily employed to investigate the resistance and propulsion aspects of a stroke. Bixler *et al.* [2007] created a computational fluid dynamics (CFD) model of a swimmer in the glide position and verified and validated their results against the experimental testing of both a mannequin and a human participant. With this model they were able to measure 6% increase in drag from the bare mannequin to the mannequin with briefs. Although this provides a high fidelity of analysis, they do not specify the time taken to solve each trial. It is imagined that with a mesh count of 2.6 million cells this would take a significant time to solve. The study was performed in collaboration with Speedo International and would equally be supposed that the target focus would be to investigate swimming garments and accessories, for which it is well adept. To be used in the context of UUS and assessing technique and or performance it may be viewed to be ill-suited.

Von Loebbecke *et al.* [2009], however, used a fully unsteady CFD method to analyse UUS. The significant limitation of this method was the time to solve for each kick, was equivalent to 250 hours of a computer time. Similarly, Cohen *et al.* [2012] investigated UUS but employing smooth particle hydrodynamics (SPH) instead, but again do not disclose the required solution time.

Despite the drawbacks associated with the time penalty of these techniques they are well established analytical methods and thus typically provide reliable results. Both the CFD and SPH methods provide quantitative results —as in Cohen *et al.* [2012] which quantified the effect of stroke frequency on thrust produced. They are also capable of portraying the data visually and consequently making effects such as vortex shedding at the end of the extension phase of the leg kick—down-kick—, quite apparent. They both also illustrate that it is only in this phase of the cycle, that a vortex is shed and that in the flexion phase of the cycle —up-kick— there is no vortex. Von Loebbecke *et al.* [2009] also show the thrust profile during each kick, exhibiting a peak thrust of approximately 750 N for the male athlete.

These methods provide accurate a reliabel results, however, at the expense of time. Lighthill [1971] proposes a numerical method for estimating the thrust and fluid force loadings on a fish. Webb *et al.* [2012] investigated its eligibility to be used for calculating these metrics for human UUS as opposed to fish propulsion. They concluded that model might be used for UUS although some of the finer aspects of the technique may be missed. As corroborated by Bertetto *et al.* [2001]; Singh and Pedley [2012] this Lighthill model typically provides correct phasing and often mean values of the generated thrust but may overestimate the magnitude of the forces. Further detail of the Lighthill model is discussed in Section 4.3.

Another alternative method of computationally analysing human swimming is exemplified in the SWimming hUman Model (SWUM) developed by Nakashima *et al.* [2007].This model simulates the human body as a series of 21 elliptic cones to which a range of parameters are individually applied. These include, external dimensions, density and hydrodynamic coefficients obtained from experimental data. Each segment is defined in space and its angle relative to the global reference system. It is capable of estimating the fluid forces on each segment and hence on the entire body. It achieves this by firstly contemplating each truncated elliptical cone individually. Each cone is then broken

down further into strips, or plates, in the longitudinal axis of the segment. The inertial and drag forces are assumed then to act at the centre of these strips. The surface of the strip is subdivided into small quadrangles. It is upon these that it assumes the buoyancy force acts. The model also determines whether the segment is in or out of the water and applies the buoyancy force accordingly. The model then proceeds to integrate all the forces in the longitudinal axis of each segment. The summation of all the truncated elliptical cones then provides the system with the external forces and moments with which it solves its governing equations.

While many of these computation methods facilitate analysis of swimming and or UUS, one of the important aspects of the trade-off metrics in performance is not accounted for; energy expenditure.

2.1.3 Energy Cost of Locomotion

The efficiency of a system is simplified as the ratio of the useful energy out of the system to the total energy in. In order to estimate the overall efficiency, therefore, quantifying the energy usage is paramount.

Twomey *et al.* [2010] investigated four different algorithms which analysed accelerometer data to estimate energy expenditure in gait at different forward velocities. These algorithms demonstrated high level of accuracy as compared with the gold standard of indirect calorimetry (the root-mean-square error (RMSE), normalised to one, ranging from 0.065737 to 0.135009). The accuracy of these results, however, depends upon a reference dataset which is initially used to regress the accelerometer data. They also acknowledge that despite the high level of accuracy, the results are also affected by scenarios which interfere with the accelerometer data; including coughing and talking. It is imagined then that transferring this methodology directly to UUS would be problematic.

An aspect that would still be required for the reference dataset is known levels of energy expenditure for different activity levels. Their reference data was gathered from indirect calorimetry. This technique exploits the fact that the heat that a living organism produces is a function of the ratio of O_2 inhaled and CO_2 exhaled. In the study a mask was placed over the subjects' mouth and nose and the expressed gasses measured while performing the assigned task. The heat energy is then related to the overall energy

expenditure. Thus by measuring this gaseous ratio, heat energy can be inferred and subsequently be regressed to provide energy expenditure [Twomey *et al.* 2010].

Reis *et al.* [2010] and Zamparo and Swaine [2012] used similar methodology to measure the energy expenditure of swimmers directly; the former measured energy expenditure during breaststroke swimming in the pool while the latter measured the energy expenditure of a subject performing freestyle technique on their swimming ergometer.

Measuring these gasses in a laboratory is common and so the swimming ergometer is well suited for this type of analysis. Zamparo and Swaine [2012] note peak $\dot{V}O_2$ in the region of $60.11\,\mathrm{ml\,kg^{-1}\,min^{-1}}$ for freestyle technique using their ergometer. Measuring these data in a pool by contrast is more challenging. Reis *et al.* [2010] used the a CSMEG K4B2 snorkel —as depicted in Figure 2.4 —to measure the breath-by-breath gaseous exchange for breaststroke, recording peak $\dot{V}O_2$ at $65.28 \pm 11.36\,\mathrm{ml\,kg^{-1}\,min^{-1}}$. Barbosa *et al.* [2005] used the same snorkel to measure energy expenditure of national level butterfly swimmers, finding a linear relationship between energy expenditure and velocity ($R^2 = 0.683$). For reference, the peak energy expenditure was approximately $105\,\mathrm{ml\,kg^{-1}\,min^{-1}}$ at $1.36\,\mathrm{m\,s^{-1}}$. It could be a suitable if not valuable method for acquiring reference data periodically. However, although it is able to record the breath-by-breath energy expenditure of the swimmer, similarly to the pressure sensing device in Section 2.1.1, it would be cumbersome and unrealistic realistic to use on a frequent basis with athletes.

Furthermore, the measured rate of energy consumption does not provide an instantaneous response and measurements are typically taken over a period where the the metabolic rate has reached steady state [Twomey *et al.* 2010]. In this gait example, the task was performed for between two and three minutes prior to a 20 s sample recorded for analysis. In the land-based ergometer, each task was performed for 60 s over which a 30 s sample was used for analysis. In the breaststroke example each sample was taken over a 20 s period. In contrast to gait especially, UUS at *race-pace* is considered to be much more arduous and it would not be feasible to perform multiple consecutive trials for the duration required for steady state to be achieved.

Boitel *et al.* [2010], however, was able to use this methods for assessing performance of elite monofin athlete. In this example the athletes were operating at sub-maximal conditions and with the aid of the K4B2 snorkel, were able to sustain the stroke for sufficient time that measurements could recorded. This consisted of the four highest

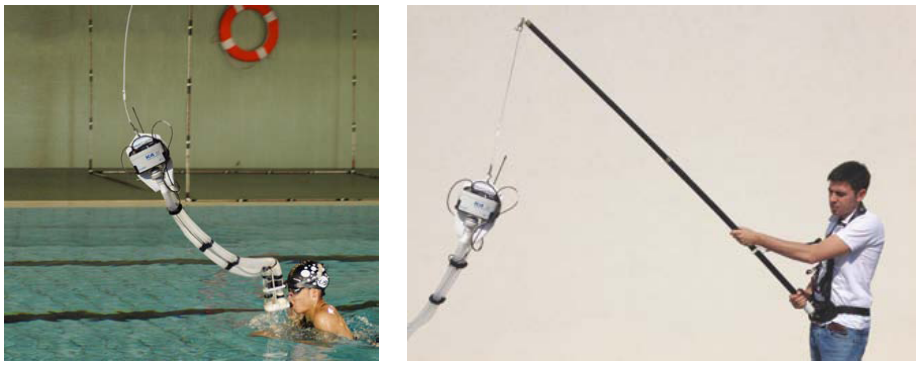

(a) (b)

FIGURE 2.4: COSMEG K4B2 breath-by-breath snorkel facilitating *in-situ* gas exchange analysis of swimming. [COSMED 2012]

consecutive, 10 s $\dot{V}O_2$ averages during the final 120 s of each trial. The mean $\dot{V}O_2$ of all eight athletes for the trials was $42.6 \pm 6.9\,\mathrm{ml\,kg^{-1}\,min^{-1}}$. In this study they observed significantly lower energy consumption kicking 10% above the athletes' preferred kick frequency than 10% and 15% below their preferred kick frequency. This an interesting finding as energy expenditure would typically be expected to increase with frequency. The authors suggest this could be artefacts of the trial and subsequent investigations would be recommended.

While this is shown to be applicable to surface and monofin swimming, it is a method suited to aerobic conditions. In the context of UUS, the body is fully submerged and consequently the athlete would not inspire oxygen until re-surfacing. It is unclear what affect performing UUS while able to inhale and exhale would then have on any observations made using this methodology.

Expended energy pertains to the mechanical work done by the body. Musculoskeletal models - which will be discussed in more detail in Section 2.2 - simulate the kinetics of a musculoskeletal system. They can therefore be interrogated to estimate the muscular energy expenditure required for a given task. The total energy associated with a muscle is comprised of both mechanical energy and heat energy. The model proposed by Anderson and Pandy [2001] evaluated the mechanical work to account for 31.2% of the total estimated energy. Umberger *et al.* [2003] developed a computational muscle model that would then estimate the total energy expenditure of a simulated musculoskeletal model. Umberger [2010] then utilised this model in evaluating the energy cost in the stance and swing phase of the gait cycle. Similar results, for both trends and magnitude of gross

and net metabolic power were observed between the simulation and experimental data; approximately 4.5 Wkg^{-1} from the experimental data and 5 Wkg^{-1} from the model data at the participants' preferred stride rate.

2.2 Musculoskeletal Modelling

Musculoskeletal modelling simulates the dynamics of a rigid-body system in a biological context. Given the correct morphological data, any organism can be modelled (e.g. Wehner *et al.* [2010] investigated fractures in rat femurs), however, those most commonly found are that of the human body, or part thereof. These models provide insight into many different areas from classification in clinical research [Cleather and Bull 2012; Saraswat *et al.* 2010; Worsley *et al.* 2011] to geometric optimisation of industrial equipment [Dubowsky *et al.* 2008; Rasmussen *et al.* 2009]. With reference to performance related to sport, they have been employed to minimise joint forces exhibited in wheelchair propulsion [Dubowsky *et al.* 2008], performance indicators in badminton [Kwan *et al.* 2010] and used for analysis of cross country skiing [Holmberg and Lund 2008]. As far as swimming is concerned however, Nakashima and Yugo [2007] is the only instance of musculoskeletal modelling demonstrated. Published in 2007 in the proceedings of a conference, it is lacking in detail and analysis. Subsequently there appears to be no further published work on the topic.

Musculoskeletal models subsequently fall into two principal forms; *forward dynamics* and *inverse dynamics*. They both require boundary conditions and external forces to be specified, such as fluid forces or ground reaction forces. Forward dynamic models also require the muscle forces to be stipulated and from these data it is able to infer the body's resultant motion. Inverse dynamics in contrast requires the segment motions to be prescribed and infers the muscle forces necessary to achieve the given motion under the known boundary conditions.

2.2.1 Specifics of a Musculoskeletal Model

The specific software that is used to develop the model in this thesis is the AnyBody Modelling System (AMS). The AMS is a commercial software for conducting inverse dynamic musculoskeletal modelling and is cited in many publications [AnyBody 2011].

For each model in the AMS bones are represented as rigid body segments in three-dimensional space. Each segment has a mass and inertia property and six degree of freedom (DOF); three in translation and three in rotation. In order for the equations of motion to be solved, each DOF must be constrained in some manner. In the AMS this is achieved by using *joints* and *drivers*. There are two main categories of joints, hinge and spherical. A hinge joint connects two segments, permitting a single axis rotation about the two segments - e.g. the knee joint - and removes two DOF. A spherical joint connects two joints leaving the relative rotational DOF free - e.g. the hip joint, analogous to a ball and socket joint. It is then for the user to define the manner in which these constraints are implemented to facilitate motion.

In the context of a lower limb cycling model [Purdue *et al.* 2010], for example (as seen in Figure 2.5), the root node is at the pelvis and is assumed to be rigidly attached to the saddle, which in turn is at a fixed position in space and so no translation is permissible. The same is true of the node on each foot segment relative to the pedal node. At the foot, rotation is prevented in yaw and roll, but left free to pitch about the pedal, leaving only the pitch rotation to be prescribed. The position of the foot is therefore dictated by the position of the pedal node. This pedal node location is driven in x and y-axis by a time-variable *linear driver* while the z-axis position is driven by a time-invariable linear driver, i.e. a constant position. In this example, it is these coordinates that are varied to solve the optimisation criteria.

FIGURE 2.5: An example of a cycling musculoskeletal model from [Purdue *et al.* 2010].

The remaining segment motions kinematics are driven from optical motion capture data (described in further detail in Section 2.3.1). These data provided the three-dimensional coordinates of multiple markers (> 3) on each segment of the body - torso and lower limbs. These markers are replicated in the AnyBody model as nodes rigidly attached to the respective segments. Three-dimensional linear drivers are then prescribed to each node using the time-variable data from optical motion capture. In reality, only three markers are required to determine a segment's position and orientation, and so there is redundancy built into the model. Due to experimental errors (e.g. image processing methods or soft tissue artefacts), the model's constraints (e.g. joints or segment lengths) and the assumption that the segments are rigid bodies, driving all the nodes with the acquired data will cause the simulation to fail. The AMS therefore has an optimisation procedure which deals with these over-constraints. This is achieved by using a statistical method by permitting a small variation of each node in user-defined axes. An optimisation process then determines the optimal position of each node in the system (that represents the reflective markers) relative to its specific segment. Hence using these data, the segment locations and rotations are defined for this example.

An alternative method to driving a model from point data is to drive the relative segment angles, i.e. the joint angles - for example, knee flexion angle. This has the advantage of being more anatomically intuitive, particularly in analysing the swimmer's kinematics and its effect on performance.

2.3 Acquiring Human Kinematics

2.3.1 Digitised Video

Video analysis has played a traditional role in sports analysis. It can provide a cheap, non-invasive and reliable process with which to obtain metrics that can be analysed to improve an athlete's performance. In the world of swimming, video analysis has been used to easily determine fundamental parameters, including swim velocity and stroke rates [Seifert *et al.* 2007], which can otherwise be difficult to acquire. Additionally, video analysis can be used to determine human kinematics of swimming. As illustrated in Figure 2.6, Ohgi [2002] manually digitised two synchronised video cameras to produce a three-dimensional reconstruction of a swimmer's freestyle arm stroke. It required

markers on the swimmer's shoulder, elbow, wrist and metacarpophalangeal joint. Additionally it required placing two remotely controlled pan-tilt cameras underwater, one diagonally left and in-front of the swimmer and the other diagonally left and behind the swimmer. A series of calibration markers were also hung from the lane markers to facilitate in the three-dimensional reconstruction.

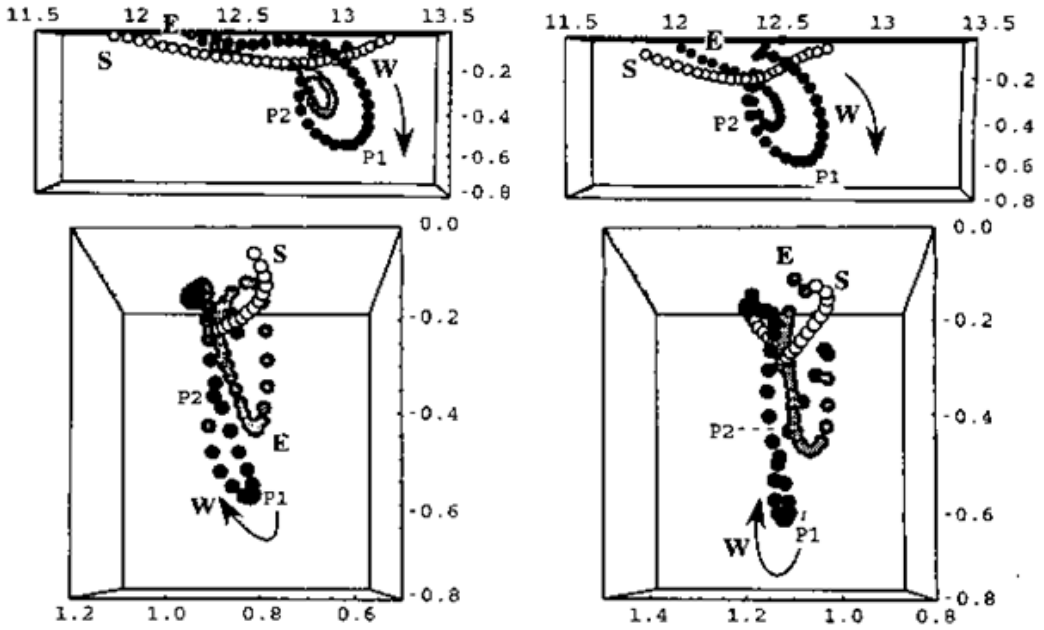

FIGURE 2.6: A 3D reconstruction of a freestyle arm stroke, produce by manual digitisation. S,E and W represent the path taken by the shoulder, elbow and wrist respectively [Ohgi 2002]

This set-up is able to provide the location of specific points in time and space. If these markers are strategically placed on the swimmer, their kinematics may be determined by the manual digitisation process. This typically requires a user to click on each marker in each frame of the video. Furthermore, this process needs to be undertaken for each camera. For example, if the *Sony EVI-D30* camera used by Ohgi [2002] had a frame rate of 50 frames per second (fps) and the time for one arm stroke one second and the operator had to accurately select four markers in each frame, for each camera, the operator would have had to select 400 points for just one arm cycle. While this is not a computationally expensive nor fundamentally challenging task, it is laborious and monotonous, and hence it is prone to human error. The process of digitisation, however, may be sped up by using computer software to automate the procedure. Although Wilson *et al.* [1999] finds the automated process to be less accurate than a human performing the same

task (selecting three points to determine the angle between them), they deduce that the automated process to be within error ranges reported in other literature and therefore clinically acceptable (error range for 12 angles: $0.028° - 0.556°$).

2.3.2 Optical Motion Capture

An alternate method for acquiring human kinematics is by using a semi-automated optical motion capture process. There are numerous commercially available systems on the market, including Codamotion [Codamotion 2013], PhaseSpace [PhaseSpace 2013] and Vicon [Vicon 2013]. The biomechanics laboratory in the the Faculty of Health Sciences at the University of Southampton have a Vicon MX T-series system installed. In this laboratory the kinematics for Purdue *et al.* [2010] were acquired. The kinematics are obtained in a more automated process but not too dissimilar to the manual process described in Section 2.3.1.

In this method, markers are placed at specific anatomical locations on the participant's body. The exact number and location varies depending on the protocol being followed, however many are based upon the Helen-Hayes method [Kadaba *et al.* 1990]. Current methods typically favour three markers on each segment with additional *technical* markers and marker *clusters* [Collins *et al.* 2009]. The markers are small spherical polystyrene balls, wrapped in retroreflective Scotchlite^{TM} tape. Their size varies depending on where they are located, from 2 mm diameter on a finger to 14 mm on the thigh for example.

Surrounding the participant are an array of 12 GigE cameras (six 4-megapixel and six 16-megapixel with a sample rate of 120 Hz), each encircled by an array of near infra-red LEDs. The emitted light from the LEDs is reflected by the markers into the lenses of the cameras. Each camera has an on-board image processing unit. By filtering out all the light frequencies other than than the infra-red and near infra-red, the image is processed to determine the centroid location (in pixels) of each of the markers in its direct field of view. These data are then sent back to a central computer. Using the data from the 12 cameras, the software is then able to calculate the real-world coordinates for each of the markers [Kadaba *et al.* 1990], during the course of filming. Other information, such as analogue force or Electromyography (EMG) data may also be centrally recorded [Dubowsky *et al.* 2008] thus creating a completely synchronised and real-time output of video, force and EMG. The data produced from this process is highly accurate and

typically used as a gold standard to which to compare other systems [Kwakkel 2008]. Madgwick *et al.* [2011] used Vicon's Nexus system with which to validate their system base on inertial measurement units (IMUs).

While optical motion capture techniques are widely accepted to produce reliable and accurate data for use in biomechanical analysis, it relies on high-quality expensive hardware which is best suited to remain in a fixed location such as a laboratory. Consequently, there are restrictions on the size of the acquisition space. This is often not problematic where there is sufficient room to perform the task, such as for gait analysis. For biomechanical analysis of sprinting or long-jump in athletics for example, a laboratory may well be inadequate. Furthermore, where the task under scrutiny requires a specific environment in which to perform, a laboratory may be ill-suited as compared to the native environment. This is especially true of swimming where the hydrodynamic and buoyancy forces have significant effect on the athlete. Even in the full-body swimming ergo in [Zamparo and Swaine 2012], for example, these forces are unaccounted for. A system such as this would most probably provide insightful analysis, however, it is not representing nor capturing the true scenario.

Despite the drawbacks outlined in the previous paragraph, researchers from Manhattan Mocap [ManhattanMocap] (affiliated to New York University, USA) however managed to acquire kinematic data of an elite athlete, diving in from the block and performing swimming underwater dolphin kick. Currently there are no academic publications of their findings but it is possible to view initial video evidence posted on their website[2]. From these videos, it appears that they have managed to capture the full kinematics of the athlete and most importantly, captured in the native environment. What is also apparent from the video is the numerous staff and equipment required to capture the motion for this one athlete in their normal environment, both of which would be potentially prohibitive to undertake regular assessment of for example, an entire Olympic squad.

One of the challenges with optical motion capture methods is marker occlusion —where the marker becomes occluded from the line of sight of the camera. This could be be as a result of a participant's limb passing in front of a marker or in the case of the

[2]Motion capture of butterfly: `http://youtu.be/_BGTt9e-Dek` *Date Accessed: 04/03/2013*

swimming example, entrained bubbles in the water as the body or hand enters or re-enters the water. One purpose of having a multi-camera, multi-marker system is to try to minimise these occurrences such that each maker should be visible by at least two cameras or that each segment has at least three markers visible to the cameras at any given time. The system also relies upon light reflecting from the markers into the cameras and the algorithms able to ascertain these reflections as markers. Additional reflections appearing in an image —light reflecting off metallic handlebars of a bicycle, for example— may cause the algorithms to confuse which are markers and which are noise.

When observing the video [2]closely it is clear that the auto-recognition of the markers *drops-out* momentarily near the free-surface, particularly as the athlete enters the water. One might attribute this to the markers becoming occluded by the entrained bubbles or because of noise in the data due to reflections from these bubbles or even the free-surface.

2.3.3 Inertial Sensors

Historically IMUs have been used in the aviation industry for determining the orientation of aeroplanes and hence used for in-flight navigation. Typically these devices were large heavy mechanical devices by comparison to modern MicroElectroMechanical systems (MEMS) devices. MEMS technology has enabled IMUs to become much smaller and lighter such that they have become ubiquitous in popular consumer technology such as smartphones and tablets - both fuelling demand and driving progress. Consequently they have become acceptably sized and thus sparked great interest in using them for kinematic and biomechanical analysis. Companies such as Xsesns [Xsens 2013], Sensorize [Sensorize 2013] and Shimmer [Shimmer Research 2013] have each produced MEMS products which have each been used in biomechanical analysis. Similarly to the aeroplane, IMUs attached to a segment of a human body is able to determine the segment's orientation relative to a global reference. If IMUs are attached to each segment then each segment's orientation is known relative to the global and hence one can infer the relative angles between segments.

Three-axis orientation may be achieved using an accelerometer, a rate-gyroscope, a magnetometer and a global positioning system (GPS) unit, or a combination thereof. To provide tri-axis Euler rotation angles, each component typically consists of a collection

of three sensors aligned to each axis of reference (with the GPS where only one component is required). An accelerometer measures the acceleration ($a\,[\mathrm{m\,s^{-2}}]$) - including acceleration due to gravity (g) - a rate-gyroscope angular velocity ($\omega\,[\mathrm{rad\,s^{-1}}]$) a magnetometer the strength and direction of the Earth's magnetic field ($H\,[\mu\mathrm{T}]$), and a GPS unit the geographic latitude and longitude relative to Earth ($\phi_E, \lambda_E\,[^\circ]$).

Miyazaki [1997] integrated a single rate-gyroscope in order to obtain gait metrics including stride length and walking velocity. Williamson and Andrews [2001], however, progressed to combine a rate-gyroscope with an accelerometer using each component to calculate orientation. For each of the individual components there are errors associated with their measurements, however in combining them with a fusion algorithm it is intended to reduce these [Woodman 2007]. With this in mind, Williamson and Andrews [2001] placed one sensor on a participant's thigh and one on their shank. By knowing the inclination of these segments they were then able to calculate the relative angle between them and hence determine the knee joint angle. They used a goniometer as their reference to which to compare the sensor derived data. They concluded that the error between the goniometer and the sensor data (maximum 2.4°) was an improvement on that that they found in the literature ([Luinge *et al.* 1999] published errors exceeding 5°).

To further reduce errors, it is possible to use absolute positioning systems or take *pseudomeasurements*, assumptions about the kinematics.

Brodie *et al.* [2008] for example, developed a custom fusion algorithm to utilise accelerometer, gyroscope, magnetometer, thermometer and GPS data to analyse downhill ski racing. Their sensor fusion algorithm managed to increase position accuracy from $\pm 5\,\mathrm{m}$ to $\pm 1.5\,\mathrm{m}$ and IMUs orientation error from $\pm 20^\circ$ to $\pm 5^\circ$.

Foxlin [2005] alternatively, used the observation that during the gait cycle the foot will be periodically planted to the ground. These location are recognisable as spikes in the accelerometer data. Furthermore, at these locations the foot velocity while in contact with the ground is zero. It was then demonstrated that using these pseudomeasurements it was possible to reduce the velocity error growth, proportional to time-cubed, to proportional to the number of steps taken.

While these methods may improve the errors in the system, they may also be impractical in scenarios other than for their intended situation. One of the fundamental constraints with the optical motion capture methods is that they are generally confined to the indoors. A fundamental constraint with GPS is the necessity of having line of sight visibility to orbiting satellites and thus necessary to be outdoors. In the example of swimming, in the UK a least, it is impracticable to acquire data outdoors. Furthermore, except at the start and turn phases in swimming [Le Sage *et al.* 2011], pseudomeasurements are limited to generalistic assumptions about the stroke. Although Dadashi *et al.* [2012] produced an algorithm to processes accelerometer and rate-gyroscope data using biomechanical constraints and cited a $0.6 \pm 5.4\,\mathrm{cm\,s^{-2}}$ difference to their comparison. However, the assumptions included, for example, that the sacrum will roll equally about the long axis of the pool. It was also constrained to further assumptions attributed to freestyle only were it was assumed that peaks in velocity would be constant due to *steady regime of swimming*. While they have demonstrated these assumptions valid for freestyle, they would not necessarily be valid for butterfly of breaststroke, for example, where the magnitudes of the velocity peaks vary intra-stroke. Furthermore, the assumption of roll potentially only holds-true for the sacrum and not intuitively so for other segments thus preventing individual segment analysis.

As with in the previous examples [Brodie *et al.* 2008; Foxlin 2005] the algorithms used to determine the sensors orientation are an implementation of a Kalman filter. Unlike the previous examples, however, Sabatini [2006] and Madgwick *et al.* [2011] only used three sensors to determine the sensor's orientation; a tri-axis accelerometer, rate-gyro and magnetometer. Data from these components all fed into a non-linear Kalman filter, or *extended Kalman filter (EKF)*, where the accelerometer and magnetometer both work towards reducing the error from the integration of the rate-gyro. Sabatini [2006] developed an EKF, specifically for use in the field of human movement adding. Similarly Madgwick *et al.* [2011] produced an EKF which demonstrated errors of $< 0.6°$ for static cases and $< 0.8°$ for dynamic cases.

Expanding upon the use of IMUs to calculate a single joint angle, results of this kind therefore gives rise to the possibilities of a full body sensor network (BSN) - a system that is self-contained, portable and provides reliable and representative data.

Many of the published examples of human kinematics are in the context of sports and

athlete monitoring. Of those demonstrated, the Xsens system has been widely evaluated. Much of the background work is presented in the doctoral thesis at the University of Twente [Roetenberg 2006]. Implementations of its use including in kinematic acquisition of a snowboarder [Kruger *et al.* 2011], skiier [Brodie *et al.* 2008] and rower [Tessendorf *et al.* 2011], and has recently been adopted by the English Institute of Sport (EIS)[3]. Results from the Xsens devices have been shown to demonstrate good agreement with their benchmark - Kruger *et al.* [2011] showed a maximum mean deviation of 4.8° (±0.3°) concluding it to be suitable for biomechanical analysis in a field-based setting. The primary drawback from using a system such as Xsens's or that presented by Vlasic *et al.* [2007], for example, is the size and weight of the equipment. Each of these systems use nodes on each segment, comprising of the three tri-axis sensors but are connected to a central processing unit by wires which make the system bulky and undesirable. Additionally, the battery packs are external to the sensor nodes and would make these systems impractical for capturing the motion of a swimmer.

IMUs have also been investigated from a more clinical perspective [Bergmann *et al.* 2009] investigated a wearable sensor network to ascertain its suitability for determining anatomical joint angles of the lower limbs during stair climbing. They compared the IMUs results with an optical motion capture method and found a strong correlation between the two systems (range from 0.93 to 0.99) as well as a mean RMS error of 4° across all the joint angles. They concluded that the system was sufficient for both clinical and research uses.

An alternative off-the-shelf IMU is produced by [Shimmer Research 2013]. From publications they appear to have mostly been used for clinical applications such as for gait analysis [Greene *et al.* 2010] and also the monitoring of conditions such as Parkinson's disease [Lorincz *et al.* 2009]. Schulze *et al.* [2012], however, presented the results of on-going research into using 9DOF Shimmer sensors for evaluation of knee joint angle. Once more, the data calculated orientation angles from the sensors were compared to a Vicon optical motion capture system. Similarly, they conclude a strong overall correlation (0.99 with an overall RMSE of 2.72) which is satisfactory for a clinician's point of view.

[3]Xsens welcomes EIS as new customer
http://www.xsens.com/en/news/movement-science-news/xsens-welcomes-the-english-institute-of-sport-eis-as-a-new-customer *Date Accessed : 05/03/2013*

Both the Xsesns and Shimmer products support wireless Bluetooth capabilities and the Shimmer sensors also has the capacity to log data locally to SD card. The individual sensors are of similar dimensions and mass; the Shimmer measures $53 \times 32 \times 19$mm and weighs 27g while the Xsens is $53 \times 38 \times 21$mm and weighs 30g. However, if creating a full body BSN consisting of 17 9DOF, as with the Xsesns MVN BIOMECH,[4] for example, the Xsesns all-up weight is 1930g (Figure 2.7(a)). In comparison an equivalent system of Shimmer sensors would weight 459g (concealed under the blue tape in Figure 2.7(b)).

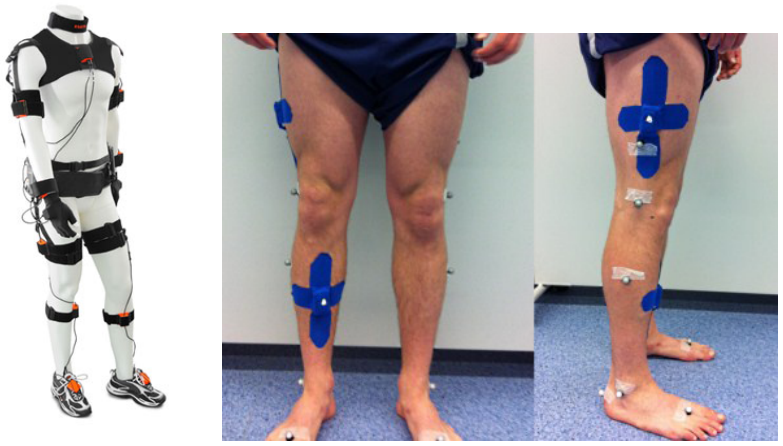

(a) (b)

FIGURE 2.7: An example of the Xsesns (a) body sensor network [3] and the Shimmer sensors (under the blue tape) (b) being validated against an optical motion system [Schulze *et al.* 2012].

2.4 Summary

By exploring published material one begins to appreciate and comprehend the vast quantity of work relating to swimming performance undertaken by other researchers around the World. It is apparent that performance of swimming is a much researched topic. It is also apparent that performance is inextricably linked between the energetic cost associated with moving the body, the pattern of motion or technique adopted and the consequential resistive and propulsive forces.

From this search it would suggest that quantifying the energy expenditure of a swimmer using musculoskeletal modelling is unprecedented. Studies have been undertaken

[4] Xsens MVN BIOMECH 3D kinematic measurement system
http://www.xsens.com/en/general/mvn-biomch *Date Accessed: 05/03/2013*

to measure this experimentally, but none using musculoskeletal methods. Musculoskeletal models have, however, been demonstrated successfully in the estimation of energy expenditure for a gait cycle. The gait cycle is an habitual activity for the majority and therefore, as might be expected, much research of this cycle has been undertaken. It also lends itself more easily to musculoskeletal modelling than swimming, most significantly because of the medium in which it occurs. As has been described, the force loadings are of significant importance in the musculoskeletal modelling process. A gait cycle in the medium of *air* experiences negligible resistance to the body motion and is generally ignored. The significant reaction forces are experienced at the foot when in contact with the ground. These ground reaction forces are easily measured using force platforms, for example. The challenge then for a swimmer, is to measure or estimate these forces. While there is no ground reaction force as such, the hydrodynamic forces are clearly significant.

It is perhaps the challenge of determining and implementing these interaction that has made it this an area in which little research has been published. CFD, SPH and even the SWUM model are each capable of providing these force data. However, their primary limitation is the time to solve each time step and the challenge of integrating these methods into a holistic model. Conversely, Lighthill's theory on fish propulsion has been demonstrated to represent these forces reasonably well in terms of trends and phasing, while perhaps not capturing the magnitude of the forces so well. Furthermore, this numerical approximation has the significant attraction of its ease of implementation and assumed speed at obtaining a solution.

Prior to the research presented in the subsequent chapters of this thesis, there has been no holistic methods for performance analysis of human UUS. No previous example was found that begins with the capturing of the athlete swimming, deduces their kinematics, models the fluid force interactions, simulates their muscle activities and provides an estimation of the energy expended for the original kinematics. Consequently there appears not to be any computation optimisation of UUS which addresses both the athlete's propulsion and muscular energy expended.

Equally, there have been no publications found which attempt to use a network of IMUs to capture human kinematics for use in musculoskeletal models, particularly of swimmers.

The subsequent chapters addresses these identified limitation in current understandings and procedures; facilitating and contributing to detailed analysis of human UUS. The chapter immediately following, introduces the starting point of this path; the process by which the initial experimental data is captured.

Chapter 3

Software Developed for Experimental Data Capture

As a prerequisite to the computational modelling, it is necessary to be able to acquire experimental data to complement the computational data and methods. This chapter provides an overview of *iDAQ* —*i*mage and *D*ata *A*c*Q*uisition— the software developed for this purpose and developed concurrently to the musculoskeletal model.

The software was further developed for providing the engineering support to British Swimming (BS) as part of the SwimSIM project. For this project it was also necessary to be able to acquire experimental data but to also —as discussed in Section 2.1.1— analysis it and feedback the findings poolside, immediately following the trial. Prior to the project SwimSIM, BS did not have any such software or hardware capacity.

Consequently, iDAQ —and other hardware developed by other SwimSIM researchers— was developed to facilitate the collection of experimental data required for both this thesis and the theses of the other researchers, as well as in providing support to BS.

3.1 Development Overview

Image and data acquisition software, *iDAQ*, was developed in *Matlab* with a graphical user interface (GUI) for easy of operation. As implied by its name, iDAQ was developed to acquire synchronous image and analogue data. More extensively, however, it

facilitates the calibration, acquisition, synchronisation, processing, interrogation, dissemination, storage and annotation of the data immediately after each trial —all of which happens poolside.

The synchronised video and data can be displayed side-by-side for immediate interrogation by those involved in the trial. This small but significant capability was not possible prior to the SwimSIM project. In displaying the data in this way allows for quantitative feedback encouraging informed discussion and thus creates a cognitive link for the athlete, between the task just completed and the evidence-based results. In addition to this, statistical analysis can be provided following each run allowing for more insightful analysis. These statistics, for example, may include: mean and standard deviation velocity; mean stroke rate; mean velocity per stroke; and in freestyle and backstroke, mean drag forces experienced for left and right arm phases. The data, along with any comments taken, are also automatically saved allowing a trial to be re-opened and revisited at a later date. The feedback screen for a specific trial can be saved as an image and printed as a reference to quickly and easily refer back to. Figure 3.1 shows the poolside feedback centre being utilised for athlete performance analysis at the London Aquatic centre.

Development of iDAQ began in August 2010. The need for synchronous force and video data became clear following SwimSIM's first testing session with elite athletes the month previous. It initially consisted of a simple user interface with the capacity to acquire and store data and the version was trialled in Southampton on 13th September, 2010. Its remit grew rapidly as more demand was placed on viewing the data immediately after acquiring a run. By the 2nd November 2010, in Loughborough —SwimSIM's second testing session with elite athletes— iDAQ had expanded to incorporate a dedicated feedback screen. This enabled controls necessary for setting up and acquiring the video and data, to be separated from what was displayed to the coaches and athlete. Over the subsequent years continual improvements were made to the system to increase capabilities as well as speed of operation.

By the time of the pre-Olympic training camp at the London Aquatic centre in April 2012, the iDAQ software had expanded further to having customised feedback screens for analysing freestyle and backstroke, butterfly, underwater undulatory swimming (UUS) and breaststroke. It was also able to interact with submerged light strips for interaction with the athlete during the test. Networking multiple computers together increased the

set up time for each run as one machine could be preparing for the next acquisition while another providing analysis and feedback to the athlete and coaches. Another significant development by this point was the incorporation of inertial sensor data into both the acquisition and feedback elements of the system. For example, this enabled the athlete's roll to be quantified highlighting asymmetries in the technique that could be improved.

To quantify the level of testing that has been performed and the impact that iDAQ has had; in total, project SwimSIM has tested 103 participants, conducted over 1725 measurement runs requiring 90 days of pool testing. This included 16 individual test sessions for BS (37 days in total) and resulting in 90% of the London 2012 Olympic team having their technique analysed.

(a)

(b)

FIGURE 3.1: Two images showing the feedback arrangement and acquisition set up at the pre-Olympic squad camp, April 2012.

3.2 iDAQ Arrangement

The flowchart in Figure 3.2 provides an overview of how the system is arranged. iDAQ is capable of acquiring upto eight analogue feeds and one camera, and outputting two analogue voltages.

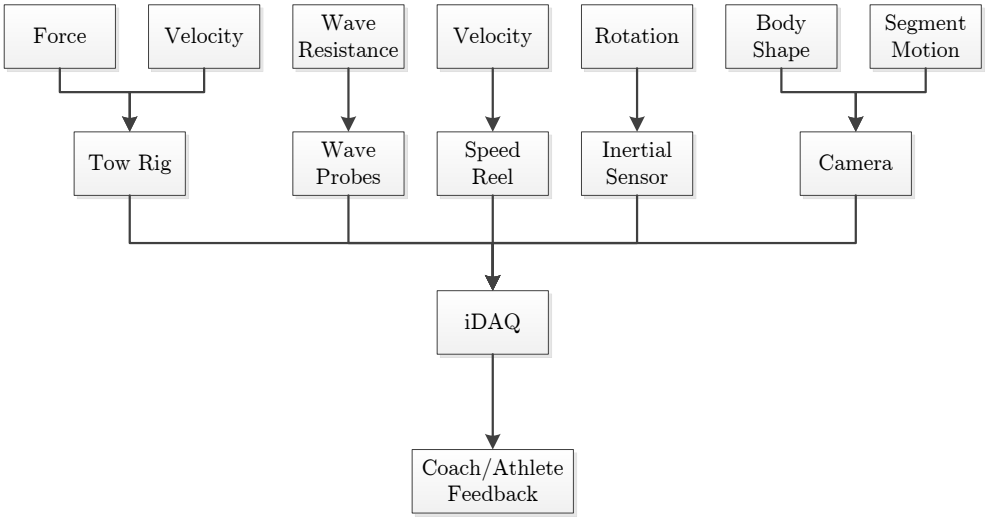

FIGURE 3.2: A flowchart detailing the overview of iDAQ and it's connected system.

In the context of UUS, when over-speeding the athlete the eight input feeds would include three force data, one velocity data and one light input. The force data are acquired from linearly varying displacement transformers fixed to three force blocks, each connected to the tow rig. When simply measuring speed theses channels are unused. The speed data originates from a rotary encoder outputting 250 pulses per revolution. These are subsequently converted into a linearly varying voltage proportional to the frequency of pulses.

As shown by [Lyttle 1999], the wave resistance of an athlete becomes negligible below 0.9 m from the free-surface. When testing UUS, therefore, this component is not measured. The iDAQ system, however, was developed for analysis of surface swimming strokes as well as UUS where the wave component is significant. The iDAQ system, therefore, has the capacity to measure this drag component should it be required for the particular testing undertaken.

Initially to synchronise the video and data, an LED was placed in view of the camera and was also connected to an input line on the data acquisition board. When the LED is illuminated a step change would be recorded in the voltage. By manually aligning these markers the video and data could be synchronised.

The process is now more automated; to synchronise the force and velocity data with the camera, the absolute timestamps from each data packet and from each frame respectively are recoded. When played back, any offset between these are removed. The LED however, is used as a verification tool that ensures the data are suitability synchronised.

One of the key aspects of this experimental process is capturing the motion. This is achieved by use of a bespoke camera buggy with a boom which reaches into the water, on the end of which are two cameras, one to be fed-into iDAQ and the other for a small monitor situated on the buggy so the operator can see what they are recording. The camera used provides frames at approximately 25 Hz, which can be deinterlaced to increase frame rate to 50 Hz. The camera and camera buggy can be seen in Figure 3.3.

The two sub-figures of Figure 3.4 depict the iDAQ GUI and the UUS specific feedback screen respectively. The velocity profile can be seen and as well as a frame from the video. Other metrics such as mean speed and mean inter kick velocities can seen in 3.4(b).

The video frame is synchronised to the displayed data in the graph. The precise time and hence instantaneous velocity associated with the displayed video frame is indicated by the vertical red line in the graphs of the two sub-figures. The user may then play, pause, and step forwards of backwards through the video and for which the synchronised line will move accordingly.

(a)

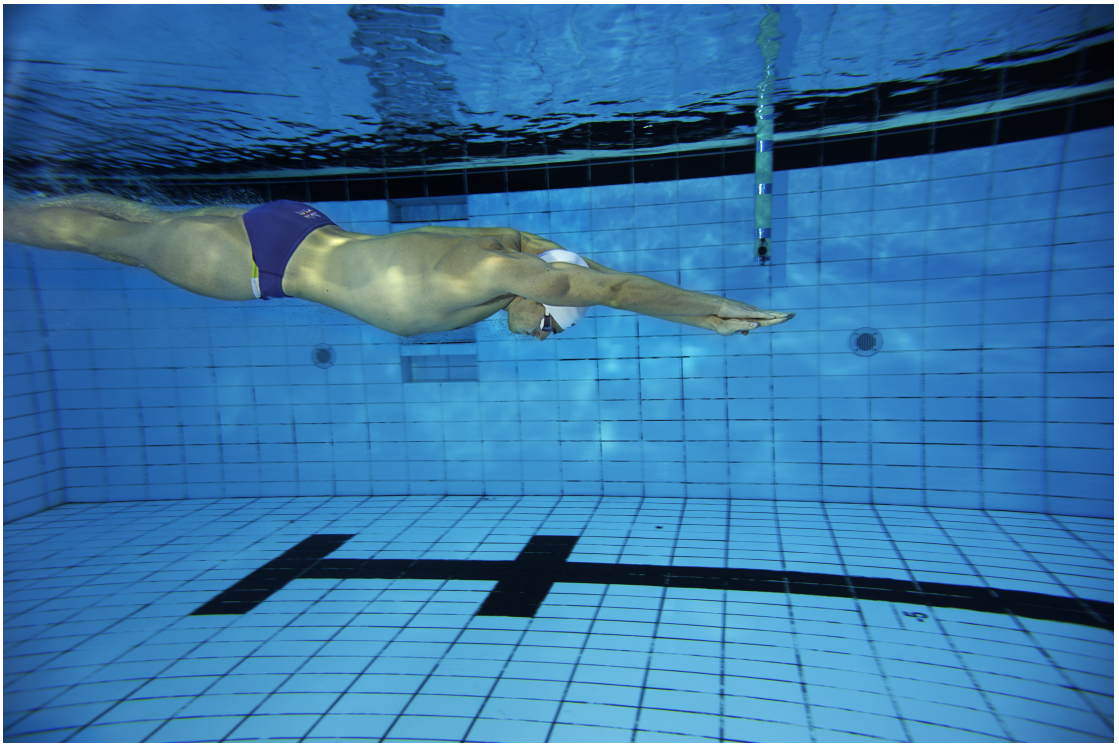

(b)

FIGURE 3.3: Above and below views of the moving camera buggy.

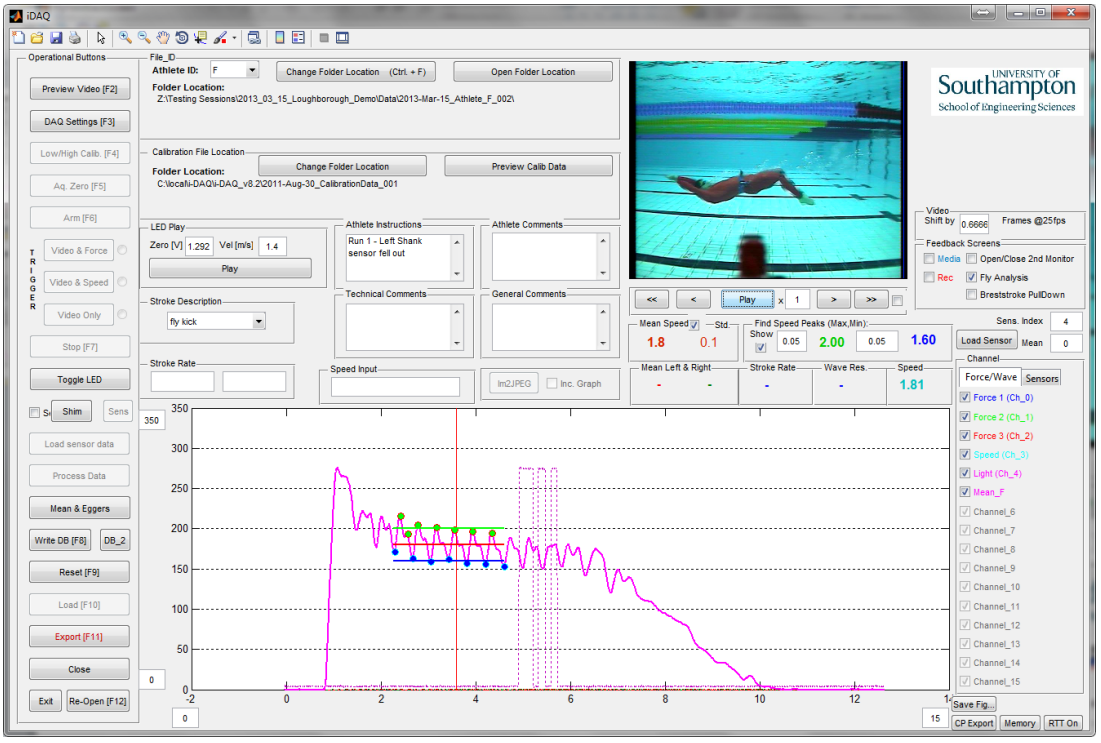

(a)

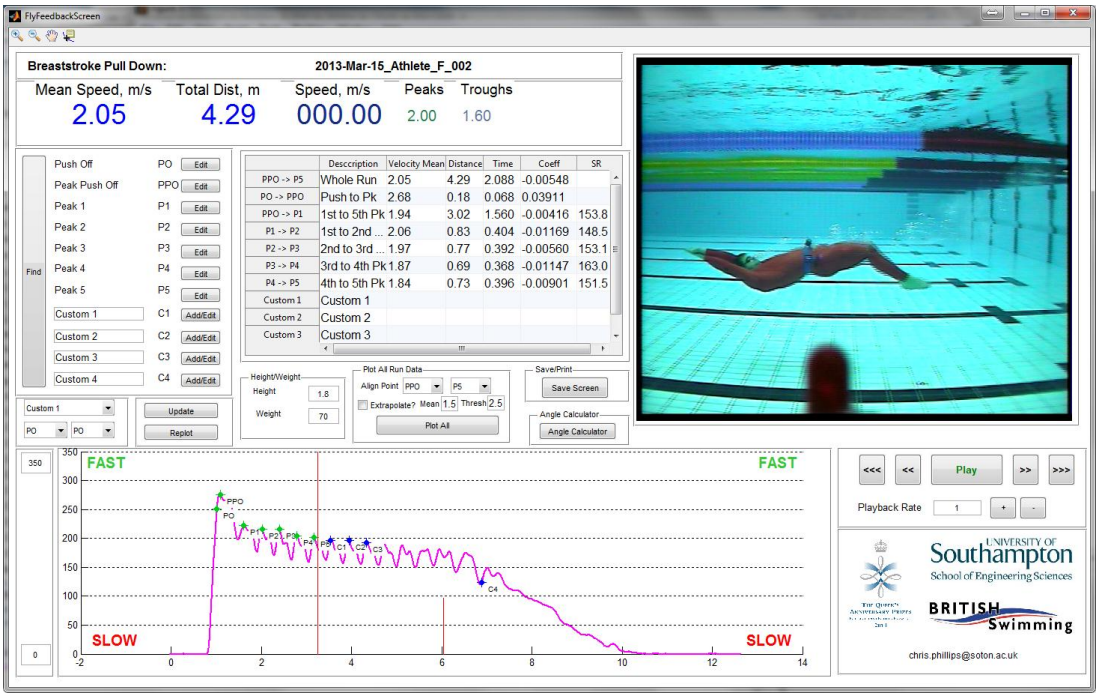

(b)

FIGURE 3.4: Screen captures of (a) the iDAQ GUI and (b) the UUS specific feedback screen.

An additional feature of iDAQ, is the ability to overlay the velocity traces of numerous runs, and example of this can be seen in Figure 3.5. By directly comparing the velocity traces, it becomes more intuitive as to which technique is fastest, for example. The velocity data for each run is also integrated to estimate the displacement from the point of comparison. Using this strategy, it is possible to see which trace and hence which technique would achieve a certain distance first.

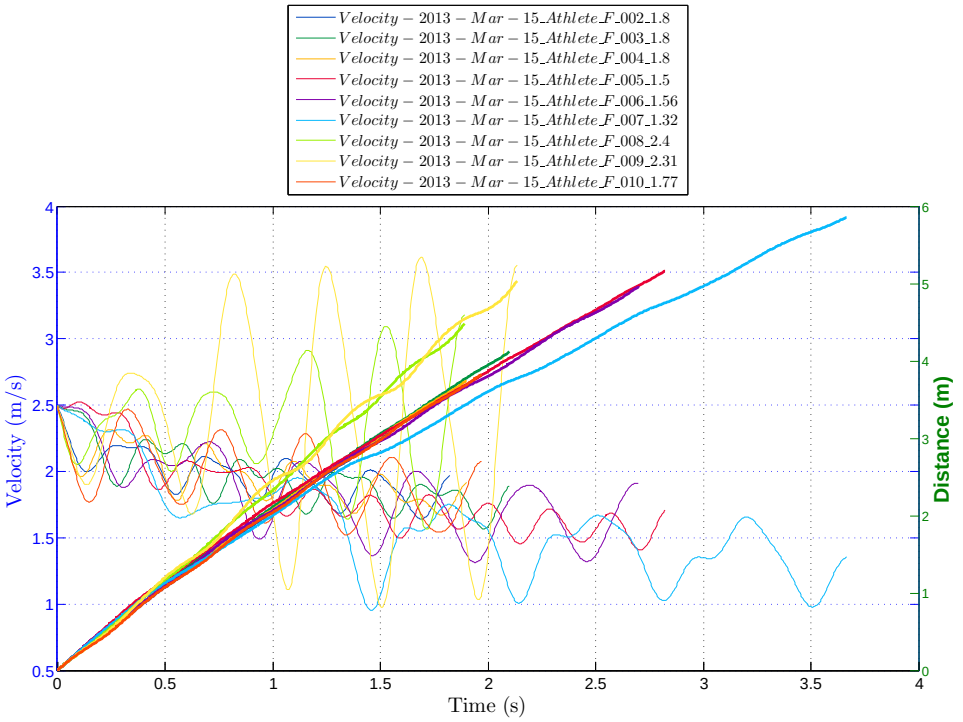

FIGURE 3.5: The velocity traces of a series of runs overlaid and the calculated distance for each.

3.3 Summary

These sections provide an overview of the developed software and processes by which the experimental data for the testing sessions of project SwimSIM are obtained and moreover how the experimental data for this thesis are acquired. The subsequent chapter then discusses the development of the musculoskeletal model, for which much of the necessary data was acquired through iDAQ.

Chapter 4

Model Development

This chapter details the model developed for use in the subsequent chapters. It commences with Section 4.1 which provides details of the musculoskeletal model beginning with a description of the reference system for clarity. It then continues with details of how the musculoskeletal model is constructed, how the motion is defined and which joints are driven. The section then concludes with how the external constraints and forces are applied to the model.

Section 4.2 details how the kinematics for this thesis are obtained and how the relevant joint angles and parameters are deduced and interact with the musculoskeletal model.

The deduction of the environmental forces using the kinematics are discussed in Section 4.3, with particular focus applied to the Lighthill theory which is the chosen method to calculate the thrust and fluid forces on the body from the prescribed kinematics.

4.1 The Musculoskeletal Model

4.1.1 Anatomical Reference System

The software used to develop the model and used throughout this thesis is the AnyBody Modelling System (AMS)[AnyBody 2011]. The model's reference system is consistent with that of the International Society of Biomechanics (ISB). This reference provides a standardised classification system with which the anatomy of the human body can be suitably defined.

The description of direction relative to the human body is described by pairs of terms relating to opposing directions. These anatomical terms of direction are summarised and tabulated in Table 4.1 with the second term the opposite to the first.

TABLE 4.1: Anatomical terms of direction for a human

Term 1	**Description**	**Term 2**	**Description**
Anterior (Ventral)	Towards the front of the body	*Posterior (Dorsal)*	Towards the rear of the body
Superior	Towards the head	*Inferior*	Towards the feet
Cranial	Towards the head	*Caudal*	Toward the coccyx
Medial	Towards the mid-line of the body	*Lateral*	Away from the midline of the body
Proximal	Toward the trunk (torso)	*Distal*	Away from the trunk (torso)
Superficial	Towards the surface of the body	*Deep*	Towards the interior of the body

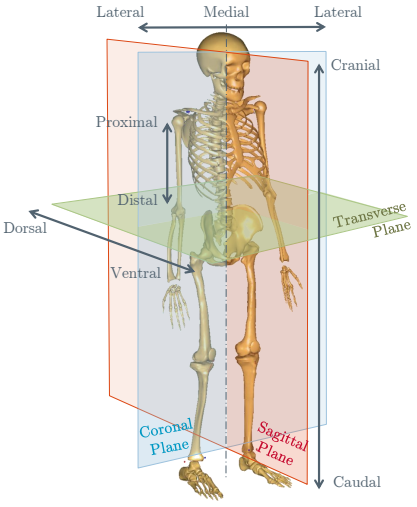

FIGURE 4.1: AnyBody reference system - defining the three anatomical planes; Coronal, Sagittal, Transverse

The *anatomic position* (as depicted in Figure 4.1) is defined as standing with feet slightly apart, arms lowered to the side and both palms and feet pointing forward. There are three orthogonal planes in which the body is described; *Coronal*, *Sagittal* and *Transverse*. While in the anatomic position, the Coronal plane divides the body into *anterior* and

posterior halves, running through a left to right, or *Transverse* axis. The Sagittal plane divides the body into left and right halves while the Transverse plane divides the body into *superior* and *inferior* halves. The *longitudinal axis* is defined as the intersection of the Coronal and Sagittal planes — running vertically through the mid-line of the body.

Movement of the body is facilitated through joints, about which segments are able to articulate or translate. Each joint facilitates motion with specified constrains. For example, the knee joint is considered to be a simple hinge-joint and therefore only permits flexion and extension of the knee, constraining rotation in the other axes. The model therefore only requires the time varying knee flexion to be defined.

The hip joint by contrast is modelled as a spherical joint, permitting rotations in all three axes. The model therefore requires hip flexion-extension, abduction-adduction and internal-external rotation to be prescribed.

Similarly to anatomical directions, there are specific pairs of terms for joint motions. These are summarised in Table 4.2.

TABLE 4.2: Anatomical terms of motion for a human

General Function	**Term**	**Action**
Bending movement which modifies the angle between segments	*Flexion* *Extension*	*decreases* the angle *increases* the angle
Movement of segment relative to mid-line of body	*Abduction* *Adduction*	*away from* the mid-line *towards* the mid-line
Axial rotation relative to mid-line	*Internal Rotation* *External Rotation*	*towards* the mid-line *away from* the mid-line
Vertical movement	*Elevation* *Depression*	*superior* direction *inferior* direction
Specific Function	**Term**	**Action**
Bending movement of the entire foot segment	*Dorsiflexion* *Plantarflexion*	*raising* toes superiorly *lowering* toes inferiorly

Examples of these anatomical motions particularly relevant to underwater undulatory swimming (UUS) are illustrated in Figure 4.2. In 4.2(a), the green model (i) abducts both hips and both arms (glenohumeral joint) by 45° to obtain the posture of the red

model. This model then (ii) flexes the hands and plantarflexes the foot each by 45° to obtain the blue model.

The green model in 4.2(b) (i) pitches forward by 45° at the pelvis to obtain the red model. The hip and glenohumeral joint of this model then (ii) flex 45° to obtain the blue model. The elbow and knee then (iii) flex 45° to obtain the posture in the orange model.

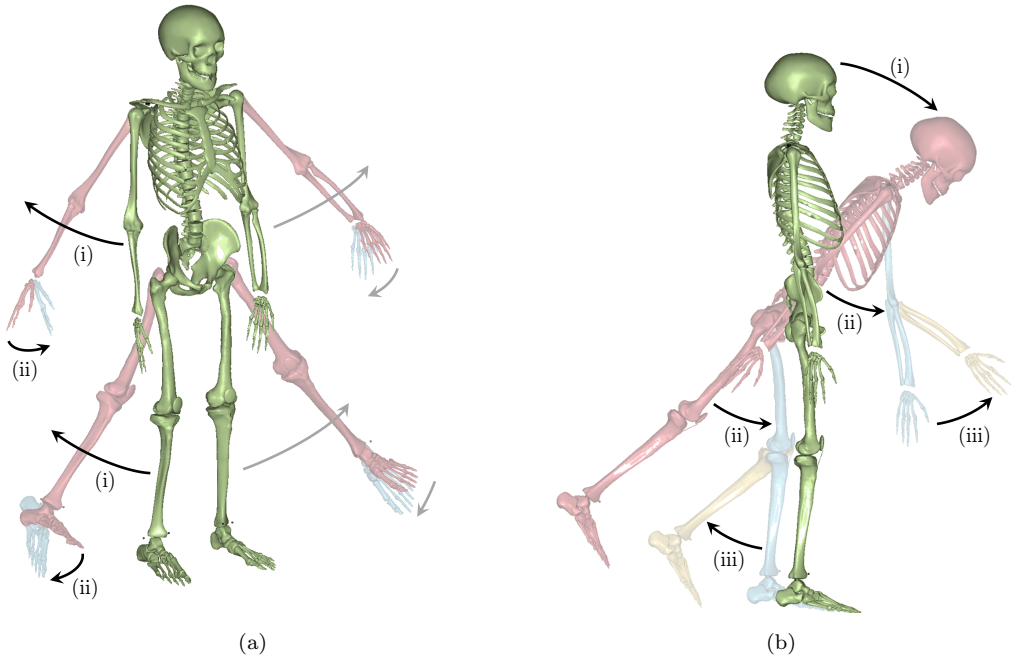

FIGURE 4.2: Definition of the joint kinematics in (a) from an isometric view and (b) in the Sagittal plane.

4.1.2 Skeletal Components

The total number of bones, joints and muscles in the human body is disputed, however, Hollins [2001] defines the human body as having 206 bones, 187 skeletal joints and 620 voluntary muscles. In a computational model where each parameter must be controlled it is impractical, if not unachievable, to model each of these bones, joints and muscles. The model developed in this chapter is based upon the *FreePostureMove* model (available from the AnyBody managed model repository (AMMR)) in which the following joints are defined by default; ankle, knee, hip, pelvis-thorax, sterno-clavicular, glenohumeral, elbow, wrist and the pelvis segment relative to the origin - a total of 17 joints.

In order to drive the orientation of each segment it is necessary to provide the model with the temporal angle of each joint. Obtaining this information can be more complex for some joints than others, particularly at large joint angles.

For example, raising one's arm from their side by 45° may be achieved by abducting the glenohumeral joint by 45°. However, in order to raise one's arm above their head, there is a complex motion of the clavicle, scapular and humerus. These complex interactions are difficult to quantify, particularly in the methods described to obtain the kinematics of a human swimming. Therefore to model the arm raised above the head, the relative angle between the humerus and the mid-line of the body could more easily measured and then the magnitude of the joint angles inferred from previous data. In the AMS there is an inbuilt algorithm called called the *Spine Rhythm* which implements this concept for the displacement of the spine for a given pelvic-thoracic flexion angle. A similar algorithm called *Shoulder Rhythm* already exists, however, it is not accurately representative for large joint angles which would be experienced in UUS.

An alternative strategy, is to assume that the kinematics of the arm motion has little effect on propulsion in UUS in comparison to the torso and the lower limbs. For fish of thunniform or carangiform there is little motion in this section of the body. Therefore, any change in motion to influence propulsion would emanate from the inferior aspects of the body and thus provide a consistent effect on energy expenditure also. Based upon these assumptions and in the interest of simplicity, the arms are excluded from the developed model[1].

The resultant skeletal model is depicted in Figure 4.3. The bones are represented by rigid body segments and connected by frictionless joints. The motion at these joints are controlled by explicit or implicit drivers. The quantities of these components in the model are detailed in Table 4.3

The explicit, or driven, joints in this model are the: z-axis rotation (see Figure 4.3) of the pelvis segment relative to the global origin (pitch); ankle-plantar, knee and hip flexion for each leg; and pelvis-thorax extension. The temporal data for these joint angles are imported from individual *.txt* files. Any large momentary rate of change in joint angle

[1]With the foresight that this model maybe developed in the future, the capabilities of driving the motion of the arms and the implementation of the fluid forces as with the other body segments are implemented. But with limitations of data acquisition of these elements they are simply excluded from the model and musculoskeletal analysis.

TABLE 4.3: A list of the component parts of the musculoskeletal model

.

Component	Quantity
Rigid body segments	36
Rigid body DOFs	222
Frictionless joints	137
Explicit/implicit drivers	85
Muscles in trunk	203
Muscles in each leg	158
Total muscles	519

will result in very large instantaneous forces generated in the model and may cause the simulation to fail. It is unlikely that any sudden change in joint angle is experience in reality and is probably an error generated in the determination of the kinematics. The imported joint angle data are therefore filtered with a 6 Hz Butterworth filter to remove what is deemed to be high frequency noise.

4.1.3 Force Components

As well as the kinematic components of the model, it is also necessary to define any external loadings on the model (forces due to gravity are accounted for internally in the software). For a swimmer, it is considered that these forces consist of hydrostatic forces (buoyancy) and hydrodynamic forces due to the movement of the body relative to the water.

The hydrostatic forces will be different for different subjects and different techniques. These forces are calculated in the AMS and are applied at the centre of mass of each segment individually. The direction is opposite to that of gravity and their magnitudes proportional to the volume of the displaced water. The mass and density of each segment are already incorporated into the model and so the magnitude of the buoyancy on a particular segment (B_{seg}) is calculated as,

$$B_{seg} = \rho_f \, V_{disp} \, g \tag{4.1}$$

where ρ_f is the density of the fluid, V_{disp} the volume of the displaced fluid and g the acceleration due to gravity. The displaced fluid volume by each segment is determined as,

$$V_{disp} = \frac{m_{seg}}{\rho_{seg}} \tag{4.2}$$

where m_{seg} and ρ_{seg} are the mass and density of the segment, respectively.

The buoyancy forces are indicated by vectors in Figure 4.3 as blue arrows. The magnitude of the arrow is proportional to the magnitude of the buoyancy force on the segment to which it is attached.

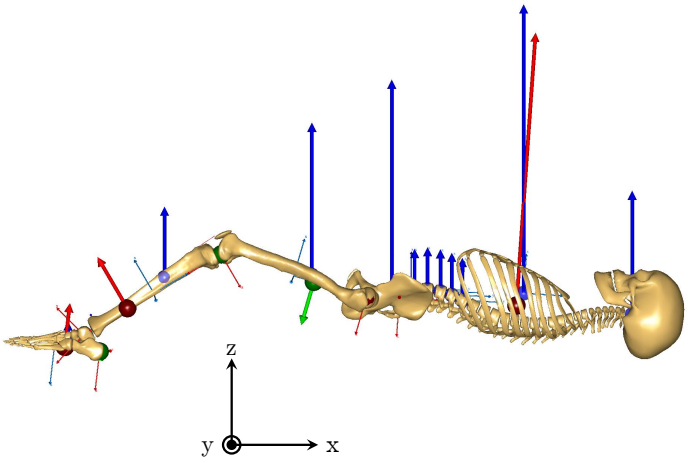

FIGURE 4.3: The AnyBody model with the external forces visualised. The blue arrows are the buoyancy forces applied to each segments' centre of mass. The green is the hydrodynamic force in the positive direction and applied at the time varying centre of pressure on the segment. Similarly the red arrow is the hydrodynamic force in the negative direction.

Dynamic pressure from the fluid also acts on each of the body segments. The segments are modelled as rigid body segments and as such it is possible to integrate the pressure over the segment and apply as a point load at the centre of pressure perpendicular to the segment's long axis. Because of the changing of directions of segments, both positive and negative relative forces may be experienced. To avoid numerical problems in determining the magnitude of the forces and their point of application, the positive and negative forces and points of application are modelled separately.

The point of application of the positive and negative forces are represented as green and red spheres, respectively, in Figure 4.3. The exact point of application is determined later in Equation 4.17. These nodes are rigidly attached to the respective segment. The displacement of each node is constrained to the long-axis of the respective segment and are driven by temporal data imported from *.txt* files.

The magnitude of the positive and negative forces are visualised as green and red arrows, respectively, in the Figure 4.3. Their direction is perpendicular to the respective segment and their temporal magnitudes are similarly imported from *.txt* files. The point of application therefore is coincident to the respective green or red node.

4.1.4 Muscle Components

Actuators are necessary to create and control the motion of connected rigid bodies. In the human body these actuators are the muscles, which produce a force while in contraction. There are three major muscles types in the human body; *smooth*, *cardiac* and *skeletal*. The last are under voluntarily control, controlling the body's motion and hence it is these which are of interest. To achieve the motions described in Table 4.2 muscles are typically arranged in opposing pairs. Ligaments connect each muscle to the bones at an *origin* and *insertion* point. The origin and insertion points in each muscle pair would then be on opposite sides of the respective joint. While one muscle in a pair contracts and flexes the elbow joint, for example, the opposite relaxes and elongates; similarly the inverse occurs to extend the elbow joint.

An individual muscle may be visualised as a number of *fascicle*, beginning and terminating with tendons and ensheathed by the *epimysium*, as depicted in Figure 4.4 [2]. Each fascicle contains blood vessels and a bundle of muscle fibres and is itself ensheathed by the *perimysium*. The major constituent part of each of muscle fibre is the contractile element, or *myofibril*. Each myofibril is composed of thick (*myosin*) and thin (*actin*) filaments. It is these filaments that slide over each other as the muscle relaxes and contracts, lengthening and shortening the muscle's length [Ethier and Simmons 2007].

Muscle fibres are subdivided into three categories; *slow oxidative* (slow twitch), *fast oxidative* (intermediate twitch) and *glycolytic* (fast twitch). All three are similar in that

[2] Image adapted from: `http://training.seer.cancer.gov/anatomy/muscular/structure.html` *Date Accessed: 06/04/2013*

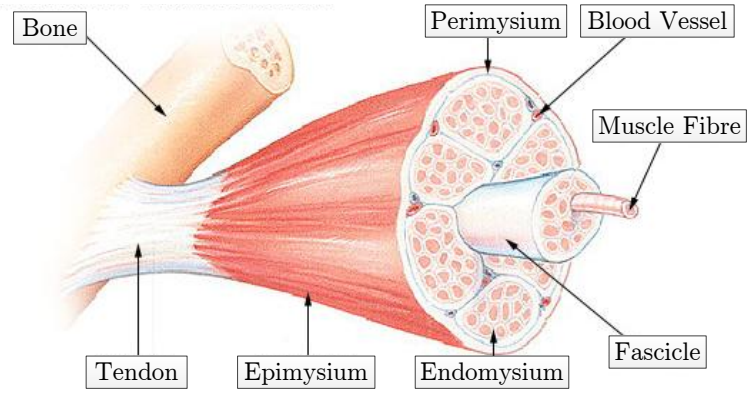

FIGURE 4.4: The anatomy of a skeletal muscle[2].

they produce adenosine triphosphate (ATP) —the mode by which energy is released for contractions— but differ in how ATP is produced. Slow twitch fibres produce ATP *aerobically* —an efficient and sustainable pathway that requires the presence of O_2. Alternatively, fast twitch fibres produce ATP *anaerobically* —a less efficient pathway which does not require O_2 but does produce lactic acid as a by-product which is detrimental to performance. Intermediate twitch fibres normally produce ATP aerobically, however, they can be switched to produce ATP anaerobically.

The maximum force a muscle can produce is proportional the number of muscle fibres it contains and is therefore proportional to its physiological cross-sectional area (PCSA),

$$PCSA = \frac{v_m}{l_f} \tag{4.3}$$

where v_m is the muscle volume and l_f the length of the muscle fibre. However, because the muscle fibres may run parallel to the tendons or at an oblique angle —γ, the *pennation angle*— the total force exerted in the axial direction is also proportional to $cos(\gamma)$. Therefore, the static force in the axial direction at the neutral fibre length (F_0) is,

$$F_0 = PCSA\ f_m\ cos(\gamma) \tag{4.4}$$

where f_m is the force per unit area generated by the muscle fibres, or *specific tension*.

Furthermore, the force exerted by the muscle at the tendon's insertion points is also influenced by the length and contractile velocity of the muscle. The AMS defines this

as the current muscle *strength*, where

$$Strength = F_0 \left(\frac{2\, L_m}{\bar{L}_f} - 1 \right) \left(1 - \frac{\dot{L}_m}{V_0} \right) \tag{4.5}$$

where L_m is the current muscle length, $\bar{L}_f$ the neutral fibre length, $\dot{L}_m$ the current contractile velocity and V_0 the maximum contractile velocity. Therefore the strength of the muscle will diminish to zero as L_m becomes half or L_f or the contractile velocity approaches its maximum [AnyBody 2011].

The AMS has three default models —ranging in complexity— with which to replicate the anatomy of a muscle. The available models are *AnyMuscleModel*, *AnyMuscleModel2ELin* and *AnyMuscleModel3E* the details of which are described in Table 4.4.

The three models are based on classic phenomenological models by Hill [1938] which interprets the muscle as mechanical components. While these models do not attempt to represent the microscopic elements of muscle contraction, they, unlike other models which require solving differential equations, are computationally less demanding and reproduce many properties of muscle behaviour quite well [Damsgaard *et al.* 2006]. They utilise a contractile element (CE) to represent the muscle and springs to replicate the passive elastic (PE) and serial elastic (SE) properties of the muscle. A schematic of the three model type is depicted in Figure 4.5.

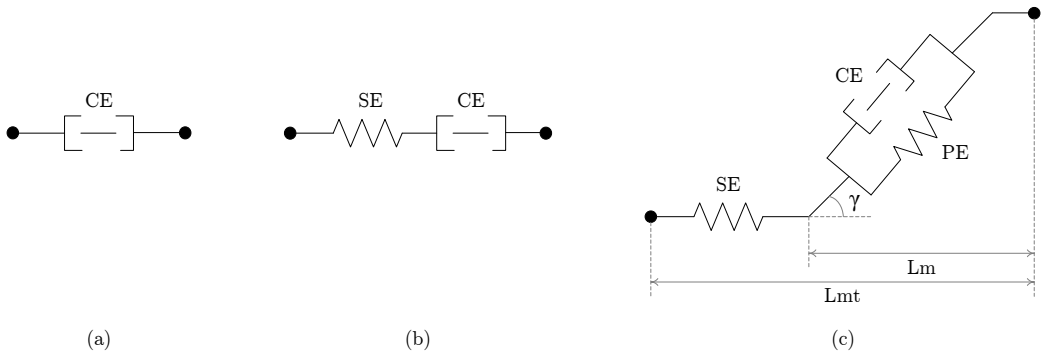

FIGURE 4.5: Schematic of the three muscle models available in the AMS. Where CE is the contractile element, PE the passive elastic element, and SE the serial elastic element. γ is the pennation angle of the muscle fibres.

The premise for having three models of varying complexity to represent what is complex structure, is the notion that obtaining reliable and accurate data for many muscles - particularly smaller muscles - is difficult to obtain. Therefore, where the data for specific

TABLE 4.4: Muscle models available in the AMS (adapted from [AnyBody 2011])

Model	**Description**
AnyMuscleModel	The most simple model where strength in the muscle is constant and proportional to the PCSA of the specific muscle at its neutral length. This model is therefore independent of muscle length and contraction velocity but has been demonstrated to work reasonably well for moderate contraction velocities and small joint angle variation. The only controllable variable is, F_0.
AnyMuscleModel2ELin	This model is an implementation of model (b) in Figure 4.5 and utilises the strength parameter of Equation 4.5. It contains a contractile element which represents the muscle and a spring in series which accounts for the passive elasticity of the tendon. When the muscle is stretched, therefore, there is always a contractile force. The controllable parameters for this model are; F_0, $\bar{L}_f$, the tendon length at no load (Lt_0), the tendon elasticity ($\bar{\epsilon}$, i.e. the strain in the tendon at F_0) and V_0
AnyMuscleModel3E	This is a full implementation of a Hill-type muscle of which Figure 4.5(c) is a schematic. It accounts for the pennation angle of the fibres and the passive elasticity of the muscle as well as the serial elasticity of the tendon by the inclusion of the sprung elements S_{PE} and S_T, respectively. The editable parameters for this model are the same as AnyMuscleModel2ELin except it does not require V_0. It also includes the pennation angle of the muscle fibres at the muscle's neutral position ($\bar{\gamma}$ and the proportion of fast to slow twitch muscle fibres (Fc_{fast}). The Fc_{fast} parameter is used in combination with $K1$ and $K2$ which are used to provide a reasonable relationship with fibre composition and L_f. The concept being that while muscle strength is inversely proportional to contraction velocity, long fibres with higher Fc_{fast} should have higher V_0 and so this is determined in this model.

muscles are available more complex models may be employed. Conversely, where data are limited a more simplistic model may be used rendering fewer estimations of unknown parameters.

Naturally muscles do not always extended directly from and origin point to an insertion

point. They may go via another point or wrap over a physical surface - a bone or another muscle for example. The AMS mimics this by allowing the path the muscle takes to be explicitly defined by a series of via points or by specifying that the muscle must take the shortest path from origin to insertion point while wrapping around a specified geometry. Both methods enable the muscle to slide with no friction, however, the latter is more computationally expensive as it must take into account the orthogonal forces imposed on the geometry.

Many of these physiological parameters in the AMS have been recorded from cadaver studies, including the base model which is developed here. It is a parametrised model capable of geometric scaling in terms of segment dimensions, muscle origin, insertion, via points and strength. The lower limb anatomy is based upon the Klein-Horsman [2007] dataset obtained from a cadaver (age = 77 years, height = 1.74 m, $\text{mass}_{\text{total}}$ = 105 kg). The resultant model is defined with respect to segment length and total body mass. Therefore, by assigning the body mass and individual segment lengths, the remaining properties of the model are scaled accordingly.

A detailed list of muscles (and corresponding muscle groups) is detailed in Appendix C, Table C.2. In summary, there are 203 muscles represented in the trunk and 158 in each leg; totalling 519. The majority of the muscles in the lower limbs are modelled as AnyMuscleModel3E as sufficient data of these muscles are available. The muscles of the trunk, however, are mostly AnyMuscleModel2ELin as fewer data are available. Furthermore, the range of motion of the trunk is comparatively less than the legs and as such the priority of the muscle models is reasonable.

The muscles of the model were collated into different groups for later analysis. These include; pelvic-thorax (PT), hip, knee and foot flexors and extensors, as well as those deemed to be significant to core stability. Detailed list of which muscles where classified into which group may be found in Appendix C.

Nakashima *et al.* [2012] used a musculoskeletal model to provide data for a lookup-table when optimising an arm trajectory. In this example they found that the default arm strength parameters of the model were significantly underestimating the maximum torque the model was capable of producing as compared with experimental data. They concluded that the participant of their study was significantly stronger than the default model equivalent. They therefore, increased these muscle parameters to enable the

model to attain the experimental data. It is not stated by what factor these parameters were increased. In observing the differences between the experiential and the simulated torque in the figures of [Nakashima *et al.* 2012], the experimental data is approximately double the model's default. It is therefore assumed that was the same factor that was applied to the muscle parameters in order to make the simulated data agree with the experimental. Without the exact muscle parameters for every muscle for elite swimmers published, this same scale factor from the default strength settings was used in the musculoskeletal model in this thesis.

4.2 Acquiring Human Kinematics

A necessity of the musculoskeletal model is that the kinematics are explicitly defined. For the UUS model here, they are obtained using the manual digitisation process as described in Section 2.3.1. It is a simple method which has been used to good effect by others. To obtain better integration with the other aspects of the model a bespoke *Matlab* script was written in facilitate this process.

The first process is to record underwater video footage and, for subsequent analysis, measure the velocity of the participant performing the particular trial. As part of the support provided to British Swimming (BS) the *iDAQ* software was produced - a *Matlab* based graphical user interface (GUI) - which amongst others is capable of recording synchronous video and velocity data (for other capabilities see Appendix D).

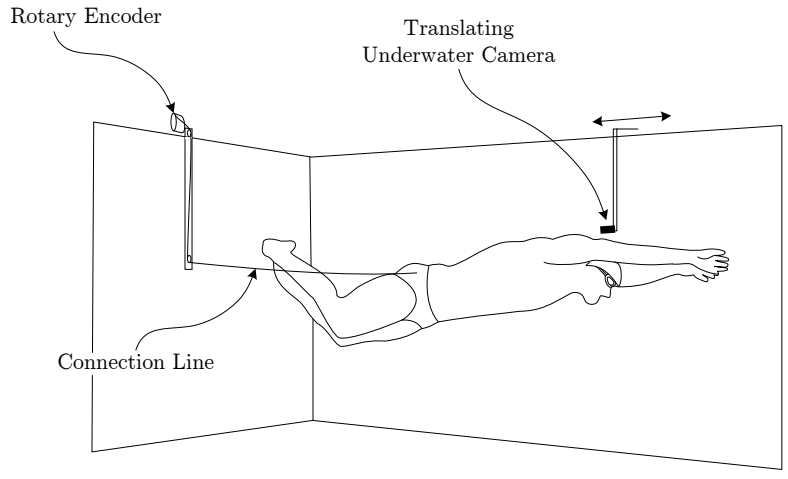

FIGURE 4.6: A schematic of the video and velocity acquisition arrangement.

For the model developed here, it is assumed that the kinematics occur in the sagittal plane and about which the left and right of the body is symmetrical. Consequently an underwater camera, which translates remaining orthogonal to the sagittal plane, is linked to a computer running iDAQ and provides the video feed. The velocity is obtained by connecting a low-stretch, lightweight Dynema^{TM}line to the side of the participant's hip (see schematic in Figure 4.6). The line is connected to the side of the hip because it is assumed that the translation and rotation of this location relative to the centre mass is minimal and thus minimise any error in the acquisition. Furthermore, many athletes are used to being connected to a line at this location and it is minimally invasive and unimpeding. The opposite end of the line is wound around a rotary encoder and a reel upon which as small resistance is applied; both are secured to the poolside. As the participant, connected to the line, swims away from the poolside they unspool the reel and hence rotate the encoder. The rotary encoder produces 250 pulses per revolution which are converted to a linearly varying analogue voltage. This analogue source is calibrated and connected to the acquisition laptop via a 6009NI^{TM}USB analogue data acquisition board. The video and velocity data are then acquired at 25 Hz and 250 Hz, respectively, using iDAQ.

The video and velocity data are then loaded into the *Matlab* script. From here, the video is trimmed to include only the desired video frames necessary for analysis. In each of these frames the joint centres and anatomical location are selected. These comprise of the tip of the toes, centre of rotation of the ankle, knee hip, shoulder and wrist, and fingertip —the elbow location is selected in the first frame and assumed to maintain a constant relative location between the shoulder and wrist throughout (thus helping to reduce user input). Two consistent points are also selected on the upper and lower pelvis to provide its orientation (see Figure 4.8). It is assumed, therefore, that when in the anatomic position an imaginary line between these points are parallel to an imaginary line drawn between the hip and shoulder locations. From selecting these points in each frame the respective joint angles required for the model can be obtained. These joint angles are derived in accordance with the ISB and as used by the AMS.

In addition the height of the participant is entered into the script. The participant's height is equivalent to the parametric length from the tip of the toes to the shoulder location in pixels and so a pixel-to-metre scale factor is determined. Using this scale factor the segment lengths are determined in each frame. Because of user error in

digitising the image in each frame each segment length is prone to vary between frames and is identified in Figure 4.7

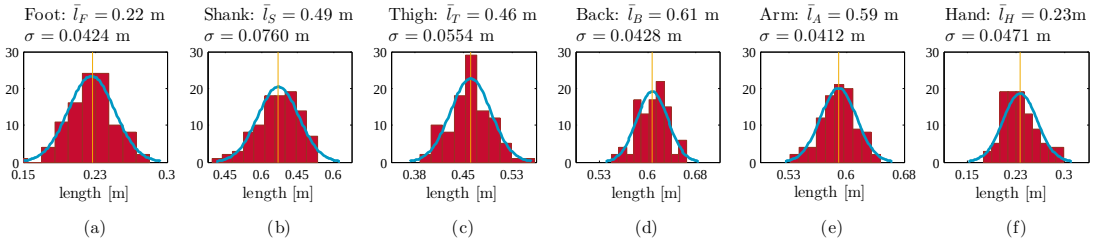

FIGURE 4.7: Example of the variation in the calculated segment lengths due to errors attributed to the digitisation process; foot, shank, thigh, back, upper-arm, lower-arm and hand respectively.

The mean value is then chosen as the representative segment length. These segment lengths and joint angles then provide the necessary inputs into the musculoskeletal model.

4.3 Thrust Fluid Model

4.3.1 Lighthill Model

Sir M. James Lighthill was an accomplished fluid dynamicist of his time and, amongst other contributions, mathematically theorised the propulsive forces for undulatory fish swimming using a momentum conservation approach [Lighthill 1971]. This work has formed the basis for much work since. The similarities between human UUS and fish propulsion has been discussed in Chapter 2. Lighthill's theory for fish locomotion, is therefore chosen as the method for determining thrust and side-forces for this musculoskeletal model. As compared to other numerical methods —for example, computational fluid dynamics (CFD) or smooth particle hydrodynamics (SPH)— it requires significantly less computational time measured (see Chapter 2). Webb *et al.* [2012] investigated it's appropriateness for modelling the fluid forces associated with human swimming, concluding it has the potential to provide detailed insight into the hydrodynamics of UUS.

The thrust calculated using Lighthill's theory in this thesis is compared to experimental $R-T$ data and is demonstrated to match the phasing and trend of the experimental data (Figure 4.10). Furthermore, the magnitudes of the calculated peak thrust are shown

to be of similar magnitudes to a similar case Von Loebbecke *et al.* [2009] but where the thrust was deduced using CFD (see discussion in Section 5.4). It is concluded from these observations, that the Lighthill model provides a suitable, appropriate and efficient methods for determining the thrust and hydrodynamic loadings for the musculoskeletal model.

Lighthill sections a fish —or swimmer— into n strips along its length, where each strip may be described in global coordinates $x(a,t)$, $z(a,t)$ in terms of a parametric distance a, along the body at time t, where $0 < a < l$ and the constant l is the parametric length of the body (refer to Figure 4.8).

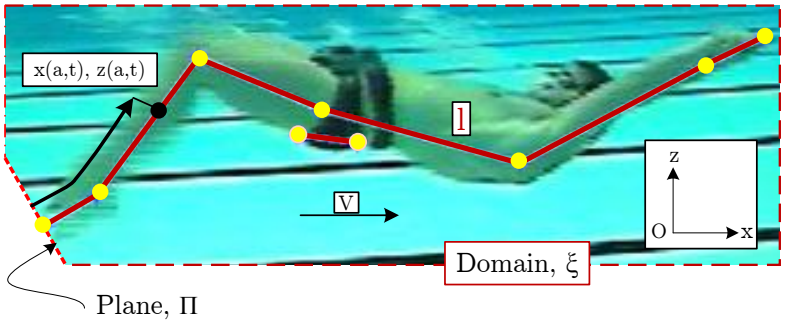

FIGURE 4.8: Lighthill Reference System

In order to avoid resultant complications due to vortices, Lighthill only contemplates the momentum of the water within the bound domain ξ [Lighthill 1970]. This area encapsulates the fish's motion but is further bound by plane Π at the fish's tail, which remains perpendicular to the tip. This therefore excludes the wake and hence any vorticity that it may include. This also requires that no vortices are shed from further upstream as Wu [1971] observed these interacted with the body downstream. However, Wu observed this phenomena in fish with dorsal and ventral fins which as described by Singh and Pedley [2012], this occurs as geometries become infinitely thin; as with fins. A human performing UUS, however, is presumed not to have such geometries and thus conforms with the proviso as per Lighthill [1971].

Lighthill then describes the momentum per unit length of the fish as,

$$mw(-\frac{\partial z}{\partial a}, \frac{\partial x}{\partial a}) \tag{4.6}$$

where m is the mass per unit area [Lighthill 1970] and w is the velocity component tangential to the spinal column,

$$w = \frac{\partial z}{\partial t}\frac{\partial x}{\partial a} - \frac{\partial x}{\partial t}\frac{\partial z}{\partial a}. \tag{4.7}$$

The horizontal u component is therefore,

$$u = \frac{\partial x}{\partial t}\frac{\partial x}{\partial a} + \frac{\partial z}{\partial t}\frac{\partial z}{\partial a}. \tag{4.8}$$

Lighthill [1971] then defines the momentum within ξ as the integral of Equation 4.6 from 0 to l with respect to a. Differentiating this expression with respect to time obtains the net forces, or the rate of change of momentum. He observes that this expression may be written as the sum of three elements:

1. rate of change of due to convection of momentum out of ξ across plane Π
2. rate of change due to the pressure force acting across Π
3. minus the reactive force (T, Q) with which the fluid acts on the fish.

Expressed mathematically and in the respective order as per described, the rate of change of momentum in ξ is,

$$\frac{d}{dt}\int_0^l mw\left(-\frac{\partial z}{\partial a}, \frac{\partial x}{\partial a}\right) = \left[-umw\left(-\frac{\partial z}{\partial a}, \frac{\partial x}{\partial a}\right) + \frac{1}{2}mw^2\left(\frac{\partial x}{\partial a}, \frac{\partial z}{\partial a}\right)\right]_{a=0} - (T, Q). \tag{4.9}$$

Substituting u from Equation 4.8 into Equation 4.9, it can be rearranged making the thrust generated for propelling the fish through the water (T) and the transverse force acting on the fish (Q), the subject of the equation and in terms of w (see Appendix E for working), hence

$$(T, Q) = \left[mw\left(\frac{\partial z}{\partial t}, -\frac{\partial x}{\partial t}\right) - \left(\frac{1}{2}mw^2\left(\frac{\partial x}{\partial a}, \frac{\partial z}{\partial a}\right)\right)\right]_{a=0} - \frac{d}{dt}\int_0^l mw\left(-\frac{\partial z}{\partial a}, \frac{\partial x}{\partial a}\right). \tag{4.10}$$

As stated m is the mass per unit area, such that

$$m(a) = \frac{1}{4}\pi\rho s(a)^2 \tag{4.11}$$

where ρ is the water density and s is the depth of the cross-section, which varies with a.

The cross-sectional variation is determined from a three-dimensional body scan; provided by Speedo® and depicted in Figure 4.9(a). One datum provided by the scan is the height of the navel from the base of the feet. By digitising these locations in the image (the blue points) a scale factor of pixels to metres is obtained. The width of the upper and lower limbs are then digitised as well as the width of the trunk relative to the midline of the body (the magenta points). The pixel displacement of these point is then multiplied by the scale factor providing these dimensions in metres.

If a scan of the participants is available, this process maybe performed for each individual. If, however, a scan is not available, by measuring the height of the participant's navel from their feet, a relative factor can be determined between themselves and the default. In assuming the same relative proportions for the other dimensions this relative factor may then be applied to the default dimensions.

The original scan is of the participant in the anatomical position, however, it is necessary to determine the width in the assumed position for UUS; i.e. ankles together and arms raised above the head with interlocking hands. Assuming there is no space between the segments in this position, the silhouette of this posture is represented as the red and green lines in Figure 4.9(b). The horizontal location of the red points is the calculated width as described above. Although the width above the shoulder (at the neck) is the sum of the neck and the upper-arm. The vertical location of the nodes is determined from the segment lengths obtained in Section 4.2.

The blue line is then the total width along the body's length. Because each segment is divided into n strips (Section 4.3.1) and it is necessary to know the width at each segment, the magenta line is a linear interpolation of the blue line based upon the predetermined vertical location of the location of the strip centres.

Figure 4.10 shows an example of the predicted thrust from Equation 4.10 compared with the $R-T$ measured experimentally for the same run from which the kinematics was deduced for implementation in the fluid force model. Without performing additional measurements it is not possible to extract the thrust directly from the $R-T$ data [Webb *et al.* 2012]. It is apparent however, the similarity of the phasing and trends between the two datasets reaffirming Singh and Pedley [2012], for example.

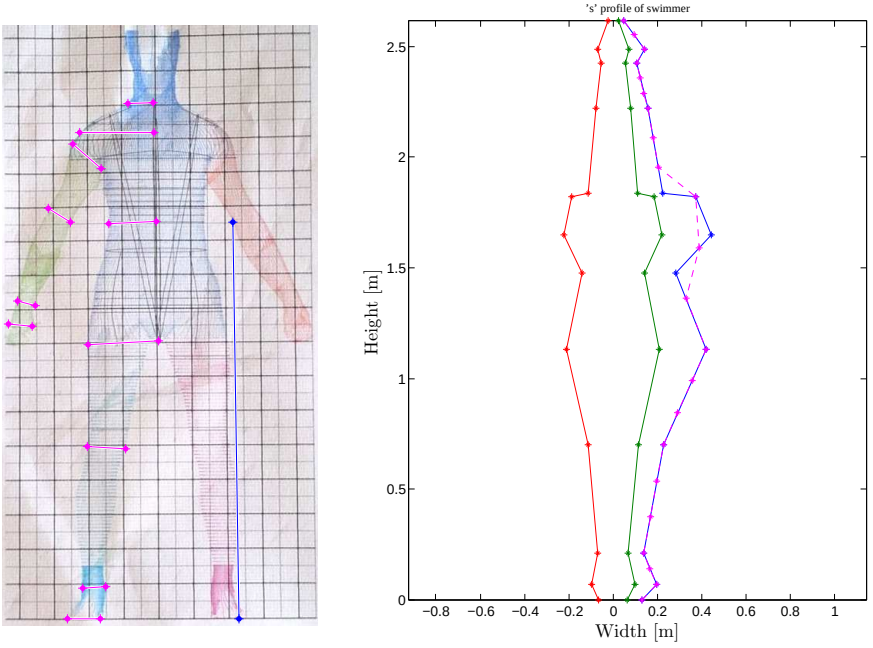

(a) (b)

FIGURE 4.9: (a) A three-dimensional scan used in calculating the cross-sectional variation of the participant. The digitised widths include; foot, ankle, knee, half-hip, half-naval-waist, half-shoulder, half-neck, upper-arm, elbow, wrist and hand. Also selected is the height of the navel. (b) illustrates the computed axial width profile. The red and green lines are the computed right and left outline of the body about the body midline ($x = 0$). blue line is therefore the total computed cross-sectional width. The magenta line is a linear interpolation of the blue line whose sample points (number and location) are dependent on the number of strip for each segment.

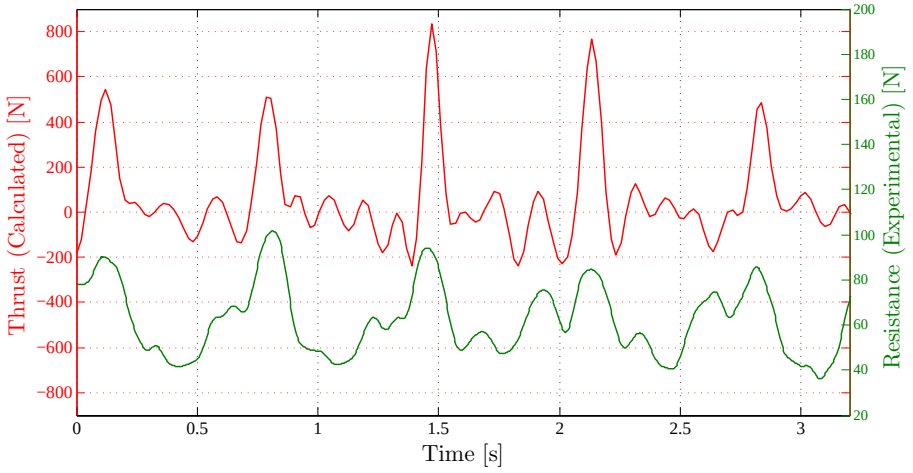

FIGURE 4.10: An example comparison of the predicted thrust from Equation 4.10 and $R - T$ measured experimentally.

4.4 Encompassing Script

The different components of Sections 4.1, 4.2 and 4.3 are incorporated into a single encompassing *Matlab* script. The work flow for this script is illustrated in Figure 4.11.

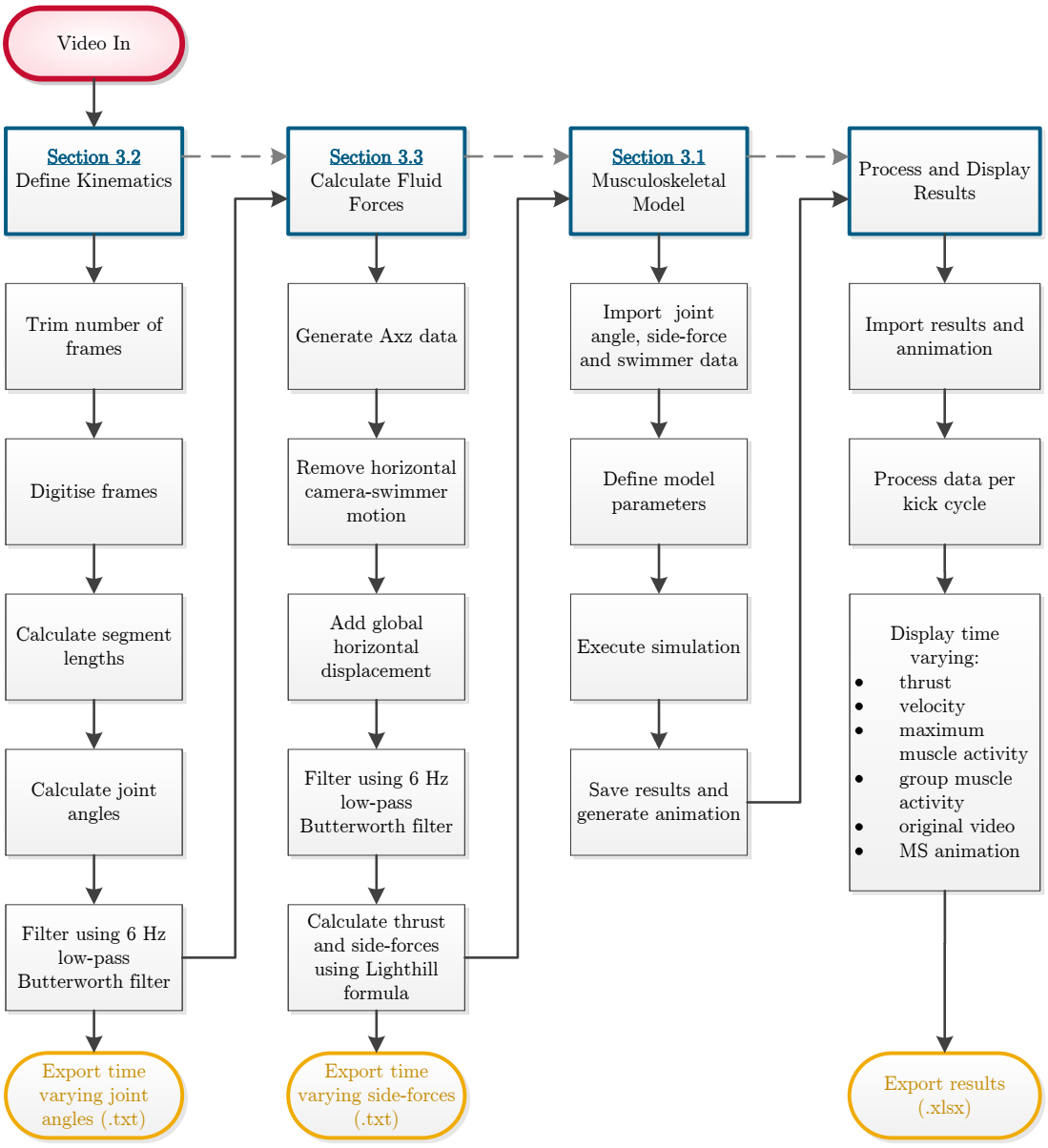

FIGURE 4.11: The work-flow of the encompassing script.

The video data is loaded into the software as well as synchronised velocity data where available. The video is trimmed to include an integer number of kick cycles. The first frame index of each kick cycle should also be recorded. The images of these respected frames are then digitised generating the temporal joint angles and the segment lengths.

The joint angles can then be filtered using a Butterworth filter or as a Fourier approximation. The default setting is to use a 6 Hz low-pass filter. Each joint's angle is then individually exported as a text file (e.g. *Left_Knee_Flextion.txt*) as an $Nt \times 2$ array where Nt is the total number of digitised frames and the first column of the array is the time vector and the second the angle data.

Because of the previously mentioned segment length variation from frame to frame, each of the digitised point data are recalculated for use in the Lighthill equation. They are recalculated using the mean segment length and the determined joint angles. The formula also requires the body to be sectioned into strips. The desired number of strips for each segment is then specified. Using a linear interpolation, these point data are re-sampled for each segment along the body. These data are then stored in the array Axz. The Axz array is of dimensions $3 \times n + 1 \times Nt$, where n is the total number of strips along the body

$$n = \sum_{i}^{7} Ns_i, \tag{4.12}$$

and Ns is the total of strips for the ith segment.

The first row of the Axz array is the parametric distance (a) along the body of each sample point - such that the value of element $Axz(1, n+1, 1)$ is equal to the total length of the swimmer - and the second and third the x and z coordinates respectively.

Because of the video acquisition process, the swimmer does not necessarily remain in a constant location in terms of the horizontal image axis. In order to remove this relative translation, it is assumed that the hands should remain at a constant location in horizontal image axis. In each frame, therefore, the location of the finger tips in the horizontal axis is subtracted from each of the x-coordinates of the Axz array. Because Equation 4.10 is dependent on $\frac{\partial x}{\partial t}$ and $\frac{\partial x}{\partial a}$ the global displacement is then added to each x-coordinate of the Axz array. This displacement is determined by integrating the velocity data where available or by assuming a constant velocity and integrating this data accordingly.

The Axz array is then re-sampled, in the time-dimension using a cubic spline interpolation, to generate an enlarged Axz dataset ready for evaluation of the Lighthill formula.

A numerical implementation of Equation 4.10 is then used to evaluate the thrust T at each time step, as well as the side-force Q on each strip along the body. In order to

export the side-force data for use in the musculoskeletal model, however, the positive and negative forces need to be determined for each segment and their respective centre of effort. Assuming the segments to be quasi-static rigid bodies, the moment (M) about the joint centre expressed as

$$M_S = \boldsymbol{r}_S \cdot \boldsymbol{F}_S \tag{4.13}$$

$$= r_{S_1} f_{S_1} + r_{S_2} f_{S_2} \ldots r_{S_n} f_{S_n} \tag{4.14}$$

$$\equiv \sum_{i=1}^{N_S} r_{S_i} f_{S_i} \tag{4.15}$$

where $\boldsymbol{F}_S = \{f_{S_1}, f_{S_2} \ldots, f_{S_i}\}$ where f_{S_i} is the force on the ith strip of segment S and $\boldsymbol{r} = \{r_{S_1}, r_{S_2} \ldots, r_{S_i}\}$ where r_{S_i} is the distance of the ith strip from the centre of rotation.

The total force on the segment is equivalent to the rate of change of momentum and expressed as

$$F_S = \int_0^{l_S} \boldsymbol{m} \frac{d\boldsymbol{w}}{dt} da. \tag{4.16}$$

The centre of effort of this force is then defined as,

$$R_S = \frac{\boldsymbol{r}_S \cdot \boldsymbol{F}_S}{\int_0^{l_S} \boldsymbol{m} \frac{d\boldsymbol{w}}{dt} da} \equiv \frac{\sum_{i=1}^{N_S} r_{S_i} f_{S_i}}{\int_0^{l_S} \boldsymbol{m} \frac{d\boldsymbol{w}}{dt} da} \tag{4.17}$$

Decoupling the total force into positive and negative forces avoids complications as the net force approaches zero.

Equations 4.16 and 4.17 are then used to calculate the positive and negative components by only considering positive and negative w for each respectively. This then results in a positive and negative, decoupled moment of force on each segment whose magnitude and centre of effort is individually exported as a *.txt* file in the same format as the joint angle.

The musculoskeletal model then has all the necessary anatomical, kinematic and environmental parameters to import. The model is then automatically scaled based on the imported segment lengths and total body mass.

Other settings which are also defined at this stage include the the inverse dynamic solver type (default to type *poly* Rasmussen *et al.* [2001]) and whether to save a copy of the animation and the time-step factor. The time-step factor determines the simulation time-step as a factor of the original video. This makes easier the process of synchronising the simulated animation to the original video.

The inverse dynamics of the AnyBody model is then executed from the *Matlab* script.

All the data from the completed inverse dynamic simulation is then saved to the corresponding folder as the imported data. These saved data are then imported into the original *Matlab* script. These data are then processed and automatically divided into individual kick cycles thus providing a mean value of each metric for the entire simulation as well as its standard deviation.

These metrics pertain to the performance of the captured UUS technique, including; useful work done, total work done by the muscles, over-all efficiency and Strouhal number (for which kick amplitude is determined as the maximum vertical displacement of the node at the tip of the toes in each kick). Also extracted from the data is the contribution of the muscles by group.

It is inferred from the energy work-flow in Figure 2.1 that the overall efficiency (η_O) of UUS can be expressed as

$$\eta_O = \frac{W_O}{E}, \tag{4.18}$$

where W_O is the useful work out and E the input energy. Equation 4.18 can be broken down in to three efficiency stages where energy is lost;

$$\eta_O = \eta_m \cdot \eta_T \cdot \eta_D \tag{4.19}$$

where η_m , η_T , η_D are the metabolic, transmitted and delivered efficiency, respectively.

At the first stage, the input energy is converted into muscle work (W_M). The second stage then uses this work to induce the kinematics where the surface of the swimmer is opposed by the hydrostatic (buoyancy) and hydrodynamic work of the surrounding fluid.

This has components W_O and W_W which are the useful and wasted work, respectively. The over all efficiency may then be expressed as

$$\eta_O = \frac{W_M}{E} \cdot \frac{W_O + W_W}{W_M} \cdot \frac{W_O}{W_O + W_W}. \tag{4.20}$$

The propulsive efficiency (η_P) is defined as the product of η_T and η_D and hence the ratio of the useful work to the muscle work where

$$\eta_P = \frac{W_O}{W_M}, \tag{4.21}$$

where

$$W_O = \int T\,(t)\ V\,(t)\,dt, \tag{4.22}$$

where T is the thrust (calculated from Equation 4.10), V the measured velocity, and

$$W_M = \sum_{i=1}^{N_m} \int F_{m_i}\,(t)\ \dot{L}_{m_i}\,(t)\,dt, \tag{4.23}$$

where N_m is the total number of muscles, F_{m_i} is the force in the contractile element of the ith muscle and $\dot{L}_{m_i}$ the time derivative of its length.

Once the performance metrics have been calculated, the entire dataset is saved as a *.mat* file which can be reloaded into the script on another occasion. Finally the values of key data and locations of the exported and generated files are exported to a *.xlsx* spreadsheet for easy reference. The spreadsheet also contains a macro which simply loads the dataset of the highlighted cell into the *Matlab* script.

4.5 Summary

This chapter has detailed the development of the musculoskeletal model for use in analysis of UUS. It demonstrates the manner in which the required data are determined and applied to the developed model, as well as performance metrics which can be obtained from the data.

The following chapter utilises this model and process in a case study which analyses two different techniques of an elite athlete.

Chapter 5

UUS Case Study of an Elite Athlete

5.1 Introduction

At the British pre-Olympic training camp, a world record-holding sprint athlete was investigating his ability to propel himself underwater following a dive or turn. It was suggested to him by the technical advisor, that he might make improvements by a greater articulation of his pelvis so as to generate a whole body wave that would travel from his shoulders through to his toes, growing in amplitude as it progressed. The technical advisor suggested that this would expend less energy as it was a more fluid body-motion and postulated that the body would almost travel along a continuous path so as minimising disturbance to the water.

The developed methodology presented in the previous chapters is employed in this chapter as an analysis tool to investigate the performance attributes of the athlete's current technique and compare to the advisor's suggested technique. This comparison is first investigated poolside with interaction with the advisor and athlete. Further post-processing was then undertaken to compare the techniques using the developed musculoskeletal model. Finally, using the musculoskeletal analysis, the kinematics are tuned around the initial techniques to investigate potential for further improvements.

5.1.1 Pre-Study Findings

The advice for this technique change was based upon the technical advisor's intuition and was neither a proven nor dis-proven hypothesis. Firstly, to verify these suggestions the athlete's instantaneous velocity was measured using the system described in Section 4.2.

Using the poolside equipment it was found that the mean velocities attained were comparably similar (see Figure 5.1). This was despite having only practised the new technique immediately before acquisition and in contrast to his usual technique which he had honed and was accustomed to.

This therefore led to the conclusion that both techniques were equally fast, however, the latter was at a decreased kick frequency. Furthermore, the athlete also commented that he believed the new technique had the effect of transferring the load on his legs to his torso and ultimately required a lower energy expenditure.

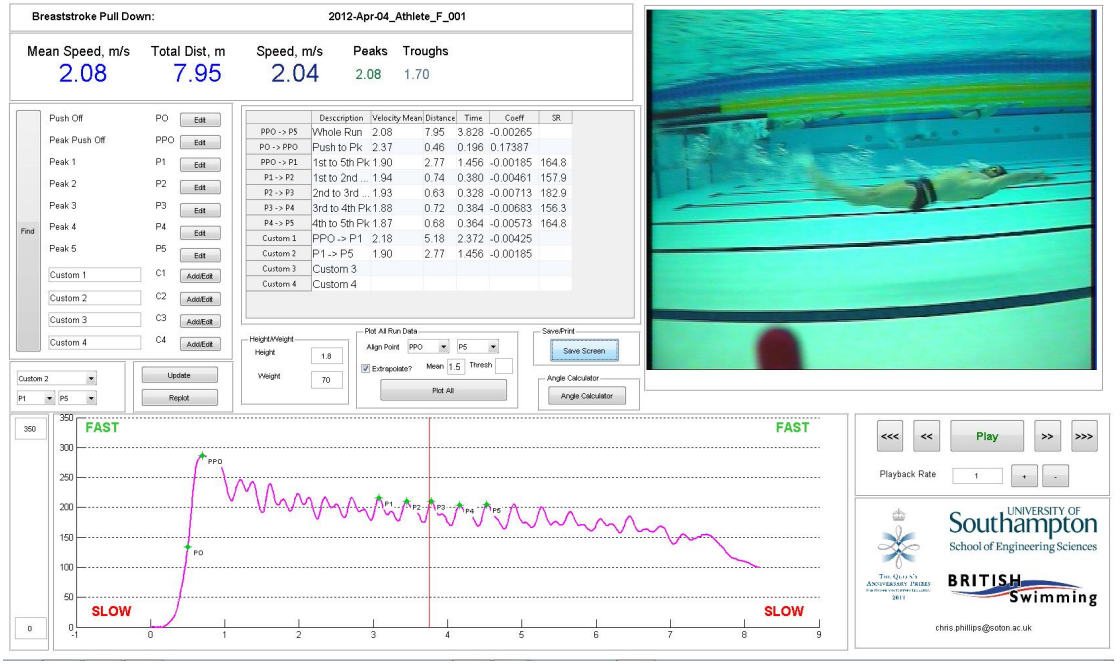

(a)Race-refined UUS technique (T_1).

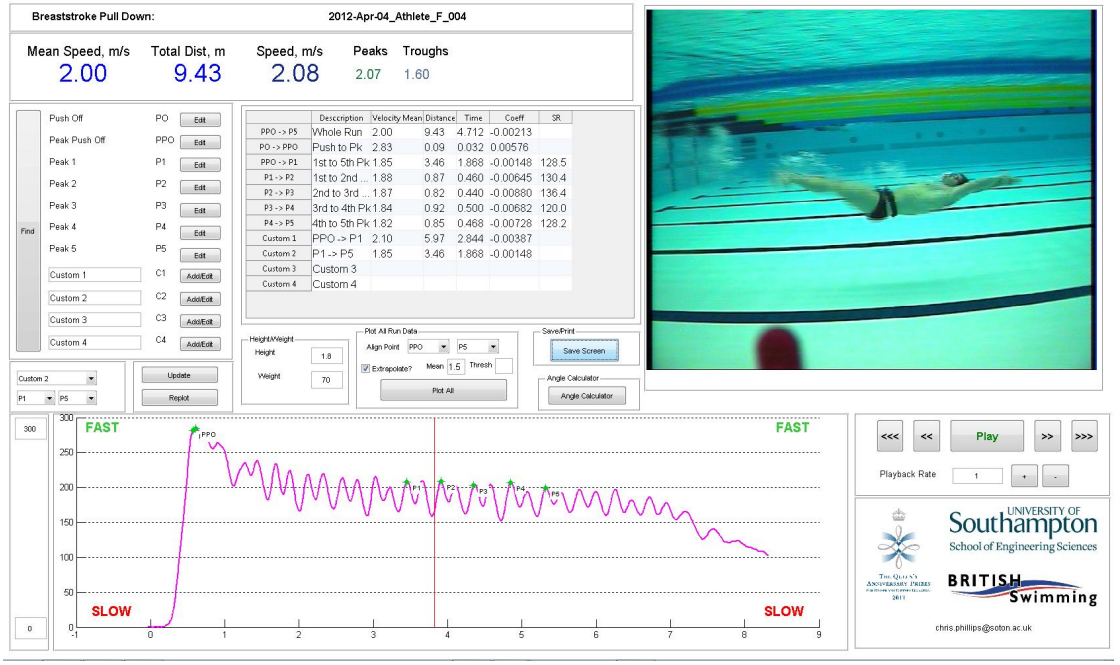

(b)Carangi/anguilliform technique (T_2)

FIGURE 5.1: The pre-study results displaying the velocity profile of the two UUS techniques.

5.2 Aims and Objectives

Even in acknowledgement of the combined wealth of experience of the world record-holding athlete and technical advisor, there was no quantifiable evidence to prove or

disprove the anecdotes in Section 5.1.1.

The aim of this chapter is to therefore utilise the methods described in Chapter 4 to quantify the effect of the athlete's technique variations, determining; thrust, velocity, energy expenditure and hence propulsive efficiency, as well as analysing the variation in muscles loadings, if any, between the two techniques. From these findings, it is intended to provide quantitative guidance as to which technique, or variant of, would be most suited to this particular athlete given his specialist disciplines (100 m and 50 m backstroke).

5.3 Methodology

As described in detail in Chapter 4, the synchronised image and velocity data required for the study were acquired using the pool based system and manually digitised to obtain the kinematics (as per the description in Section 4.2). The technique, T_1, was his race-refined technique and a more thunniform style with flexion/extension of the knee joint providing the propulsion. T_2, was the alternative technique which was more undulatory with the intention of generating a whole body wave, replicating a more carangi- anguilliform.

Using these kinematics, the fluid loadings and resultant thrust were then calculated (as per the description in Section 4.3). The inverse dynamic process was then executed to obtain the muscle forces using a scaled musculoskeletal model based on the athlete's height and weight (as per the description in Section 4.1).

5.4 Results and Discussion

The Lighthill and musculoskeletal model took ˜30 min to solve the ten kick cycles for each technique. The results from which are are analysed in this section, beginning with analysis of the kinematics and then the produced thrust, muscle loadings and energy expenditure of each technique.

The kinematic variations may be observed in the sequence and overlaid images of Figure 5.2. The images are overlaid and centred at the head (orange dash-dot line) and

comprise of three characteristic body positions of each technique; at the beginning of the up-kick, the toes at the highest point of the kick cycle and in the body's mid-line on the down kick. The dashed red lines indicate the maximum range of motion between the two techniques.

While it is apparent there is little variation in the amplitude at the hands, the magnitude of the displacement of the pelvis is clearly much greater in T_2 (Figure 5.2(b)) than in T_1. The pelvis' range of motion for T_1 is indicated in Figure 5.2 as the dotted blue line. This is further verified in Figure 5.5 and confirms that the motion the athlete achieved is consistent with that intended.

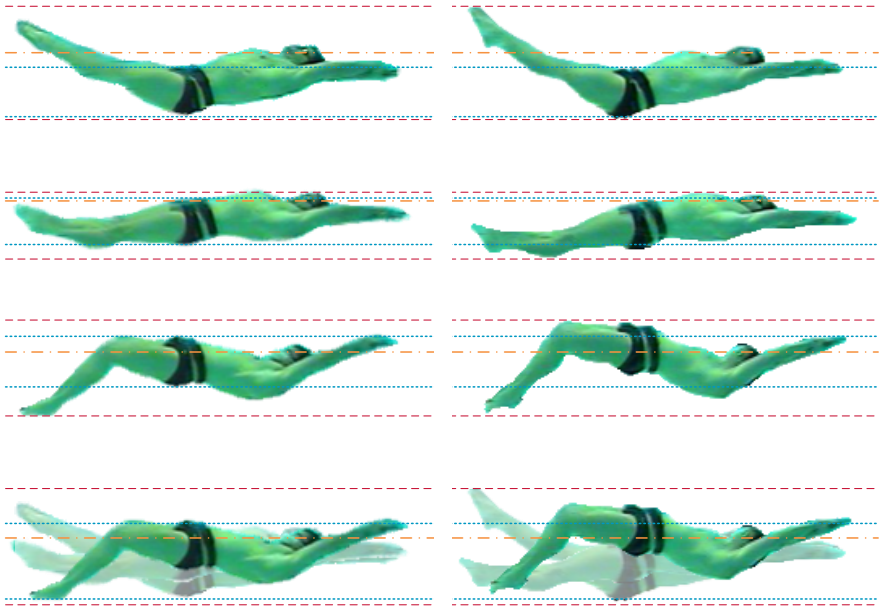

(a)T1 (b)T2

FIGURE 5.2: Beginning, middle and end frame of kick cycle for T_1 (a) and T_2 (b). The dotted blue lines indicate the pelvis' range of motion for T_1 and the dashed orange lines the extent of the maximum range of motion.

The variation in the segment lengths from the digitisation process is shown in the histograms of Figures 5.3 & 5.4. The mean sgement lengths are indicated by the orange vertical bar and displayed above each sub-figure. The mean variation between T_1 and T_2 is 3.97 %, typically with the variation inversely correlated to the segment length ($correl = -0.82$).

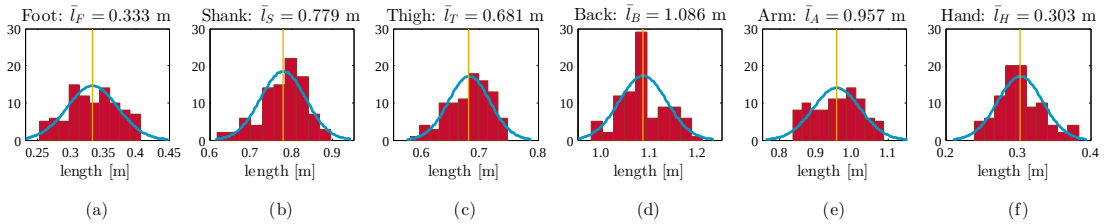

FIGURE 5.3: Variability in segment length for T_1; foot, shank, thigh, back, arm, hand.

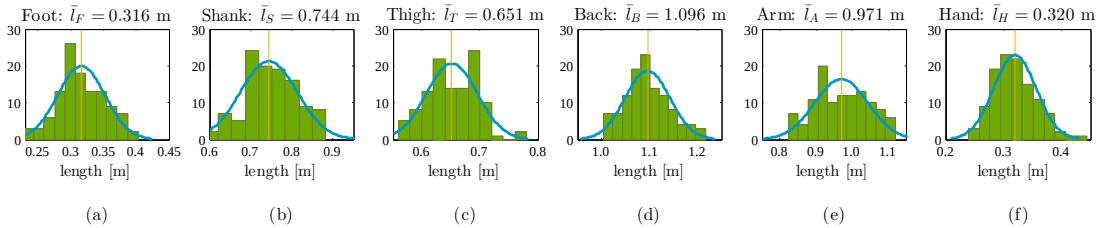

FIGURE 5.4: Variability in segment length for T_2; foot, shank, thigh, back, arm, hand.

The joint angles obtained for the ten kick cycles were divided into individual kicks and a mean joint angle for a single kick was obtained for each technique ($\bar{T}_1$ and $\bar{T}_2$). Figure 5.5 displays these characteristic joint angles, normalised to one kick cycle, for each of the two techniques ($\bar{T}_1$ solid red line and $\bar{T}_2$ solid green line). These sub-figures detail how the kinematic variations between the two techniques differ —the detail of which is potentially indistinguishable from the video alone.

The key results from the simulations can be seen in Table 5.1. A significant reduction of 11.2 % (see Appendix F) in mean maximum muscle activity ($\bar{M}_{max}$) was observed from T_1 to T_2. There was similarly a reduction in mean muscle activity in the trunk ($\bar{A}_{Tr}$) and the legs ($\bar{A}_{LL}$ and $\bar{A}_{LR}$), with the legs experiencing the most with a 26.2 % reduction and consequently a relative shift in muscle loadings ($\bar{A}_{L:T}$) of 8.8 % from the legs to the torso. This evidence corroborates the anecdotal evidence offered by the athlete at the time of testing (Section 5.1.1). Furthermore, despite a 12.4 % calculated reduction in thrust, the measured velocities only differed by $0.04\,\mathrm{m\,s^{-2}}$.

For both techniques there are two peaks of positive thrust. Figure 5.6(a) shows the maximum coinciding with change of direction of the toes as the knee and hip joints begin to extend. This implies that the extension phase of the kick produces significantly more thrust than the flexion phase, corroborating with data in the literature [Cohen *et al.* 2012; Von Loebbecke *et al.* 2009].

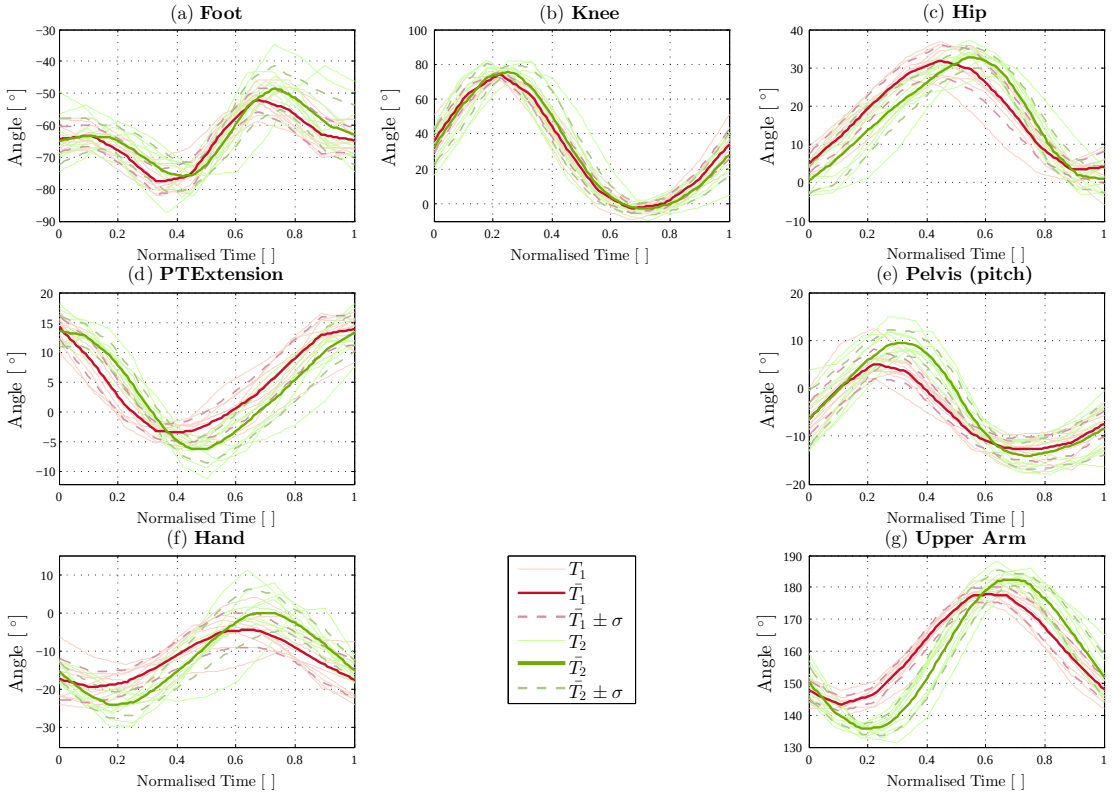

FIGURE 5.5: Joint angles for $\bar{T}_1$ (red) and $\bar{T}_2$ (green); ankle, knee, thigh, PT, pitch, upper-arm, hand.

TABLE 5.1: Results from the simulations for T_1 and T_2

	$\boldsymbol{T_1}$	(*std.*)	$\boldsymbol{T_2}$	(*std*)	$\boldsymbol{T_1 \rightarrow T_2}[\%]$
$\bar{M}_{max}$	0.84	(0.6)	0.75	(0.55)	−11.2
$\bar{A}_{Tot}$	11.9	(4.75)	0.75	(3.82)	−23.0
$\bar{A}_{Tr}$	5.33	(2.42)	4.31	(2.12)	−19.1
$\bar{A}_{LL}$	3.30	(1.63)	2.43	(1.23)	−26.2
$\bar{A}_{L:T}$	1.24		1.13		−8.8
$\bar{T}$ [N]	99.1	(353)	86.8	(492)	−12.4
$\bar{V}$ [m s^{-2}]	1.90	(0.13)	1.86	(0.15)	−2.2
W_M [Nm]	3981		4223		6.1
W_O [Nm]	693		729		5.2
η_P	0.174		0.173		−0.8
St	0.96		1.0		0.3
$\bar{f}$ [Hz]	2.75		2.23		−18.8
$\bar{A}$ [m]	0.66	(0.03)	0.8	(0.04)	20.0

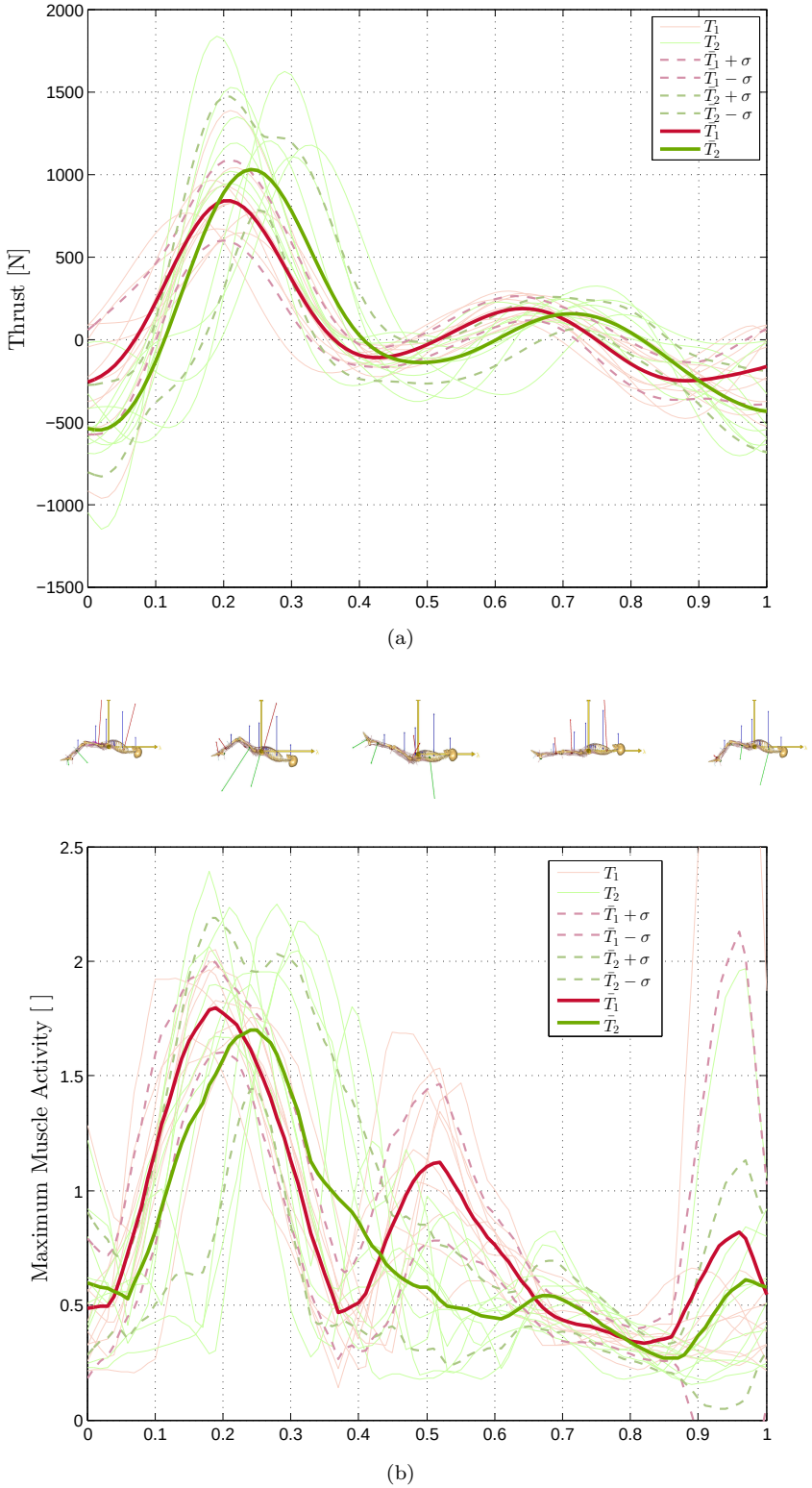

FIGURE 5.6: Thrust (a) and maximum muscle activity (b) with standard deviation, for $\bar{T}_1$ and $\bar{T}_2$.

It was also found that for $\bar{T}_1$ and $\bar{T}_2$ respectively, 95.5 % and 92.3 % of the net thrust originated from the foot segment, in agreement with [Von Loebbecke *et al.* 2009]. It is

also observed that the combined shank and foot segment produce 95.1 % of the total net thrust for T_1, a reduction from the foot segment alone.

The mean and standard deviation for the peak thrust from the cycles was 841 N(247) and 1031 N(275) for T_1 and T_2, respectively. As a comparison, the male athlete in [Von Loebbecke *et al.* 2009] produced a peak thrust of about 750 N. This comparison, however, was recorded at a mean velocity of 1.31 $\mathrm{m\,s^{-1}}$, compared to 1.86 $\mathrm{m\,s^{-1}}$ in T_2 for this athlete. This difference in velocity, as well as any kinematic differences, may account for the disparity in the absolute magnitudes. The more significant deduction, however, is that the calculated thrust for T_1 and T_2 was determined in an order of seconds, whereas each cycle in [Von Loebbecke *et al.* 2009] required equivalent to 250 hours of computer time for each kick-cycle. Despite the dramatic differences in calculation times, the magnitude of the forces are relatively comparable.

It is interesting to note that the Strouhal number has remained relatively unchanged, despite the changes in $\bar{f}$ and $\bar{A}$. This may illustrate a natural response to the body's power limit, or an element of subconscious maintenance of perceived efficiency by the athlete. Furthermore, with the maintenance of Strouhal number, the muscle activities between runs may be directly compared.

The maximum muscle activity for these simulations can be seen to peak at roughly the same phase of the cycle as the peak thrust (Figure 5.6) as the knee begins to extend. There is also a smaller peak of the maximum muscle activity for the first technique which is not present in the second. This occurs as the toes change direction from the extension phase to the flexion phase and the knee begins to flex.

Upon inspection of Figure 5.6(a) & (b), it is apparent that the cycle is divided into a thrust followed by a recovery phase. The first half of the cycle (the extension phase), generated 82.6 % and 83.2 % ($\bar{T}_1$ and $\bar{T}_2$, respectively) of total propulsive thrust and 64.9 % and 70.7 % of total muscle activity ($\bar{T}_1$ and $\bar{T}_2$). Using the musculoskeletal model, it is possible to investigate in more depth which muscles and muscle groups are being recruited, at which part of the cycle and to what extent.

Figure 5.7 is an example of the activity pattern of the muscle groups about the ankle joint with the context of the joint angle. It shows the maximum activity of the grouped muscles coinciding with the maximum rate of joint angle. It also highlights the variation

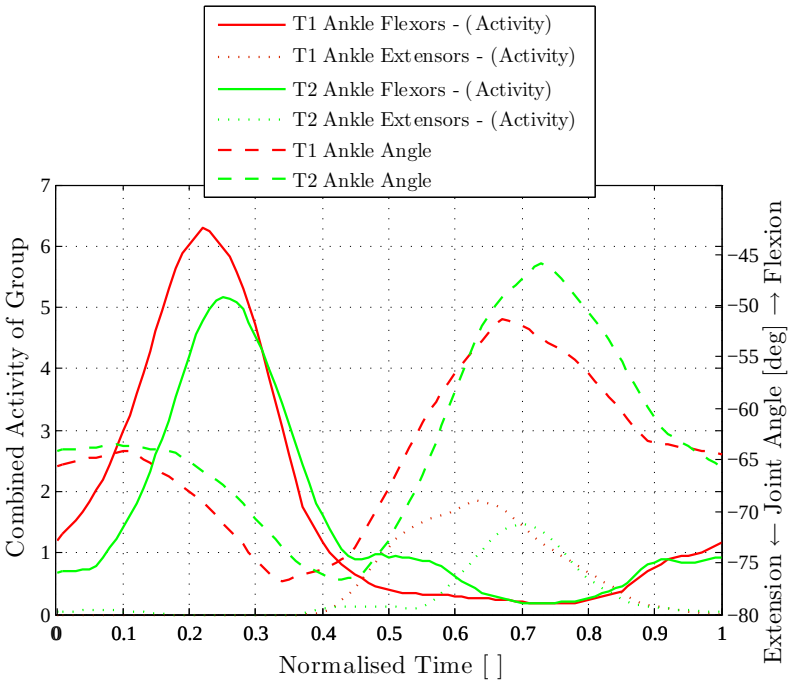

FIGURE 5.7: Flexor (solid) and extensor (dotted) activity of the ankle joint for $\bar{T}_1$ (red) and $\bar{T}_2$ (green), with the context of ankle flexion angle (dashed).

in motion between $\bar{T}_1$ and $\bar{T}_2$. For example, it can be seen that there is reduction in peak activity for both the ankle flexor and extensor groups. There is a phasing difference, particularly prevalent in the second period of the cycle; the joint angle in $\bar{T}_2$ reduces more for a lower peak in the extensors' activity.

Figures 5.8 and 5.9 provides an insight in to the activation levels for each muscle in the trunk and legs for both T_1 and T_2. The histogram shows the normalised frequency for which each muscle exceeds a threshold activation level; grey $> \mathbf{0.02}$, blue $> \mathbf{0.1}$, green $> \mathbf{0.5}$ and red $> \mathbf{0.75}$.

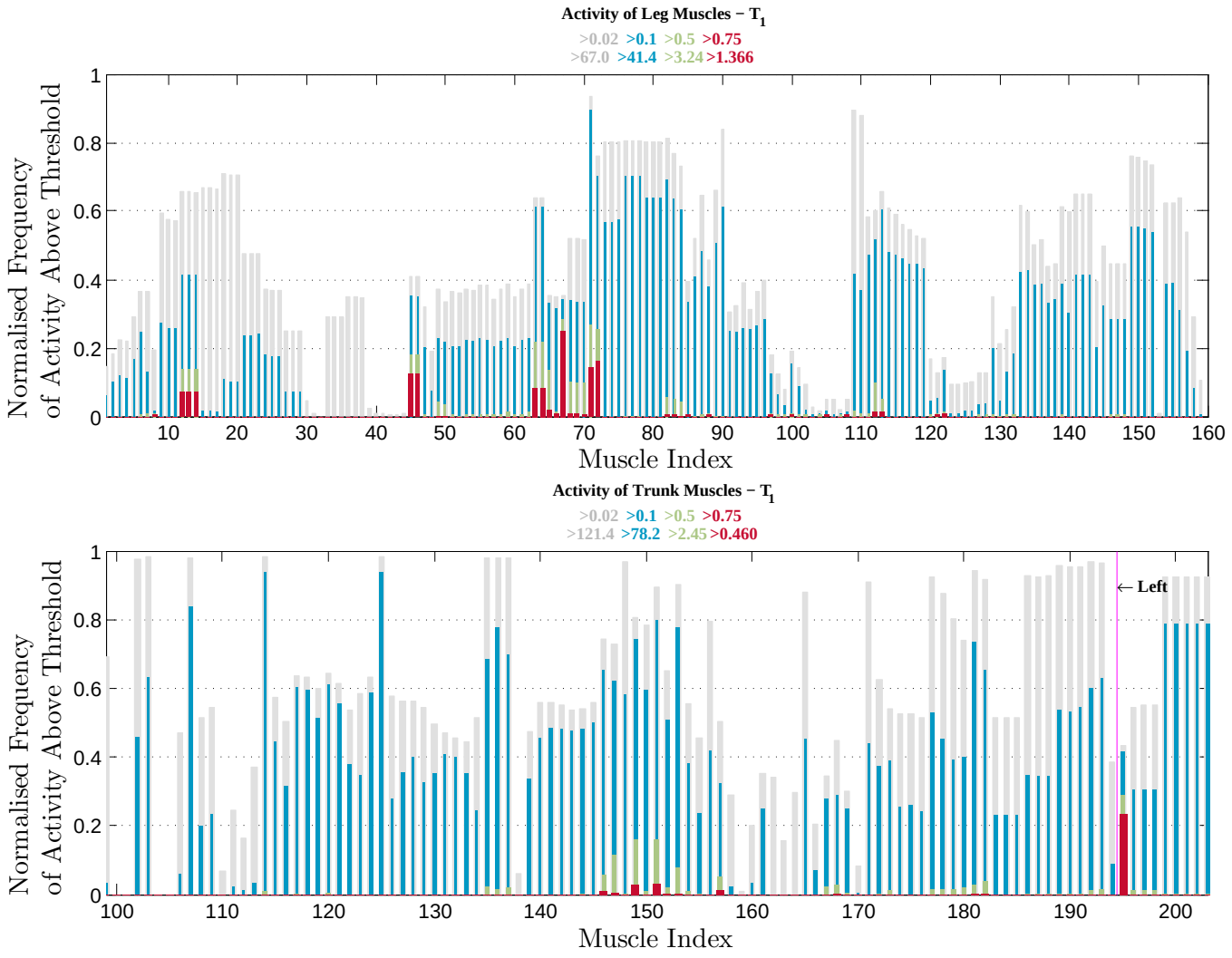

FIGURE 5.8: Histograms displaying the frequency of muscle activity levels in T_1 where they exceed 0.03, 0.1, 0.5 and 0.75.

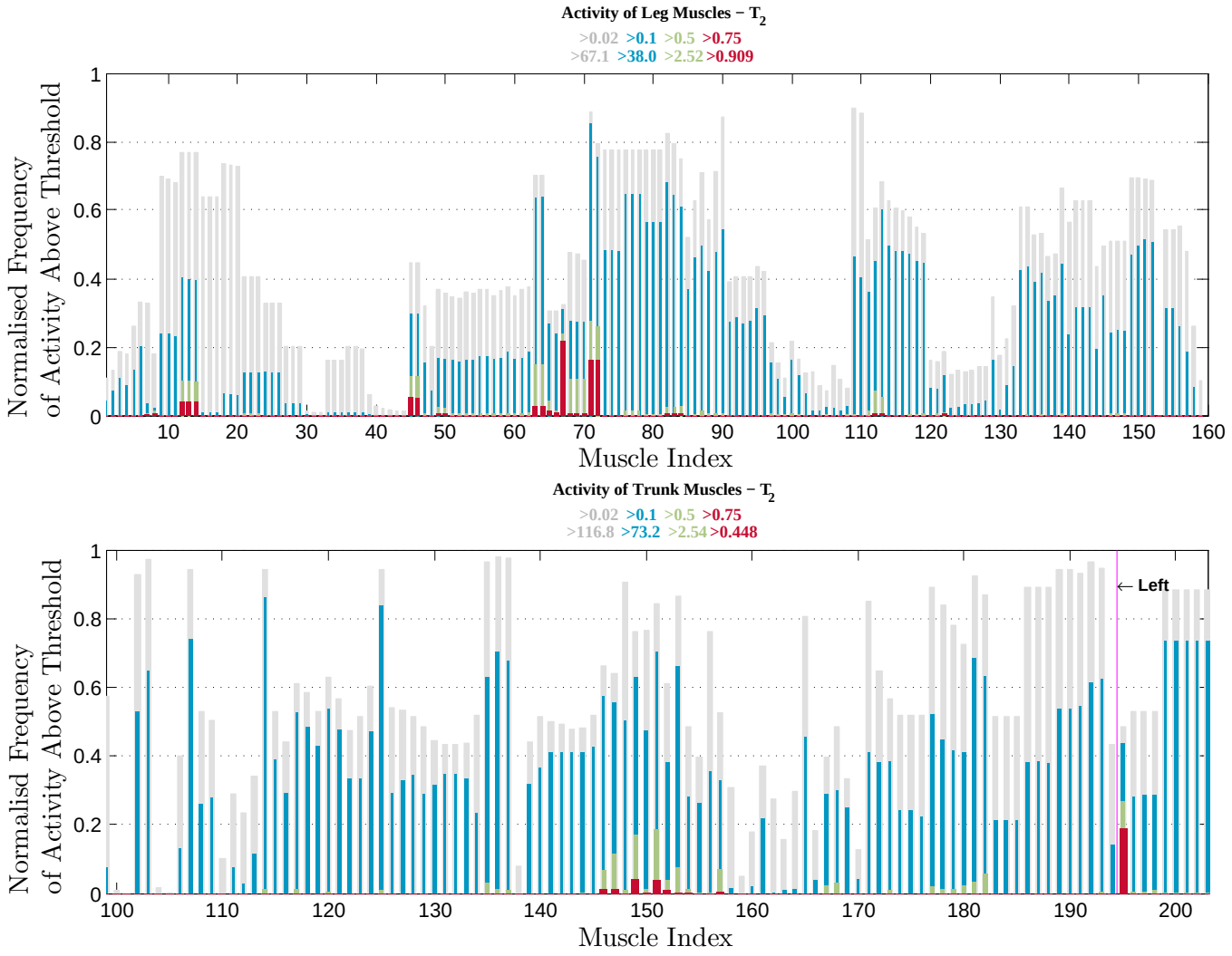

FIGURE 5.9: Histograms displaying the frequency of muscle activity levels in T_2 where they exceed 0.03, 0.1, 0.5 and 0.75.

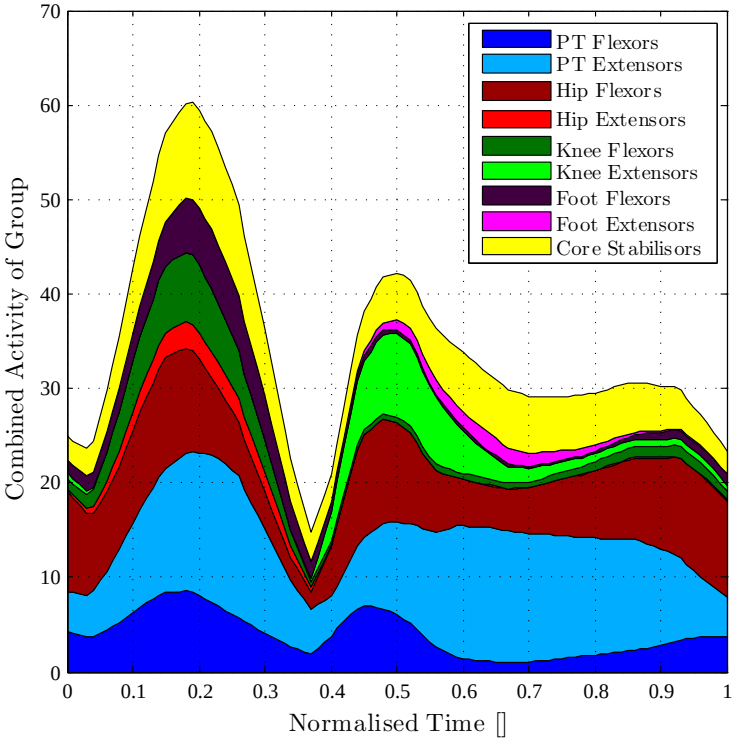

(a)

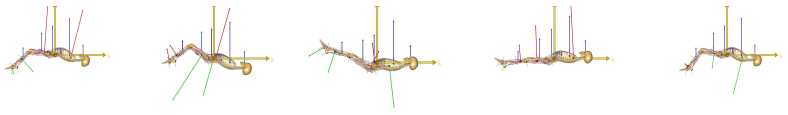

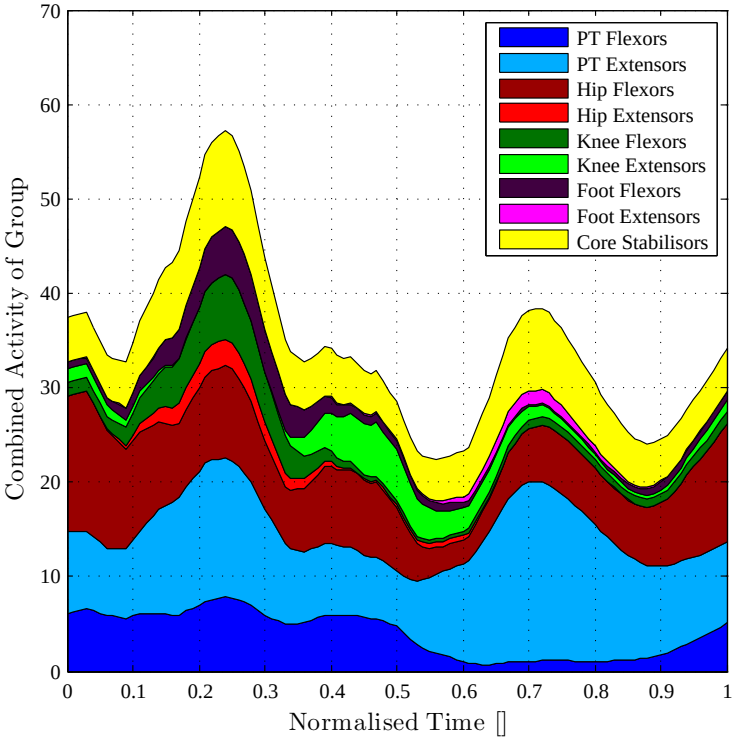

(b)

FIGURE 5.10: Area plot for $\bar{T}_1$ and $\bar{T}_2$ of the combined activity of each muscle separated into their respective group.

An increase in combined activity can be observed (Figure 5.10(a) & (b)) in the core stabiliser muscles between $\bar{T}_1$ and $\bar{T}_2$. With many of the stabilising muscles found in the trunk, it can also be seen in the apparent shift of muscle activity from the legs to the trunk ($-8.8\,\%$, see Table 5.1).

There is also a change in activity pattern for the Pelvis-Thorax Extensors. This is most apparent at ˜0.7 of the cycle, where there is an increase in activity which is less prevalent in $\bar{T}_1$.

There is a difference between the phasing of the activations between the trials. There are two significant peaks visible in the two cases, but for $\bar{T}_1$ the first and second occur at ˜0.19 and ˜0.49 of the cycle, compared with ˜0.3 and ˜0.7 for $\bar{T}_2$.

Upon inspection of the individual muscle group it can be observed that Rectus Abdominus ($i = 195$, see Figure 5.11) and Femoris Caput Longum ($i = 67$, see Figure 5.11) —in the trunk and legs respectively— contribute a significant proportion of the activity required to produce the motion. Rectus Abdominus is associated with Pelvic-Thoracic Flexion and Biceps Femoris Caput Longum with posterior extension of the hip joint. In conjunction with Caput Brevis, it forms part of the Hamstring group for knee flexion. They each exceed activity levels of 0.75 for the longest duration of any of the muscles in their respective areas of the body (Figure 5.11) and are hence indicative of those of greater significance in underwater flykick.

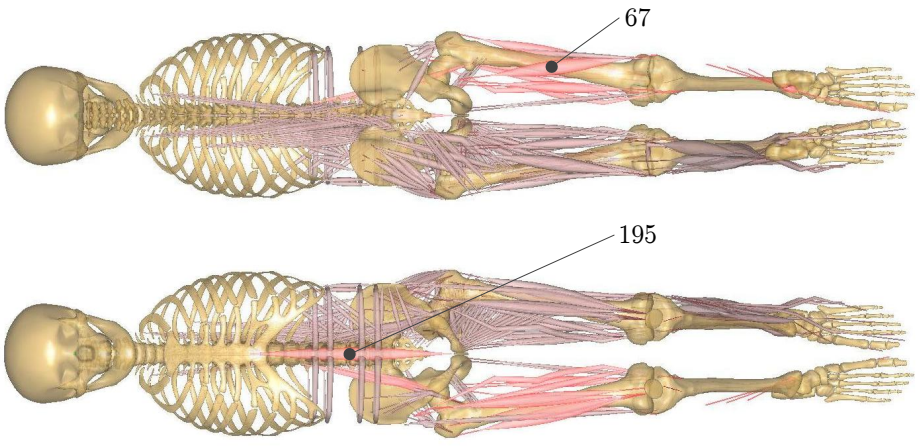

FIGURE 5.11: Scaled musculoskeletal model.

The Strouhal numbers for $\bar{T}_1$ and $\bar{T}_2$ were 0.96 and 1.0 respectively, with little variation in η_P also. But in human underwater flykick, as seen in Figure 5.6(a), there appears to be only one significant thrust production and hence one vortex shed during the cycle (Figure 11 of [Von Loebbecke *et al.* 2009]). This is in contrast to human mono-fin swimming and fish swimming, which have two [Hochstein and Blickhan 2011; Nicolas *et al.* 2007].

If it is considered that frequency component in Equation 2.1 is more correctly defined as the frequency between vortex shedding, then the apparent time period between the generated vortices for underwater flykick is therefore double that of mono-fin and fish swimming, and thus relatively half the frequency. This would therefore lead to a twofold overestimation of Strouhal number for cases where only one vortex is shed in a cycle, such as demonstrated for underwater flykick. This would account for inflated variation in theoretically optimal ranges and published values of Strouhal number for human underwater flykick, relative to mono-fin and fish swimming.

To gain greater insight into the kinematic space surrounding $\bar{T}_1$ and $\bar{T}_2$, and to explore the concept of kinematic tuning, a five term Fourier series was fitted to the joint angle and velocity data. By multiplying these Fourier coefficients by $\boldsymbol{k}$, where $\boldsymbol{k} = \{0.1 : 0.1 : 2\}$, permutations of the idealised base kinematics were generated ($\bar{T}_{1 \cdot k}$ and $\bar{T}_{2 \cdot k}$) for use in subsequent simulations.

For T_1 and T_2 experimental velocity data was used, however, for $\bar{T}_{1 \cdot k}$ and $\bar{T}_{2 \cdot k}$ a mean velocity was used as an initial input to the Lighthill model. This velocity was determined based upon the original experimental data. For the two techniques, an equivalent mean drag coefficient (C_D) was determined using the equation

$$\bar{T} = \frac{1}{2}\rho \bar{V}^2 S C_D, \tag{5.1}$$

where $\bar{T}$ is the mean thrust, ρ is the density of the water, $\bar{V}$ the athlete's mean velocity, and S frontal area (assumed to be kick amplitude (A) $\times$ breadth at pelvis (B)).

Using the initial mean velocity, the Lighthill simulation was executed to calculate the mean thrust. Using the previously calculated drag coefficient, a new mean velocity was estimated. This process was iterated until the mean velocity converged ($< 0.003 \mathrm{m\,s^{-1}}$).

The resulting transverse forces (Q) are then used as inputs for the musculoskeletal simulation in the form of body segment loads.

The musculoskeletal model was subsequently run for each instance of the newly generated datasets ($\bar{T}_{1\cdot k}$ and $\bar{T}_{2\cdot k}$). The results from which provide insight into the tuning of the kinematics for the two techniques simulated here.

Figure 5.12 shows the propulsive efficiencies as a function of Strouhal Number, illustrating the non-linear relationship between the kinematic variations of $\bar{T}_{1\cdot k}$ and $\bar{T}_{2\cdot k}$.

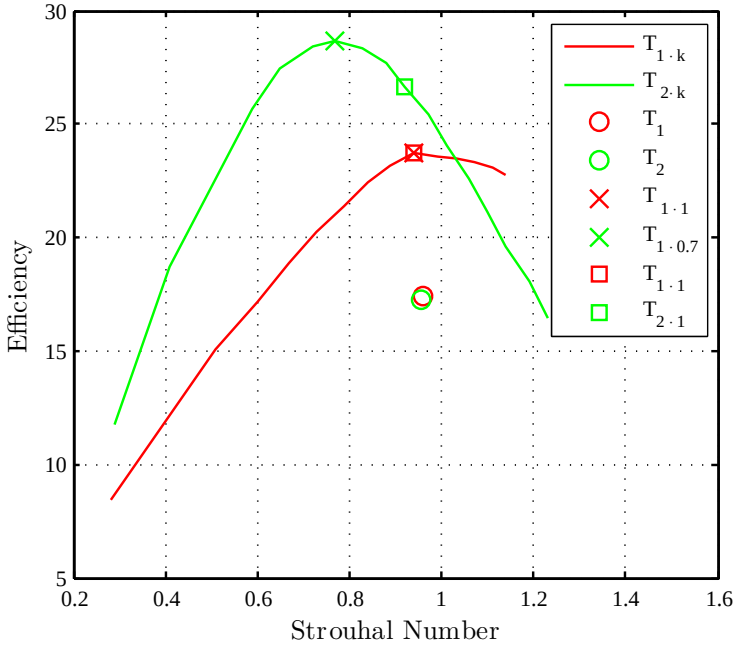

FIGURE 5.12: Relationship between kick amplitude and efficiency and Energy. The red and green solid lines represent $\bar{T}_{1\cdot k}$ and $\bar{T}_{2\cdot k}$ respectively. Red and green "□" indicate $\bar{T}_{1\cdot 1}$ and $\bar{T}_{2\cdot 1}$ and red and green "×" indicate peak efficiency which for $\bar{T}_{1\cdot k}$ is at $k = 1.0$ and $\bar{T}_{2\cdot k}$ at $k = 0.7$. Maximum η_P for $\bar{T}_{1\cdot k}$ and $\bar{T}_{2\cdot k}$ occurs at $St_1 = 0.94$ and $St_2 = 0.77$, respectively.

It is apparent from Figure 5.12 that there is an increase in efficiency from T_1 to $\bar{T}_{1\cdot 1}$ and similarly from T_2 to $\bar{T}_{2\cdot 1}$. This increase suggests that the maintenance of consistent kinematics generates higher observed efficiency.

The data shows that the base style ($k = 1$) for the first technique is at the optimal efficiency point for that technique. Contrastingly, the base style for the second technique is not at the optimal efficiency point —a decrease in the global joint angles would increase the efficiency to a maximum. This further illustrates the non-linear relationship between St and η_P, and clearly demonstrates the principle that tuning kinematics, as shown for

TABLE 5.2: Energy cost of swimming (C_S) for different disciplines

Description	C_S[kJm^{-1}]			V[m s^{-2}]		
Underwater flykick	0.57*	⇒	0.50†	1.9*	⇒	1.86†
Freestyle	1.13	⇒	1.41^{i}	1.21	⇒	1.62^{i}
			0.55^{ii}	0.9^{ii}		

*T_1; †T_2; ^{i}[Zamparo *et al.* 2000];^{ii}[Pendergast *et al.* 2003]

flying animals [Taylor *et al.* 2003], can achieve higher efficiency in underwater flykick. In changing technique, this study has demonstrated that an athlete may swim at the same Strouhal number, but their levels of efficiency might differ.

Depending on a particular strategy, however, maximising efficiency may occasionally be misleading. Hypothetically, it may be less efficient to choose to swim at a higher Strouhal number. However, with a proportional relationship between velocity and Strouhal number, it may well be faster.

It is therefore necessary to determine the energy cost of (C_S) of a particular technique to make informed decisions. Umberger [2010] used a musculoskeletal model to quantify the energy cost of locomotion for a gait cycle. In a similar way, the data from the musculoskeletal model presented here was used to determine the energy cost for the two techniques, which for T_1 and T_2 respectively, $C_S = 0.569\,\mathrm{kJm^{-1}}$ and $0.502\,\mathrm{kJm^{-1}}$.

These values of C_S are comparable with experimental values for freestyle swimming as tabulated in Table 5.2. The reduced values for underwater flykick shown here may, for example, may be explained as a consequence of variation in kinematics or the discrepancy between stroke types. More fundamentally, however, the effect of the arms was also not taken into account and neither was the muscle heat production unlike in Umberger [2010].

By analysing these results, it may be more effective for a sprint athlete to swim at a higher velocity and hence at a higher Strouhal number: for a common goldfish $St \simeq 0.4$ but for an Atlantic mackerel $St \simeq 0.25$ [Eloy 2011]. Upon observation of Figure 5.13, for example, it may be more efficient for the sprint athlete in this study to select a more knee based kick of the first technique (T_1) when swimming above $2.3\,\mathrm{m\,s^{-2}}$. The reciprocal would therefore be more appropriate for lower velocities or a longer distance swimmer,

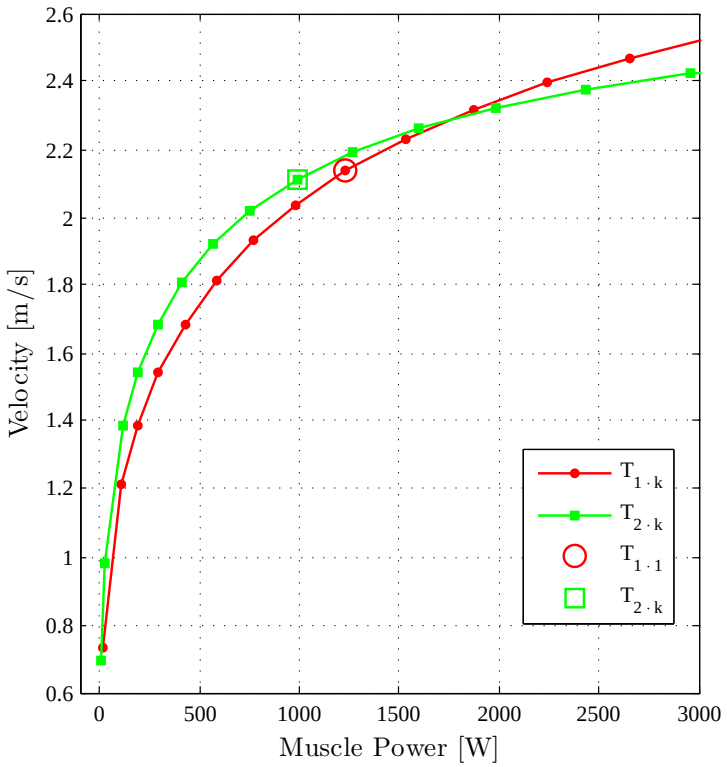

FIGURE 5.13: Relationship between power delivered by the muscles and swimming velocities for $\bar{T}_{1 \cdot k}$ (red) and $\bar{T}_{2 \cdot k}$ (green)

where conservation of energy is more applicable. It may also be strategically beneficial to seamlessly transfer from $\bar{T}_1$ to $\bar{T}_2$ as the athlete begins to slow down following a dive start or push off the wall from a turn.

5.5 Conclusions

In this chapter, Lighthill's theory of fish locomotion and a musculoskeletal model are coupled together for the analysis of UUS technique and is demonstrated in the form of a case study. The kinematics and velocity were acquired and synchronised using a non-invasive or motion restrictive arrangement. The thrust production of Lighthill is shown to be comparable to published data and is computationally inexpensive. The musculoskeletal model has been shown to provide a greater level of insight, both inter and intra simulated technique. The musculoskeletal model also provided an estimation for the energetic cost of locomotion, enabling the comparison of differing techniques and demonstrating the potential increase in efficiency associated with increased consistency.

An example of varying joint amplitude has demonstrated the potential benefit of tuning kinematics to provide a potential increase inefficiency. This provides a quantitative answer as to which technique may be preferable for an athlete when competing in short-course swimming events.

Chapter 6

Analysis of Errors in Manual Digitisation

6.1 Introduction

The thrust generated by a swimmer and the work done by their muscles are critical elements to performance. They are used in evaluating both overall and propulsive efficiencies (Equations 4.20 and 4.21). An implementation of Lighthill's formula is used to determine the thrust in the previous chapter. It is also used to evaluate the fluid loadings imported into the musculoskeletal model. A prerequisite of this formula is therefore knowing the kinematics. Furthermore, these kinematics and forces are required in the determination of the muscle forces.

As described in Section 4.2 the model's kinematic data have been derived from manual, human, digitisation of video frames. While a user may become experienced and skilled at selecting the anatomical location in the video frame, it is unlikely they would select the exact same pixel every time if they were to repeat the process n times. Is is supposed that these inconsistencies will have a bearing on the subsequent results —thrust and muscle activity— but to what degree was previously unknown. The following sections investigate the influence of these errors on the results.

6.2 Aims and Objectives

The intention of this chapter is to explore the effect of this uncertainty on both the calculated thrust and maximum muscle activity. The aims are, therefore, to

1. Quantify the thrust variation for known variation of digitised input points
2. Quantify the maximum muscle activity for variation for known variation of digitised input points

This will be achieved by fulfilling the following objectives:

1. Acquire image, velocity data of a series of underwater undulatory swimming (UUS) kicks cycles
2. Manually digitise these kick cycles
3. Evaluate the thrust and mean maximum muscle activity
4. Apply random error to pre-existing data and observe consequential thrust variation.
5. Apply random error to pre-existing data and observe consequential variation in maximum muscle activity.

6.3 Method

A non-elite, recreational swimmer provided the data for this study (male, height = 1.7 m, mass = 65 kg). To aid in selecting the post-processing phase, the participant wore a full-body custom-made Speedo® suit with black markers aligned with the joint centres as viewed from the camera. The suit, as depicted in Figure 6.1, was an orange colour to provided a high contrast of the participants body to the background of the water, making them more apparent in the digitisation process. Consequently it aided in providing a contrasting background for the black markers at the joint centres.

The synchronous velocity and video data for four kick cycles was recorded using the i-DAQ system as per the procedure in Section 4.2. These data were then loaded into

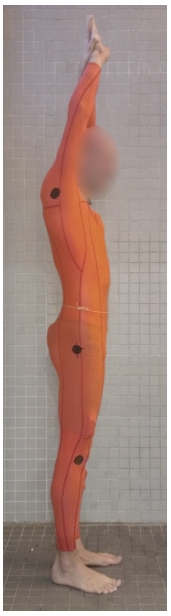

FIGURE 6.1: Participant in custom-made orange suit.

the script detailed in Section 4.4. The location of the tip of the toes, ankle, knee, hip, shoulder wrist and finger-tips were then selected in each frame. This then enabled the joint angles to be derived and subsequently the generated thrust evaluated based upon these selections (as per Section 4.3).

Following this, an array was generated consisting of a normally-distributed random errors of mean $\bar{N}_{D,i}$ and standard deviation $\sigma_{D,i}$, where subscript D is the index of the digitised point and subscript i the index of the frame. From inspection of Figure 4.7 a one standard deviation error in segment length is approximately $\pm 0.05\,\text{m}$ and hence a error contained within a radius of $0.025\,\text{m}$ from each node. Further increasing this error by $0.01\,\text{m}$ would encompass this same error with an additional allowance. It was therefore assumed that an operator would select each digitised point within a region of $\pm 0.035\,\text{m}$ of the actual joint centre, in both the horizontal and vertical axes. This measurement was then converted into pixels and was the variance of the applied error about the mean.

The random error was first applied to each location individually, beginning with the node at the tip of the toes. In each subsequent frame the random error was introduced at the individual node and the resultant thrust for that run was obtained. This process of applying a random error at an individual node in each frame was then repeated 100

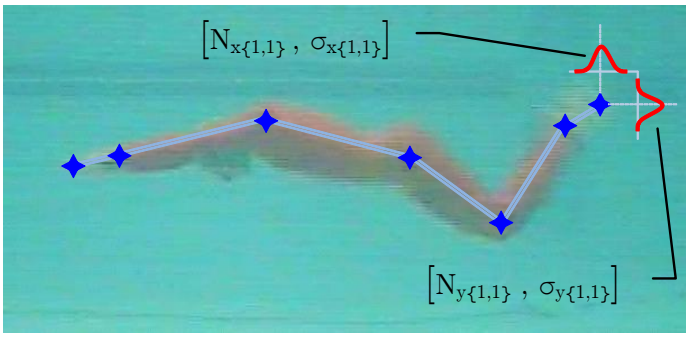

FIGURE 6.2: An annotated image illustrating the normally-distributed error applied to the digitised points. In this example the normally distributed error is applied to the node at the tip of the toe (N.B. distribution not to scale).

times. Equally, the same process was applied at the subsequent nodes, including the; knee, hip, shoulder, wrist and hand.

Having applied the error to the nodes individually, a normally-distributed error was introduced to every node in each frame and the resultant thrust determined. Similarly, this process was repeated 100 times.

In order to create a large dataset to investigate this uncertainty only the thrust from the Lighthill model was initially obtained and not the muscle activities from the musculoskeletal model. This was because of the time implication for executing the musculoskeletal model; run time approximately 15 min. Therefore a smaller dataset was created to investigate the variation in the muscle activity. This consisted of 10 runs of varying each node individually and 10 runs varying all the nodes simultaneously. The thrust was also recorded for these runs and so a comparison between the sensitivity of the thrust could be analysed between the datasets.

6.4 Results and Discussion

The thrust results from the first investigation are shown in Figure 6.3. The uppermost graph details the resultant thrust for an error applied to the node at the tip of the toe. It shows the calculated thrust for each run overlaid, providing a qualitative, visual indication of the affect. The following graphs are for the ankle, knee, hip, shoulder, wrist

and finger-tip node respectively. The lowest graph in the figure is where an independent error has been applied to each node and the resultant thrust overlaid.

It is apparent from visual inspection that the hip-node has the greatest impact on the calculated thrust and the toe the least. The significance of the node error diminishes as the node location moves away from the hip —as borne-out in the quantified data of Table 6.1. A mean standard deviation of 2.71 pix in the vertical location of the hip-node, results in a mean standard deviation of 107.9 N of thrust. A mean standard deviation of 2.70 pixels in the vertical location of the toe-node, however, results in a mean standard deviation of 18.76 N of thrust —or 82.6 % less than a similar variation of the hip-node.

TABLE 6.1: The results of the variation in thrust and joint angle, as a result of the applied error at the digitised nodes.

Mean Std. per time step		Node							
		Toe	Ankle	Knee	Hip	Shoulder	Wrist	Finger	All
X-Pos	[pix]	3.89	3.86	3.82	3.85	3.82	3.86	3.87	-
Y-Pos	[pix]	2.70	2.75	2.72	2.71	2.73	2.70	3.85	-
Ankle Angle	[°]	5.33	7.26	2.37	0	0	0	0	9.35
Knee Angle	[°]	0	2.39	4.39	2.47	0	0	0	5.57
Hip Angle	[°]	0	0	2.49	2.47	0	0	0	3.52
PT Angle	[°]	0	0	0	1.87	1.89	0	0	2.69
GH Angle	[°]	0	0	0	1.87	3.81	1.92	0	4.77
Wrist Angle	[°]	0	0	0	0	1.95	6.88	5.15	8.94
Thrust	[N]	18.76	36.65	73.40	107.9	71.66	35.73	20.16	169.16

The results of the maximum muscle activity from the applied error of the original nodes can be visualised in Figure 6.4. Similarly to before, the uppermost graph details the temporal maximum muscle activity for each of the ten runs with an normally-distributed random error applied to the node at the tip of the toe. The subsequent graphs are the same but for variation at the ankle, knee, hip, shoulder, wrist and finger, respectively. The final graph depicts the temporal maximum muscle activity for each of the ten runs where the independently error is applied to to all the nodes.

The tabulated results (Table 6.2) show the hip-node having the most significance on the recorded thrust; exhibiting 81.1% greater influence than the toe-node. This is the same trend as found in the 100 samples-per-node study ($R^2 = 0.977$).

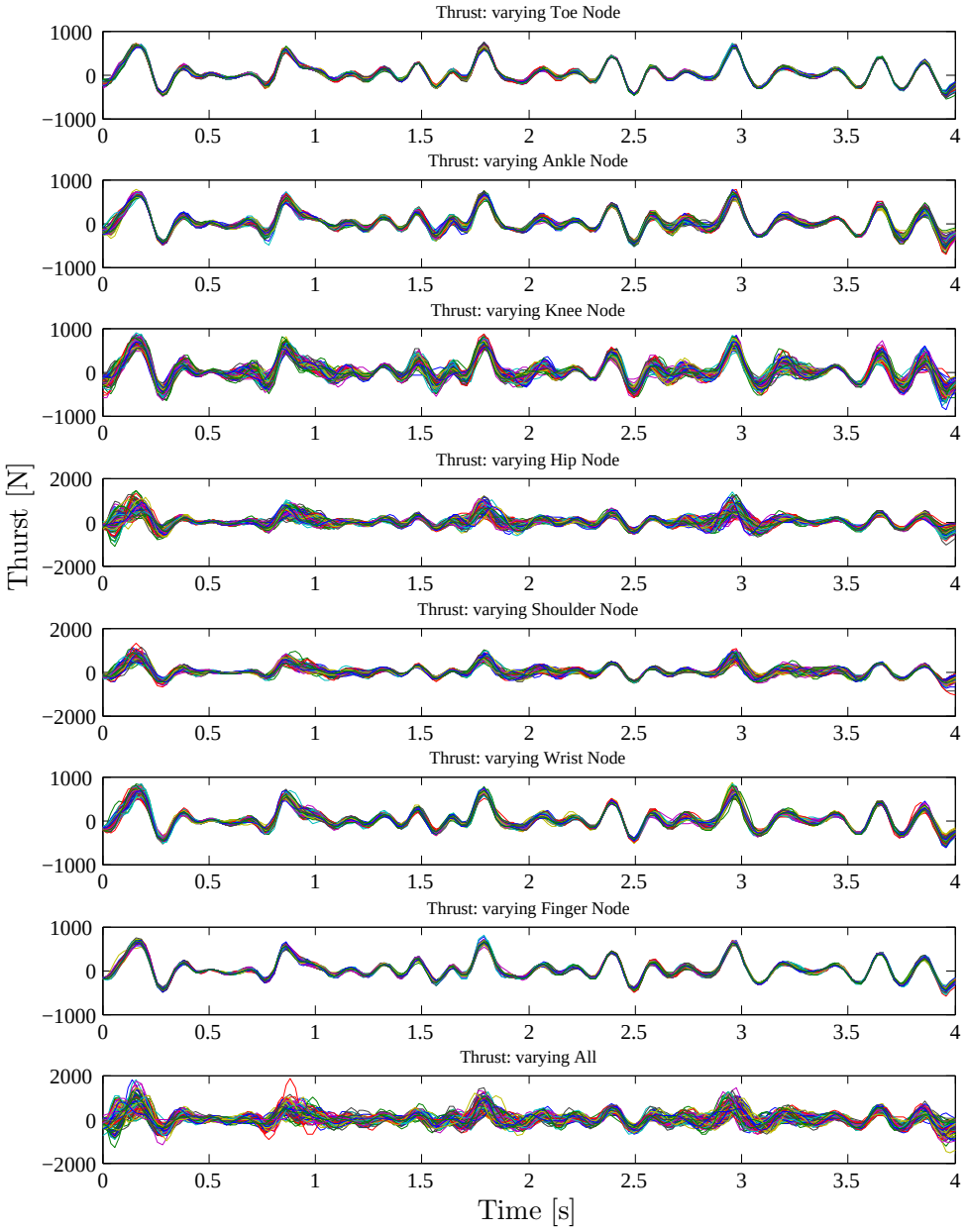

FIGURE 6.3: The variation of the determined thrust as a consequence of the introduced error. Firstly the error is introduced to the node at the tip of the toe and the resultant thrust is illustrated in the top graph. The approach is then applied to the ankle, knee, hip, shoulder, wrist and finger tip and whose results are illustrated in the subsequent graphs. The final graph, is the resultant thrust having introduced an independent error at each of the nodes simultaneously.

While the variation of the hip-node has the most impact on the thrust, the knee-node has the greatest influence on the maximum muscle activity; followed by the hip-node. The mean standard deviation of maximum muscle activity when varying just the knee node is equivalent to 60.5% of the variation when an error was applied to all nodes. The finger- and toe-node are shown to have the least and second-least influence on the

maximum muscle activity, respectively.

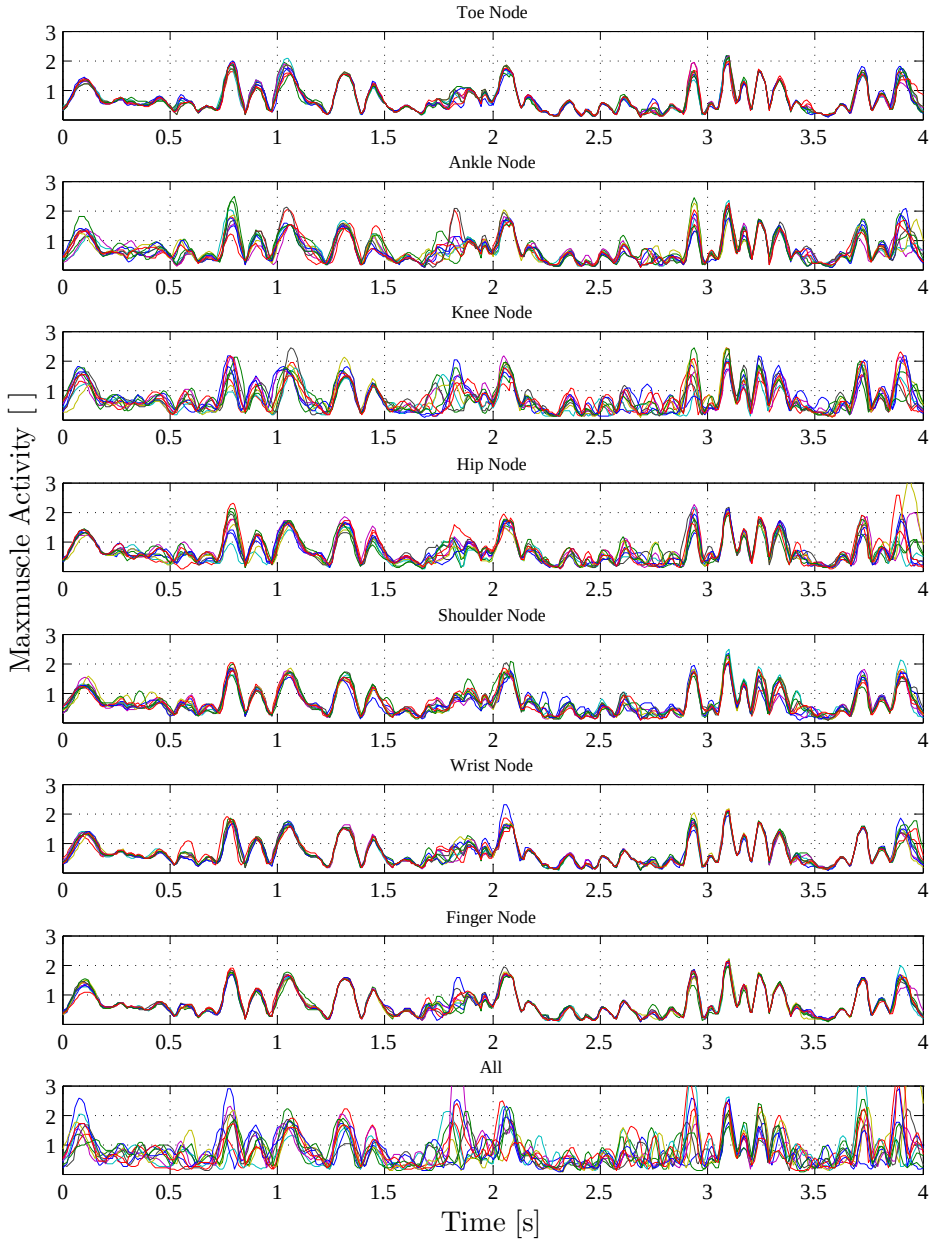

FIGURE 6.4: The variation of the calculated maximum muscle activity as a consequence of the introduced error. Firstly the error is introduced to the node at the tip of the toe and the resultant thrust is illustrated in the top graph. The approach is then applied to the ankle, knee, hip, shoulder, wrist and finger tip and whose results are illustrated in the subsequent graphs. The final graph, is the resultant maximum muscle activity having introduced an independent error at each of the nodes simultaneously.

The reason for the trend in the error diminishing with increasing distance from the hip-node can be seen by observing both Figure 6.2 and the data in Table 6.1. The hip-node has an influence on four joints; knee, hip and pelvic-thorax joints, as well as the glenohumeral joint of the shoulder. This hip node is therefore the central node in the

TABLE 6.2: The results of the variation in thrust and maximum muscle activity as a result of the applied error at the digitised nodes.

Mean of Std. (each time step)		Node							
		Toe	Ankle	Knee	Hip	Shoulder	Wrist	Finger	All
X-Pos	[pix]	3.78	3.66	3.73	3.74	3.66	3.66	3.62	-
Y-Pos	[pix]	3.72	3.89	3.95	3.61	3.74	3.83	3.74	-
Thrust	[N]	17.87	37.12	73.63	94.91	71.04	41.88	34.75	174.71
MaxMuscle Activity	[ ]	0.0625	0.1459	0.2081	0.1578	0.1148	0.0727	0.0565	0.344
Std. of Mean									
Thrust	[N]	0.971	1.599	1.871	2.608	1.133	1.845	1.228	6.996
MaxMuscle Activity	[ ]	0.0058	0.0198	0.0451	0.0340	0.0150	0.0094	0.0095	0.0532

chain. The nodes further from this central node influence fewer joints, such that the end nodes, the toe and finger-tip, influence only one joint —the ankle and wrist respectively. As they have less influence on the overall kinematics of the body hence they should have less impact on the calculated thrust.

Upon inspection of Equation 4.10 it is reasonable to deduce that the $\frac{\partial z}{\partial t}$ component of the toe-node ($a = 0$) will have large influence upon the thrust and thus the influence of digitised error of this node should too, have more influence upon the result. However, because the point locations are re-calculated based upon the derived joint angles, the vertical displacement of the tip of the toe is determined as a compound of the pitch, hip, knee and ankle joints. Upon inspection of the geometry of the kinematic chain, the influence of a joint angle change on the vertical toe-node displacement, is proportional to the horizontal distance between the joint centre and the toe-node.

It, too, is perhaps not surprising that an error at the knee-node has been shown to have the greatest influence on the muscle activity. The knee joint moves through the greatest angular range of motion and the distal end of the lower limb produces the largest net thrust [Von Loebbecke *et al.* 2009]. From an anatomic perspective, the knee now is part of two segments; the femur and the tibia. There also numerous, highly active muscles —with regards to UUS— which span this joint (for example, see histogram in

Figure 5.8 and corresponding data in Appendix C). With the kinematic, force loading and anatomical factors combined, it would explain the observation of the influence of an error at the knee-node.

The mean standard deviation of the thrust values of the two differing techniques studied in Chapter 5 were 353 N and 492 N for T_1 and T_2 respectively (refer to Table 5.1). Due to the imposed errors, the maximum mean standard deviation of the thrust in in this chapter was 175 N. Assuming that the error of the digitised points of the case study in Chapter 5 did not exceed ± 5 pix, in either vertical of horizontal position of the true location, the standard deviation of the thrust in each run exceeded what would be the expected error due to error in the digitisation process. It is therefore suggested, that the observed mean standard deviation in each of the two runs was most likely due to intra-run variation of in kinematics —i.e. inconsistencies in the technique. Furthermore, despite these intra-run variations, the inter-run variations were determined to be significantly different ($p < 0.05$).

Table 6.2 also displays the standard deviation of the mean thrust and mean maximum muscle activity. The greatest variation in both metrics occurs when errors are applied to all nodes, equating to 6.996 N and 0.0532 respectively. In the context again of the results for T_1 and T_2 of Chapter 5, these errors would be 7.06% of the thrust and 6.33% of the maximum muscle activity for T_1, and 8.06% of the thrust and 7.09% of the maximum muscle activity for T_2. While these figures are each less than the observed differences between T_1 and T_2, they are not negligible and at most could account for between 51.0 % and 72.0% of the observed differences between the two techniques. This, however, does assume that the digitised points all contain errors of 0.035 m variance about the true location.

6.5 Conclusions

It was shown that running ten instances of the erroneous digitised nodes, provided the same results in thrust variation as running 100 instances.

This study has identified the hip- and knee-nodes as being the most influential on the sensitivity of the thrust and maximum muscle activity. It reaffirmed the intra-run inconsistencies in the kinematic techniques displayed in the case study of Chapter 5, implying

the standard deviations stated in the results was not mostly due to errors in the process of the kinematic acquisition. It does, however, highlight that when investigating subtle changes in technique style, the errors in the processing could become influential on the outcomes. It would therefore be suggested, that for future studies investigating such changes, the data in Tables 6.1 and 6.2 should be consulted. If necessary, it would be recommended to perform a statistical investigation such as this to give confidence in the findings.

Chapter 7

Joint Angle Optimisation

The previous chapters have described and demonstrated a computational model replicating human underwater undulatory swimming (UUS), with the joint kinematics driven from real data and the consequential hydrodynamic and muscle forces determined. Chapter 5 compares two UUS techniques in a case study where the impact of the coaching intervention is quantified. The content of this chapter, however, sets out an example whereby joint kinematics may be optimised from a theoretical perspective. Such optimisation could provide coaches and athletes points of reference from which to guide their training.

7.1 Introduction

Iterative, trial and error based approach to technique refinement is reliant on the person implementing the change to firstly *be able* to implement a change and secondly implement the correct change as communicated from the coach. It also relies on the coach to devise the intervention in the first instance —which is typically a result of their skill and intuition. This can obviously be trialled by the athlete and between them they may determine one is better than the other. They may seek to then trial numerous different techniques until they iterate to an optimal.

A shortcoming of this approach, for example, is that it is difficult to account for inter-trial variation due to factors not directly resulting from the technique change —notably fatigue.

Although difficult to quantify, the self-optimisation and evolution of techniques by elite athletes should not be undervalued nor underestimated. Much time will have been spent refining their technique where, analogous to simple evolutionary principles, the outcome of a race may decide its fate. However, as illustrated in Chapter 5, subtle variations to an already world-class style may invoke a marginal performance gain.

Similarly to a coach's iterative approach to technique evaluation, Chapter 5 went some way to identify what changes in specific technique had on performance. Unlike a real athlete, the computational model does not suffer from errors due to fatigue. Studies do though become limited by computational resources. Here, the exploratory study was limited to varying amplitude changes across all the joints angles by equal magnitude.

This chapter addresses these previous limitations by implementing a fully independent joint angle optimisation. While it would be naive to suggest an athlete would implement the findings immediately, what it seeks to identify are techniques which may theoretically increase performance and provide a basis for future trialling. It is then for the coach and athlete to explore these findings and pursue that which is perceived to be the optimal.

7.2 Aims and Objectives

The principal aims of this chapter are therefore to,

- enable theoretical optimisation of human UUS kinematics and
- identify theoretical solutions that a coach and athlete may seek to implement.

These aims will be realised through the creation of a multi-objective optimisation model which utilises the previously developed musculoskeletal model. This process will be achieved by

- obtaining Fourier coefficients which describe an existing kinematic dataset,
- generating an initial sample-plan based on specified bounds of the initial Fourier coefficients,
- executing the simulation at the identified sample points,

- building a Kriging model of the function,
- searching the model for expected improvements in the target functions,
- re-executing the simulation at the point of maximum expected improvement,
- repeating search and re-execution until specified convergence or goal is achieved
- identify optimal solution(s).

7.3 Methodology

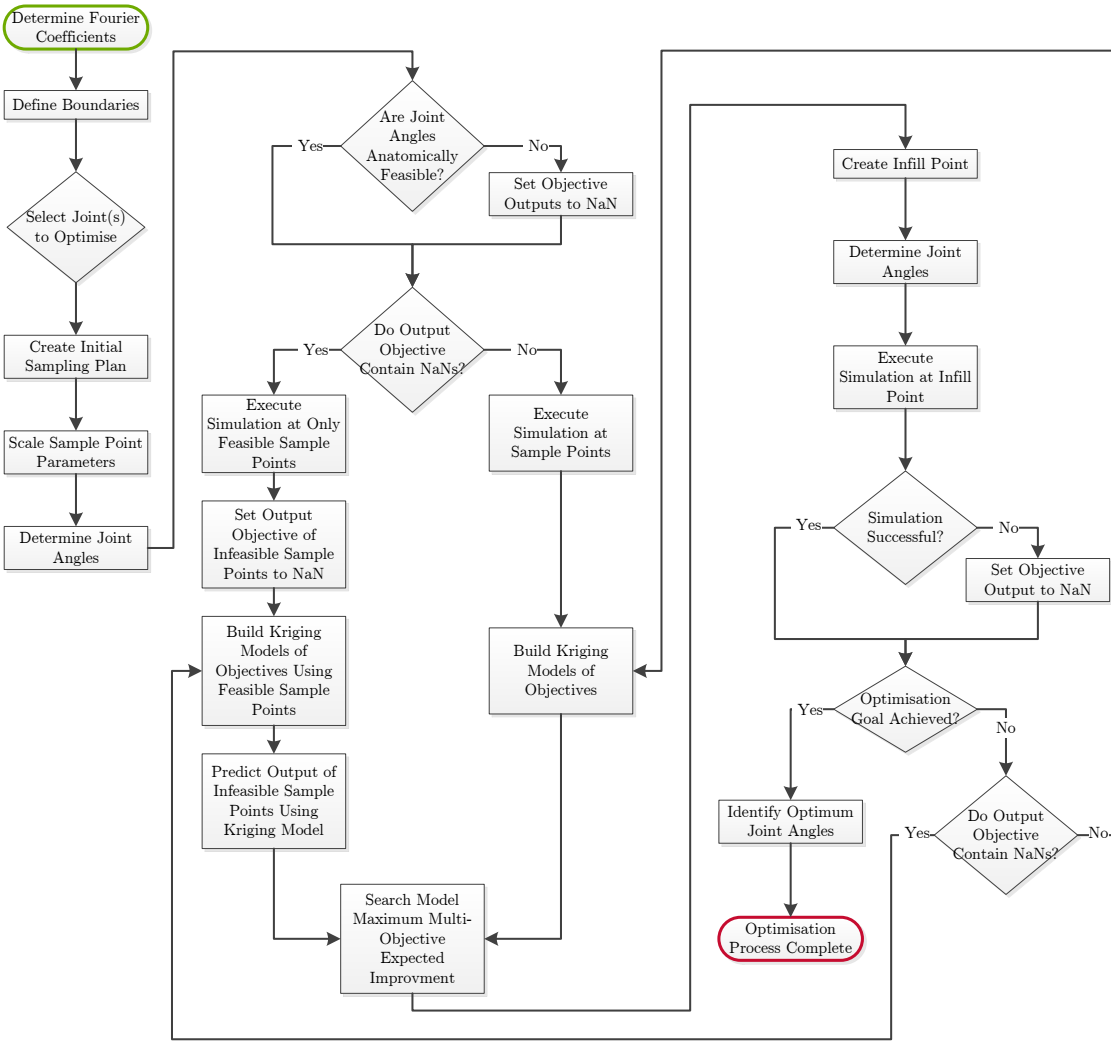

FIGURE 7.1: The optimisation process.

To demonstrate the multi-objective optimisation of the UUS kinematics, three joint angles were optimised. Following the identified importance of the hip articulation in

TABLE 7.1: The R-squared fit of the Fourier series to the original joint angle data.

	Ankle	Knee	Hip	Pitch	Pelvis-Thorax	Shoulder	Wrist
R-Squared Fit	0.5602	0.8662	0.7762	0.6772	0.7103	0.8329	0.6450

Chapter 5 the three joints selected were the hip, pelvis-thorax and the pelvic rotation in the saggital plane (pelvic-pitch).

The kinematics from T_1 in Chapter 5 were also used here as the baseline and for the joints which were not optimised. A Fourier series is the summation of terms of sine and cosine functions to create a continuous periodic function [James 2001]. The original joint kinematics are periodic and are assumed to be smooth continuous functions. Therefore, a Fourier decomposition of each joint angle was performed and yielded the constituent Fourier coefficients of these joint angles. By using a Fourier sequence to described the kinematics, the temporal joint angle profile can then be manipulated by modifying these coefficients [e.g. Phillips *et al.* 2010; Purdue *et al.* 2010]. The first two pairs of coefficients for both the sine and cosine, as well as the mean joint angle, were then selected for the optimisation process —thus generating $k = 15$ $(3\times(2+2+1))$ variables for optimisation. The goodness-of-fit for each joint using two pairs of Fourier coefficients is displayed in Table 7.1. It shows that the knee and shoulder joints are best represented by this series, but ankle least so. Possible reason for these errors is that the Fourier fit generates a smooth continuous dataset, where each kick cycle would be an exact replica. However, because the original joint angle data are generated from data of an athlete performing ten repeated kick cycles, it is reasonable to assume there will be some inter-kick variation.

In order to limit the scope of the optimisation process, bounds were placed on the k variables. The mean coefficients were bound to within $\pm 10^\circ$ of the baseline mean joint angle. The mean, maximum and minimum sine and cosine terms of the ten baseline kick-cycles were then found. The upper and lower bounds for these terms were the mean ± 1.25 of the difference of the maximum/minimum from the mean. These bounds enabled a wide kinematic space to be searched while equally attempting to limit its scope to a design space which could be searched in the time frame permitted.

While these efforts attempt to limit the design space to be searched, there remains a potentially infinite number of permutations of the design design variables within the

constrained bounds[1]. To perform a full, direct search of this space would be intractable. To overcome this, a Kriging model is employed to emulate the transfer function of the input parameters to the output; thus a surrogate for the actual simulation. This surrogate may then be interrogated to identify an optimal solution. The Kriging model is generated by relating a series of known input parameters and their subsequent output values. Thus more sample points better replicate the function under observation.

The optimisation theory and process for the following content has been adapted from the book *Engineering Design via Surrogate Modelling* [Forrester *et al.* 2008]. The methods of which have been demonstrated in Forrester and Keane [2009], for example. While efforts have been undertaken to utilise the theory effectively, it is primarily used as a tool to perform the optimisation. The process of optimisation is illustrated in the flowchart in Figure 7.1 and elaborated upon below.

Having selected the variables to be optimised, a k-dimensional normalised Latin hypercube is generated. Its content is refined to optimally fill the design space with n sample points, which in this study $n = 75$. These sample points therefore produced an $n \times k$ array of normalised values for the initial sampling plan. The normalised parameters were then scaled according to the imposed bounds and hence generated an $n \times k$ array of Fourier coefficients to describe the selected joint angles[2].

As per the detailed description in Chapter 4, the computational UUS simulation was executed for each of these n sample points. Since this was also a contrived dataset based upon a genuine dataset where the original velocity had been measured, the thrust and hence velocity generated by the kinetics was estimated in the same manner as described in Chapter 5.

The resultant mean thrust and mean maximum muscle activity was recorded for each sample point. These were chosen as the metrics for the target function, or the objective, of the model. Hence the goal of the optimisation was to optimise the Fourier coefficients to maximise mean thrust and minimise mean maximum muscle activity.

[1] Theoretically each variable may take an infinite number of values between the bounds. In reality, however, as the step size tends towards zero and the number of potential discrete points tends to infinite, the effect of moving from one discrete point to the next will become increasingly more negligible.

[2] If optimising other joints, the script would at this stage check to ensure that the resultant kinematics are anatomically capable of being reproduced —e.g. the knee joint does not exhibit hyper-extension. If they are not anatomically realisable, the corresponding output values are set to *NaN* (not a number) and the simulation is not executed for these input parameters

The mean thrust and mean maximum muscle activity were chosen because maximising thrust will increase the velocity of the swimmer while minimising maximum muscle activity will minimise the energy required —thus increasing performance (recall Equation 4.21). One is reminded that the musculoskeletal model also has an in-built optimisation loop which too seeks to minimise the maximum muscle activity. It seeks to minimise this across all of the muscles in each time-step when deducing the required forces in the muscles —which in itself could be considered a surrogate for energy expenditure. The coefficient of determination between the maximum muscle activity and the work out (derived from Equation 4.22) in the results of Chapter 5 was 0.9975. It is therefore considered appropriate that this metric should be used for fulfilling the aims of this study.

Any sample point at which the simulation failed to compute an output are referred to as imputed points. The output values at these imputed points were then set to *NaN* (not a number). Using the successful input parameters and the corresponding output values, two Kriging models of the two objective metrics were produced. These Kriging models were then employed to re-estimate the output values of the imputed points. These imputed data are then re-introduced to the array of input and output variables.

The model then uses the Kriging models of the two objective functions to search the design space for the maximum multi-objective expected improvement in the output [Forrester *et al.* 2008]. Once found, it establishes the normalised input variables at this location in the design space. This point is then referred to as the first infill point.

The derived normalised input variables were then re-scaled to generate the Fourier coefficients. Using these data, a new set of joint angles were obtained and the UUS simulation re-run and the two output objectives recorded. Subsequently, any sample or infill point that failed to produce an output, the corresponding output values were set to NaN.

This process was then repeated for a further $I = 150$ infill points.

7.4 Results and Discussion

The optimum joint angles were found for each objective. These were determined as the coefficients that maximised the thrust and minimised the mean maximum muscle

activity for the thrust and muscle activity objectives, respectively.

The thick lines in Figure 7.2(a) are the joint angles which produced the maximum thrust from the optimisation of the hip, pelvis-thorax and pitch angles. Similarly the thick lines in 7.2(b) are the joint angles which produce the minimum mean maximum muscle activity in the study (these data were hence generated from the respective Fourier coefficients). The faint lines of corresponding colours are each of the derived joint angles generated in pursuit of the optimal solution.

The smooth and periodic nature of the optimised joint angles in contrast to the inter-cycle variation of the athlete-produced kinematics —particularly prevalent in the ankle joint data.

In observing Figure 7.2(a), the optimised solution for maximum thrust, shows the pelvic-thorax joint angle, out of phase with the pelvic-pitch. By contrast, Figure 7.2(a) shows these joints to be in phase for the solution of minimum maximum muscle activity.

The pelvic-thorax in the maximum thrust objective has two obvious frequency components with one of greater magnitude than the other, but in Figure 7.2(b) they are of equal magnitude.

Also the hip joint for the maximum thrust case, has two oscillations for each oscillation of the knee joint, but in the minimum activity case there is only one per knee oscillation.

These observation suggest that the optimum solution for maximising thrust is to increase the magnitude of and frequency of oscillations of the joint angles —in other words, kick at higher frequency and larger amplitude. The concept of minimising muscle activity, however, is clearly in tension with this philosophy.

Despite searching for the solution as to what is *the best* UUS technique, there are in reality probably many solutions and hence a trade-off. This trade-off between the two objectives —maximising thrust and minimising maximum muscle activity— are displayed in Figure 7.3(a) as a Pareto front between the two metrics. The same trend is observed between thrust and the total work done by the muscles as seen in Figure 7.3(b).

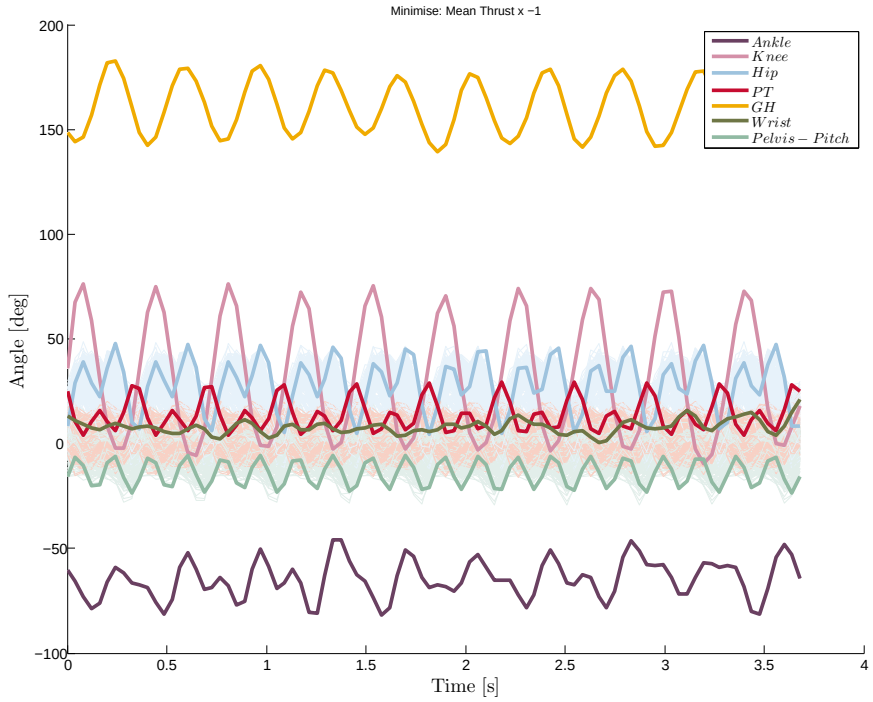

(a)Maximum Mean Thrust

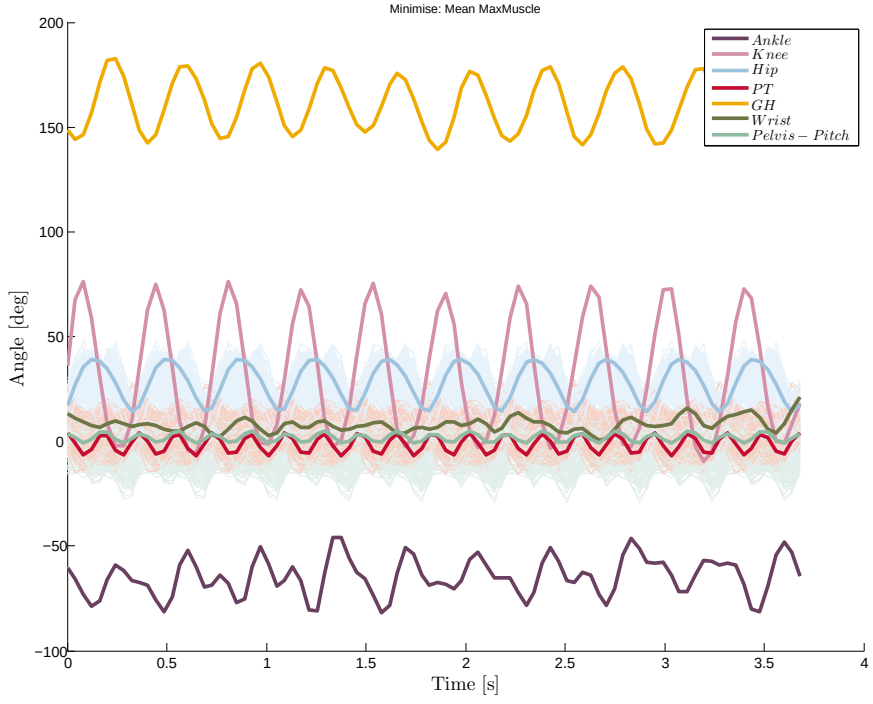

(b)Minimum Maximum Muscle Activity

FIGURE 7.2: The joint angles for all the executed runs $(n + I)$ are plotted as thin lines in the two figures. (a) also displays the optimal joint angles, plotted as thicker lines, for the maximum thrust produced. Similarly, (b) displays the optimal joint angles for the minimum maximum muscle activity.

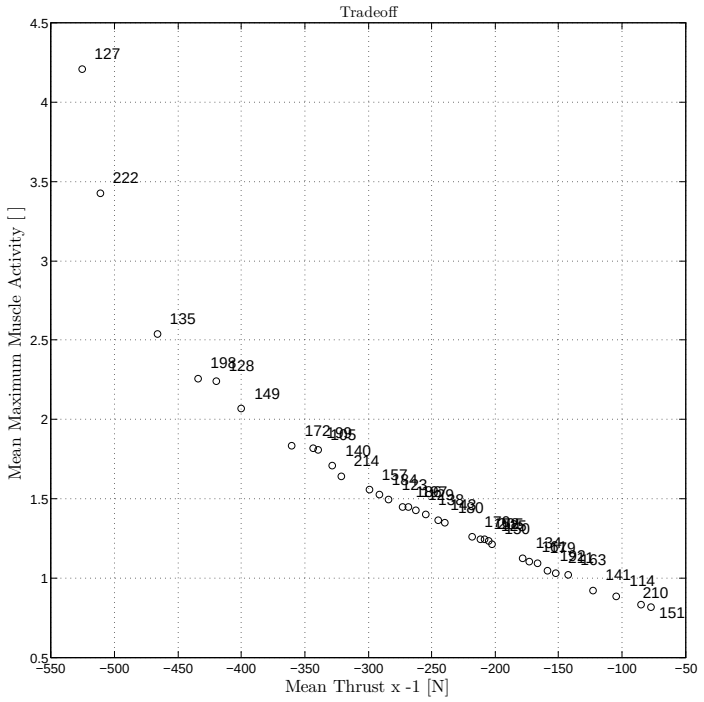

(a)Mean Thrust

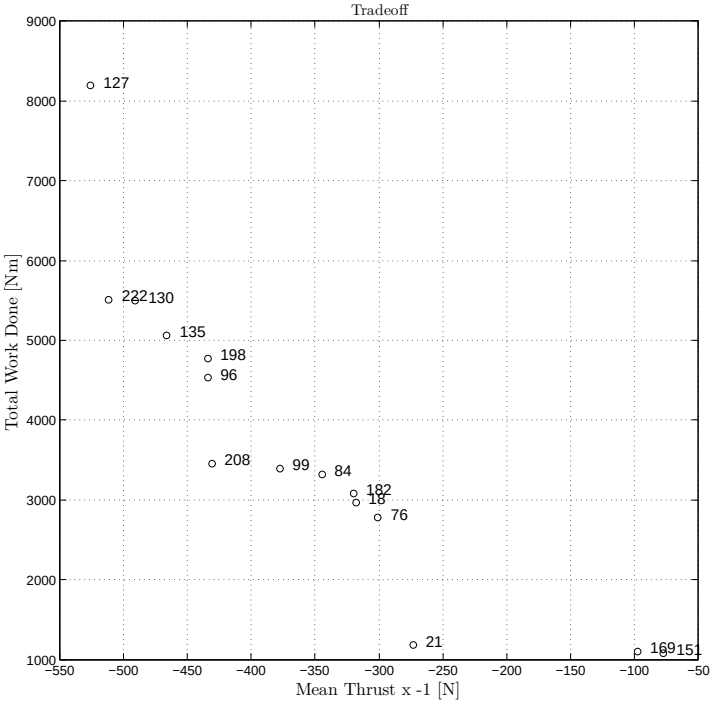

(b)Mean Thrust

FIGURE 7.3: The Pareto front trade-off between (a) the maximum muscle activity and thrust, and between (b) the total work done by the muscles and thrust. (The numbers indicate the sample point)

Figure 7.4 shows the baseline kinematics overlaid with the optimum joint angles that are at either end of the Pareto from and a third which is in the middle. These correspond to the kinematics for producing maximum thrust, minimum muscle activity and a compromise between the two. These plots also show how these optimised kinematics differ from the baseline. The optimised solutions for both objectives suggest the pelvis-thorax and pelvis-pitch would benefit from an increase in frequency from the baseline. In the hip, however, this would only be beneficial in maximising thrust.

For the hip the figure suggests it would be beneficial from an increased mean amplitude for all solutions, however, this is again in tension in the pelvis-thorax and pelvis-pitch angles. The mean joint angle of the original pelvis-thorax is approximately the same mean amplitude as the intermediate solution, where as in the pelvis-pitch it is between the intermediate and maximum thrust solutions.

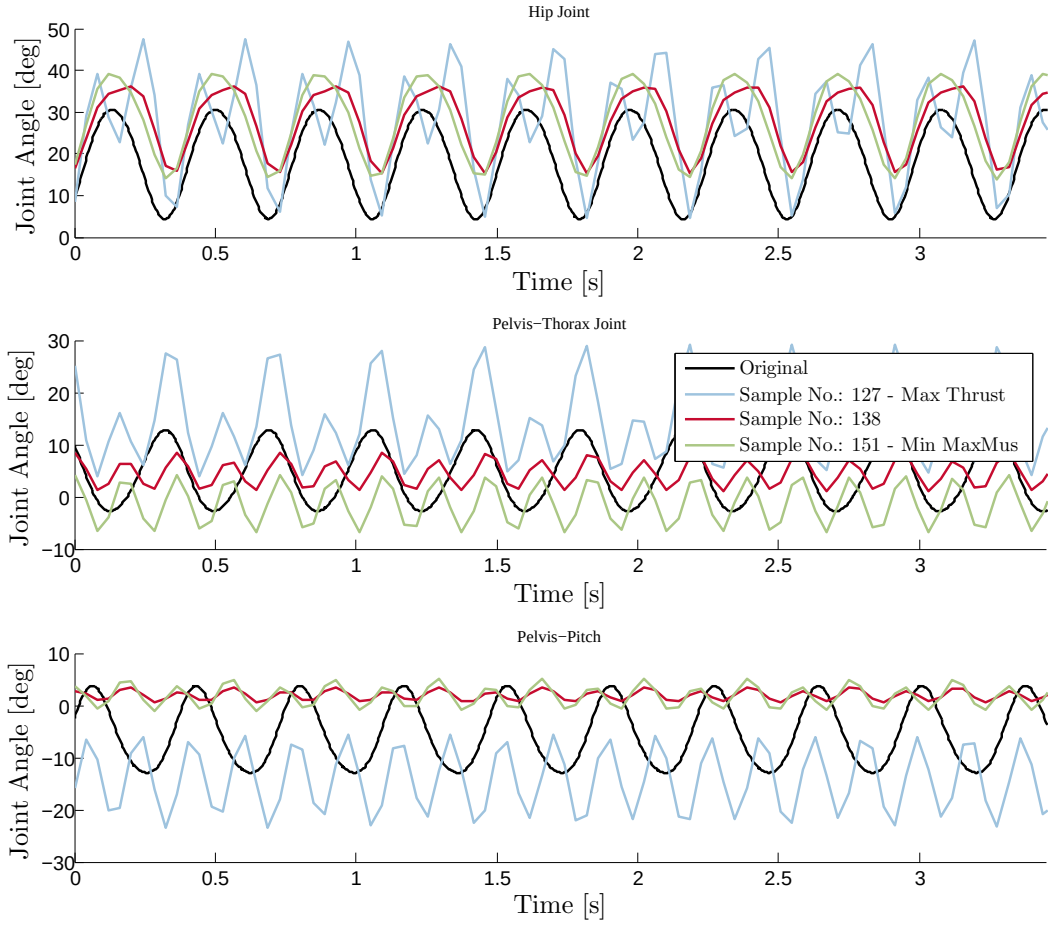

FIGURE 7.4: A comparison of the optimised joint angles; hip (a), pelvis-thorax (b) and pelvis-pith (c). The black lines in each are the original joint angle data, the blue joint angles which produce the maximum thrust, the green those which produce minimum maximum muscle activity and the red the run which lies in-between the two extremes of the Pareto front.

While these kinematics are optimised for the respective objective, they are different to the baseline. This is particularly apparent with regards the frequency of oscillation in maximising thrust. Replicating these kinematics exactly, therefore, may be excessively challenging or unrealisable. However, specific observations may be attainable and suitable for further investigation.

The sub-figures of Figure 7.5 depict the inter-Fourier coefficient interactions with two objective functions; maximising mean thrust 7.5(a) and minimising the mean maximum muscle activity 7.5(b). The displayed coefficients were the mean joint angle of the hip, pelvis-thorax and pelvis pitch which are indices $1, 6$ and 11, and columns 1, 4, and 7 of the tile plots, respectively. The other selected coefficients were the principal sine and cosine coefficients for the same joint angles. These indices are 2,4 for the hip (columns 2 and 3), 7,9 for the pelvis-thorax (columns 5 and 6) and 12,14 for the pelvic-pitch (column 8).

The horizontal axes of each plot are the normalised bounds of the coefficient of the specific row and the vertical axes the normalised bounds of coefficient to which it is compared. The colour scale is the value of the objective at that intersection.

For both figures, the desired optimum solution in each tile, is toward the red region. Where the colour bands are horizontally or vertically aligned, it implies there are no interactions between these coefficients and the objective. An observation from the second column (first sine term of the hip joint angle) of Figure 7.5(a) for example, is that the optimum solution for this coefficient for this objective would be towards zero as the highest thrust values are whent this parameter is towards zero in the second, seventh and eighth rows, and is not significantly influential in the remaining interactions.

However, this is not the case in many other columns, for example column 6, there is a conflict for the optimum value of this parameter. Equally, the colour gradient in each tile of Figure 7.5(a) and the respective tile in Figure 7.5(b) are typically reversed. These antagonisms are therefore both indicative of the complexity of the problem and representative of the trade-off between the two objectives.

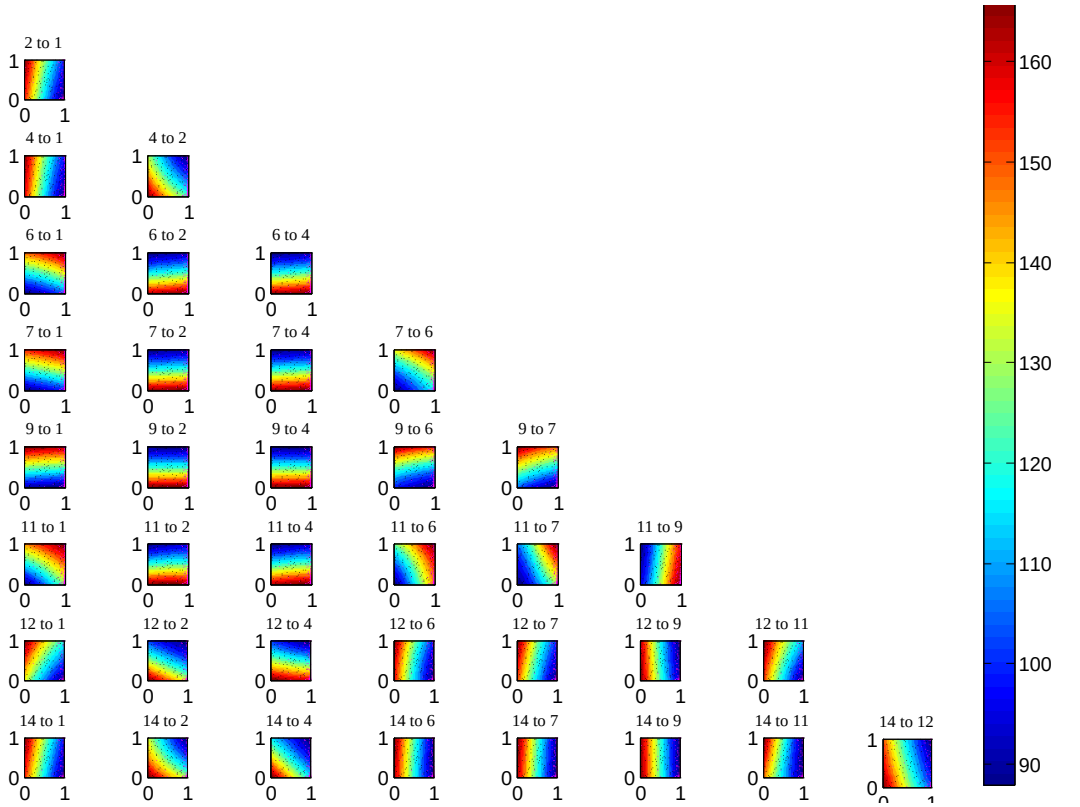

(a)Mean Thrust

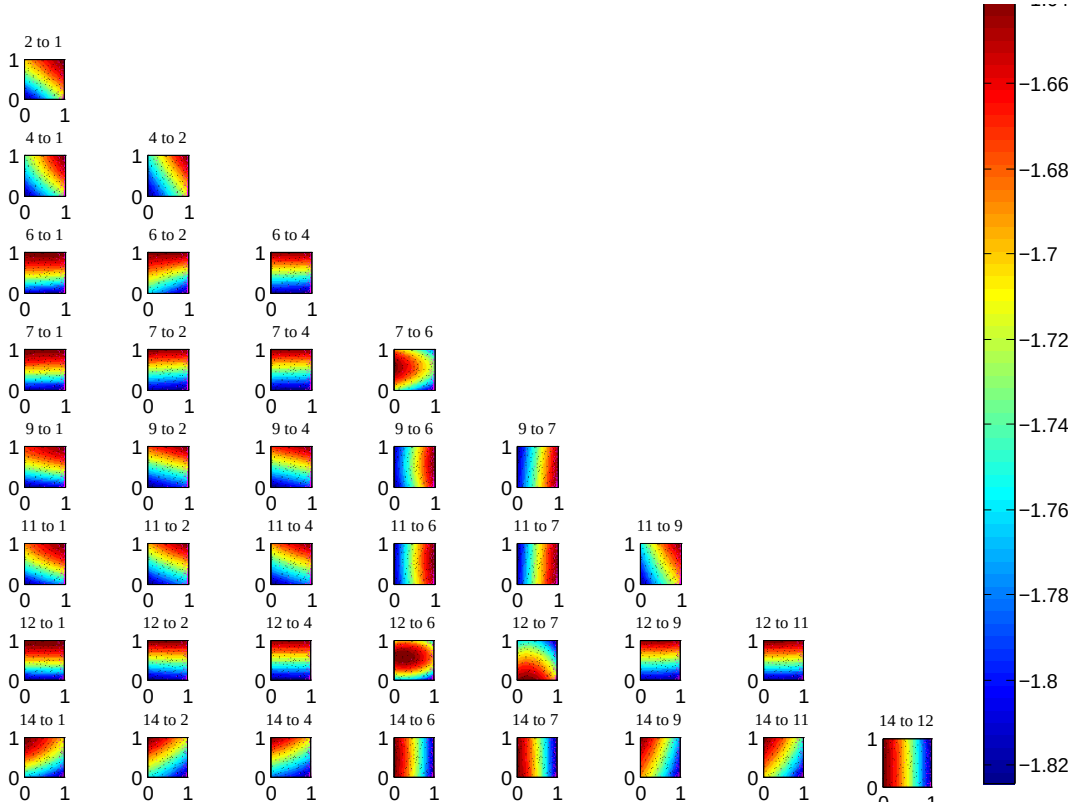

(b)Mean Maximum Muscle Activity

FIGURE 7.5: Tiled contour plots of the input parameters and the resultant output of the objective function, where (a) is the thrust output and (b) the maximum muscle activity output. The horizontal axis of each plot is corresponds to the first number of the individual title and the vertical axis the second number in the title. These numbers correspond to the index of the plotted coefficient. The first column of each plot is interaction of the mean joint angle of the hip with the other coefficients and the objective function. The second and third are the similarly the interactions of the principle sine and cosine terms of the hip joint angle, respectively.

7.5 Conclusions

This chapter has demonstrated how the developed model can be employed to theoretically optimise joint kinematics for a specified single- or multi-objective scenario. In this demonstration the hip, pelvis-thorax and pelvis-pitch were optimised with the objectives to maximise thrust and minimise maximum muscle activity. A trade-off between the two objectives was subsequently discovered. The joint kinematics at either spectrum of this trade-off and a compromise between the two, were each observed to be different from the original baseline kinematics. It was shown, as would logically be expected, that increasing the frequency of the kick increased the thrust produced but simultaneously increased the energetic cost. It is acknowledged that not all aspects of the optimised kinematics may be realisable. However, solutions at both ends of the trade-off exhibit a doubling of oscillation frequency of the pelvis-thorax and pelvis-pitch as compared to the baseline and a single oscillation of the knee joint and therefore provides scope for further pool-based investigations.

The following chapter investigates how the acquisition of the joint kinematics could be improved. This is an aspect that would benefit further investigation of the findings from this chapter, as it could more easily and more accurately determine how closely replicated the implemented kinematics by an athlete might be to the theoretical optimum.

Chapter 8

Alternative Methods of Kinematic Acquisition

The previous chapters of this thesis have described the development of a musculoskeletal model to simulate human underwater undulatory swimming (UUS). It has also been shown that in order to analyse a particular technique it is necessary to provide the model with the kinematics of the technique. In the previous studies, the kinematic data has been calculated by manually digitising video frames of an athlete performing the technique under observation. This is a significant stage in the process as a whole, as it is these data which are used to calculate both the thrust and the muscle activities —the effects on which have been examined in Chapter 6.

This chapter investigates alternative and potentially semi-automated methods to acquire UUS joint kinematics by using image processing and inertial measurement units (IMUs). This would improve upon the current operator time and be a method of acquiring more accurate and three-dimensional UUS kinematics. The deduced muscle activities of manually digitised and IMUs driven joint kinematics are also compared.

8.1 Introduction

The determination of the technique's kinematics are a significant aspect of the musculoskeletal modelling process. Image processing techniques and data derived from IMUs have discussed in Chapter 2 as providing accurate joint kinematic data. Using IMUs

also has the benefit that the actual motion of the segment is directly measured at the time rather than through a post-processed method, such as with manual digitisation, where the segment motion is inferred from the video.

IMUs also offer potential for reducing the post-processing times required for determining the joint kinematics[1].

An additional limitation of the digitised method employed in the previous studies is the restriction of confining the kinematics to two-dimensional motion. While observing elite athletes it would be typical to see motion out of the saggital plane. Two video frames of an athlete performing UUS simultaneously viewed from above and to the side, are displayed in Figure 8.1. It is evident from comparing these two instances that there are additional rotations exhibited, but not captured using the current manual digitisation approach. However, from purely observing these frames it is inconclusive whether these postures are attained from, for example, rotation and abduction of the hip joint, rolling at the ankle-plantar joint, or a combination thereof.

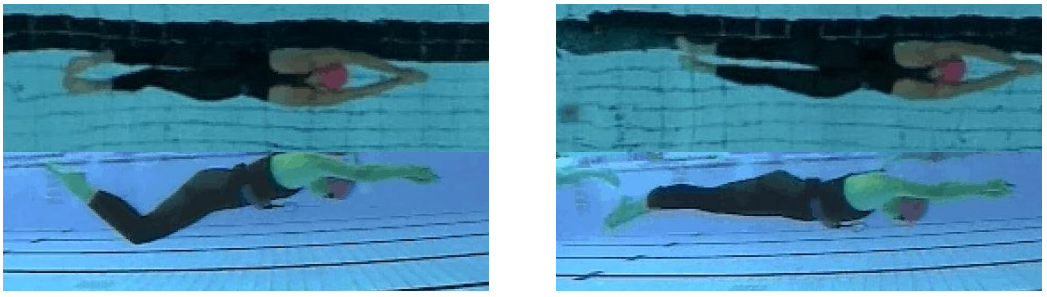

(a) (b)

FIGURE 8.1: Sequence of two frames of a UUS technique, observed from directly over the athlete and to the side.

[1] For example; a 5 s extract of video recorded at 25 Hz will contain 125 frames necessary to digitise and may contain ten kick cycles. If it were to take an operator 10 s to accurately digitise each frame, this would approximately take 20 min of the operator's time. While calculating the joint angels from the digitised data would take $\sim$ 2 s and a further $\sim$ 3 s to export. Calculating and exporting the thrust and side-forces using an implementation of Equation 4.10 would consume $\sim$ 3 s of computational time. Executing the musculoskeletal model and calculating the muscle forces for the ten kick cycles would take $\sim$ 180 s of computational time. Saving the simulation data, musculoskeletal animation, processing the results and saving the findings to a database, a further $\sim$ 90 s. The digitisation process would therefore consume approximately 82% of the total time for analysis.

8.1.1 Kinematic Acquisition using Image Processing

Computer vision and image processing techniques have been used substantially in recognition and tracking of human motion capture Moeslund [2001]. Similar techniques have also been employed in aquatic environments. For example, Karlekar and Fang [2010] used computer vision techniques to monitor a populated swimming pool for identification of persons at risk of drowning, while Eng *et al.* [2008] used these techniques to segment swimming outlines for automated stroke quantification.

8.1.1.1 Method

A threshold-based approach has been investigated to obtain the silhouette of a swimmer performing UUS. This comprised of taking an RGB format colour frame and searching within each plane for pixels within a defined threshold. The pixel thresholds were defined as pixels values greater than 90, 125 and 190 for the respective RGB image planes. Pixels found to be within this range were given a value of *logic 1*. Similarly, those outside the threshold range were set to *logic 0*. Holes were defined as a pixel, or a defined maximum number of a collection of adjacent pixels of the same logical state, surrounded by the opposing state. In this trial, the hole size was defined 500 pixels. A bounding-box was then fitted around the silhouette and the corresponding centre determined.

8.1.1.2 Results and Discussion

Selected frames of a trial of one UUS kick-cycle can be viewed in Figure 8.2. The frames on the left show the initial recorded video and on the right the image processing results. A green box identifies the bound area of the *logic 1* pixels and its centre of area displayed as the magenta cross.

Further research would need to be performed to subsequently use this silhouette as a means of explicitly defining the joint kinematics. However, the initial observations show that it is feasible to identify the swimmer's outline using a threshold technique. The processing time for this method was approximately one second per kick-cycle; a significant improvement upon the manual digitisation process.

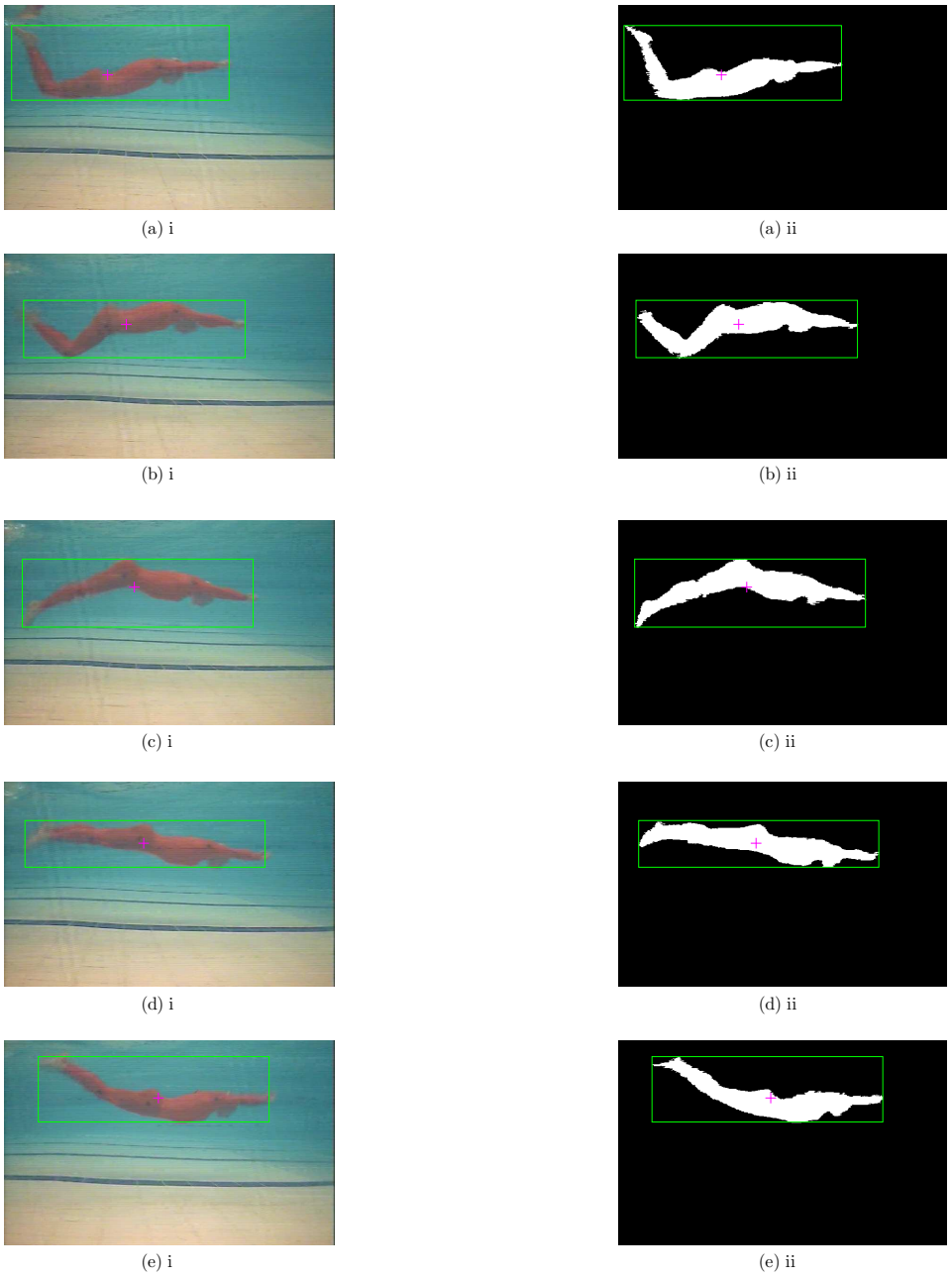

(a) i (a) ii

(b) i (b) ii

(c) i (c) ii

(d) i (d) ii

(e) i (e) ii

FIGURE 8.2: This sequence of images shows a sequence of images from one kick cycle, detailing the silhouette of a swimmer using image processing techniques.

This trial is helped by the athlete wearing a full length orange suit as it contrasts with its surroundings; facilitating thresholding techniques. In image Figure 8.2 (b)ii however, it is apparent that the algorithm has failed to identify the athlete's foot. This is the down-kick of the cycle and hence the point at which the foot is moving fastest and hence appears as a blur in the frame. The video was recoded at 25 interlaced images per second and later expanded to 50 deinterlaced frames per second. While a human may easily interpret the image to infer where the foot is, this is a more challenging issue to perform

computationally. It is therefore suggested that if this approach is to be investigated further a suitably high frame rate is required to mitigate blurring of the captured image.

8.1.2 Kinematic Acquisition using IMUs

Section 2.3.3 discusses how IMUs have been employed in acquiring three-dimensional human kinematics; for example, Dadashi *et al.* [2012]; Le Sage *et al.* [2011] used IMUs to investigate stroke metrics and achieved velocity. Having searched available sources, however, there appears to be a very limited number of people researching musculoskeletal modelling in UUS and furthermore, none that appear to have used IMUs for obtaining kinematics of human UUS.

Favre *et al.* [2009] for example, used IMUs in acquiring the kinematics of the knee joint in a gait cycle. What is prosed here is to the use similar concepts, but to use IMUs to capture the kinematics of UUS. Using sensor fusion algorithms, it is possible to determine the global orientation of each of the motes [e.g. Madgwick *et al.* 2011; Sabatini 2006]. Therefore, by attaching a mote to each of the segments of interest it is then possible to obtain the relative angles between them.

This section investigates the feasibility of using IMUs for kinematic acquisition. The derived kinematics are used to drive a musculoskeletal simulation and results compared with those obtained from the manual digitisation process.

8.1.2.1 Method

Particularly when working with elite athletes, it is prudent to be as minimally invasive as possible when acquiring data. With this consideration, the IMUs used in this study are 9 degree of freedom (DOF) Shimmer^{TM} units, which are compact relative to comparable products ($53\,\text{mm} \times 32\,\text{mm} \times 19\,\text{mm}$). Each *mote* contains a tri-axis accelerometer ($\pm 6\,\text{m}\,\text{s}^{-2}$), rate gyroscope ($\pm 500\,^{\circ}/\text{s}$) and magnetometer ($\pm 4.5\,\text{Ga}$).

The capability of the Shimmer sensors for deriving angular rotations has been demonstrated in [Denchfield *et al.* 2012]. Good agreement was also shown in comparisons of the derived angles from the Shimmer motes and data from a Vicon MX T-Series optical motion capture system [Vicon 2013]; as shown in Figure 8.3.

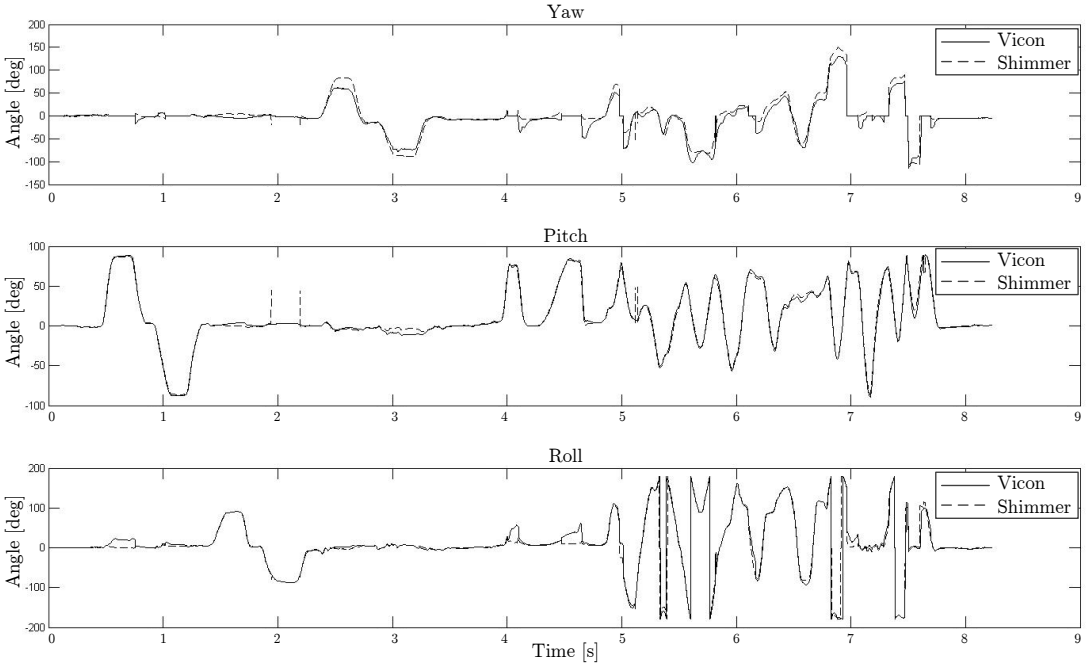

FIGURE 8.3: Euler angles derived from the Shimmer motes and the Vicon MX T-Series [Vicon 2013].

Each mote also contains an on-board processor, a 450 mAh rechargeable Li-ion battery, microSD storage (max 2 Gb) and Bluetooth communications device. The sensing devices are housed in a non-waterproof casing. Therefore, to prevent against water ingress, they were placed inside two separately sealed plastic bags.

The same participant in Chapter 6 wearing the full-body custom-made Speedo® suit, was used in this trial. This suit also had specifically designed pockets in which to accommodate the individual motes. In order to capture the same kinematic motion of the manual digitisation proces, the motes were placed on the shank, thigh, posterior pelvis and sternum, as indicated in Figure 8.4.

The experimental data was acquired as described in Chapter 3. In addition, the mote data was triggered to log to disk prior to each run. The mote data was also synchronised to the image data by aligning the absolute time of the first video frame, with the absolute time of the first date sample. Prior to the run, the participant was requested stand in the anatomical position for ten seconds and then lay horizontally with the head in the direction of travel and body axis parallel to this direction. This procedure was used as a calibration posture from which the sensor orientations are set to zero.

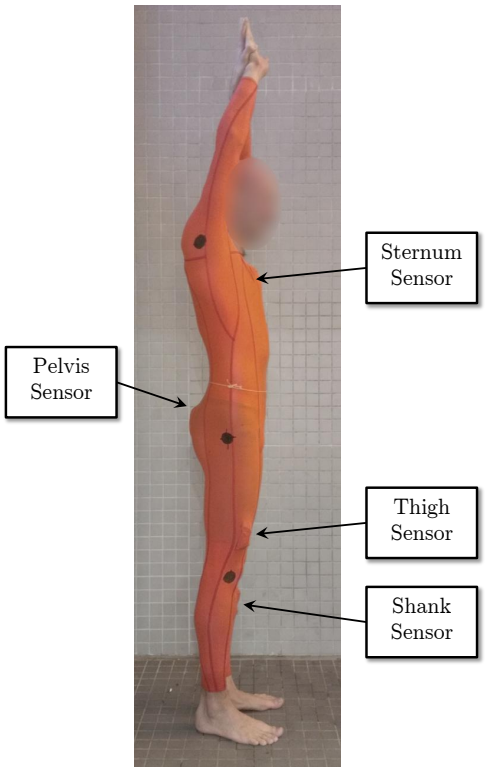

FIGURE 8.4: The participant wearing the custom-made sensor suit. The IMUs were located as labelled; on the shank, thigh, pelvis and sternum.

Following the run, the data was wirelessly downloaded from the motes and the data processed to determine the relative joint angles in quaternion format. Quaternion angles were used as they do not suffer from gimbal lock, unlike Euler angles.

An additional skeletal model was created in the AnyBody Modelling System (AMS). Similar to the model in the previous chapters, this model comprised of trunk and lower limbs. A dummy segment was rigidly attached to each of the shank and thigh segments as well as the pelvis and sternum segments —each representing the location of the motes. These dummy segments were each driven by time-varying quaternion angles relative to the global origin. This is the first observation of an AnyBody musculoskeletal model being directly driven using quaternion data from IMUs.

The kinematics analysis of the AMS was then executed using sensor-derived data. Equivalent Euler angles were derived for the knee, hip, pelvis-thorax and pelvic-pitch joint angles and then exported to respective files.

The manual digitisation process of the acquired video frames for five kick-cycles was

performed. The fluid-force and musculoskeletal models were subsequently run for the manually digitised dataset. Following this, the knee, hip, pelvis-thorax and pelvic pitch angles from the manual digitisation process were replaced by joint angles (originally determined from the IMUs) exported by the new AnyBody model.

8.1.2.2 Results and Discussion

A comparison between the joint data derived from manually digitising the video data and the processed data from the IMUs, is shown in Figure 8.5. The knee angle appears to be a close match between the two acquisition methods, the result of which is borne out in the data presented in Table 8.1, with a high coefficient of determination (R^2) for this joint. Visually, the hip and pelvis-thorax joint also appear comparable. Despite this, however, the R^2 values for these joints are less than that of the pelvis-thorax which visually does not appear to be as closely matching. The coefficient of determination is a metric of how close the trends are between the two series and as such the pelvis-thorax, although clearly showing a different amplitude, better represents the trends. While the hip and pelvis-pitch have similar amplitudes between the two methods, the phasing is not.

TABLE 8.1: The R-squared correlation between the joint angles produced by the manual digitisation process and the sensor driven model.

	Knee	Hip	Pelvis-Thorax	Pelic-Pitch
R^2	0.9387	0.4271	0.7465	0.4286

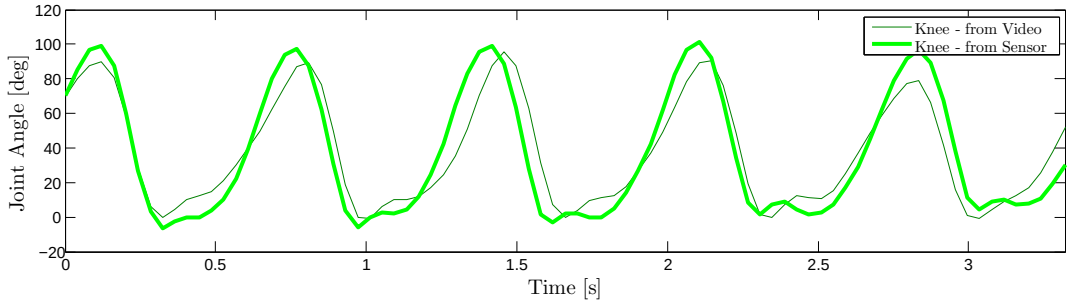

(a) Knee Joint

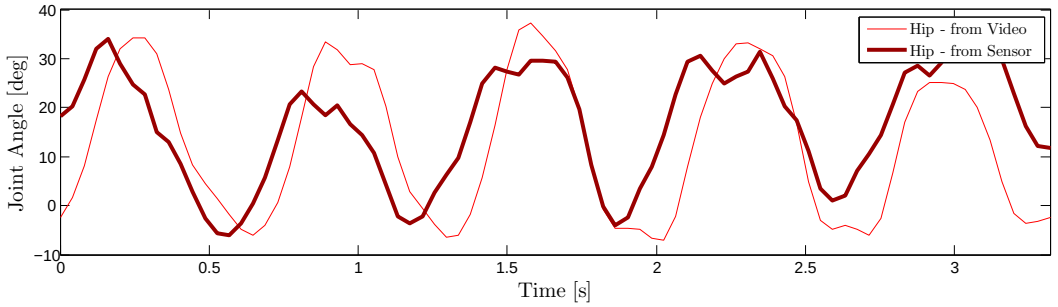

(b) Hip Joint

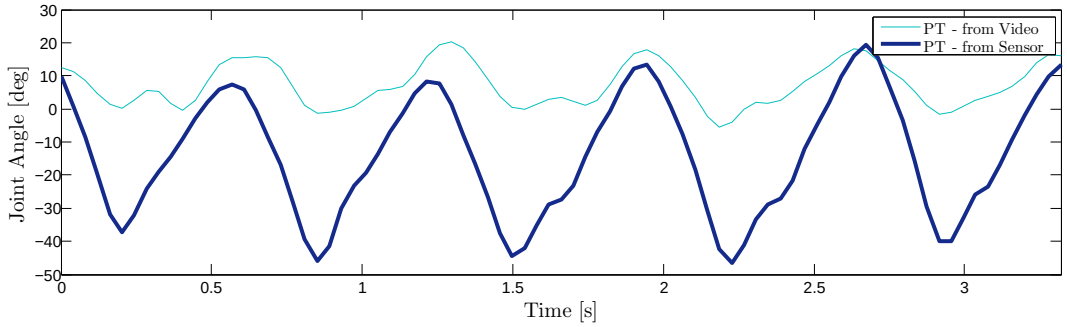

(c) Pelvis-Thorax Joint

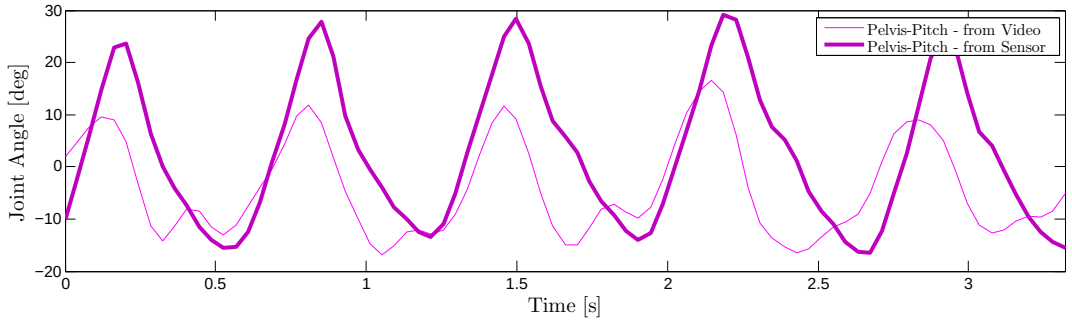

(d) Pelvic Pitch

FIGURE 8.5: Joint angles from different methods.

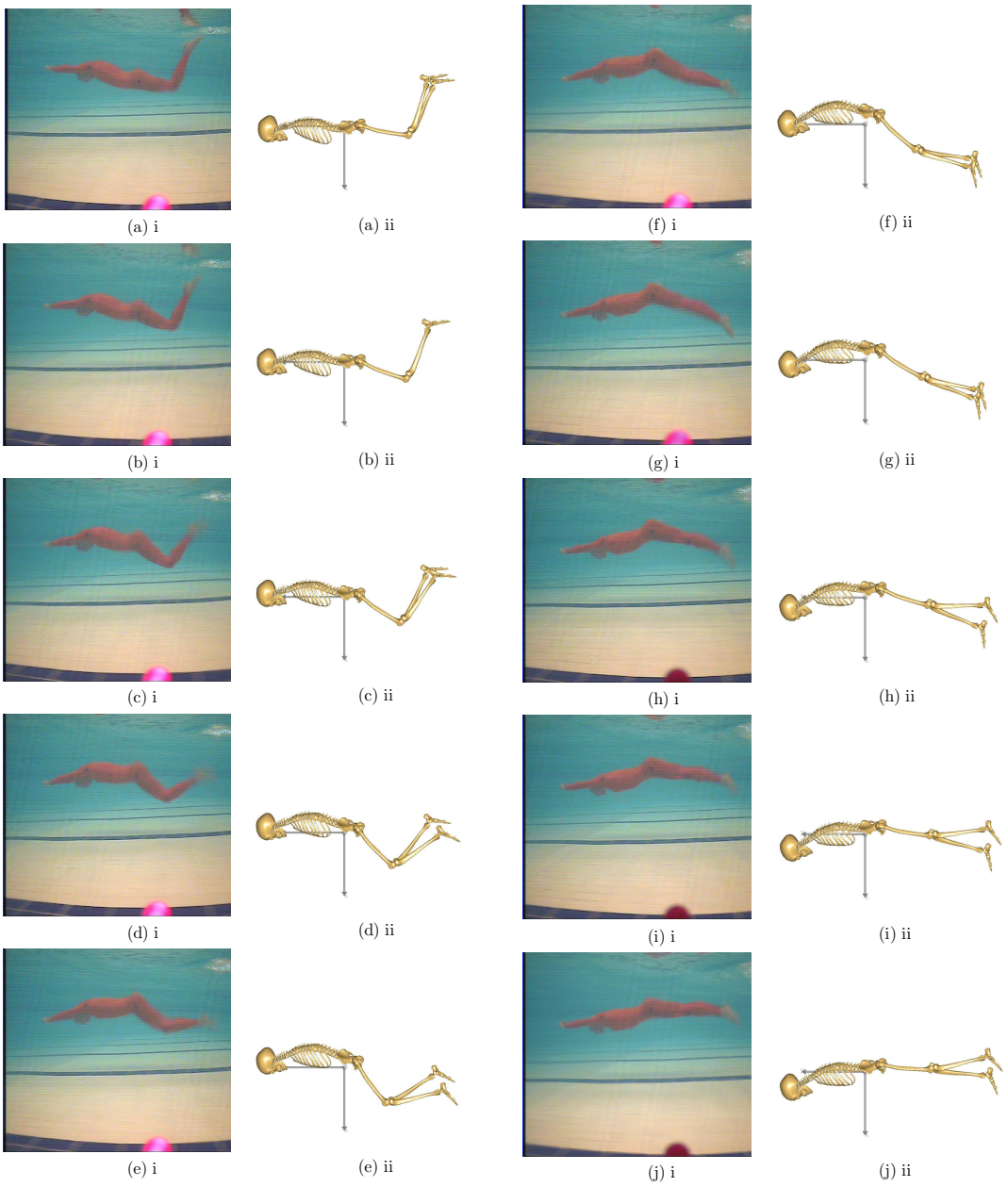

FIGURE 8.6: Sequence of images from the video and the animation of the sensor driven model —Part 1.

Frames *a* through *r* of Figures 8.6 and 8.7 depict both frames from the original video of the participant performing UUS and the equivalent frame from the animation of the mote-driven musculoskeletal model. Acquired at 25 Hz and deinterlaced to 50 Hz, these 18 frames depict one kick-cycle of the UUS technique. From a visual comparison of the two frames, the IMUs appear to capture real kinematics well. The most apparent discrepancy, however, would be the in the pelvis-thorax which appears to be overestimated (fame (n), for example), similar to the observations made from inspection of Figure 8.5.

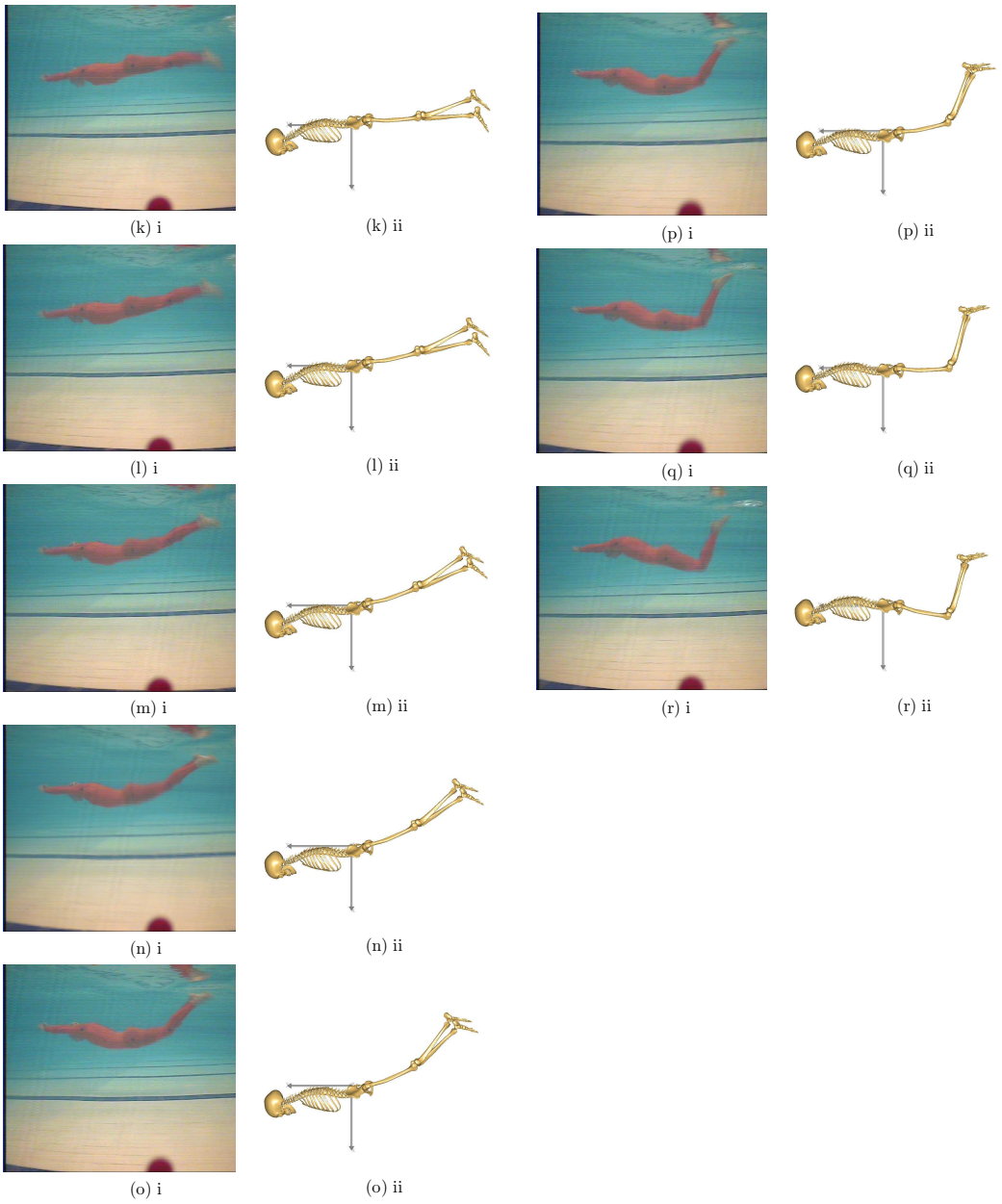

FIGURE 8.7: Sequence of images from the video and the animation of the sensor driven model —Part 2.

Upon further inspection of the frames in Figures 8.6 & 8.7 it is apparent that there is some discrepancy between the knee flexion of the left and right knee. This variation highlights a key challenge of capturing the kinematics using IMUs. If the position or rotation of any of the sensors is disturbed following the calibration stance, then errors in the determined kinematics will be observed. In this example, this error is manifested in a phase shifting of the left and right knee flexion.

While examples of laboratory based verifications of IMUs may be found in the literature, this is the first example of underwater swimming being captured using such methods. In contrast to the laboratory, here there are additional challenges of the interaction of the fluid forces on the sensor. As a first example, when the sensors remain in place, the results are encouraging and offer advantages over the previous methods. Further development in ensuring the sensor remains in place following the calibration pose would be encouraged.

Although it has not been investigated, it may be useful to combine the image processing technique to obtain the outline of the swimmer, with the IMUs method. By obtaining the silhouette of both the original video and the animation, a correlation between the two could help to verify captured kinematics.

The maximum muscle activity for each simulation —the manually digitised and the IMUs simulations— are displayed in Figure 8.8. By inspection, it is clear that the two methods of kinematic input has produced similar results in muscle activity. The mean and standard deviation of the maximum muscle activity for digitised-generated and IMUs generated trials wass 0.543 ± 0.2321 and 0.575 ± 0.252, respectively.

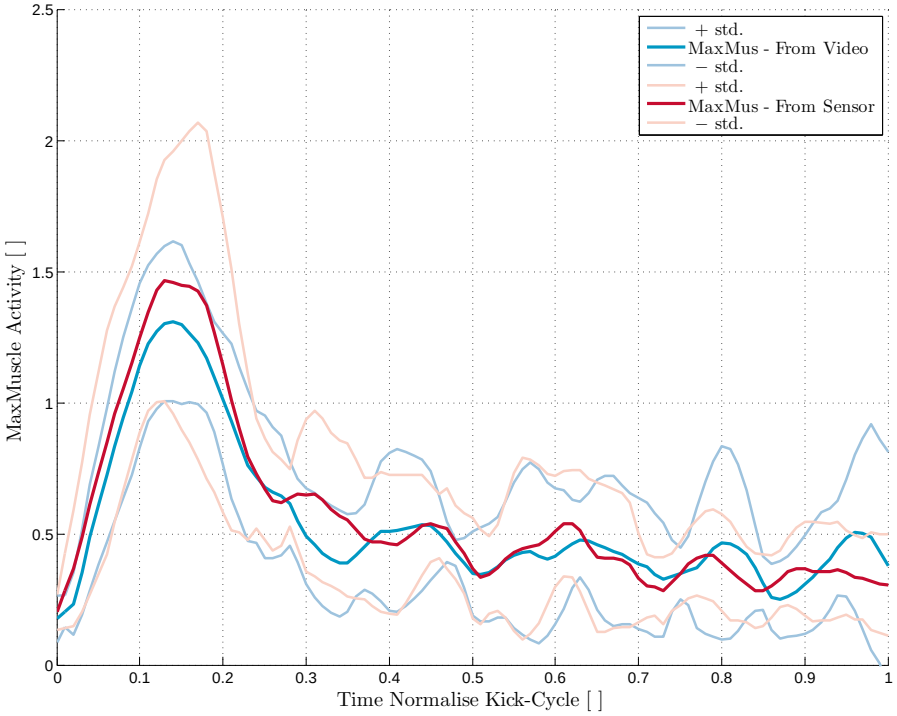

FIGURE 8.8: The mean calculated maximum muscle activity of five cycles for the kinematic datasets obtained from manual digitisation (blue line) and IMUs (red line). The faint thin lines are one standard deviation above and below the mean for the respective dataset.

8.2 Conclusions

This chapter has investigated the potential for alternative methods in the capturing of joint kinematics. An example of how computer vision processes might be utilised has been shown with encouraging results. This first step demonstrates the feasibility of obtaining the silhouette of a swimmer performing UUS using colour thresholding strategies. Further research would need to be conducted to enable this process to be sufficiently capable of transforming the captured silhouette into usable joint kinematics. It is also identified that for this process to suitably capture the full outline of the athlete, firstly the athlete must be sufficiently contrasting in colour to the surroundings and the frame rate at which the video is recorded should be sufficiently high to avoid blurring of the image.

Using IMUs as a method of capturing joint kinematics in UUS has been demonstrated here for the fist time. The knee, hip and pelvis-pitch angles derived from the IMUs exhibit close agreement to the manual digitisation process and captures the participant's motion well as compared to the respective video frames. For the pelvis-thorax joint, while the trend agrees closely with the manually digitised data, the amplitude is larger. It is suggested that while neither are wrong, that the two methods actually provide measurements of different parameters.

The musculoskeletal model was executed for both input types and the observed maximum muscle activities were similar in both trend and of mean value. From this proof of concept study, it is concluded that IMUs could be used as a suitable alternative method in the determination of UUS joint kinematics. Additional research is suggested into the location and number of the IMUs required to accurately capture the full body kinematics of UUS.

Chapter 9

Summary and Conclusions

This thesis has developed a novel, fully functional musculoskeletal model with which detailed analysis of human underwater undulatory swimming (UUS) can be performed. The experimental and processing methods for two methods of acquiring the athlete's kinematics have also been developed. A model based upon fish locomotion is coupled with the musculoskeletal model to provide the fluid loadings for the simulation. Detailed analysis of two techniques of an elite athlete has demonstrated this process in a case study. Energy expended by the simulated muscles is estimated. Combined with the measured velocity and predicted thrust, the propulsive efficiency for each technique is determined.

Elite swimming is a highly competitive sport. At this professional level, the difference between a podium finish and not, can be measured in fractions of a second. While improvements in specific performance metrics may deliver a marginal improvement, it is through the accumulation of marginal gains that the winning margins are created. Quantifying performance in elite sport is therefore fundamental in identifying and implementing improvements. Within the umbrella of elite swimming, there are many disciplines and much scope for improvement in each. Similarly, there are numerous methods and techniques available to elite athletes and their coaches with which to analyse and identify potential for performance. The trade-off between energy expenditure, thrust generated and attained velocity are identified as key aspects to performance.

The underwater phase of a competitive, elite, Fédération Internationale de Natation (FINA) governed race is a significant proportion of the race distance —irrespective of

the event. Human UUS is a technique employed by athletes to propel themselves through the water in this phase of a freestyle, backstroke and butterfly race. Submerged UUS has also been demonstrated in the literature as having the capacity to be significantly faster than surface swimming and hence the extent to which it may be performed is limited by FINA.

Through personal communications with British Swimming (BS) coaches and athletes, often UUS is an aspect that is not frequently perceived to be a strength of many athletes in the Great Britain (GB) squad. When observing the previous two Olympic games, Beijing (2008) and London (2012), it is apparent that many GB athletes —and other nations'— did not make full use of the allowed underwater distance. Despite these perceptions, GB athletes remained competitive. It is likely, therefore, that improvements in UUS offer scope for overall performance gains.

From a review of previous swimming research in Chapter 2, it was identified that there was a lack of suitable methods for simultaneously quantifying the energy expenditure thrust and velocity for a particular technique. The scope of this thesis is to enable such a process and this was achieved through fulfilling the objectives set out in Chapter 1.

9.1 Experimental Data Acquisition

Analysis of both temporal force-based and velocity measurements have been documented as a method of performance quantification and a method of investigating performance gains in swimming. Prior to the commencement of Project SwimSIM, BS did not possess the capability to undertake studies of this kind. Previous to the conception of iDAQ, there too was no other software published for use in swimming capable of synchronous image, force and velocity acquisition with immediate feedback. The iDAQ software and the bespoke hardware described in Chapter 3 was subsequently developed in part to fulfil this limitation in BS's capabilities by providing a suitable method of acquisition of experimental performance data. The software was also developed in part to facilitate the acquisition of experimental data required for this thesis and those of the other researchers of Project SwimSIM.

9.2 Development of Computational UUS Model

A computational model of human UUS has been created and is detailed in Chapter 4. This model creates the subsequent pathway by which investigations pertaining to UUS may be conducted.

Image and velocity data are captured using iDAQ as described in Chapter 3. From manually digitising the athlete's joint centres, two-dimensional joint kinematics of the UUS technique are determined. These data then provide the necessary input data for both the fluid force and musculoskeletal models.

An implementation of Lighthill's equation for deducing the thrust and side forces acting on a fish has been employed to estimate these same forces but in the context of a human. The time-varying forces are calculated in less than one second for ten UUS kick cycles. This implementation successfully captures the profile of the resultant thrust and provides comparable peak thrust to examples of other more advanced computational methods presented in the literature, hence demonstrating significant temporal advantages.

A bespoke musculoskeletal model of UUS has been developed. The model is scalable proportionately to the height and weight of the athlete. Using the established body segment properties, the hydrostatic (buoyancy) forces are calculated by the model. The model's kinematics are driven by temporally defined anatomical joint angles. Temporal hydrodynamic forces from explicitly defined input data are also imposed on the model. The model employs an inverse dynamics solver to calculate the muscle parameters at each time-step. Subsequently these data can be analysed and used to estimate the energy expended (work done) by the muscles. In determining this metric and the useful work out, the propulsive efficiency of the original technique can be determined.

This process enables the contribution of different muscle groups to be established for each trial. In addition, the extent of which individual muscles for each trial are activated beyond predefined threshold may be visualised and quantified. These tools therefore establish the means with which to analyse a UUS technique and compare and contrast other techniques performed by the same athlete or another. By not only quantifying the difference in terms of propulsive efficiency, for example, this methodology also facilitates analysis of the muscular system to ascertain the effect of the technique change and where these changes occur.

9.3 Technique Evaluation: A Case Study

Analysis of an elite athlete's two varying UUS techniques using the developed model was conducted in the form of a case study. The coach had an intuition that performing UUS in a more carangiform type motion would propel the swimmer faster through the water. From the feedback provided by iDAQ, it was shown that the measured velocity of the two techniques varied by only $0.04\,\mathrm{m\,s^{-1}}$, with the newly-implemented and previously untrialled technique only marginally slower. Furthermore, the anecdotal evidence through athlete feedback was that the newly implemented technique was perceived to be more efficient although there was a feeling that the distribution of the work had moved from their lower limbs to their torso.

In simulating ten kick-cycles of the two runs in the developed musculoskeletal model, it was verified that the two techniques were significantly different. The more carangiform-type technique showed both a significant reduction in energy and a relative shift of the muscle loadings from the legs to the torso.

It was also observed that that for the new technique, the athlete had a lower kick-rate. With no explicit instruction to do so, kick amplitude was seen to increase. The consequence of these actions was only a 0.3% variation in Strouhal number between the two runs. This phenomenon has previously been observed in flying animals which have been shown to tune their kinematics to maintain an optimum Strouhal number.

A further investigation was conducted to vary the amplitude of the joint-angle and in so doing, modify the Strouhal number. This found that for the athlete's original technique, the exhibited Strouhal number was at the optimal efficiency. It was demonstrated for the second technique, however, that by reducing the Strouhal number by approximately 10% the efficiency could increase by approximately 3%.

The findings suggested the choice of kinematic type should depend upon attained swimming velocity and race strategy. Ultimately, there was a trade-off between swimming velocity and energy expended. Strategy choice would therefore be dependent on the race event. It was concluded that for the sprint athlete in this case study, it would be preferential to use a more knee based kick, akin to thunniform, when swimming above $2.3\,\mathrm{m\,s^{-1}}$ and a more carangiform when at velocities less than this.

Rationale was also provided as to why published Strouhal numbers for human UUS are typically shown to be outside of the optimal range published for undulatory swimming; the range in which most fish and cetaceans inhabit. Strouhal number is often used a surrogate metric for performance; Strouhal number being a function of the time between shed vortices. In the analysis of this case study and from the reviewed literature, it is suggested that overestimation of Strouhal number for human UUS is due to insufficient accounting of the shedding of vortices. Whereas the kinematics of a fish produces a shed vortex at the equivalent up- and down-kick, using data from the case study and corroborative published data, it is shown that human UUS only sheds a vortex on the down-kick. Yet in published calculations of Strouhal number for human UUS this is not accounted for. It is therefore suggested that the evaluation of Strouhal number is typically overestimated by a factor of two. With this amendment, determined Strouhal number of human UUS would approach on the idealised optimum range.

9.4 Analysis of Errors in Manual Digitisation Process

The hip-node was identified as being most influential on the production of thrust, followed by the knee joint. Equally, the knee-node was shown to be most influential on the sensitivity of the maximum muscle activity, followed by the hip-node. It reaffirmed the intra-run inconsistencies in the kinematic techniques displayed in the case study of Chapter 5, implying the standard deviations stated in the results was not mostly due to errors in the process of the kinematic acquisition. It does, however, highlight that when investigating subtle changes in technique style, the errors in the processing could become influential on the outcomes. It would therefore suggest that for future studies investigating such changes, it may be necessary to perform a statistical investigation into the sensitivity of the findings to the error in the kinematic acquisition.

9.5 Joint Angle Optimisation

Chapter 7 demonstrated how the previously developed model can be employed to theoretically optimise joint kinematics for a specified multi-objective scenario. In this demonstration the hip, pelvis-thorax and pelvis-pitch were optimised with the objectives to maximise thrust and minimise maximum muscle activity. A trade-off between the two

objectives was subsequently discovered. The joint kinematics at either spectrum of this trade-off, and a compromise between the two, were each observed to be different from the original baseline kinematics. It was shown, as would logically be expected, that increasing the frequency of the kick increased the thrust produced but simultaneously increased the energetic cost. It is acknowledged that not all aspects of the optimised kinematics may be realisable. However, solutions at both ends of the trade-off exhibit a doubling of oscillation frequency of the pelvis-thorax and pelvis-pitch as compared to the baseline and a single oscillation of the knee joint and therefore provides scope for further pool-based investigations.

9.6 Alternative Methods of Kinematic Acquisition

This chapter has investigated the potential for alternative methods in the capturing joint kinematics. An example of how computer vision processes might be utilised has been shown with encouraging results. This first step demonstrates the feasibility of obtaining the silhouette of a swimmer performing UUS using colour thresholding strategies. Further research would need to be conducted to enable this process to be sufficiently capable of transforming the captured silhouette into usable joint kinematics. It is also identified that for this process to suitably capture the full outline of the athlete, firstly the athlete must be sufficiently contrasting in colour to the surroundings, and the frame rate at which the video is recorded should be sufficiently high to avoid blurring of the image.

Using inertial measurement units (IMUs) as a method of capturing joint kinematics in UUS has been demonstrated here for the fist time. The knee, hip and pelvis-pitch angles derived from the IMUs exhibit close agreement to the manual digitisation process and captures the participant's motion well as compared to the respective video frames. While the trend agrees closely with the manually digitised data of the pelvis-thorax joint, the amplitude is larger. It is suggested that whilst neither are incorrect, the two methods actually provide measurements of different parameters.

The musculoskeletal model was executed for both input types and the observed maximum muscle activities were similar in both trend and of mean value. From this proof of

concept study, it is concluded that IMUs could be used as a suitable alternative method in the determination of UUS joint kinematics.

9.7 Future Work

This thesis has provided the first step towards accurately modelling human UUS. The focus was to develop a fully functioning model, where joint kinematics could be captured and calculated. They were then to be used to predict fluid loadings and propulsive thrust, all of which were then used as input data in determining the muscle forces required to reproduce the kinematics by means of a musculoskeletal model.

In producing this holistic and fully functioning model, the constituent components may each be investigated and further refined. A potential first step of this process of refining was demonstrated in Chapter 8.

Key aspects of the model development in which future research is encouraged, include:

- validation and or verification of the musculoskeletal model;
- alternative scaling methods of the properties of the musculoskeletal model - such as muscle mass, maximum muscle force etc.;
- accounting for the energy expended in heat production within the muscle and utilising this in the determination of energy cost of locomotion;
- a more accurate model for determining the fluid loading;
- quantity and placement of IMUs for capturing full body kinematics;
- detailed investigation of capturing and simulating three-dimensional joint kinematics in each component of the model.

Future studies using the model would include:

- full body joint optimisation for a range of prescribed kick frequencies and amplitudes;
- sensitivity of energy expenditure to increased strength of targeted muscles;

- comparing and contrasting techniques of elite and non-elite, long distance and short distance athletes.

Appendix A

Documentation of Ethical Approval

UNIVERSITY OF Southampton

E04/Aug 2010/ v1.1

Christopher Phillips
Room 2037, Building 28
University of Southampton

12 August 2010

Dear Christopher

Ethics Submission No: SoHS-ETHICS-2010-027
Title: SwimSIM Testing Program

I am pleased to confirm **full approval** for your study has now been given. The approval has been granted by the Faculty of Health Sciences Ethics Committee.

You are required to complete a University Insurance and Research Governance Application Form (IRGA) in order to receive insurance clearance before you begin data collection. The blank form can be found at http://www.soton.ac.uk/corporateservices/rgo/regprojs/whatdocs.html

You need to submit the following documentation in a plastic wallet to Dr Martina Prude in the Research Governance Office (RGO, University of Southampton, Highfield Campus, Bldg. 37, Southampton SO17 1BJ):

- Completed IRGA Research Governance form
- Copy of your research protocol/School Ethics Form (final and approved version)
- Copy of participant information sheet
- Copy of SoHS Risk Assessment form, **signed**
- Copy of your information sheet and consent form
- Copy of this SoHS Ethical approval letter

Continued overleaf

Your project will be registered at the RGO, and then automatically transferred to the Finance Department for insurance cover. **You can not begin recruiting until you have received a letter stating that you have received insurance clearance.**

Please note that you have ethics approval only for the project described in your submission. If you want to change any aspect of your project (e.g. recruitment or data collection) you must request permission from the Ethics Committee and RGO (students should discuss changes with their supervisor before submitting the request to the Ethics Committee).

Yours sincerely

Professor Sue Latter
Chair, FoHS Ethics Committee

t: +44 (0)23 80 597959
e: sml@soton.ac.uk
f: +44 (0)23 80 597900

Appendix B

Author Publications

B.1 Propulsive Efficiency of Alternative Underwater Fly-kick Technique for Swimmers

Propulsive efficiency of alternative underwater flykick techniques for swimmers.

Christopher W.G. Phillips[1,*], Stephen R. Turnock[1], Alexander I.F. Forrester[1], Dominic A. Hudson[1]
[1] *Faculty of Engineering and the Environment, University of Southampton, Southampton, SO17 1BJ*

Abstract
The analogy between the powertrain of a ship and that of a human swimming is used to evaluate the efficiency of underwater flykick. For the first time we demonstrate here that by coupling Lighthill's theory on fish locomotion with human musculoskeletal modelling, it is possible to evaluate each component of the human powertrain and thereby compare differing techniques. This is demonstrated using a study of an elite athlete performing two different techniques; one more knee-based or *thunniform*, and the second more *carangiform*/*anguilliform*. In finding the mean kinematics of each technique, it is firstly shown that maintaining consistency of technique leads to an increase in propulsive efficiency. It is further demonstrated that in changing technique an athlete may swim at the same kick rate but have different propulsive efficiency and it is therefore necessary to determine the energy cost to evaluate different techniques. For the sprint athlete in this case study, it was shown to be more effective to swim with a *thunniform* technique when at higher velocities and a*nguilliform* for lower velocities.

***Keywords*: Human swimming, dolphin kick; underwater undulatory swimming; musculoskeletal model; propulsive efficiency**

Introduction
Underwater flykick - often underwater undulatory swimming (UUS), dolphin kick or the 5th stroke - can be a significant proportion of an elite long course competitive swimming race, accounting for up to 30% of its total distance. It was so constrained following the men's Butterfly at the 1996 Olympic Games, where Pankratov won the 100 m event having swum 40% of the race underwater [1]. Despite this demonstration of its effectiveness, it was typically observed that in the London 2012 Olympic Games many athletes failed to take full advantage of the allocated distance. The techniques adopted varied amongst elite athletes [2]. Typically it is opinion and intuition that are used to coach the swimmer. For example, with regards to best technique; [3] attribute most of the propulsive forces within the stroke to the region from just above the ankle to the toes and conclude that foot motion and ankle flexibility could have a large impact on performance. [4], however, suggest that ankle flexibility has little impact on net streamwise forces.

We seek inspiration from the comparable problem of designing a ship to maximise its overall propulsive efficiency. An understanding of the interaction of all the components of the power train from the main engine through to the propeller is required [5] to achieve maximum efficiency.

The aim of the work presented is to combine knowledge of hydrodynamic mechanisms, which convert specific human body motion into propulsion, with an inverse analysis that infers the necessary human muscular activity necessary to generate such a motion. Thereby to deduce the actual propulsive efficiency relating output power against the actual muscular power required.

Through indirect measurements, we demonstrate the validity of our hypothesis that the component stages of human underwater propulsive efficiency can be directly analysed rather than inferred. The influence of specific changes in technique can then be understood through measurement of underwater motion alone. A case study using a 50m backstroke World champion swimmer with two contrasting techniques of underwater flykick, one more thunniform (T_1) and the other more anguilliform (T_2), is used to illustrate the analysis.

Flykick Propulsive Efficiency
Figure 1 compares the power trains of both humans and ships. For a ship, a low speed Diesel engine burning fuel generates rotary motion which is transmitted through a gearbox and shafting to a propeller. This propeller generates a propulsive thrust which overcomes the ship's resistance to motion. All

* chris.phillips@soton.ac.uk

the individual stages need to be matched to achieve a maximum overall propulsive efficiency. This is typically expressed in terms of the ratio of effective power to delivered power.

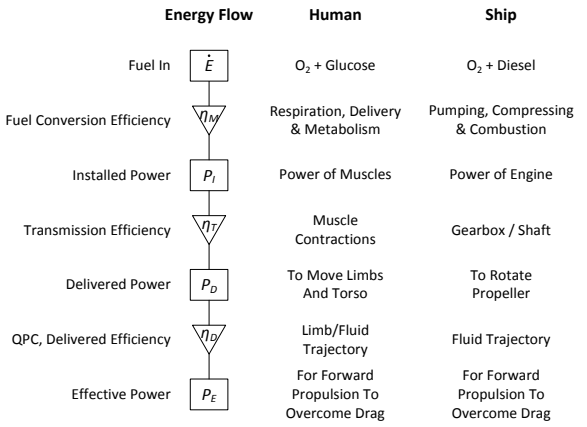

Figure 1: Energy Flow and Similarities Between Humans and Ships

Figure 2 Comparison of body position at three instants through an underwater flykick. These correspond to maximum and minimum vertical range of toes as well as an almost horizontal mid position. Images are centred on the head. (a) Technique 1 – thunniform, less motion in torso/hips. (b) Technique 2 – carangiform/anguilliform, whole body motion creates greater range of travel of feet.

Figure 2 shows the energy available to the swimmer in underwater flykick is converted into appropriate muscular contractions that develop a rearward wave-like motion which travels along the body. This results in a propulsive thrust (body reaction) associated with the fluid momentum created. The muscle contractions have to work against the resistance to motion of the surrounding fluid. The swimmer's speed will be determined by the balance of thrust through the cycle against that of resistance (or drag, D) of the body. Maximising the stroke length and vertical toe flick speed will increase thrust. Lighthill's elegant theory [6] describes fish propulsion which is computationally efficient [7], although there is the potential to overestimate magnitudes [8,9].

Despite advances in computational fluid dynamics (CFD) either with conventional finite volume based techniques [3] or smooth particle hydrodynamics [4], Lighthill's theory is chosen [10] as the most effective method of determining the relationship between body motion and thrust as well as the loading the muscles need to overcome.

Determining the relationship between muscular effort and propulsive thrust has been attempted for some swimming strokes using land-based machines. These measured the effective power delivered by an athlete and also their energy consumption by monitoring oxygen consumption ($\dot{V}O_2$)[11]. Alternatively, it is possible to simultaneously measure active drag [12–14] and metabolic power ($\dot{E}$) using $\dot{V}O_2$ directly during swimming [15].This enables athletes' aerobic energy expenditure and propulsion to be measured. Neither of these techniques, however, are currently practical for underwater flykick.

A recent development is the use of an inverse approach applied by a computational musculoskeletal method which infers the muscle activity necessary to develop a kinematic motion and estimates each muscle's length and activity [16]. In this work the *AnyBody Modelling System* (AMS)[17] is applied. Muscle activity here is the force in each muscle normalised by the maximum force it can produce. By using this activity, an estimation of the metabolic cost may be evaluated [18,19]. Work in Japan using the SWUM model [20] has indicated that a musculoskeletal model can be used in surface swimming [21] with encouraging but limited analysis of the results.

The overall efficiency (η_O) is the ratio of effective power (thrust (T) × velocity (V)) to the energy supplied to the muscles ($\dot{E}$); hence

$$\eta_O = \frac{TV}{\dot{E}}. \quad (1)$$

Equation (1) can be broken down into the three efficiency stages where energy is lost; metabolic efficiency (η_M), tramsmitted efficeincy (η_T) and quasi-

propulsive coefficient (QPC) or delivered efficiency (η_D).

$$\eta_O = \eta_M \cdot \eta_T \cdot \eta_D \quad (2)$$

As shown by Figure 1, the input energy at the first stage is converted into muscle activity (W_M). The second stage uses this work to induce the motion where the surface of the swimmer is opposed by the hydrostatic loading (buoyancy) and hydrodynamic motion of the surrounding fluid ($Qw + Tv$, where Q is transverse force, T is forward thrust and w & v the relative water velocity components). The final stage is the ratio of the useful work (Tv) to that of the overall work done on the fluid. The total system can be expressed over one oscillatory cycle

$$\eta_O = \frac{W_m}{\dot{E}} \cdot \frac{\sum Qw + \sum T\,v}{W_m} \cdot \frac{\sum T\,v}{\sum Qw + \sum T\,v}. \quad (3)$$

The propulsive efficiency (η_P) is therefore the product of η_T & η_D and hence

$$\eta_P = \frac{\sum Tv}{W_m}. \quad (4)$$

Here η_P for each technique is therefore determined by the ratio between the useful work out (W_O) and the work done by the muscles (W_M), where

$$W_O = \int T(t)V(t)\,dt, \quad (5)$$

where T is thrust, V the measured athlete velocity, and

$$W_M = \int F_m(t)\dot{L}_m(t)\,dt, \quad (6)$$

where F_m is the force in the contractile element of the muscle and $\dot{L}_m$the time derivative of the muscle length.

The oscillatory motion of a swimmer's flykick can be characterised in terms of a Strouhal number (St) (7) which relates the oscillatory speed of the feet to the mean speed through the water [22],

$$St = \frac{\bar{A}\bar{f}}{\bar{V}}, \quad (7)$$

where $\bar{A}$ is the mean amplitude of the kick, $\bar{f}$ the mean kick frequency and $\bar{V}$ the swimmer's mean velocity. This is analogous to the advance ratio (J) used for a ship propeller [5], which relates translational speed to propeller rotational speed. It is hypothesised that similar to altering the pitch of a propeller, changing flykick technique will alter the St value for maximum efficiency. Table 1 compares typical St for fish and cetaceans, human mono-fin swimming and underwater flykick. It demonstrated that St of underwater flykick is typically much higher. In flying animals, for example, kinematics are tuned for an optimal St [23,24] and the same would be expected for underwater propulsion.

Table 1: Published Strouhal Numbers (St) for fish, cetaceans and humans

Description	St			Ref.
Fish and cetaceans	0.2	->	0.4	[25]
Human mono-fin	0.35	->	0.68	[26]
Underwater flykick	0.42	->	0.53	[2]
	0.8	->	0.93	[27]
	1.05	->	1.37	[28]
	1.06	->	1.21	[3]

Experimental Study

Synchronised image and velocity data required for the study were acquired using a pool based system [7,26]. The velocity data is provided in the electronic supplementary material. As the body motion in underwater flykick is assumed symmetrical about the sagittal plane, two-dimensional (2D) kinematics are acquired from a submerged camera moving with the swimmer.

While a participant performed two techniques (T_1 and T_2), their velocity information was gathered by means of a trailing low-stretch, lightweight Dynema™ line and a rotary encoder. The line was connected to the athlete by a thin strap around their waist, in such a way as to not impinge on their motion. It was then wound around a reel connected to a rotary encoder, with a small resistance applied to prevent over-spin. The rotary encoder converted the 250 pulses per revolution of the encoder into a linearly varying analogue voltage. This analogue source was calibrated and connected to a laptop via a 6009NI™ USB analogue data acquisition board. The velocity and video data were acquired and recorded at 250 Hz and 25 Hz respectively, using *Matlab* software [29].

A world-class elite male athlete (height 1.82 m and mass 84 kg) performed the two differing techniques, both in the supine position and in the same session. In both he strived to maintain a constant depth and

heading, and performed a minimum of ten kicks for each technique. The first technique was his race-refined technique, thought to exhibit a more knee based or thunniform style (T_1).

The second technique (T_2) strove towards a more anguilliform/carangiform, with a body wave originating from the shoulders, travelling through to the toes and growing in amplitude. The concept was that greater articulation of the pelvis would facilitate the growth of the generated wave along the body. Having practiced the new technique, the athlete repeated the acquisition process as before.

Kinematic Processing

A *Matlab* based script was used to analyse the kinematics of ten leg kicks by digitising the acquired video for the corresponding run. The joint centres and anatomical locations were selected in each frame. These comprised the tip of the toes, ankle, knee, hip, shoulder, wrist and fingertip. The elbow location is selected in the first frame and assumed to maintain a constant relative location between the shoulder and wrist throughout a run. Two consistent points are also selected on the upper and lower pelvis to provide its orientation (see Figure 3). The coordinates of these points are provided in the electronic supplementary material. The beginning of the up-kick signified the start of each cycle. The first phase of the cycle is, therefore, the extension of the knee joint and upward movement of the toes until full extension is achieved. The latter phase is the recovery of the legs initiated with knee flexion.

The athlete's joint angles are defined using the joint coordinate system (JCS) of the International Society of Biomechanics (ISB) [30] and used by the AMS.

To explore the mean kinematics of the two techniques T_1 and T_2, they were subdivided into the 10 kick cycles. Each cycle was then normalised in time and the characteristic mean joint angles and velocity profile were obtained for the two conditions. A five term Fourier series was subsequently fitted to these joint angle data. Using these coefficients a further two data sets, $\bar{T}_1$ and $\bar{T}_2$, were created as idealised kinematics based upon the original T_1 and T_2 respectively, each with the same number of kicks. To gain greater insight into the kinematic space surrounding $\bar{T}_1$ & $\bar{T}_2$, and to explore the concept of kinematic tuning, multiplying the Fourier coefficients by $\boldsymbol{k}$, where $\boldsymbol{k} = \{0.1{:}\,0.1{:}\,2\}$, permutations of the idealised base kinematics were generated ($\bar{T}_{1\cdot k}$ and $\bar{T}_{2\cdot k}$) for subsequent simulations.

Hydrodynamic Forces; Lighthill's Theory

Lighthill analysed the thrust generation of fish using a momentum conservation approach. Numerically, this can be achieved by sectioning a fish or swimmer into n strips along its length, where each strip may be described in global coordinates in terms of a parametric distance a along the body at time t (Figure 3). Lighthill envisages a bound area ξ, encapsulating the fish's motion but excluding the wake and hence is bound by plane Π at the fish's tail, which remains perpendicular to the tip. [6] expresses the rate of change of momentum in this control volume in terms of (i) the rate of change due to convection of momentum out of ξ across plane Π; (ii) plus the rate of change due to pressure forces acting across Π; (iii) minus the reactive forces with which the fluid acts on the fish.

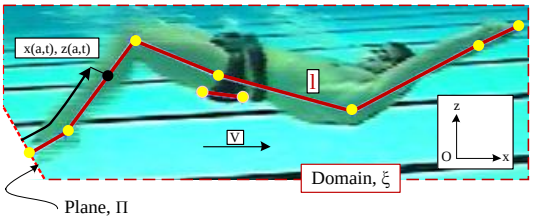

Figure 3: Lighthill reference system

The thrust generated for propelling the fish through the water (T) and the transverse force acting on the fish (Q) is

$$(T,Q) = \left[mw\left(\frac{\partial z}{\partial t}, -\frac{\partial x}{\partial t}\right) - \left(\frac{1}{2}mw^2\left(\frac{\partial x}{\partial a}, \frac{\partial z}{\partial a}\right)\right)\right]_{a=0} - \frac{d}{dt}\int_0^l mw\left(-\frac{\partial z}{\partial a}, \frac{\partial x}{\partial a}\right) da \quad (8)$$

for the prescribed kinematics, where m is the mass per unit length ($m(a) = 0.25\pi\rho s(a)^2$, where ρ is the water density and s is the depth of the cross-section) and w is the velocity component perpendicular to the direction of a.

For T_1 and T_2 experimental velocity data was used, however, for $\bar{T}_{1\cdot k}$ and $\bar{T}_{2\cdot k}$, a mean velocity was used as an initial input to the Lighthill model. This velocity was determined based upon the original experimental data. For the two techniques, an equivalent mean drag coefficient (C_D) was determined using the equation

$$\bar{T} = \frac{1}{2}\rho \bar{V}^2 S C_D, \quad (9)$$

where $\bar{T}$ is the mean thrust, ρ is the density of the water, $\bar{V}$ the athlete's mean velocity, and S frontal area (assumed proportional to kick amplitude (A) × breadth at pelvis (B)).

Using the initial mean velocity, the Lighthill simulation was executed to calculate the mean thrust. Using the previously calculated drag coefficient, a new mean velocity was estimated. This process was iterated until the mean velocity converged ($< 0.003\, ms^{-1}$). The resulting transverse forces (Q) are then used as inputs for the musculoskeletal simulation in the form of body segment loads.

Musculoskeletal Model

Figure 8 shows the musculoskeletal model scaled to the height and mass of the athlete. As the influence of the arm motion would be small, these were excluded. Table 2 details the number of simulated muscles in groups and other kinematic components divided between the body segments.

Table 2: Audit of musculoskeletal model

	Quantity
Rigid body segments	36
Rigid body DOFs	222
Frictionless Joints	137
Explicit/Implicit Drivers	85
Muscles in Trunk	203
Muscles in Leg	158
Total Muscles	519

In order to deduce the muscle activities, the AMS employs an inverse dynamics solver for which the kinematics and external forces must be defined. In this study, the driven kinematics were: the z-axis rotation of the pelvis segment relative to the global origin; ankle-plantar, knee and hip flexion; and pelvis-thorax extension. The model was kinematically over-determinant, in as much as there were more muscles than degrees of freedom. The AMS default third order polynomial recruitment solver was therefore used to estimate the normalised muscle activity of each muscle, (x_i, where $i \in \{1, \dots, M\}$ where M is the total number of muscles). For any motion generated by the body, it is supposed that it will be achieved in the most efficient way across all the muscles, minimising the necessary energy. The target function for the muscle recruitment solver is therefore to minimise the maximum muscle activity [31]. This provides a single metric which can be used as a surrogate when comparing techniques.

The muscles were grouped by action for later analysis. These included core muscles and flexors and extensors for the Pelvis-Thorax, hip, knee and ankle.

Results and Discussion

The results start with examination of the kinematics, followed by analysis of the produced thrust, muscle loadings and the energy expenditure.

Figure 4 shows the variation in an example joint angle (ankle) for T_1 and T_2. Also plotted is the minimum and maximum range of the kinematics for $\bar{T}_{1\cdot k}$ and $\bar{T}_{2\cdot k}$. The amplitude of the angle is proportional to the scalar k and the magnitude of which varies between T_1 and T_2.

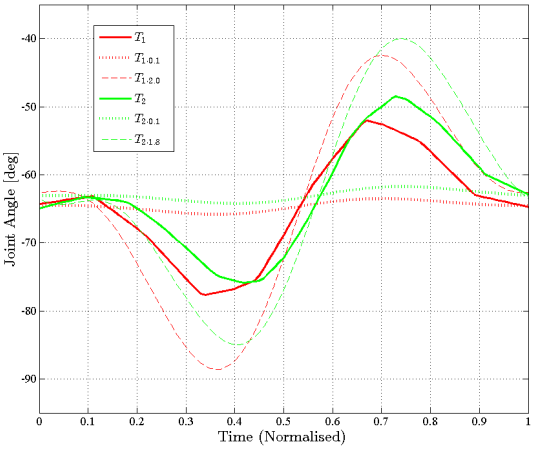

Figure 4: Example joint angle data obtained for ankle joint. The solid dark and light lines are the experimental data from $\bar{T}_1$ & $\bar{T}_2$ respectively. The dotted lines are the minimum and dashed lines the maximum from the contrived dataset $\bar{T}_{1\cdot k}$ and $\bar{T}_{2\cdot k}$.

The Lighthill and musculoskeletal model took ~30 minutes to solve for each technique (ten kicks per technique) - results are shown in Table 3. It shows an 11.2% reduction in mean maximum muscle activity ($\bar{M}_{max}$) was observed from T_1 to T_2. Similarly, there was a reduction in mean muscle activity in the trunk ($\bar{A}_{Tr}$) and the legs ($\bar{A}_{LL} + \bar{A}_{RL}$), with the legs experiencing the most - a 26.2% reduction and consequently a relative shift in muscle loadings ($\bar{A}_{L:T}$) of 8.8% from the legs to torso.

Despite a 12.4% calculated reduction in thrust, the measured velocity only reduced by $0.04\,ms^{-1}$. This infers that the total resistance of the second trial must also have reduced.

Table 3: Results from the simulations for T_1 & T_2

	T_1	(std.)	T_2	(std.)	$T_1 \rightarrow T_2$
$\bar{M}_{max}$	0.84	(0.60)	0.75	(0.55	-11.2%
$\bar{A}_{Tot}$	11.9	(4.75)	9.18	(3.82	-23.0%
$\bar{A}_{Tr}$	5.33	(2.42)	4.31	(2.12	-19.1%
$\bar{A}_{LL}$	3.30	(1.63)	2.43	(1.23	-26.2%
$\bar{A}_{L:T}$	1.24		1.13		-8.8%
$\bar{T}\ [N]$	99.1	(353)	86.8	(492)	-12.4%
$\bar{V}[ms^{-1}]$	1.90	(0.13)	1.86	(0.15	-2.2%
$W_M\ [Nm]$	3981		4223		6.1%
$W_O\ [Nm]$	693		729		5.2%
η_P	0.174		0.173		-0.8%
St	0.96		1.0		0.3%
$\bar{f}\ [Hz]$	2.75		2.23		-18.8%
$\bar{A}\ [m]$	0.66	(0.03)	0.8	(0.04	20.0%

For both techniques there are two peaks of positive thrust. Figure 5 (a) shows the maximum coinciding with change of direction of the toes as the knee and hip joints begin to extend. This implies that the extension phase of the kick produces significantly more thrust than the flexion phase, corroborating with data in the literature [4,32].

It was also found that for T_1 & T_2 respectively, 95.5% and 92.3% of the net thrust originated from the foot segment, in agreement with [3]. It is also observed that the combined shank and foot segment produce 95.1% of the total net thrust for T_1, a reduction from the foot segment alone.

The mean(std.) peak thrust from the 10 cycles was $841\,N$ (247) and $1031N$ (275) for T_1 and T_2 respectively. The male athlete in [3] produced a peak thrust of about $750\,N$, however, this was recorded at a mean velocity of $1.31\,ms^{-1}$, compared to $1.86\,ms^{-1}$ in T_2 . This variation could be attributed to the participating athlete being a good sprint athlete and good at underwater flykick, or to the combination of the velocity disparity and similarly the kinematic variation, which has been shown here to produce variable thrust and velocity.

(a) Mean Thrust for $\bar{T}_1$ & $\bar{T}_2$

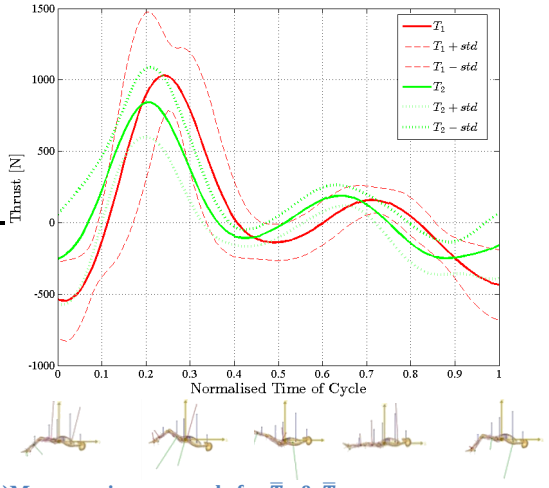

(b)Mean maximum muscle for $\bar{T}_1$ & $\bar{T}_2$

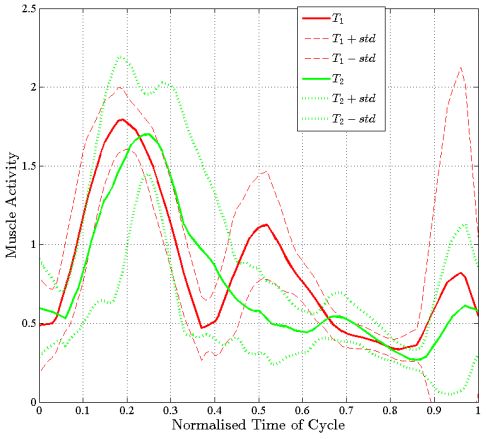

Figure 5: Normalised to one cycle, (a) shows the mean thrust for $\bar{T}_1$ (dark) & $\bar{T}_2$ (light) and (b) the mean muscle activity for $\bar{T}_1$ (dark) & $\bar{T}_2$ (light). The dashed lines and the dotted lines are one S.D. above and below the relative data.

It is interesting to note that the Strouhal number has remained relatively unchanged, despite the changes in $\bar{f}$ and $\bar{A}$. This may illustrate a natural response to the body's power limit, or an element of subconscious maintenance of perceived efficiency by the athlete. Furthermore, with the maintenance of Strouhal number, the muscle activities between runs may be directly compared.

The maximum muscle activity for these simulations can be seen to peak at roughly the same phase of the cycle as the peak thrust (Figure 5) as the knee begins to extend. There is also a smaller peak of the maximum muscle activity for the first technique which is not present in the second. This occurs as the toes change direction from the extension phase to the flexion phase and the knee begins to flex.

Upon inspection of Figure 5(a) & (b), it is apparent that the cycle is divided into a thrust followed by a recovery phase. The first half of the cycle (the extension phase), generated 86.2% & 83.2% ($\bar{T}_1$ & $\bar{T}_2$ respectively) of total propulsive thrust and 64.9% & 70.7% of total muscle activity ($\bar{T}_1$ & $\bar{T}_2$).

Using the musculoskeletal model, it is possible to investigate in more depth which muscles and muscle groups are being recruited at which part of the cycle and to what extent.

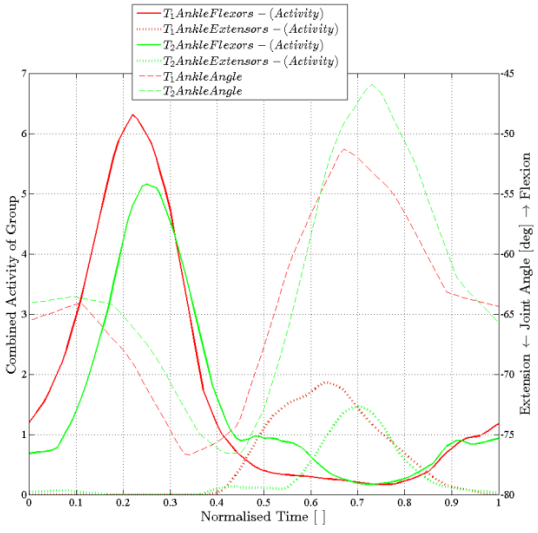

Figure 6: Flexor (solid) and extensor (dotted) activity of the ankle joint for T_1 (dark) & T_2 (light), with the context of ankle flexion angle (dashed).

Figure 6 is an example of the activity pattern of the muscle groups about the ankle joint with the context of the joint angle. It shows the maximum activity of the grouped muscles coinciding with the maximum rate of joint angle. It also highlights the variation in motion between $\bar{T}_1$ & $\bar{T}_2$. For example, it can be seen that there is reduction in peak activity for both the ankle flexor and extensor groups. There is a phasing difference, particularly prevalent in the second period of the cycle; the joint angle in $\bar{T}_2$ reduces more for a lower peak in the extensors' activity.

An increase in combined activity can be observed (Figure 7 (a) & (b)) in the core stabiliser muscles between T_1 and T_2 . With many of the stabilising muscles found in the trunk, it can also be seen in the apparent shift of muscle activity from the legs to the trunk (-8.8%, see Table 3).

There is also a change in activity pattern for the Pelvis-Thorax Extensors. This is most apparent at ~0.7 of the cycle, where there is an increase in activity which is less prevalent in $\bar{T}_1$.

(a) $\bar{T}_1$

(b) $\bar{T}_2$

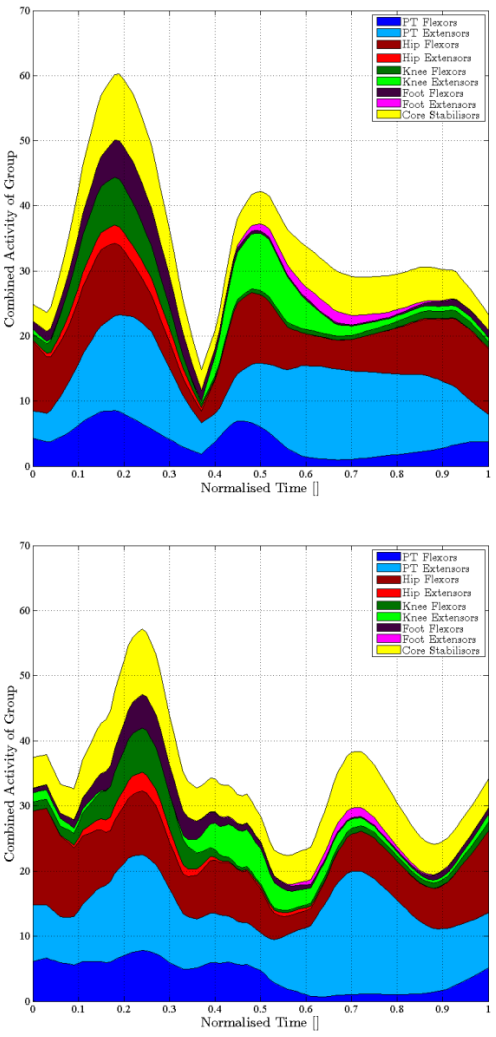

Figure 7: Area plot of combined activity of each muscle separated into the respective activity group.

There is a difference between the phasing of the activations between the trials. There are two significant peaks visible in the two cases, but for $\bar{T}_1$ the first and second occur at ~0.19 & ~0.49 of the cycle, compared with ~0.3 & ~0.7 for $\bar{T}_2$.

Upon inspection of the individual muscle group it can be observed that Rectus Abdominus ($i = 195$, see Figure 8) and Femoris *Caput Longum* ($i = 67$, see Figure 8) - in the trunk and legs respectively - contribute a significant proportion of the activity required to produce the motion. Rectus Abdominus is associated with Pelvic-Thoracic Flexion and Biceps Femoris *Caput Longum* with posterior extension of the hip joint. In conjunction with *Caput Brevis*, it forms

part of the Hamstring group for knee flexion. They each exceed activity levels of 0.75 for the longest duration of any of the muscles in their respective areas of the body (Figure 8) and are hence indicative of those of greater significance in underwater flykick.

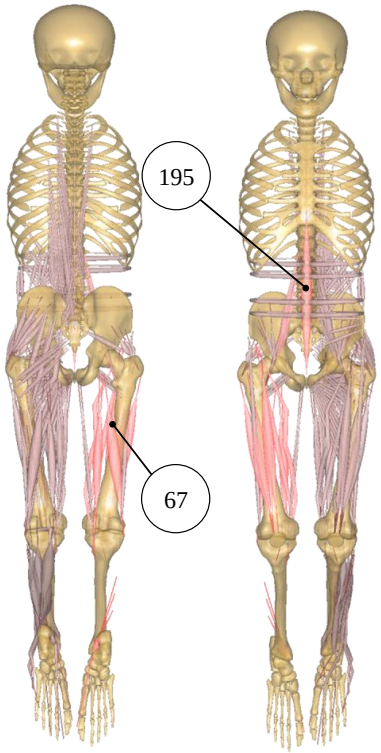

Figure 8: Coronal Plane of the musculoskeletal model in Posterior and Anterior views. Showing all muscles on the body's left and muscles on body's right are those which have a higher frequency of activation. Those which are highlighted on the right have activity levels which exceed 0.75 for more than 5% of the cycle. Indicated muscles 195 and 67 are Rectus Abdominis and Biceps Femoris Caput Longum respectively.

The Strouhal numbers for $\bar{T}_1$ and $\bar{T}_2$ were 0.96 and 1.0 respectively, with little variation in η_P also. But in human underwater flykick, as seen in Figure 5 (a), there appears to be only one significant thrust production and hence one vortex shed during the cycle (Figure 11 of [3]). This is in contrast to human mono-fin swimming and fish swimming, which have two [26,27].

If it is considered that frequency component in Equation (2) is more correctly defined as the frequency between vortex shedding, then the apparent time period between the generated vortices for underwater flykick is therefore double that of mono-fin and fish swimming, and thus relatively half the frequency. This would therefore lead to a twofold overestimation of Strouhal number for cases where only one vortex is shed in a cycle, such as demonstrated for underwater flykick. This would account for inflated variation in theoretically optimal ranges and published values of St for human underwater flykick, relative to mono-fin and fish swimming.

The datasets $\bar{T}_{1\cdot k}$ and $\bar{T}_{2\cdot k}$ provide insight into the tuning of the kinematics for the two techniques simulated here.

Figure 9 shows the propulsive efficiencies as a function of Strouhal Number, illustrating the non-linear relationship between the kinematic variations of $\bar{T}_{1\cdot k}$ and $\bar{T}_{2\cdot k}$.

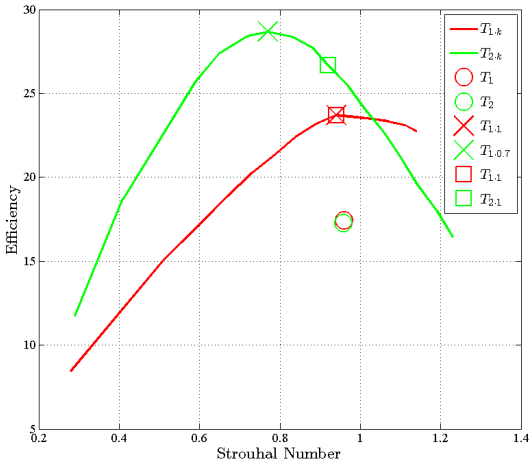

Figure 9: Relationship between kick amplitude and efficiency and Energy. Dark and light solid lines represent $\bar{T}_{1\cdot k}$ & $\bar{T}_{2\cdot k}$ respectively. Dark & light '⊡' indicate $\bar{T}_{1\cdot 1}$ & $\bar{T}_{2\cdot 1}$ and dark & light 'X' indicate peak efficiency which for $\bar{T}_{1\cdot k}$ is at $k = 1.0$ and $\bar{T}_{2\cdot k}$ at $k = 0.7$. Maximum η_P for $\bar{T}_{1\cdot k}$ & $\bar{T}_{2\cdot k}$ occurs at $St_1 = 0.94$ & $St_2 = 0.77$, respectively.

It is apparent from Figure 9 that there is an increase in efficiency from T_1 to $\bar{T}_{1\cdot 1}$ and similarly from T_2 to $\bar{T}_{2\cdot 1}$. This increase suggests that the maintenance of consistent kinematics generates higher observed efficiency.

The data shows that the base style ($k = 1$) for the first technique is at the optimal efficiency point for that technique. Contrastingly, the base style for the second technique is not at the optimal efficiency point - a decrease in the global joint angles would increase the efficiency to a maximum. This further illustrates the nonlinear relationship between St and η_P, and clearly demonstrates the principle that tuning kinematics, as shown for flying animals [23], can achieve higher efficiency in underwater flykick. In changing technique, this study has demonstrated that an athlete may swim at the same Strouhal number, but their levels of efficiency might differ.

Depending on a particular strategy, however, maximising efficiency may occasionally be misleading. Hypothetically, it may be less efficient to choose to swim at a higher Strouhal number. However, with a proportional relationship between velocity and St, it may well be faster.

It is therefore necessary to determine the energy cost of (C_s) of a particular technique to make informed decisions. [19] used a musculoskeletal model to quantify the energy cost of locomotion for a gait cycle. In the same way, the data from the musculoskeletal model presented here was used to determine the energy cost for the two techniques, which for T_1 and T_2 respectively, $C_s = 0.569\ kJm^{-1}$ and $0.502\ kJm^{-1}$.

Table 4: Cost of locomotion (C_s) for different disciplines.

Description	$C\ [kJm^{-1}]$	$V\ [ms^{-1}]$
Underwater flykick	0.57* -> 0.50†	1.9* -> 1.86†
Freestyle	1.13 -> 1.41[i]	1.21 -> 1.62
	0.55 [ii]	0.9

*T_1; † T_2; [i] [33]; [ii] [34]

These values of C_s are comparable with experimental values for freestyle swimming as tabulated in Table 4. The reduced values for underwater flykick shown here may, for example, be explained as a consequence of variation in kinematics or more fundamentally, the discrepancy between stroke types. The impact of the arms was also not taken into account within this paper.

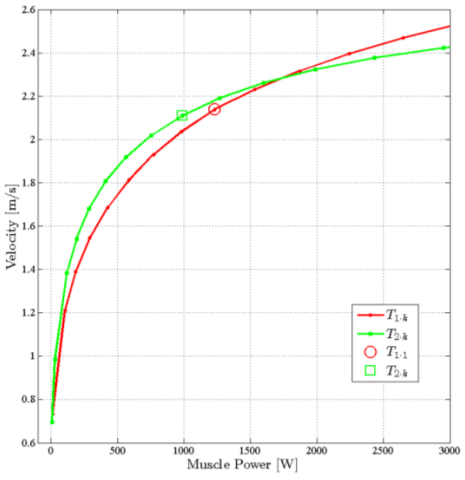

Figure 10: Relationship between power delivered by the muscles and swimming velocities for $\overline{T}_{1\cdot k}$ (dark) & $\overline{T}_{2\cdot k}$ (light).

By analysing these results, it may be more effective for a sprint athlete to swim at a higher velocity and hence at a higher St number: for a common goldfish $St \simeq 0.4$ but for an Atlantic mackerel $St \simeq 0.25$ [35]. Upon observation of Figure 10, for example, it may be more efficient for the sprint athlete in this study to select a more knee based kick of the first technique ($\overline{T}_1$) when swimming above $2.3\ ms^{-1}$. The reciprocal would therefore be more appropriate for lower velocities or a longer distance swimmer, where conservation of energy is more applicable. It may also be strategically beneficial to seamlessly transfer from $\overline{T}_1$ to $\overline{T}_2$ as the athlete begins to slow down following a dive start or push off the wall from a turn.

Conclusions

In this paper, Lighthill's theory of fish locomotion and a musculoskeletal model have been coupled together for the analysis of swimming technique and is demonstrated in the form of a case study. The kinematics and velocity were acquired and synchronised using a setup which is non-invasive or motion restrictive. The thrust production of Lighthill is comparable to published data and is computationally inexpensive. The musculoskeletal model has been shown to provide a greater level of insight, both inter and intra simulated technique and provide an energetic cost of locomotion, enabling the comparison of differing techniques and demonstrating the potential increase in efficiency associated with increased consistency. An example of varying joint amplitude has demonstrated the potential benefit of tuning kinematics to provide a potential increase in efficiency. This provides a quantitative answer as to which technique may be preferable for an athlete when competing in short swimming events.

References

1 Forman, S. 1996 Swimming at the 1996 Atlanta Summer Games: Men's 200 metres Butterfly. *www.sports-reference.com*.

2 Collard, L., Auvray, E. & Bellaunay, I. 2011 Comparison of performance levels over 25 m by 11 expert swimmers using anguilliform-like and carangiform-like techniques ; eel-like swimming versus carangiform-like swimming. *International Journal of Performance Analysis in Sport* **11**, 26–33.

3 Von Loebbecke, A., Mittal, R., Mark, R. & Hahn, J. 2009 A computational method for analysis of underwater dolphin kick hydrodynamics in human swimming. *Sports Biomechanics* **8**, 60–77. (doi:10.1080/14763140802629982)

4 Cohen, R. C. Z., Cleary, P. W. & Mason, B. R. 2012 Simulations of dolphin kick swimming using smoothed particle hydrodynamics. *Human movement science* **31**, 604–19. (doi:10.1016/j.humov.2011.06.008)

5 Molland, A. F., Turnock, S. R. & Hudson, D. A. 2011 *Ship Resistance and Propulsion: Practical Estimation of Ship Propulsive Power*. 1st edn. New York, USA: Cambridge University Press.

6 Lighthill, M. J. 1971 Large-Amplitude Elongated-Body Theory of Fish Locomotion. *Proceedings of the Royal Society of London. Series B, Biological Sciences* **179**, 125–138.

7 Webb, A. P., Phillips, C. W. G., Hudson, D. A. & Turnock, S. R. 2012 Can Lighthill's Elongated Body Theory Predict Hydrodynamic Forces in Underwater Undulatory Swimming? *Procedia Engineering* **00**, 1–6.

8 Bertetto, A. M., Picasso, B. & Ruggiu, M. 2001 Fish and ships : can fish inspired propulsion outperform traditional propulsion based systems ? *Built Environment* **53**. (doi:10.2495/MT010261)

9 Borazjani, I. & Sotiropoulos, F. 2008 Numerical investigation of the hydrodynamics of carangiform swimming in the transitional and inertial flow regimes. *The Journal of experimental biology* **211**, 1541–58. (doi:10.1242/jeb.015644)

10 Singh, K. & Pedley, T. J. 2012 Modelling lateral manoeuvres in fish. *Journal of Fluid Mechanics* **697**, 1–34. (doi:10.1017/jfm.2012.1)

11 Zamparo, P. & Swaine, I. L. 2012 Mechanical and propelling efficiency in swimming derived from exercise using a laboratory-based whole-body swimming ergometer. *Journal of applied physiology (Bethesda, Md. : 1985)* **113**, 584–94. (doi:10.1152/japplphysiol.00324.2012)

12 Hollander, A. P., De Groot, G., Van Ingen Schenau, G. J., Toussaint, H. M., De Best, H., Peeters, W., Meulemans, A. & Schreurs, A. W. 1986 Measurement of active drag during crawl arm stroke swimming. *Journal of sports sciences* **4**, 21–30. (doi:10.1080/02640418608732094)

13 Kolmogorov, S. V. & Duplishcheva, O. A. 1992 Active drag, useful mechanical power output and hydrodynamic force coefficient in different swimming strokes at maximal velocity. *Journal of Biomechanics* **25**, 311–318. (doi:10.1016/0021-9290(92)90028-Y)

14 Webb, A. P., Banks, J., Phillips, C. W. G., Hudson, D. A., Taunton, D. J. & Turnock, S. R. 2011 Prediction of passive and active drag in swimming. *Procedia Engineering* **13**, 133–140. (doi:10.1016/j.proeng.2011.05.063)

15 Reis, V. M., Marinho, D. A., Barbosa, F. P., Reis, A. M., Guidetti, L. & Silva, A. J. 2010 Examining the accumulated oxygen deficit method in breaststroke swimming. *European journal of applied physiology* **109**, 1129–35. (doi:10.1007/s00421-010-1460-4)

16 Damsgaard, M., Rasmussen, J., Christensen, S. T., Surma, E. & De Zee, M. 2006 Analysis of musculoskeletal systems in the AnyBody Modeling System. *Simulation Modelling Practice and Theory* **14**, 1100–1111. (doi:10.1016/j.simpat.2006.09.001)

17 AnyBody 2011 *The AnyBody™ Modeling System*. V5.0.1 edn. Aalborg, Denmark: AnyBodyTech.

18 Umberger, B. R., Gerritsen, K. G. M. & Martin, P. E. 2003 A model of human muscle energy expenditure. *Computer methods in biomechanics and biomedical engineering* **6**, 99–111. (doi:10.1080/1025584031000091678)

19 Umberger, B. R. 2010 Stance and swing phase costs in human walking. *Journal of the Royal Society, Interface / the Royal Society* **7**, 1329–40. (doi:10.1098/rsif.2010.0084)

20 Nakashima, M., Satou, K. & Miura, Y. 2007 Development of Swimming Human Simulation Model Considering Rigid Body Dynamics and Unsteady Fluid Force for Whole Body. *Journal of Fluid Science and Technology* **2**, 56–67. (doi:10.1299/jfst.2.56)

21 Nakashima, M. & Yugo, M. 2007 DEVELOPMENT OF A FULL-BODY MUSCULO-SKELETAL SIMULATOR FOR SWIMMING. *11th International Symposium on Computer Simulation in Biomechanics*. , 59–60.

22 Rohr, J. J. & Fish, F. E. 2004 Strouhal numbers and optimization of swimming by odontocete cetaceans. *Journal of Experimental Biology* **207**, 1633–1642. (doi:10.1242/jeb.00948)

23 Taylor, G. K., Nudds, R. L. & Thomas, A. L. R. 2003 Flying and swimming animals cruise at a Strouhal number tuned for high power efficiency. *Nature* **425**, 707–11. (doi:10.1038/nature02000)

24 Nudds, R. L., Taylor, G. K. & Thomas, A. L. R. 2004 Tuning of Strouhal number for high propulsive efficiency accurately predicts how wingbeat frequency and stroke amplitude relate and scale with size and flight speed in birds. *Proceedings. Biological sciences / The Royal Society* **271**, 2071–6. (doi:10.1098/rspb.2004.2838)

25 Triantafyllou, G. S., Triantafyllou, M. S. & Grosenbaugh, M. A. 1993 Optimal Thrust Development in Oscillating Foils with Application to Fish Propulsion. *Journal of Fluids and Structures* **7**, 205–224. (doi:10.1006/jfls.1993.1012)

26 Nicolas, G., Bideau, B., Colobert, B. & Berton, E. 2007 How are Strouhal number, drag, and efficiency adjusted in high level underwater monofin-swimming? *Human movement science* **26**, 426–42. (doi:10.1016/j.humov.2007.03.002)

27 Hochstein, S. & Blickhan, R. 2011 Vortex re-capturing and kinematics in human underwater undulatory swimming. *Human movement science* **30**, 998–1007. (doi:10.1016/j.humov.2010.07.002)

28 Von Loebbecke, A., Mittal, R., Fish, F. E. & Mark, R. 2009 Propulsive efficiency of the underwater dolphin kick in humans. *Journal of biomechanical engineering* **131**, 054504. (doi:10.1115/1.3116150)

29 MATLAB In press. *The Mathworks Inc.* 2012b edn. Natick, Massachusetts, USA: The Mathworks Inc.

30 Jakab, F., Farkas, S. & Tóth, J. 2002 ISB recommendation on definitions of joint coordinate system of various joints for the reporting of human joint motion—part I: ankle, hip, and spine. *Journal of biomechanics* **35**, 543–548. (doi:10.1556/MaSeb.65.2012.2.7)

31 Rasmussen, J., Damsgaard, M. & Voigt, M. 2001 Muscle recruitment by the min/max criterion -- a comparative numerical study. *Journal of biomechanics* **34**, 409–15.

32 Von Loebbecke, A., Mittal, R., Fish, F. E. & Mark, R. 2009 A comparison of the kinematics of the dolphin kick in humans and cetaceans. *Human movement science* **28**, 99–112. (doi:10.1016/j.humov.2008.07.005)

33 Zamparo, P., Capelli, C., Cautero, M. & Di Nino, A. 2000 Energy cost of front-crawl swimming at supra-maximal speeds and underwater torque in young swimmers. *European Journal of Applied Physiology* **83**, 487–491. (doi:10.1007/s004210000318)

34 Pendergast, D. et al. 2003 Energy balance of human locomotion in water. *European journal of applied physiology* **90**, 377–86. (doi:10.1007/s00421-003-0919-y)

35 Eloy, C. 2011 Optimal Strouhal number for swimming animals. **281**, 1–21.

Nomenclature

Symbol	Description	Units
$\bar{A}$	Mean Kick Amplitude	m
$\bar{A}_{LL}$	Mean Left Leg Activity per sec.	s^{-1}
$\bar{A}_{L:T}$	Ratio of Leg to Trunk Activity	s^{-1}
$\bar{A}_{Tot}$	Mean Total Activity per sec.	s^{-1}
$\bar{A}_{Tr}$	Mean Trunk Activity per sec.	s^{-1}
a	Parametric Distance Along Body	m
B	Breadth at Pelvis	m
C_D	Drag Coefficient	
C_S	Energy Cost of Locomotion	kJm^{-1}
D	Drag	N
$\dot{E}$	Metabolic Power In	W
F_m	Force in Contractile Element of Muscle	N
$\bar{f}$	Mean Kick Frequency	Hz
J	Advance Ratio	
k	Kinematic Multiplication Factor	
$\dot{L}_m$	Contractile Velocity of Muscle	ms^{-1}
M	Number of Muscles	
$\bar{M}_{max}$	Mean Max Muscle Activity	
m	Mass per Unit Length	kgm^{-1}
n	Number of Strips Along Body	
P_D	Delivered Power	W
P_E	Effective Power	W
P_I	Installed Power	W
Q	Force Perpendicular to Body	N
S	Frontal Area	m^2

St	Strouhal Number ($\frac{\bar{A}\bar{f}}{\bar{V}}$)	
T	Swimmer Thrust	N
t	Time	s
V	Swimmer Velocity	ms^{-1}
v	Water Velocity Component Parallel to Body	ms^{-1}
W_M	Muscle Work Done	Nm
W_O	Work Out	Nm
w	Water Velocity Component Perpendicular to Body	ms^{-1}
x_i	Muscle Activity of i^{th}Muscle	
η_D	Delivered Efficiency or Quasi-Propulsive Coefficient (QPC)	
η_M	Fuel Conversion Efficiency	
η_O	Overall Efficiency	
η_P	Propulsive Efficiency (W_O/W_M)	
η_T	Transmission Efficiency	
ξ	Area Encapsulating Motion	
Π	Reference Plane Perpendicular to Body at Origin	

B.2 Optimisation of a Bicycle Chainring to Aid in Rehabilitation of Athletes Suffering from Patellofemoral Pain Syndrome

ELSEVIER

Available online at www.sciencedirect.com
ScienceDirect
Procedia Engineering 2 (2010) 3151–3156

Procedia Engineering

www.elsevier.com/locate/procedia

8th Conference of the International Sports Engineering Association (ISEA)

Optimisation of a bicycle chainring to aid in rehabilitation of athletes suffering from patellofemoral pain syndrome (PFPS)

Phillips C.W.G.[a], Forrester A.I.J.[a]*, Purdue A.I.[a] and Stokes M.J.[b]

[a]*School of Engineering Sciences, University of Southampton, Southampton, SO17 1BJ, UK*
[b]*School of Health Sciences, Univcersity of Southampton, Southampton, SO17 1BJ, UK*

Received 31 January 2010; revised 7 March 2010; accepted 21 March 2010

Abstract

Patellofemoral Pain Syndrome (PFPS) is a frequently occurring problem whose causation is multifactorial. Supposed triggers include mal-tracking patella due to an imbalance in the muscles of the quadriceps. There are numerous treatments for the pain; for example, strengthening of the quadriceps shows good clinical results. In this study, the geometry of a bicycle chainring has been optimised to increase the recruitment of Vastus Medialis Oblique (VMO). The intention is to strengthen VMO as part of a rehabilitation program to relieve the pain associated with PFPS.

Keywords: Knee Injuries, PFPS, Rehabilitation

1. Introduction

Patellofemoral Pain Syndrome (PFPS) is a general term given to a pain experienced underneath the patella. The pain is most poignant during exercising but may also be felt in menial, daily tasks such as climbing and descending stairs. It is particularly prevalent in adolescents as well as young adults accounting for up to 10% of visits to sports medicine clinics [1]. PFPS has also been observed as being the most common injury experienced by runners [2].

Owing to the multi-factorial nature of PFPS, it is uncertain as to its exact causation. Abnormal tracking of the patella [3], patella dysplasia and delayed onset of Vastus Medialis Obliquus (VMO) relative to Vastus Lateralis (VL), however, are thought to play a role in the source of the pain. Due to the anatomy of the knee, during flexion of the lower limb, the patella experiences a lateral movement. This movement however, is resisted by VMO, the medial retinacular structures and the prominence of the lateral facet of the trochlea [4]. If VMO is weakened

* Corresponding author. Tel.:+44 238 059 2713
E-mail address:alexander.forrester@soton.ac.uk.

1877-7058 © 2010 Published by Elsevier Ltd.
doi:10.1016/j.proeng.2010.04.125

therefore, or its onset delayed in comparison to VL, the lateral movement associated with flexion cannot be resisted to the same extent, hence causing mal-tracking of the patella in the femoral trochlea (Souza et al. linked VM weakness to Patellofemoral pain).

Treatments that resolve the pain and restore the previous range of motion are plentiful but lack substantive evidence. Rehabilitation by means of exercise therapy, however, is common practice and previous clinical trials with quadriceps strengthening have produced good results [1], complementing the conclusions of Doucette et al.[5] who concluded that strengthening exercises of VMO could improve patella stability.

Cycling is a well-known exercise used for rehabilitation purposes, enabling the patient to exercise and strengthen their muscles without applying potentially damaging impulse loading to the joints and surrounding tissues. During cycling numerous muscles are recruited, particularly the quadriceps. Where a patient is suffering from PFPS however, it may be desirable to focus preferential recruitment of VMO.

Recent studies by the authors have shown that by altering the geometry of a bicycle chainring, different muscles are recruited to varying extents. The eventual aim of this research is to increase the strength of VMO in order to counterbalance the pull of VL [6] and hence effectively pull the patella back into normal alignment, relieving the pain underneath. The aim of this paper is to perform an optimisation study that will vary a bicycle's chainring geometry to preferentially recruit VM and while ensuring the onset of the VM is at the same point in time as VL.

The long-term objectives of this study would be the ability to offer a bespoke chainring that suits the anatomy of an individual patient. This may prove to be a more time-efficient method of the rehabilitation process, which may eliminate the continued supervision of their physiotherapist and thus reduce consultation time.

2. Methods

A series of experiments were undertaken to acquire specific torque output for a variety of cadences, for one male rider who is of a competitive standard. This data was then collated to provide a cadence-torque profile for the cyclist, which is then utilised in the geometric chainring optimisation.

AnyBody 4.0.2 was the musculoskeletal modeling program used for this study, which solves the problem by inverse dynamic method, utilising the software's muscle recruitment algorithm [7]. The three-dimensional bicycle model, available from the AnyBody repository AMMRV 1.0, was used as a basis for the study (see Figure 1). The model consists of ~287 simple Hill-type muscles. Preprogrammed into the repository model is also the posture and body motion of the cyclist, which was used as the foundation for the cyclist's motion during the study, i.e. the simulation anthropometrics did not match the rider for whom the torque data was collected.

To reduce the complexity of the model in the interest of minimising computational cost, the model did not include arms as it is assumed that they play little role in the desired analysis and can therefore be omitted. VMO is not defined explicitly in the computer model and the entire Vastus Medialis (VM) group is targeted for increased recruitment.

As previously mentioned, it has been shown that by altering the geometry of the chainring, muscles may be recruited to varying extents during a single rotation of the cranks, when compared to a regular circular chainring. By varying the shape of the chainring, one is effectively changing the local cadence for a given crank angle, in turn affecting the torque at that instance. Given the cadence, the relative torque can hence be looked up from the experimental data. In this optimisation study where hundreds of chainring shapes were investigated, it was clearly impracticable to collect torque data for each design. We therefore employed a surrogate model of the relationship between torque, local cadence and power. In this model the torque is defined by 10 Fourier coefficients (plus a constant) each of which are represented by a *Kriging* Gaussian process based model [8] fitted through 25 experimental points. This model was embedded within the chainring optimization process, essentially providing a continuous look-up table from which to obtain the torque profile for a given chainring.

Reflecting the torque parameterisation, we also described the cadence in terms of a Fourier series. The coefficients of the series control the cadence profile, hence the geometry, and in turn the torque profile. If all the coefficients except the first are set equal to zero, then the cadence will be constant and consequently the chainring will be circular. If all the coefficients are then defined less than or greater than zero, the cadence profile will change and hence the chainring becomes non-circular. Our aim was to find the Fourier coefficients ($a_1,\ldots,a_{10}$) which increase activity of VM (by increasing the metabolic power (Pmet) of VM in the AnyBody model) compared to a standard circular chainring. More formally, we maximize the maximum Pmet in the right VM plus the maximum Pmet in the left VM:

$$\max_{a_1,\ldots,a_{10}} \quad Pmet_{\max,R} + Pmet_{\max,L} \tag{1}$$

Subject to a constraint, $g(a_1,\ldots,a_{10})$ the left maximum being within 10% of the right:

$$\left| \frac{Pmet_{\max,R} - Pmet_{\max,L}}{Pmet_{\max,R}} \right| < 0.1 \tag{2}$$

Figure 1: Image of AnyBody 3D Bicycle Model

Direct numerical optimisation of this problem was computationally too expensive and a surrogate model was used in lieu of calls to the AnyBody simulation. A Matlab surrogate modeling toolbox [9] was employed, which is able to run the 3D bicycle model through the AnyBody console.

We began with a 10-dimension Latin hypercube defining 100 points in the design space at which to sample the model. The inverse dynamics operation is run for the defined coefficients, calculating $Pmet_{max}$ for each occurrence, which are then stored in a matrix in the MATLAB workspace.

Once the initial data points have been retrieved, a multidimensional (Kriging) surface map is fitted to these points. The code then searches the map for the coefficients with the maximum expected improvement in $Pmet_{max}$ multiplied by the probability of meeting the left/right muscle balance constraint:

$$\max_{a_1,\ldots,a_{10}} \quad E\left[I(a_1,\ldots,a_{10})\right] P\left[g(a_1,\ldots,a_{10}) < 0.1\right] \tag{3}$$

It is then possible to select the coefficients that generate the greatest values of Pmet from the surface model. These coefficients are then used to determine the chainring geometry. The process continues until the chainring shape is deemed to have converged on an optimal solution.

3. Results and Discussion

The optimised Fourier coefficients (from the 13th simulation) lead to the optimised chainring geometry as seen in Figure 2(a). The optimal design has three large peaks, which corresponds to the three dominant peaks in the local crank velocity (Figure 2(b)), and is rather asymmetric, alluding to the complexity of the study.

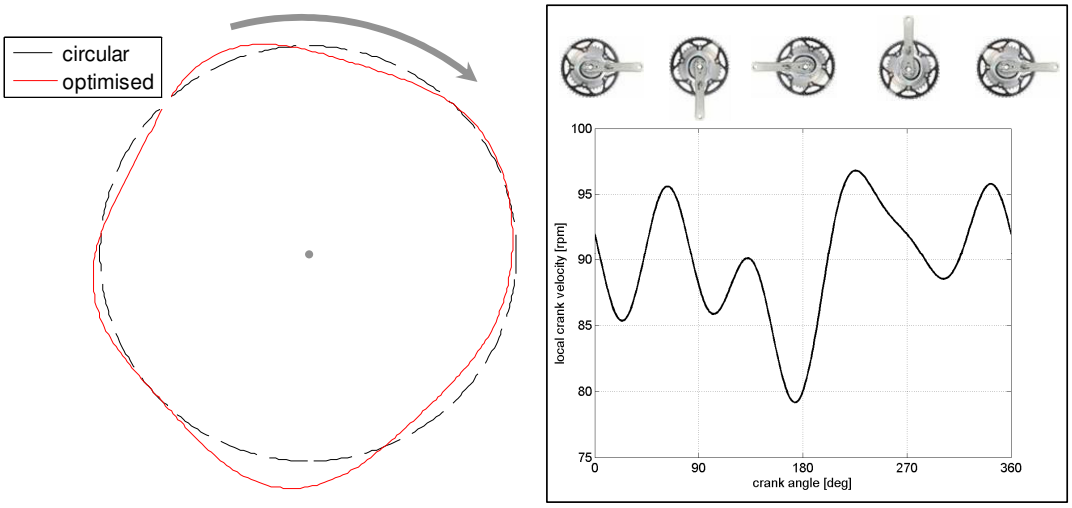

Figure 2 (a) Chainring geometry; before and after optimisation; (b) Local crank velocity during one revolution of the cranks

On inspection of the chainring Figure 2, the optimized shape appears to be reasonably logical. If it is imagined that in its current orientation, the right crank is in the forward-horizontal position, then as the chainring begins to rotate clockwise past the horizontal, the local radius of the chainring increases (where the chain would attach). This causes a decrease in the local crank velocity and an increase in Pmet to produce the necessary torque. It can be seen in Figure 3(a) that the peak in Pmet occurs at ~ 45°, which is just after the peak in the radius. The local velocity increases again as radius reduces slightly, before decreasing once more as the right crank passes through the downward-vertical and the radius is once more increased; this pattern then continues through the revolution. The geometric maxima are seen when either crank is near to the horizontal, during the transition from a lower to higher local velocity.

Figure 3(a) is showing the how Pmet varies with respect to crank angle; for both a circular chainring and the optimised chainring. For both, there are two distinct peaks where the right and left VM respectively are activated. The maxima occur when the crank for the respective leg is between the forward-horizontal and downward-vertical position; this is the same irrespective of which chainring is used. However, in the case of the optimised chainring, it appears that the muscles are not working as efficiently and hence Pmet increases with the lower local velocity.

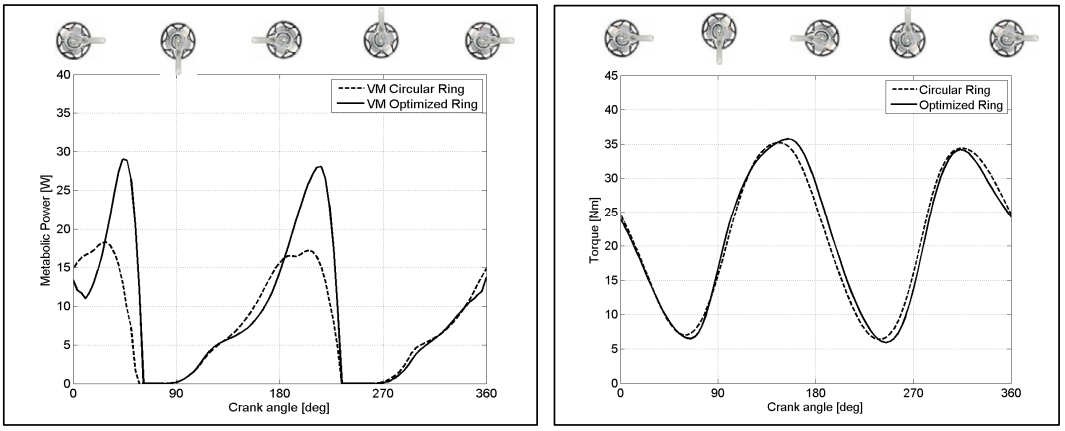

Figure 3: (a) Results from optimisation of Pmet, showing Pmet of VM before, and Pmet of VM afterwards;
(b) Torque Profile for one revolution of the cranks

It can be seen from Figure 3 that it was possible to optimise a bicycle chainring to increase the activation of VM. There is definite increase in the peak-to-peak metabolic power of VM (58.9%), as well as a 16.9% rise in the mean metabolic power during one revolution compared to a conventional, circular chainring. These peaks also coincide with the latter part of knee extension, which is when activity of VMO is thought to be most prominent [10].

The torque profile during the revolution is a fairly regular sinusoidal type curve, generating a power output of ~200W and a cadence of ~90rpm (both the target values). It is however, slightly delayed on the down-stroke of the left crank, but marginally ahead on the down-stroke of the right crank, when compared to that of a circular chainring. This may pertain to the delay in the peaks of Pmet.

As a consequence of increasing VM however, Pmet of VL and Vastus Intermedius (VI) also increases. This is a reasonable concurrence, as the Vasti group is activated for leg extension. Although it may be assumed that if there is an imbalance in the muscles and the intention is to increase the weaker, the stronger ought to be worked less by comparison. However, due to the relative sizes of the muscles, VL will have more influence on the motion, over VM. Nevertheless, it is increasing $Pmet_{max}$ of VM by 58.9% from its norm, which will aid in adding bulk to that muscle. It also trains the muscles to activate at the same time, which has also been suggested as a cause of the pain.

4. Conclusion

This study further supports the notion that by altering the geometry of a bicycle chainring, it is possible to affect the muscle recruitment. The next step would be to employ motion capture to the cyclist's kinematics and to manufacture their optimised chainring, comparing the theoretical results with experimental. It would also be of interest to see if a generic chainring could be used for a range of subjects, in a rehabilitation program. The effect of pronation of the foot and saddle height may also be of interest of further investigation, as these may both affect the extent to which VM is activated, particularly in relation to VL. The optimised shape of the chainring presented in this study is asymmetric, but with two distinct radial increases perpendicular to the cranks. It may therefore be of interest to reduce the optimisation to that of an ellipse, with only two parameters.

Having demonstrated this technology in the specific field of cycling as means of rehabilitation for people with PFPS, there is the possibility that this work may spinout into other research areas involving musculoskeletal

modeling and analysis, rehabilitation or even performance enhancements in elite sports, where it is desired that the patient or athlete increase the strength of a certain muscle.

References

[1] Bily W, Trimmel L, Mödlin M, Kaider A and Kern H. Training Program and Additional Electric Muscle Stimulation for Patellofemoral Pain Syndrome: A Pilot Study. *Arch Phys Med Rehabil*. 2008;**89**:1230-6.

[2] Taunton JE, Ryan MB ,Clement DB, McKenzie DC, Lloyd-Smith DR and Zumbo BD. A retrospective case-control analysis of 2002 running injuries. *Br. J. Sports Med*. 2002;**36**:95-101

[3] Fulkerson JP and Shea KP. Current concepts review: disorder of patellofemoral alighment. *J. Bone Joint Surg Am*. 1990;**72**:1424-9

[4] Naotaka S, Zong-Ping L, James A and Kai-Nan A. The influence of weakness in the Vastus Medialis Oblique muscle on the Patellofemoral joint: an in vitro biomechanical study. *Clinical Biomechanics*. 2000;**15**:335-339

[5] Doucette SA, Goble EM, The effect of exercise on patella tracking in lateral patella compression syndrome. *Am J SportMed.*1992;**20**:434-40

[6] Powers C, Landel R & Perry J. Timing and intensity of vastus muscle activity during functional activities in subjects with and without patellofemoral pain. *Physical Therapy*, 1996;**76:**946

[7] Rasmussen J, Damsgaard M, Voigt M. Muscle recruitment by the min/max criterion – a comparative numerical study, *J Biomechanics* 2001;**34**:409-415

[8] Forrester AIJ and Keane AJ, Recent advances in surrogate-based optimisation, Progress in Aerospace Sciences, 45(1-3), 50-79 (doi:10.1016/j.paerosci.2008.11.001)

[9] Forrester AIJ, Sóbester A and Keane AJ, Engineering Design via Surrogate Modelling: A Practical Guide, John Wiley & Sons, Chichester, 240 pages, ISBN 978-0-470-06068-1

[10] Liebf F and Perry J. Quadriceps function: an anatomical and mechanical study using amputated limbs. *J. Bone Joint Surg*. 1968;**50:**1535

Appendix C

Detailed List of Muscles and Associated Muscle Group(s)

C.1 Muscles of the Upper Body

TABLE C.1: Trunk muscles by groups.

Index	Muscle Group	Muscle Name	Action 1	Action 2	Action 3
98	**Multifidi**	MFdL1L3	Core Stability		
99		MFdL2L4	Core Stability		
100		MFdL3L5	Core Stability		
101		MFdL4S1	Core Stability		
102		MFdL5S1	Core Stability		
103		MFmL1L4	Core Stability		
104		MFmL2L5	Core Stability		
105		MFmL3S1	Core Stability		
106		MFmL4Sacrum	Core Stability		
107		MFmL5Sacrum	Core Stability		
108		MFtsL1L5	Core Stability		
109		MFtsL1S1	Core Stability		
110		MFtsL2L5	Core Stability		
111		MFtsL2S1	Core Stability		
112		MFtsL3Ligament	Core Stability		
113		MFtsL4Sacrum	Core Stability		
114		MFtsL5Sacrum	Core Stability		
115		MFtstL1SIPS	Core Stability		

TABLE C.1: (continued)

Index	Muscle Group	Muscle Name	Action 1	Action 2	Action 3
116		MFtstL2SIPS	Core Stability		
117	**Erector**	ILplL1CI	Vert. Col. Extension		
118	**Spinae**	ILplL2CI	Vert. Col. Extension		
119		ILplL3CI	Vert. Col. Extension		
120		ILplL4CI	Vert. Col. Extension		
121		LTplL1SIPS	Vert. Col. Extension		
122		LTplL2SIPS	Vert. Col. Extension		
123		LTplL3SIPS	Vert. Col. Extension		
124		LTplL4SIPS	Vert. Col. Extension		
125		LTplL5Ilium	Vert. Col. Extension		
126		ILptC5SIPS	Vert. Col. Extension		
127		ILptC6SIPS	Vert. Col. Extension		
128		ILptC7CI	Vert. Col. Extension		
129		ILptC8CI	Vert. Col. Extension		
130		ILptC9CI	Vert. Col. Extension		
131		ILptC10CI	Vert. Col. Extension		
132		ILptC11CI	Vert. Col. Extension		
133		ILptC12CI	Vert. Col. Extension		

Table C.1: (continued)

Index	Muscle Group	Muscle Name	Action 1	Action 2	Action 3
134		LTptT1L1	Vert. Col. Extension		
135		LTptT2L2	Vert. Col. Extension		
136		LTptT3L3	Vert. Col. Extension		
137		LTptT4L4	Vert. Col. Extension		
138		LTptT5L5	Vert. Col. Extension		
139		LTptT6S1	Vert. Col. Extension		
140		LTptT7S2	Vert. Col. Extension		
141		LTptT8S3	Vert. Col. Extension		
142		LTptT9S4	Vert. Col. Extension		
143		LTptT10Sacrum	Vert. Col. Extension		
144		LTptT11Sacrum	Vert. Col. Extension		
145		LTptT12Sacrum	Vert. Col. Extension		
146	**Psoas Major**	PMT12I_TM	Hip Flexion	Hip External Rotation	Vert. Col. Flexion
147		PML1I_TM	Hip Flexion	Hip External Rotation	Vert. Col. Flexion
148		PML1T_TM	Hip Flexion	Hip External Rotation	Vert. Col. Flexion
149		PML2I_TM	Hip Flexion	Hip External Rotation	Vert. Col. Flexion
150		PML2T_TM	Hip Flexion	Hip External Rotation	Vert. Col. Flexion
151		PML3I_TM	Hip Flexion	Hip External Rotation	Vert. Col. Flexion

TABLE C.1: (continued)

Index	Muscle Group	Muscle Name	Action 1	Action 2	Action 3
152		PML3T_TM	Hip Flexion	Hip External Rotation	Vert. Col. Flexion
153		PML4I_TM	Hip Flexion	Hip External Rotation	Vert. Col. Flexion
154		PML4T_TM	Hip Flexion	Hip External Rotation	Vert. Col. Flexion
155		PML5_TM	Hip Flexion	Hip External Rotation	Vert. Col. Flexion
156		PML5T_TM	Hip Flexion	Hip External Rotation	Vert. Col. Flexion
157	**Quadratus**	QLC12_CI	Vert. Col. Lat. Flexion	Thoracic Rib Cage Depression	
158	**Lumborum**	QLL1_CI	Vert. Col. Lat. Flexion	Thoracic Rib Cage Depression	
159		QLL2_CI	Vert. Col. Lat. Flexion	Thoracic Rib Cage Depression	
160		QLL3_CI	Vert. Col. Lat. Flexion	Thoracic Rib Cage Depression	
161		QLL4_CI	Vert. Col. Lat. Flexion	Thoracic Rib Cage Depression	
162	**Obliquus**	OEC7_RS	Vert. Col. Rotation	Vert. Col. Lat. Flexion	
163	**Externus**	OEC8_RS	Vert. Col. Rotation	Vert. Col. Lat. Flexion	
164		OEC9_RS	Vert. Col. Rotation	Vert. Col. Lat. Flexion	
165		OEC10_RS	Vert. Col. Rotation	Vert. Col. Lat. Flexion	
166		OEC11_CI	Vert. Col. Rotation	Vert. Col. Lat. Flexion	
167		OEC12_CI	Vert. Col. Rotation	Vert. Col. Lat. Flexion	
168	**Obliquus**	OICI_C12	Vert. Col. Rotation	Vert. Col. Lat. Flexion	
	Internus				

TABLE C.1: (continued)

Index	Muscle Group	Muscle Name	Action 1	Action 2	Action 3
169		OICI_C11	Vert. Col. Rotation	Vert. Col. Lat. Flexion	
170		OICI_C10	Vert. Col. Rotation	Vert. Col. Lat. Flexion	
171		OICI_RS1	Vert. Col. Rotation	Vert. Col. Lat. Flexion	
172		OICI_RS2	Vert. Col. Rotation	Vert. Col. Lat. Flexion	
173		OICI_RS3	Vert. Col. Rotation	Vert. Col. Lat. Flexion	
174	**Semispinalis**	Left.SEL1T8	Vert. Col. Extension	Vert. Col. Rotation	
175		Left.SEL1T10	Vert. Col. Extension	Vert. Col. Rotation	
176		Left.SEL1T11	Vert. Col. Extension	Vert. Col. Rotation	
177		Left.SEL2T9	Vert. Col. Extension	Vert. Col. Rotation	
178		Left.SEL2T10	Vert. Col. Extension	Vert. Col. Rotation	
179		Left.SEL2T11	Vert. Col. Extension	Vert. Col. Rotation	
180		Left.SEL2T12	Vert. Col. Extension	Vert. Col. Rotation	
181		Left.SEL3T11	Vert. Col. Extension	Vert. Col. Rotation	
182		Left.SEL3T12	Vert. Col. Extension	Vert. Col. Rotation	
183	**Thoracic**	Left.MFL1T8	Vert. Col. Extension		
184	**Multifidi**	Left.MFL1T9	Vert. Col. Extension		
185		Left.MFL1T10	Vert. Col. Extension		

TABLE C.1: (continued)

Index	Muscle Group	Muscle Name	Action 1	Action 2	Action 3
186		Left.MFL2T9	Vert. Col. Extension		
187		Left.MFL2T10	Vert. Col. Extension		
188		Left.MFL2T11	Vert. Col. Extension		
189		Left.MFL3T10	Vert. Col. Extension		
190		Left.MFL3T11	Vert. Col. Extension		
191		Left.MFL3T12	Vert. Col. Extension		
192		Left.MFL4T11	Vert. Col. Extension		
193		Left.MFL4T12	Vert. Col. Extension		
194		Left.MFL5T12	Vert. Col. Extension		
195	**Rectus Abdominis**	RA	Vert. Col. Flexion	Core Stability	
196	**Spinalis**	SPL1T3	Vert. Col. Extension		
197		SPL1T4	Vert. Col. Extension		
198		SPL1T5	Vert. Col. Extension		
199	**Transversus**	TransversusL1	Core Stability		
200		TransversusL2	Core Stability		
201		TransversusL3	Core Stability		
202		TransversusL4	Core Stability		

Table C.1: (continued)

Index	Muscle Group	Muscle Name	Action 1	Action 2	Action 3
203		TransversusL5	Core Stability		

C.2 Muscles of the Lower Limbs

Table C.2: Leg muscles by groups.

Index	Muscle Group	Muscle Name	Action 1	Action 2	Action 3	Action 4
1	**Soleus**	Medialis 1	Foot Flexion			
2		Medialis 2	Foot Flexion			
3		Medialis 3	Foot Flexion			
4		Lateralis 4	Foot Flexion			
5		Lateralis 5	Foot Flexion			
6		Lateralis 6	Foot Flexion			
7	**Gastrocnemius**	Lateralis 1	Knee Flexion			
8		Medialis 1	Knee Flexion			
9	**Flexor Digitorum**	Longus 1	Digit Flexion			
10		Longus 2	Digit Flexion			
11		Longus 3	Digit Flexion			
12	**Flexor Hallucis**	Longus 1	Foot Flexion	Big Toe Flexion		
13		Longus 2	Foot Flexion	Big Toe Flexion		
14		Longus 3	Foot Flexion	Big Toe Flexion		
15	**Tibialis Posterior**	Lateralis1	Foot Flexion		Foot Inversion	
16		Lateralis 2	Foot Flexion		Foot Inversion	
17		Lateralis 3	Foot Flexion		Foot Inversion	
18		Medialis 1	Foot Flexion		Foot Inversion	

Table C.2: (continued)

Index	Muscle Group	Muscle Name	Action 1	Action 2	Action 3	Action 4
19		Medialis 2	Foot Flexion		Foot Inversion	
20		Medialis 3	Foot Flexion		Foot Inversion	
21	**Tibialis Anterior**	Anterior 1	Foot Extension		Foot Inversion	
22		Anterior 2	Foot Extension		Foot Inversion	
23		Anterior 3	Foot Extension		Foot Inversion	
24	**Peroneus**	Brevis 1	Foot Flexion			Foot Eversion
25		Brevis 2	Foot Flexion			Foot Eversion
26		Brevis 3	Foot Flexion			Foot Eversion
27		Longus 1	Foot Flexion			Foot Eversion
28		Longus 2	Foot Flexion			Foot Eversion
29		Longus 3	Foot Flexion			Foot Eversion
30		Tertius 1	Foot Extension			Foot Eversion
31		Tertius 2	Foot Extension			Foot Eversion
32		Tertius 3	Foot Extension			Foot Eversion
33	**Extensor Digitorum**	Longus 1	Foot Extension	Digit Extension		
34		Longus 2	Foot Extension	Digit Extension		
35		Longus 3	Foot Extension	Digit Extension		
36	**Extensor Hallucis**	Longus 1	Foot Extension	Digit Extension		

Table C.2: (continued)

Index	Muscle Group	Muscle Name	Action 1	Action 2	Action 3	Action 4
37		Longus 2	Foot Extension	Digit Extension		
38		Longus 3	Foot Extension	Digit Extension		
39	**Vastus**	Lateralis Inferior 1	Knee Extension			
40		Lateralis Inferior 2	Knee Extension			
41		Lateralis Inferior 3	Knee Extension			
42		Lateralis Inferior 4	Knee Extension			
43	**Vastus**	Lateralis Inferior 5	Knee Extension			
44		Lateralis Inferior 6	Knee Extension			
45		Lateralis Superior 7	Knee Extension			
46		Lateralis Superior 8	Knee Extension			
47		Medialis Inferior 1	Knee Extension			
48		Medialis Inferior 2	Knee Extension			
49		Medialis Mid 3	Knee Extension			
50		Medialis Mid 4	Knee Extension			
51		Medialis Superior 5	Knee Extension			
52		Medialis Superior 6	Knee Extension			
53		Medialis Superior 7	Knee Extension			
54		Medialis Superior 8	Knee Extension			

TABLE C.2: (continued)

Index	Muscle Group	Muscle Name	Action 1	Action 2	Action 3	Action 4
55		Medialis Superior 9	Knee Extension			
56		Medialis Superior 10	Knee Extension			
57		Intermedius 1	Knee Extension			
58		Intermedius 2	Knee Extension			
59		Intermedius 3	Knee Extension			
60		Intermedius 4	Knee Extension			
61		Intermedius 5	Knee Extension			
62		Intermedius 6	Knee Extension			
63	**Rectus Femoris**	Rectus Femoris 1	Hip Flexion	Knee Extension		
64		Rectus Femoris 2	Hip Flexion			
65	**Semitendinosus**	Semitendinosus 1	Hip Extension			
66	**Semimembranosus**	Semimembranosus 1	Hip Extension			
67	**BicepsFemoris**	Caput Longum 1	Hip Extension	Knee Flexion		
68		Caput Breve 1	Knee Flexion			
69		Caput Breve 2	Knee Flexion			
70		Caput Breve 3	Knee Flexion			
71	**Sartorius**	Proximal 1	Knee Flexion			

Table C.2: (continued)

Index	Muscle Group	Muscle Name	Action 1	Action 2	Action 3	Action 4
72		Distal 1	Knee Flexion			
73	**Iliacus**	Lateralis 1	Hip Flexion	Hip Ext. Rot.		
74		Lateralis 2	Hip Flexion	Hip Ext. Rot.		
75		Lateralis 3	Hip Flexion	Hip Ext. Rot.		
76		Mid 1	Hip Flexion	Hip Ext. Rot.		
77		Mid 2	Hip Flexion	Hip Ext. Rot.		
78		Mid 3	Hip Flexion	Hip Ext. Rot.		
79		Medialis 1	Hip Flexion	Hip Ext. Rot.		
80		Medialis 2	Hip Flexion	Hip Ext. Rot.		
81		Medialis 3	Hip Flexion	Hip Ext. Rot.		
82	**Gluteus**	Minimus Anterior 1	Hip Abduction	Hip Int. Rot.		
83		Minimus Mid 1	Hip Abduction	Hip Int. Rot.		
84		Minimus Posterior 1	Hip Abduction	Hip Int. Rot.		
85	**Gluteus**	Medius Anterior 1	Hip Abduction	Hip Int. Rot.		
86		Medius Anterior 2	Hip Abduction	Hip Int. Rot.		
87		Medius Anterior 3	Hip Abduction	Hip Int. Rot.		
88		Medius Anterior 4	Hip Abduction	Hip Int. Rot.		
89		Medius Anterior 5	Hip Abduction	Hip Int. Rot.		

Table C.2: (continued)

Index	Muscle Group	Muscle Name	Action 1	Action 2	Action 3	Action 4
90		Medius Anterior 6	Hip Abduction	Hip Int. Rot.		
91		Medius Posterior 1	Hip Abduction	Hip Int. Rot.		
92		Medius Posterior 2	Hip Abduction	Hip Int. Rot.		
93		Medius Posterior 3	Hip Abduction	Hip Int. Rot.		
94		Medius Posterior 4	Hip Abduction	Hip Int. Rot.		
95		Medius Posterior 5	Hip Abduction	Hip Int. Rot.		
96		Medius Posterior 6	Hip Abduction	Hip Int. Rot.		
97		Maximus Superior 1	Hip Extension	Hip Ext. Rot.		
98		Maximus Superior 2	Hip Extension	Hip Ext. Rot.		
99		Maximus Superior 3	Hip Extension	Hip Ext. Rot.		
100		Maximus Superior 4	Hip Extension	Hip Ext. Rot.		
101		Maximus Superior 5	Hip Extension	Hip Ext. Rot.		
102		Maximus Superior 6	Hip Extension	Hip Ext. Rot.		
103		Maximus Inferior 1	Hip Extension	Hip Ext. Rot.		
104		Maximus Inferior 2	Hip Extension	Hip Ext. Rot.		
105		Maximus Inferior 3	Hip Extension	Hip Ext. Rot.		
106	**Gluteus**	Maximus Inferior 4	Hip Extension	Hip Ext. Rot.		
107		Maximus Inferior 5	Hip Extension	Hip Ext. Rot.		

TABLE C.2: (continued)

Index	Muscle Group	Muscle Name	Action 1	Action 2	Action 3	Action 4
108		Maximus Inferior 6	Hip Extension	Hip Ext. Rot.		
109	**Tensor Fasciae**	Latae 1	Hip Flexion			
110		Latae 2	Hip Flexion			
111	**Piriformis**	Piriformis 1	Hip Ext. Rot.			
112	**Gracilis**	Gracilis 1	Hip Flexion	Hip Int. Rot.	Hip Adduction	Knee Flexion
113		Gracilis 2	Hip Flexion	Hip Int. Rot.	Hip Adduction	Knee Flexion
114	**Adductor**	Longus 1	Hip Adduction	Hip Flexion		
115		Longus 2	Hip Adduction	Hip Flexion		
116		Longus 3	Hip Adduction	Hip Flexion		
117		Longus 4	Hip Adduction	Hip Flexion		
118		Longus 5	Hip Adduction	Hip Flexion		
119		Longus 6	Hip Adduction	Hip Flexion		
120		Magnus Distal 1	Hip Adduction	Hip Flexion		
121		Magnus Distal 2	Hip Adduction	Hip Flexion		
122		Magnus Distal 3	Hip Adduction	Hip Flexion		
123		Magnus Mid 1	Hip Adduction	Hip Extension		
124		Magnus Mid 2	Hip Adduction	Hip Extension		
125		Magnus Mid 3	Hip Adduction	Hip Extension		

Table C.2: (continued)

Index	Muscle Group	Muscle Name	Action 1	Action 2	Action 3	Action 4
126		Magnus Mid 4	Hip Adduction	Hip Extension		
127	**Adductor**	Magnus Mid 5	Hip Adduction	Hip Extension		
128		Magnus Mid 6	Hip Adduction	Hip Extension		
129		Magnus Proximal 1	Hip Adduction	Hip Flexion		
130		Magnus Proximal 2	Hip Adduction	Hip Flexion		
131		Magnus Proximal 3	Hip Adduction	Hip Flexion		
132		Magnus Proximal 4	Hip Adduction	Hip Flexion		
133		Brevis Proximal 1	Hip Adduction	Hip Flexion		
134		Brevis Proximal 2	Hip Adduction	Hip Flexion		
135		Brevis Mid 3	Hip Adduction	Hip Flexion		
136		Brevis Mid 4	Hip Adduction	Hip Flexion		
137		Brevis Distal 5	Hip Adduction	Hip Flexion		
138		Brevis Distal 6	Hip Adduction	Hip Flexion		
139	**Gemellus**	Inferior 1	Hip Ext. Rot.			
140		Superior 1	Hip Ext. Rot.			
141	**Obturator**	Externus Superior 1	Hip Adduction	Hip Ext. Rot.		
142		Externus Superior 2	Hip Adduction	Hip Ext. Rot.		
143		Externus Superior 3	Hip Adduction	Hip Ext. Rot.		

Table C.2: (continued)

Index	Muscle Group	Muscle Name	Action 1	Action 2	Action 3	Action 4
144		Externus Inferior 1	Hip Adduction	Hip Ext. Rot.		
145		Externus Inferior 2	Hip Adduction	Hip Ext. Rot.		
146		Internus 1	Hip Abduction	Hip Ext. Rot.		
147		Internus 2	Hip Abduction	Hip Ext. Rot.		
148		Internus 3	Hip Abduction	Hip Ext. Rot.		
149	**Pectineus**	Pectineus 1	Hip Flexion	Hip Adduction	Hip Int. Rot.	
150		Pectineus 2	Hip Flexion	Hip Adduction	Hip Int. Rot.	
151		Pectineus 3	Hip Flexion	Hip Adduction	Hip Int. Rot.	
152		Pectineus 4	Hip Flexion	Hip Adduction	Hip Int. Rot.	
153	**Plantaris**	Plantaris 1	Foot Flexion	Knee Flexion		
154	**Poplitues**	Poplitues 1	Hip Ext. Rot.	Knee Flexion		
155		Poplitues 2	Hip Ext. Rot.	Knee Flexion		
156	**Quadratus**	Femoris 1	Hip Ext. Rot.	Hip Adduction		
157		Femoris 2	Hip Ext. Rot.	Hip Adduction		
158		Femoris 3	Hip Ext. Rot.	Hip Adduction		
159		Femoris 4	Hip Ext. Rot.	Hip Adduction		

Appendix D

iDAQ User Manual

UNIVERSITY OF Southampton

i-DAQ User Manual

University of Southampton
Scott Michaels
Chris Phillips
Jan 2013

DAQ User Manual v2
for use with i-DAQ v9.5.2

UNIVERSITY OF Southampton
School of Engineering Sciences

Contents

UNIVERSITY OF Southampton

1. GUI Images

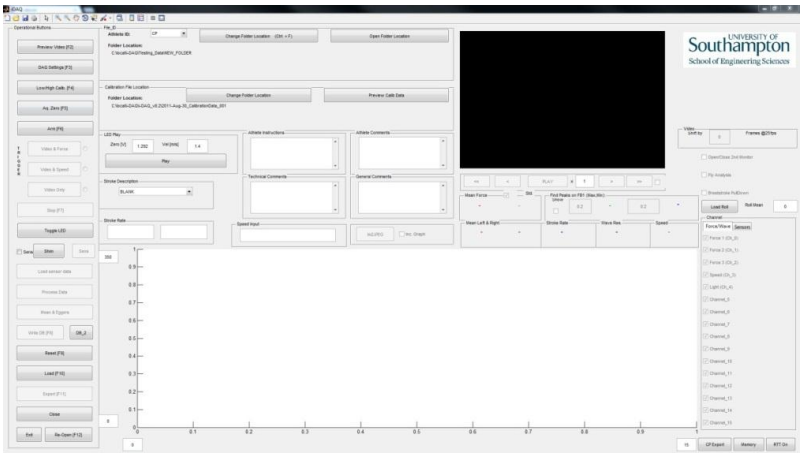

Figure 1: Main Screen

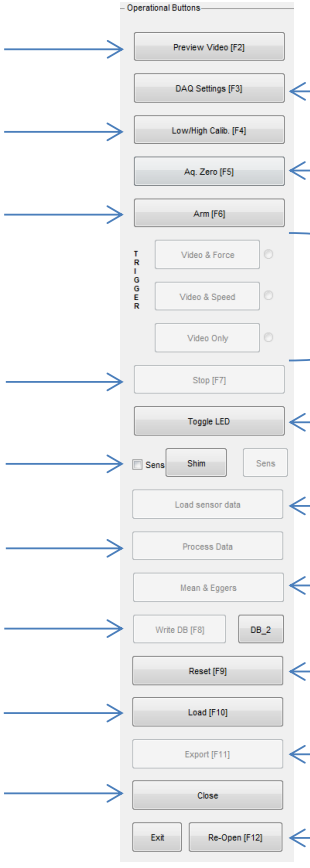

Preview Video: Displays in the video panel what the camera is currently outputting, but doesn't record

Low/High Calibration: Initialises the calibration procedure (explained later)

Arm: Prepares the system for a trigger to start the run

Stop: Finishes recording as the run ends and writes data, then launches Mean & Eggers plot to set mean period

Sensor:

Process Data: (Done automatically by "Stop" button in iDaq 9.5.2), applies calibration rates to run data. Can be used if a mistake is made while post-processing (such as clicking on a text box while selecting mean)

Write DB/DB_2: DB_2 writes results to master Excel file (takes ~17 seconds). It is recommended to do this after every run as it saves time at the end of the session and allows mid-session checks to be made

Load:

Close:

DAQ Settings: General settings for iDaq (e.g. calibration weight, etc), shouldn't need much adjusting

Aquire Zero: The first step of every run, to zero the equipment

Trigger: Radio buttons become selectable when the system is armed. **Video & Force** is appropriate when the tow rig is being used, **Video & Speed** for when the Speed system is being used, and **Video Only** for other tests using neither system (e.g. kinematic sensors only). The adjacent push button is then used to start recording as the run begins

Toggle LED: Currently not implemented

Load Sensor Data:

Mean & Eggers: (Done automatically by "Stop" button in iDaq 9.5.2), allows the user to re-select time period used to determine mean if required

Reset: Resets iDaq for next run

Export:

Re-Open: Shuts down Matlab and re-opens Matlab and iDaq. This is important to do AT LEAST every 3 or 4 runs*, preferable to do every run, or memory limit will be reached

*Note on old laptop this will need to be done **every** run

Figure 2: Operational Buttons Panel

2. Initial Setup

1) Connect both laptops to D-Link router (creating and internal network, it is recommended to disable wireless networks on both laptops) and connect to black box via USB (this carries all run data)
   - Acquisition laptop (64 bit Windows 7 machine) is used to run the data acquisition processes, feedback laptop (32 bit Windows XP machine) is used for athlete feedback, error checks, etc.
2) Configure Local Area Network (LAN)
   - LAN Properties
   - Right click TCP-IP4
   - Fix IP address in Alternate Configuration tab* (one laptop should set its own IP address, set the other to one higher, e.g. 10.12.67.67 and 10.12.67.68)
     * If this doesn't work, fix it in the General tab
   - Check access to X: drive is working (X drive is located on feedback laptop)
3) On the feedback laptop, go to Start Menu > i-DAQ > Testing Data, and create a folder with format: "YYYY-MM-DD_<Session Name>" (e.g. "2013-01-01_iDaqTest"). This is the parent folder for session data
   - Daughter folders (named "YYYY-Month-DD_Athlete_<Athlete ID>_<Run Number>") will be created automatically by i-Daq within this parent folder at the end of each run
   - Inside the daughter folders will be:
     - Force/time data
     - Matlab settings for the run
     - Time of the first video frame
     - Overview of run settings and results
     - Time of run start
     - Video clip
     - Zero data
     - Calibration files
4) Ctrl-Alt_M opens Matlab[1] from Desktop, i-Daq shortcut ("i" in top right of screen) opens i-Daq from Matlab
5) Change folder location to the parent folder in which to save the sessions data (will be on drive X:, which is a network drive both laptops can access)
6) Check settings (DefFolder.txt, located in C > local > i-Daq > Default Settings):
   - Time
   - Sample frequency
   - Calibration values

[1] Note: If Matlab version is updated, this shortcut will need to change to refer to the correct version. If iDaq is updated, the "open in" location of both the Matlab shortcut (start > all programs > matlab > r2012b (32-bit) > matlab r2012b (32-bit)) and run_idaq.m (C:\) need to change to refer to correct version

- Number of wave probes
- Hardware checkboxes

7) Check camera
   - Click Preview Video
   - Click Preview
   - If camera feed doesn't show up, go to Start > Ulead VideoStudio > VideoStudio Editor > Capture > Capture Video, and check feed is working, then try again in iDaq

8) Check NI box
   - On acquisition laptop, go so Start > Measurement & Automation > Devices and Interfaces > Dev1 > Test Panels
   - Change Mode to Continuous, Input Configuration to RSE
   - Press Start, untick Auto-Scale, check each of the 8 inputs

- - Initial Setup Finished - -

3. Calibration Procedure

Note: Speed reel system does not require calibration, old calibration files can be used.

1) Click **Low/High Calibrate**
2) Record for 10 seconds[2] with no weight and wave probes set high
3) Hang weights (default is 20kg[2]) and set wave probes low
4) Click **OK** in dialogue box to begin recording with weight (10 seconds[2])

- - Calibration data is stored in parent folder - -

5) Remove weight
6) Click **Aquire Zero**
7) Hang weights
8) Set up i-Daq for dummy run, selecting "hang weights" as stroke description
9) Click **Arm**
10) Select **Video & Force** as the trigger, then begin recording by clicking **Video & Force** (record for 10 seconds, moving wave probes up and down to simulate waves)
11) Click **Stop**, then **OK** in the dialogue box
12) Correct axis if necessary (using the numbers in the two text boxes to the left of the vertical axis)
13) Correct position of line on **Mean & Eggers** plot (automatically launched by **Stop** button)
14) Check mean force, needs to be 196.2N ± X[3]N (assuming default 20kg weight is used)
15) If the force is outside this range, repeat calibration procedure from beginning

- - Calibration Procedure Finished - -

[2] These settings can be changed in the **settings** GUI
[3] Usual degree of accuracy is ~0.5%, so 1N in this case. Depends on level of accuracy desired for the test itself

4. Run Procedure

First and foremost, it is important to remember that the person running the data acquisition has **primary responsibility for the emergency stop button[4] for the tow rig!!!** This should be located on the desk within quick and easy reach

0) Initial Checks
   - Check the folder location in which to save the sessions data
   - Check settings:
     - Time
     - Sample frequency
     - Calibration values
     - Number of wave probes
     - Hardware checkboxes

- - Begin Run Procedure - -

1) Select Athlete ID (from Athlete_ID.xlsx in iDaq folder, requires password)
2) Aquire Zero
   - If a new calibration is required, see *Calibration Procedure*, then continue from point 4 below for all subsequent runs
   - If running from a previous calibration which hasn't yet been loaded, navigate to where calibration files are stored, and select both **CalibNoLoad.daq** and **CalibWithLoad.daq**, then click **Open**.
3) Click OK to take the zero levels

- - Zero Levels Acquired - -

4) Arm Hardware
   - Click **Arm** to ready the hardware

-- Hardware Armed - -

5) Set stroke description and comments
6) Set speed (same as tow rig, e.g. 300. Conversions from ms^{-1} can be found in Speed Data.xlsx on J-Drive or in the i-Daq folder)
   - Description, comments and speed can be edited until step 12 (reset) as this is the last time data for a given run is written
7) Trigger Hardware
   - Select required **trigger** type (radio buttons), then click **associated push button** during the countdown to begin recording

- - Hardware Triggered - -

8) Randomly click LED switch (at least once per run)
9) Stop Hardware when the run ends
   - Press **Stop**. Data processing is done automatically, and Mean & Eggers plot is launched

[4] Could be assigned to an extra team member who doesn't have a specific role if there is one

- - Hardware Stopped - -

10) Mean and Eggers

- Finds the mean force over selected period and wave resistance for the run (wave resistance where appropriate). Once button is active, the following procedure can be repeated to change the period over which the mean is taken
- Click **Mean & Eggers** if required
- A bar appears on the main axes
- Drag and resize the bar to cover the data to be used for the mean force calculation
  - Passive Test: Sensible period of relatively constant force
  - Active Test: Whole number of stroke cycles
- Double click on the bar to continue
  - If wave probes are being used, a similar procedure needs to be completed for the wave data (select a time period which covers the significant range of data)
- Force statistics are displayed in GUI

- - Mean Force and Wave Resistance Calculated- -

11) Reset

- This will save the data and associated files (e.g. notes, meta-data), within the parent directory, to a unique folder with the current date, athlete ID and an incremental run number, based on that date. It will then clear the data from the workspace as well as resetting the hardware. The default setting will also be restored.
- Recommended to also click **DB_2** at this point to write data to SwimSIM_Database_01.xlsx (historic data)
- Click **Reset**

- - i-DAQ Reset –

12) Re-Open

- This will close i-Daq and Matlab, then re-open both read for the next run
- Click **Re-Open**

- - i-DAQ and Matlab will reboot –

5. Other Features

Find Peaks

Check the box to find peaks and troughs in the run data. This will look for peaks/troughs in the same portion of the run as the mean is taken from. Points will be added to the main axis to indicate those found. The two text boxes next to the resultant values control 'how big' the peaks/troughs are. This is useful for detailed analysis of active swimming

Pitch & Depth

This may be useful for passive underwater tests. It will bring up an image from the middle of the mean period and request you select four points; two points as a horizontal reference (e.g. the horizontal line pool tiles) and a second pair of points which define an axis of interest on the athlete. This will determine the angle between the lines and the separation (in pixels) from the midpoint of the first pair and the last point. This data will be saved with the rest of the run data and a figure will appear with relevant points/lines overlaid, which is also saved to the corresponding folder. Another figure will open displaying three images at 25,50 and 75% periods from where the mean was taken. This figure will be saved too

RTT On

Records RTT_on.txt (saved in parent folder), a text file containing the time the RTT (torpedo) is turned on (manually synced, so only approximate). Useful for post-processing RTT data

Preview Video

Displays current video without recording (useful for setting camera orientation)

Appendix E

Substitution in Lighthill Equation

It is assumed that the total length of the fish or swimmer remains a constant length. This maybe expressed as

$$\left(\frac{\partial x}{\partial a}\right)^2 + \left(\frac{\partial z}{\partial a}\right)^2 = 1. \tag{E.1}$$

By substituting u in Equation 4.9 for Equation 4.8, the first element in square brackets maybe simplified as follows;

$$-umw\left(-\frac{\partial z}{\partial a}\right) = \left(\frac{\partial x}{\partial t}\frac{\partial x}{\partial a} + \frac{\partial z}{\partial t}\frac{\partial z}{\partial a}\right) mw\frac{\partial z}{\partial a} \tag{E.2a}$$

$$= mw\left(\frac{\partial z}{\partial a}\frac{\partial x}{\partial t}\frac{\partial x}{\partial a} + \frac{\partial z}{\partial a}\frac{\partial z}{\partial t}\frac{\partial z}{\partial a}\right) \tag{E.2b}$$

$$= mw\left[\frac{\partial z}{\partial t}\left(\frac{\partial x}{\partial a}\right)^2 + \frac{\partial z}{\partial t}\left(\frac{\partial z}{\partial a}\right)^2\right] \tag{E.2c}$$

$$= mw\frac{\partial z}{\partial t}\left[\left(\frac{\partial x}{\partial a}\right)^2 + \left(\frac{\partial z}{\partial a}\right)^2\right] \tag{E.2d}$$

$$= mw\frac{\partial z}{\partial t}(1) \tag{E.2e}$$

$$= mw\frac{\partial z}{\partial t}. \tag{E.2f}$$

Similarly, the second element in square brackets maybe simplified as follows;

$$-umw\left(\frac{\partial x}{\partial a}\right) = -\left(\frac{\partial x}{\partial t}\frac{\partial x}{\partial a} + \frac{\partial z}{\partial t}\frac{\partial z}{\partial a}\right) mw\frac{\partial x}{\partial a} \tag{E.3a}$$

$$= -mw\left(\frac{\partial x}{\partial a}\frac{\partial x}{\partial t}\frac{\partial x}{\partial a} + \frac{\partial x}{\partial a}\frac{\partial z}{\partial t}\frac{\partial z}{\partial a}\right) \tag{E.3b}$$

$$= -mw\left[\frac{\partial x}{\partial t}\left(\frac{\partial x}{\partial a}\right)^2 + \frac{\partial x}{\partial t}\left(\frac{\partial z}{\partial a}\right)^2\right] \tag{E.3c}$$

$$= -mw\frac{\partial z}{\partial t}\left[\left(\frac{\partial x}{\partial a}\right)^2 + \left(\frac{\partial z}{\partial a}\right)^2\right] \tag{E.3d}$$

$$= -mw\frac{\partial x}{\partial t}\,(1) \tag{E.3e}$$

$$= -mw\frac{\partial x}{\partial t}. \tag{E.3f}$$

Appendix F

Bootstrap and Permutation Test (Ch.5)

The bootstrapped and permutation tests of the thrust (T) and mean maximum muscle activity (*MaxMus*) from the study in Chapter 5. The solid lines of Figure F.1 are when the first and last kick-cycles are omitted from the analysis of the two techniques —$T1_8$ and $T2_8$ respectively. The dashed lines include all kick-cycles fro the two techniques —$T1_{10}$ and $T2_{10}$. It is demonstrated from Figures F.1, F.2 and F.3 that when the fist and last kick-cycles are omitted, the difference between the two techniques becomes more significant. It is thought that this is due to errors which arise in the initiation and termination of the musculoskeletal simulation.

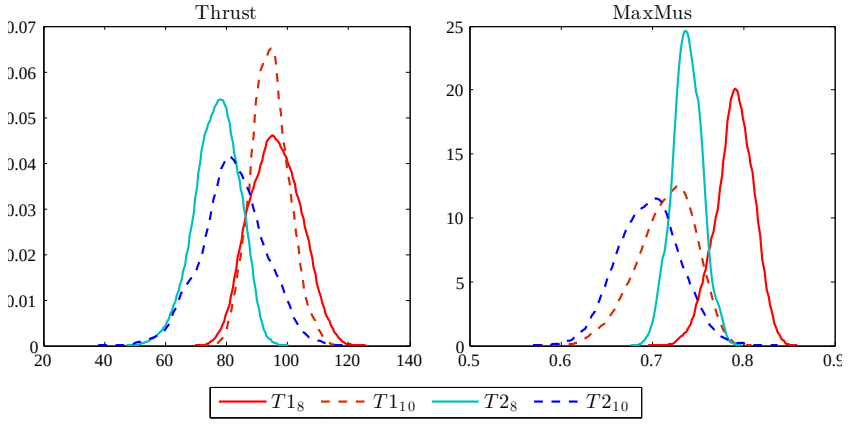

FIGURE F.1: The results of the bootstrapped thrust and maximum muscle activity (*MaxMus*). Visual inspection determines that with the first and last kick-cycles omitted, the distribution of the two techniques diverge from when all kick-cycles are included in the analysis.

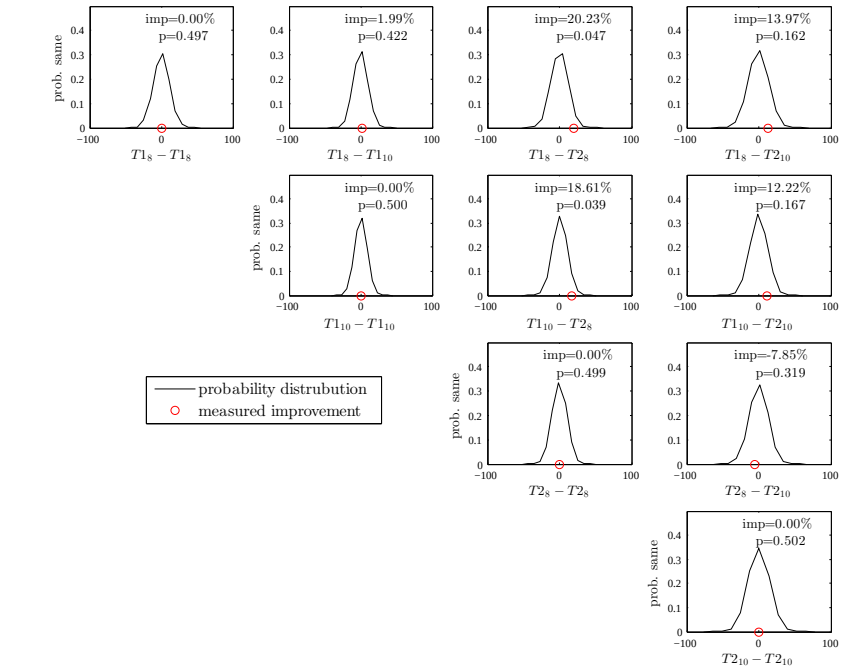

FIGURE F.2: The results of the permutation test for the thrust data. Comparing each technique (T_1 and T_2) to themselves and each other, including all ten kick-cycles (Tx_{10}) or with the first and last omitted (Tx_8).

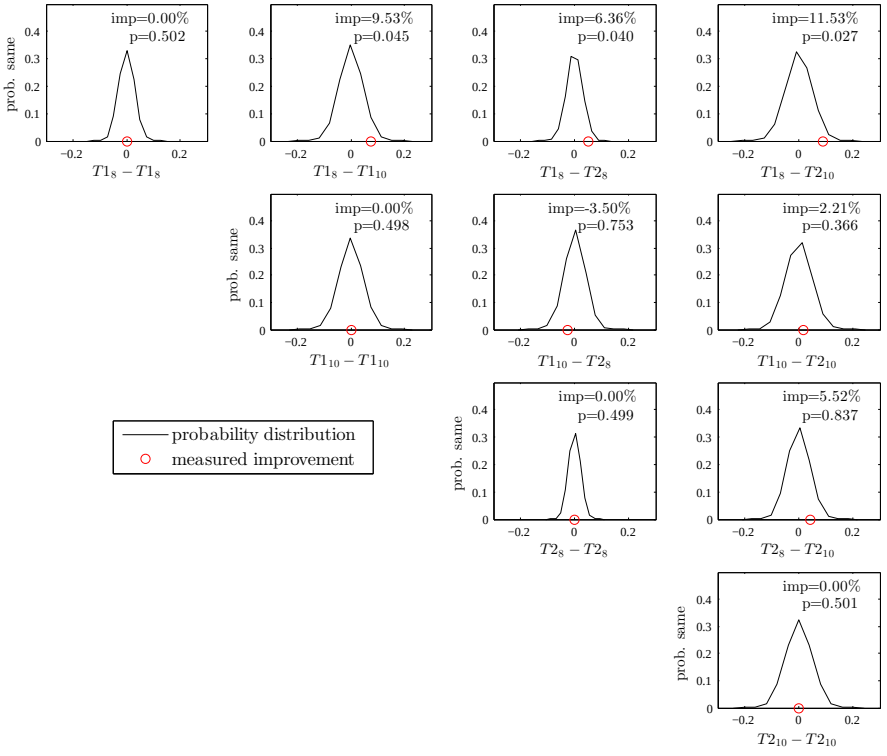

FIGURE F.3: The results of the permutation test for the maximum muscle activity data. Comparing each technique (T_1 and T_2) to themselves and each other, including all ten kick-cycles (Tx_{10}) or with the first and last omitted (Tx_8).

References

Anderson, F. C. and Pandy, M. G. (2001). Dynamic Optimization of Human Walking. *Journal of Biomechanical Engineering*, **123** (5): p. 381. DOI:10.1115/1.1392310. Available at: http://biomechanical.asmedigitalcollection.asme.org/article.aspx?articleid=1406196.

AnyBody (2011). *The AnyBody Modeling System*. V5.0.1 edn. Aalborg, Denmark: AnyBodyTech. Available at: http://www.anybodytech.com/fileadmin/AnyBody/Docs/Tutorials/main/main.html.

APLabs (2011). The website of AP Labs, an Italian research company. Available at: http://www.aplab.it/homeeng.html.

Barbosa, T. M., Keskinen, K., Fernandes, R., Colaço, P., Lima, A. and Vilas-Boas, J. (2005). Energy cost and intracyclic variation of the velocity of the centre of mass in butterfly stroke. *European journal of applied physiology*, **93** (5-6): pp. 519–23. DOI:10.1007/s00421-004-1251-x. Available at: http://www.ncbi.nlm.nih.gov/pubmed/15605282.

Bergmann, J. H., Mayagoitia, R. E. and Smith, I. C. (2009). A portable system for collecting anatomical joint angles during stair ascent: a comparison with an optical tracking device. *Dynamic medicine : DM*, **8**: p. 3. DOI:10.1186/1476-5918-8-3. Available at: http://www.pubmedcentral.nih.gov/articlerender.fcgi?artid=2684094&tool=pmcentrez&rendertype=abstract.

Bertetto, A. M., Picasso, B. and Ruggiu, M. (2001). Fish and ships : can fish inspired propulsion outperform traditional propulsion based systems ? *Built Environment*, **53**. DOI:10.2495/MT010261. Available at: http://library.witpress.com/pages/PaperInfo.asp?PaperID=2976.

Bixler, B., Pease, D. and Fairhurst, F. (2007). The accuracy of computational fluid dynamics analysis of the passive drag of a male swimmer. DOI: 10.1080/14763140601058581. Available at: http://www.informaworld.com/openurl?genre=article&doi=10.1080/14763140601058581&magic=crossref||D404A21C5BB053405B1A640AFFD44AE3.

Boitel, G., Vercruyssen, F., Alberty, M., Nesi, X., Bourdon, L. and Brisswalter, J. (2010). Kick frequency affects the energy cost of aquatic locomotion in elite monofin swimmers. *European journal of applied physiology*, **109** (6): pp. 1087–93. DOI: 10.1007/s00421-010-1450-6. Available at: http://www.ncbi.nlm.nih.gov/pubmed/20369367.

Bottoni, A., Lanotte, N., Boatto, P., Bifaretti, S. and Bonifazi, M. (2011). Technical skill differences in stroke propulsion between high level athletes in triathlon and top level swimmers. *Journal of Human Sport and Exercise*, **6** (2 (Suppl.)): pp. 351–362. DOI: 10.4100/jhse.2011.62.15. Available at: http://www.jhse.ua.es/index.php/jhse/article/viewArticle/228.

Brodie, M., Walmsley, A. and Page, W. (2008). Fusion motion capture: a prototype system using inertial measurement units and GPS for the biomechanical analysis of ski racing. *Sports Technology*, **1** (1): pp. 17–28. DOI:10.1002/jst.6. Available at: http://doi.wiley.com/10.1002/jst.6.

Cleather, D. J. and Bull, A. M. (2012). The development of lower limb musculoskeletal models with clinical relevance is dependent upon the fidelity of the mathematical description of the lower limb. Part 1: equations of motion. *Proceedings of the Institution of Mechanical Engineers, Part H: Journal of Engineering in Medicine*, **226** (2): pp. 120–132. DOI:10.1177/0954411911432104. Available at: http://pih.sagepub.com/lookup/doi/10.1177/0954411911432104.

CMAS (2012). CMAS RULES. Tech. rep., Comité des Sports Sous-Marins. Available at: http://www.cmas.org/document?sessionId=&fileId=2386&language=1.

Codamotion (2013). The website of Codamotion. Available at: http://www.codamotion.com/.

Cohen, R. C., Cleary, P. W. and Mason, B. R. (2012). Simulations of dolphin kick swimming using smoothed particle hydrodynamics. *Human movement science*, **31** (3):

pp. 604–19. DOI:10.1016/j.humov.2011.06.008. Available at: http://www.ncbi.nlm.nih.gov/pubmed/21840077.

Collard, L., Auvray, E. and Bellaunay, I. (2011). Comparison of performance levels over 25 m by 11 expert swimmers using anguilliform-like and carangiform-like techniques ; eel-like swimming versus carangiform-like swimming. *International Journal of Performance Analysis in Sport*, **11** (1): pp. 26–33. Available at: http://www.ingentaconnect.com/content/uwic/ujpa/2011/00000011/00000001/art00004.

Collins, T. D., Ghoussayni, S. N., Ewins, D. J. and Kent, J. a. (2009). A six degrees-of-freedom marker set for gait analysis: repeatability and comparison with a modified Helen Hayes set. *Gait & posture*, **30** (2): pp. 173–80. DOI:10.1016/j.gaitpost.2009.04.004. Available at: http://www.ncbi.nlm.nih.gov/pubmed/19473844.

COSMED (2012). New Snorkel for enhanced Breath-by-Breath Gas Analysis during Swimming. Tech. rep., COSMED, Rome, Italy. Available at: http://www.cosmed.com/images/pdf/productliterature/Aquatrainer_ProductGuide_EN_C02555-02-93_web.pdfhttp://www.cosmed.com/.

Dadashi, F., Crettenand, F., Millet, G. P. and Aminian, K. (2012). Front-crawl instantaneous velocity estimation using a wearable inertial measurement unit. *Sensors (Basel, Switzerland)*, **12** (10): pp. 12,927–39. DOI:10.3390/s121012927. Available at: http://www.pubmedcentral.nih.gov/articlerender.fcgi?artid=3545549&tool=pmcentrez&rendertype=abstract.

Damsgaard, M., Rasmussen, J., Christensen, S. r. T. r., Surma, E. and de Zee, M. (2006). Analysis of musculoskeletal systems in the AnyBody Modeling System. *Simulation Modelling Practice and Theory*, **14** (8): pp. 1100–1111. DOI:10.1016/j.simpat.2006.09.001. Available at: http://linkinghub.elsevier.com/retrieve/pii/S1569190X06000554.

Denchfield, S., Winden, B., Brooks, C. J., Turnock, S. R., Hudson, D. A., Forrester, A. I. and Taunton, D. J. (2012). A wireless sensor network for measuring ship responses in abnormal waves. Available at: http://eprints.soton.ac.uk/345868/.

Deschodt, V. J., Arsac, L. M. and Rouard, a. H. (1999). Relative contribution of arms and legs in humans to propulsion in 25-m sprint front-crawl swimming. *European*

journal of applied physiology and occupational physiology, **80** (3): pp. 192–9. Available at: http://www.ncbi.nlm.nih.gov/pubmed/10453920.

Dubowsky, S. R., Rasmussen, J., Sisto, S. A. and Langrana, N. A. (2008). Validation of a musculoskeletal model of wheelchair propulsion and its application to minimizing shoulder joint forces. *Journal of biomechanics*, **41** (14): pp. 2981–8. DOI:10.1016/j.jbiomech.2008.07.032. Available at: http://www.ncbi.nlm.nih.gov/pubmed/18804763.

Eloy, C. (2011). Optimal Strouhal number for swimming animals. **281**: pp. 1–21. Available at: http://arxiv.org/pdf/1102.0223.pdf.

Eng, H.-l., Toh, K.-a., Yau, W.-y. and Wang, J. (2008). DEWS: A Live Visual Surveillance System for Early Drowning Detection at Pool. *IEEE Transactions on Circuits and Systems for Video Technology*, **18** (2): pp. 196–210. DOI: 10.1109/TCSVT.2007.913960. Available at: http://ieeexplore.ieee.org/lpdocs/epic03/wrapper.htm?arnumber=4399966.

Ethier, C. R. and Simmons, C. A. (2007). *Introductory Biomechanics: From Cells to Organisms*. Cambridge texts in biomedical engineering, 1st edn. New York, USA: Cambridge University Press. Available at: http://books.google.co.uk/books?id=5-Ml5gJ34RYC&printsec=frontcover&source=gbs_ge_summary_r&cad=0#v=onepage&q&f=falsewww.cambridge.org/9780521841122http://books.google.com/books?id=5-Ml5gJ34RYC.

Favre, J., Aissaoui, R., Jolles, B., de Guise, J. and Aminian, K. (2009). Functional calibration procedure for 3D knee joint angle description using inertial sensors. *Journal of biomechanics*, **42** (14): pp. 2330–5. DOI:10.1016/j.jbiomech.2009.06.025. Available at: http://www.ncbi.nlm.nih.gov/pubmed/19665712.

Feher, J. J. (2012). *Quantitative Human Physiology: An Introduction*. Academic Press series in biomedical engineering. Elsevier Science. Available at: http://books.google.co.uk/books?id=elC9dc5FMnsC.

FINA (2010). FINA REQUIREMENTS FOR SWIMWEAR APPROVAL. Tech. rep., Fédération Internationale de Natation. Available at: http://www.fina.org/H2O/docs/rules/SWIMWEAR_APPROVAL_from_01012010.pdf.

— (2013*a*). FINA Rules & Regulations. Tech. rep., Fédération Internationale de Natation. Available at: http://www.fina.org/H2O/index.php?option=com_content&view=category&id=82:swimming-rules&Itemid=184&layout=default.

— (2013*b*). FINA WORLD RECORDS. Tech. rep., Fédération Internationale de Natation. Available at: http://www.fina.org/H2O/docs/WR_jan2013.pdf.

Forman, S. (1996). Swimming at the 1996 Atlanta Summer Games: Men's 200 metres Butterfly. Available at: http://www.sports-reference.com/olympics/summer/1996/SWI/mens-200-metres-butterfly.html.

Formosa, D. P., Mason, B. and Burkett, B. (2011). The force-time profile of elite front crawl swimmers. *Journal of sports sciences*, **29** (8): pp. 811–9. DOI:10.1080/02640414.2011.561867. Available at: http://www.ncbi.nlm.nih.gov/pubmed/21500079.

Forrester, A. I. and Keane, A. J. (2009). Recent advances in surrogate-based optimization. *Progress in Aerospace Sciences*, **45** (1-3): pp. 50–79. DOI:10.1016/j.paerosci.2008.11.001. Available at: http://linkinghub.elsevier.com/retrieve/pii/S0376042108000766.

Forrester, A. I., Sóbester, A. and Keane, A. J. (2008). *Engineering Design via Surrogate Modelling: A Practical Guide*. John Wiley & Sons Ltd. Available at: http://books.google.co.uk/books?id=ulMHmeMnRCcC&printsec=frontcover.

Foxlin, E. (2005). Pedestrian Tracking with Shoe-Mounted Inertial Sensors. *IEEE Computer Graphics and Applications*, **25** (6): pp. 38–46. DOI:10.1109/MCG.2005.140. Available at: http://ieeexplore.ieee.org/lpdocs/epic03/wrapper.htm?arnumber=1528431.

Greene, B. R., McGrath, D., O'Neill, R., O'Donovan, K. J., Burns, A. and Caulfield, B. (2010). An adaptive gyroscope-based algorithm for temporal gait analysis. *Medical & biological engineering & computing*, **48** (12): pp. 1251–60. DOI:10.1007/s11517-010-0692-0. Available at: http://www.ncbi.nlm.nih.gov/pubmed/21042951.

Grujicic, M., Arakere, G., Xie, X., LaBerge, M., Grujicic, a., Wagner, D. and Vallejo, a. (2010). Design-optimization and material selection for a femoral-fracture fixation-plate implant. *Materials & Design*, **31** (7): pp. 3463–3473. DOI:10.1016/j.matdes.2010.01.036. Available at: http://linkinghub.elsevier.com/retrieve/pii/S0261306910000506.

Hill, A. V. (1938). The Heat of Shortening and the Dynamic Constants of Muscle. *Proceedings of the Royal Society B: Biological Sciences*, **126** (843): pp. 136–195. DOI: 10.1098/rspb.1938.0050. Available at: http://rspb.royalsocietypublishing.org/cgi/doi/10.1098/rspb.1938.0050http://www.jstor.org/stable/82447?seq=2.

Hochstein, S. and Blickhan, R. (2011). Vortex re-capturing and kinematics in human underwater undulatory swimming. *Human movement science*, **30** (5): pp. 998–1007. DOI:10.1016/j.humov.2010.07.002. Available at: http://www.ncbi.nlm.nih.gov/pubmed/21684028.

Hollander, A., de Groot, G., van Ingen Schenau, G., Toussaint, H., de Best, H., Peeters, W., Meulemans, A. and Schreurs, A. (1986). Measurement of active drag during crawl arm stroke swimming. *Journal of sports sciences*, **4** (1): pp. 21–30. DOI: 10.1080/02640418608732094. Available at: http://www.ncbi.nlm.nih.gov/pubmed/3735480.

Hollins, M. (2001). *Medical Physics*. University of Bath science 16-19, 2nd edn. Nelson Thornes. Available at: http://books.google.co.uk/books?id=gXxkYhqQCtIC.

Holmberg, L. and Lund, A. (2008). A musculoskeletal full-body simulation of cross-country skiing. *Proceedings of the Institution of Mechanical Engineers, Part P: Journal of Sports Engineering and Technology*, **222** (1): pp. 11–22. DOI:10.1243/17543371JSET10. Available at: http://journals.pepublishing.com/openurl.asp?genre=article&id=doi:10.1243/17543371JSET10.

Holmér, I. (1974). Propulsive efficiency of breaststroke and freestyle swimming. *European journal of applied physiology and occupational physiology*, **33** (2): pp. 95–103. Available at: http://www.ncbi.nlm.nih.gov/pubmed/4430313.

James, G. (2001). *Modern Engineering Mathematics*. Third edn. Harlow, England: Prentice Hall PTR. Available at: http://books.google.co.uk/books?id=yY_qAAAACAAJ.

Kadaba, M., Ramakrishnan, H. and Wootten, M. (1990). Measurement of lower extremity kinematics during level walking. *Journal of orthopaedic research : official publication of the Orthopaedic Research Society*, **8** (3): pp. 383–92. DOI:10.1002/jor.1100080310. Available at: http://www.ncbi.nlm.nih.gov/pubmed/2324857.

Karlekar, J. and Fang, A. (2010). Underwater swimmer segmentation. In: *2010 IEEE International Conference on Multimedia and Expo*, pp. 619–624. IEEE. DOI:10.1109/ICME.2010.5582608. Available at: http://ieeexplore.ieee.org/lpdocs/epic03/wrapper.htm?arnumber=5582608.

Karpovich, P. V. and Millman, N. (1944). ENERGY EXPENDITURE IN SWIMMING. *American Journal of Physiology – Legacy Content*, **142** (1): pp. 140–144. Available at: http://ajplegacy.physiology.org/content/142/1/140.short.

Klein-Horsman, M. D. (2007). *The Twente lower extremity model : consistent dynamic simulation of the human locomotor apparatus*. Isbn 978-90-365-2602-9, University of Twente. Available at: http://doc.utwente.nl/58231/.

Kolmogorov, S. and Duplishcheva, O. (1992). Active drag, useful mechanical power output and hydrodynamic force coefficient in different swimming strokes at maximal velocity. *Journal of Biomechanics*, **25** (3): pp. 311–318. DOI:10.1016/0021-9290(92)90028-Y. Available at: http://linkinghub.elsevier.com/retrieve/pii/002192909290028Y.

Kruger, a., McAlpine, P., Borrani, F. and Edelmann-Nusser, J. (2011). Determination of three-dimensional joint loading within the lower extremities in snowboarding. *Proceedings of the Institution of Mechanical Engineers, Part H: Journal of Engineering in Medicine*. DOI:10.1177/0954411911426938. Available at: http://pih.sagepub.com/lookup/doi/10.1177/0954411911426938.

Kwakkel, S. P. (2008). *Human Lower Limb Kinematics Using GPS/INS*. Ph.D. thesis, University of Calgary. Available at: http://www.geomatics.ucalgary.ca/links/GradTheses.html.

Kwan, M., Andersen, M. S., Cheng, C.-L., Tang, W.-T. and Rasmussen, J. (2010). Investigation of high-speed badminton racket kinematics by motion capture. *Sports Engineering*, **13** (2): pp. 57–63. DOI:10.1007/s12283-010-0053-0. Available at: http://www.springerlink.com/index/10.1007/s12283-010-0053-0.

Le Sage, T., Bindel, a., Conway, P. P., Justham, L. M., Slawson, S. E. and West, a. a. (2011). Embedded programming and real-time signal processing of swimming strokes. *Sports Engineering*, **14** (1): pp. 1–14. DOI:10.1007/s12283-011-0070-7. Available at: http://www.springerlink.com/index/10.1007/s12283-011-0070-7.

Lighthill, M. J. (1970). Aquatic animal propulsion of high hydromechanical efficiency. *Journal of Fluid Mechanics*, **44** (02): pp. 265–301. DOI:10.1017/S0022112070001830. Available at: http://journals.cambridge.org/article_S0022112070001830.

— (1971). Large-Amplitude Elongated-Body Theory of Fish Locomotion. *Proceedings of the Royal Society of London. Series B, Biological Sciences*, **179** (1055): pp. 125–138. Available at: http://www.jstor.org/stable/76021.

Lorincz, K., Chen, B.-r., Challen, G. W., Chowdhury, A. R., Patel, S., Bonato, P. and Welsh, M. (2009). *Mercury: A Wearable Sensor Network Platform for High-Fidelity Motion Analysis*. New York, New York, USA: ACM Press. DOI: 10.1145/1644038.1644057. Available at: http://portal.acm.org/citation.cfm?doid=1644038.1644057.

Luinge, H. J., Veltink, P. and Baten, C. (1999). Estimation of orientation with gyroscopes and accelerometers. In: *Proceedings of the First Joint BMES/EMBS Conference. 1999 IEEE Engineering in Medicine and Biology 21st Annual Conference and the 1999 Annual Fall Meeting of the Biomedical Engineering Society (Cat. No.99CH37015)*, vol. 2, p. 844. IEEE. DOI:10.1109/IEMBS.1999.803999. Available at: http://doc.utwente.nl/16426/http://ieeexplore.ieee.org/lpdocs/epic03/wrapper.htm?arnumber=803999.

Lyttle, A. (1999). *HYDRODYNAMICS OF THE HUMAN BODY DURING THE FREESTYLE TUMBLE TURN*. Ph.D. thesis, The University of Western Australia.

Madgwick, S. O., Harrison, A. J. and Vaidyanathan, R. (2011). Estimation of IMU and MARG orientation using a gradient descent algorithm. In: *International Conference on Rehabilitation Robotics (ICORR)*. Available at: http://code.google.com/p/imumargalgorithm30042010sohm/updates/list.

ManhattanMocap (2012). The website of ManhattanMocap. Available at: http://manhattanmocap.com/swimming.

Miyazaki, S. (1997). Long-term unrestrained measurement of stride length and walking velocity utilizing a piezoelectric gyroscope. *IEEE transactions on bio-medical engineering*, **44** (8): pp. 753–9. DOI:10.1109/10.605434. Available at: http://www.ncbi.nlm.nih.gov/pubmed/9254988.

Moeslund, T. (2001). A Survey of Computer Vision-Based Human Motion Capture. *Computer Vision and Image Understanding*, **81** (3): pp. 231–268. DOI:10.1006/cviu.2000.0897. Available at: http://linkinghub.elsevier.com/retrieve/pii/S107731420090897X.

Molland, A. F., Turnock, S. R. and Hudson, D. A. (2011). *Ship Resistance and Propulsion: Practical Estimation of Ship Propulsive Power*. 1st edn. New York, USA: Cambridge University Press. Available at: http://books.google.co.uk/books?id=_tivZTPUgXMC&printsec=frontcover&source=gbs_ge_summary_r&cad=0#v=onepage&q&f=false.

Nakashima, M., Maeda, S., Miwa, T. and Ichikawa, H. (2012). Optimizing Simulation of the Arm Stroke in Crawl Swimming Considering Muscle Strength Characteristics of Athlete Swimmers. *Journal of Biomechanical Science and Engineering*, **7** (2): pp. 102–117. DOI:10.1299/jbse.7.102. Available at: http://joi.jlc.jst.go.jp/JST.JSTAGE/jbse/7.102?from=CrossRef.

Nakashima, M., Satou, K. and Miura, Y. (2007). Development of Swimming Human Simulation Model Considering Rigid Body Dynamics and Unsteady Fluid Force for Whole Body. *Journal of Fluid Science and Technology*, **2** (1): pp. 56–67. DOI:10.1299/jfst.2.56. Available at: http://joi.jlc.jst.go.jp/JST.JSTAGE/jfst/2.56?from=CrossRef.

Nakashima, M. and Yugo, M. (2007). DEVELOPMENT OF A FULL-BODY MUSCULO-SKELETAL SIMULATOR FOR SWIMMING. In: *11th International Symposium on Computer Simulation in Biomechanics*, pp. 59–60. Available at: http://www.swum.org/.

Nicolas, G., Bideau, B., Colobert, B. and Berton, E. (2007). How are Strouhal number, drag, and efficiency adjusted in high level underwater monofin-swimming? *Human movement science*, **26** (3): pp. 426–42. DOI:10.1016/j.humov.2007.03.002. Available at: http://www.ncbi.nlm.nih.gov/pubmed/17509711.

Ohgi, Y. (2002). *Microcomputer-based acceleration sensor device for sports biomechanics -stroke evaluation by using swimmer's wrist acceleration*. IEEE. DOI:10.1109/ICSENS.2002.1037188. Available at: http://ieeexplore.ieee.org/lpdocs/epic03/wrapper.htm?arnumber=1037188.

Pandy, M. G. (2001). Computer modeling and simulation of human movement. *Annual review of biomedical engineering*, **3**: pp. 245–73. DOI:10.1146/annurev.bioeng.3.1.245. Available at: http://www.ncbi.nlm.nih.gov/pubmed/11447064.

Pendergast, D., Zamparo, P., di Prampero, P., Capelli, C., Cerretelli, P., Termin, A., Craig, A., Bushnell, D., Paschke, D. and Mollendorf, J. (2003). Energy balance of human locomotion in water. *European journal of applied physiology*, **90** (3-4): pp. 377–86. DOI:10.1007/s00421-003-0919-y. Available at: http://www.ncbi.nlm.nih.gov/pubmed/12955519.

PhaseSpace (2013). The website of PhaseSpace. Available at: www.phasespace.com.

Phillips, C. W., Forrester, A. I., Purdue, A. I. and Stokes, M. M. (2010). Optimisation of a bicycle chainring to aid in rehabilitation of athletes suffering from patellofemoral pain syndrome (PFPS). *Procedia Engineering*, **2** (2): pp. 3151–3156. DOI:10.1016/j.proeng.2010.04.125. Available at: http://linkinghub.elsevier.com/retrieve/pii/S1877705810003796.

Purdue, A., Forrester, A. I., Taylor, M., Stokes, M., Hansen, E. and Rasmussen, J. (2010). Efficient human force transmission tailored for the individual cyclist. *Procedia Engineering*, **2** (2): pp. 2543–2548. DOI:10.1016/j.proeng.2010.04.029. Available at: http://linkinghub.elsevier.com/retrieve/pii/S1877705810002833.

Rasmussen, J., Boocock, M. and Paul, G. (2012). Advanced musculoskeletal simulation as an ergonomic design method. *Work*, **41**: pp. 6107–6111. DOI:10.3233/WOR-2012-1069-6107. Available at: http://www.scopus.com/inward/record.url?partnerID=yv4JPVwI&eid=2-s2.0-84859814100&md5=bf054ea6d6ef3c598518108f69a49e8b.

Rasmussen, J., Damsgaard, M. and Voigt, M. (2001). Muscle recruitment by the min/-max criterion – a comparative numerical study. *Journal of biomechanics*, **34** (3): pp. 409–15. Available at: http://www.ncbi.nlm.nih.gov/pubmed/11182135.

Rasmussen, J., Tø rholm, S. r. and de Zee, M. (2009). Computational analysis of the influence of seat pan inclination and friction on muscle activity and spinal joint forces. *International Journal of Industrial Ergonomics*, **39** (1): pp. 52–57. DOI:10.1016/j.ergon.2008.07.008. Available at: http://linkinghub.elsevier.com/retrieve/pii/S0169814108001212.

Reis, V. M., Marinho, D. A., Barbosa, F. P., Reis, A. M., Guidetti, L. and Silva, A. J. (2010). Examining the accumulated oxygen deficit method in breaststroke swimming. *European journal of applied physiology*, **109** (6): pp. 1129–35. DOI:10.1007/s00421-010-1460-4. Available at: http://www.ncbi.nlm.nih.gov/pubmed/20373107.

Roetenberg, D. (2006). *Inertail and Magnetic Sensing of Human Motion*. University of Twente. Available at: http://doc.utwente.nl/56176/1/thesis_Roetenberg.pdf.

Rohr, J. and Fish, F. E. (2004). Strouhal numbers and optimization of swimming by odontocete cetaceans. *Journal of Experimental Biology*, **207** (10): pp. 1633–1642. DOI:10.1242/jeb.00948. Available at: http://jeb.biologists.org/cgi/content/abstract/207/10/1633http://journals.cambridge.org/action/displayJournal?jid=FLM#.UDd8u_CXRTk.mendeleyhttp://jeb.biologists.org/cgi/doi/10.1242/jeb.00948.

Sabatini, A. M. (2006). Quaternion-based extended Kalman filter for determining orientation by inertial and magnetic sensing. *IEEE transactions on bio-medical engineering*, **53** (7): pp. 1346–56. DOI:10.1109/TBME.2006.875664. Available at: http://www.ncbi.nlm.nih.gov/pubmed/16830938.

Sagong, W., Kim, C., Choi, S., Jeon, W.-P. and Choi, H. (2008). Does the sailfish skin reduce the skin friction like the shark skin? *Physics of Fluids*, **20** (10): p. 101,510. DOI:10.1063/1.3005861. Available at: http://link.aip.org/link/PHFLE6/v20/i10/p101510/s1&Agg=doi.

Saraswat, P., Andersen, M. S. and Macwilliams, B. A. (2010). A musculoskeletal foot model for clinical gait analysis. *Journal of biomechanics*, **43** (9): pp. 1645–52. DOI:10.1016/j.jbiomech.2010.03.005. Available at: http://www.ncbi.nlm.nih.gov/pubmed/20385385.

Schmidt, M. R. (2008). *Biomechanical Analysis of Anterior Cruciate Ligament*. Ph.D. thesis, Aalborg University.

Schmidt-Nielsen, K. (1972). Locomotion: energy cost of swimming, flying, and running. *Science (New York, N.Y.)*, **177** (4045): pp. 222–8. Available at: http://www.ncbi.nlm.nih.gov/pubmed/4557340http://www.jstor.org/stable/1734532.

Schulze, M., Calliess, T., Gietzelt, M., Wolf, K. H., Liu, T., Seehaus, F., Bocklage, R., Windhagen, H. and Marschollek, M. (2012). Development and clinical validation of an

unobtrusive ambulatory knee function monitoring system with inertial 9DoF sensors. *Conference proceedings : ... Annual International Conference of the IEEE Engineering in Medicine and Biology Society. IEEE Engineering in Medicine and Biology Society. Conference*, **2012**: pp. 1968–71. DOI:10.1109/EMBC.2012.6346341. Available at: http://www.ncbi.nlm.nih.gov/pubmed/23366302.

Schwirtz, P. A., Bichler, R., Kaiser, R. and München, T. U. (2009). Method for biomechanical evaluation of the ingress and egress motion. In: *ANSYS Conference & 27th CADFEM Users Meeting*, 1, pp. 18–21. Leipzig, Germany. Available at: http://www.anybodytech.com/download.html?did=publications.files&fname=Schwirtz_2009_Methodforbiomechanicalevaluationoftheingressandegressmotion.pdf.

Seifert, L., Chollet, D. and Rouard, A. (2007). Swimming constraints and arm coordination. *Human movement science*, **26** (1): pp. 68–86. DOI:10.1016/j.humov.2006.09.003. Available at: http://www.ncbi.nlm.nih.gov/pubmed/17126942.

Sensorize (2013). The website of Sensorize. Available at: www.sensorize.it.

Shimmer Research (2013). The website of Shimmer Research. Available at: www.shimmer-research.com.

Singh, K. and Pedley, T. (2012). Modelling lateral manoeuvres in fish. *Journal of Fluid Mechanics*, **697**: pp. 1–34. DOI:10.1017/jfm.2012.1. Available at: http://www.journals.cambridge.org/abstract_S0022112012000018.

Squilacci111 (2009). Very Fast Underwater (Dolphin Kick). Available at: http://www.youtube.com/watch?v=z4py9HjKuvQ&list=FL36jcvhM2cdpEcvhtRveVpQ&index=3.

Taylor, G. K., Nudds, R. L. and Thomas, A. L. R. (2003). Flying and swimming animals cruise at a Strouhal number tuned for high power efficiency. *Nature*, **425** (6959): pp. 707–11. DOI:10.1038/nature02000. Available at: http://dx.doi.org/10.1038/nature02000http://www.ncbi.nlm.nih.gov/pubmed/14562101.

Tessendorf, B., Gravenhorst, F., Arnrich, B. and Troster, G. (2011). An IMU-based sensor network to continuously monitor rowing technique on the water. In: *2011 Seventh International Conference on Intelligent Sensors, Sensor Networks and Information Processing*, pp. 253–258. IEEE. DOI:10.1109/ISSNIP.2011.6146535. Available at: http://ieeexplore.ieee.org/lpdocs/epic03/wrapper.htm?arnumber=6146535.

Thow, J. L., Naemi, R. and Sanders, R. H. (2012). Comparison of modes of feedback on glide performance in swimming. *Journal of sports sciences*, **30** (1): pp. 43–52. DOI:10.1080/02640414.2011.624537. Available at: http://www.ncbi.nlm.nih.gov/pubmed/22168429.

Toussaint, H. and Truijens, M. (2005). Biomechanical aspects of peak performance in human swimming. *Animal Biology*, **55** (1): pp. 17–40. DOI:10.1163/1570756053276907. Available at: http://www.ingentaselect.com/rpsv/cgi-bin/cgi?ini=xref&body=linker&reqdoi=10.1163/1570756053276907.

Twomey, N., Faul, S. and Marnane, W. P. (2010). Comparison of accelerometer-based energy expenditure estimation algorithms. *Proceedings of the 4th International ICST Conference on Pervasive Computing Technologies for Healthcare*. DOI:10.4108/ICST.PERVASIVEHEALTH2010.8879. Available at: http://eudl.eu/doi/10.4108/ICST.PERVASIVEHEALTH2010.8879.

Umberger, B. R. (2010). Stance and swing phase costs in human walking. *Journal of the Royal Society, Interface / the Royal Society*, **7** (50): pp. 1329–40. DOI:10.1098/rsif.2010.0084. Available at: http://www.pubmedcentral.nih.gov/articlerender.fcgi?artid=2894890&tool=pmcentrez&rendertype=abstract.

Umberger, B. R., Gerritsen, K. G. and Martin, P. E. (2003). A model of human muscle energy expenditure. *Computer methods in biomechanics and biomedical engineering*, **6** (2): pp. 99–111. DOI:10.1080/1025584031000091678. Available at: http://www.ncbi.nlm.nih.gov/pubmed/12745424.

Vicon (2013). The website of Vicon. Available at: www.vicon.com.

Vlasic, D., Adelsberger, R., Vannucci, G., Barnwell, J., Gross, M., Matusik, W. and Popovic, J. (2007). Practical Motion Capture in Everyday Surroundings. *ACM Trans. Graph.*, **26** (3). DOI:10.1145/1239451.1239486. Available at: http://portal.acm.org/citation.cfm?id=1276421.

Vogel, S. (1994). *Life in Moving Fluids: The Physical Biology of Flow*. Princeton University Press. Available at: http://books.google.com/books?id=XBqncfXFsOIC&pgis=1.

von Loebbecke, A., Mittal, R., Fish, F. E. and Mark, R. (2009). A comparison of the kinematics of the dolphin kick in humans and cetaceans. *Human movement science*,

28 (1): pp. 99–112. DOI:10.1016/j.humov.2008.07.005. Available at: http://www.ncbi.nlm.nih.gov/pubmed/18986721.

Von Loebbecke, A., Mittal, R., Mark, R. and Hahn, J. (2009). A computational method for analysis of underwater dolphin kick hydrodynamics in human swimming. *Sports Biomechanics*, **8** (1): pp. 60–77. DOI:10.1080/14763140802629982. Available at: http://www.informaworld.com/openurl?genre=article&doi=10.1080/14763140802629982&magic=crossref||D404A21C5BB053405B1A640AFFD44AE3.

Webb, A. P., Banks, J., Phillips, C. W., Hudson, D. A., Taunton, D. J. and Turnock, S. R. (2011). Prediction of passive and active drag in swimming. *Procedia Engineering*, **13**: pp. 133–140. DOI:10.1016/j.proeng.2011.05.063. Available at: http://linkinghub.elsevier.com/retrieve/pii/S1877705811009775.

Webb, A. P., Phillips, C. W., Hudson, D. A. and Turnock, S. R. (2012). Can Lighthill's Elongated Body Theory Predict Hydrodynamic Forces in Underwater Undulatory Swimming? *Procedia Engineering*, **00** (0): pp. 1–6. DOI:10.1016/j.proeng.2012.04.123. Available at: http://linkinghub.elsevier.com/retrieve/pii/S1877705812017365.

Wehner, T., Wolfram, U., Henzler, T., Niemeyer, F., Claes, L. and Simon, U. (2010). Internal forces and moments in the femur of the rat during gait. *Journal of biomechanics*, **43** (13): pp. 2473–9. DOI:10.1016/j.jbiomech.2010.05.028. Available at: http://www.ncbi.nlm.nih.gov/pubmed/20566196.

Williamson, R. and Andrews, B. (2001). Detecting absolute human knee angle and angular velocity using accelerometers and rate gyroscopes. *Medical & Biological Engineering & Computing*, **39** (3): pp. 294–302. DOI:10.1007/BF02345283. Available at: http://www.springerlink.com/index/10.1007/BF02345283.

Wilson, D., Smith, B., Gibson, J., Choe, B., Gaba, B. and Voelz, J. (1999). Accuracy of digitization using automated and manual methods. *Physical therapy*, **79** (6): pp. 558–66. Available at: http://www.ncbi.nlm.nih.gov/pubmed/16607143.

Woodman, O. J. (2007). An introduction to inertial navigation. Tech. Rep. 696, University of Cambridge, Computer Laboratory. Available at: http://www.cl.cam.ac.uk/techreports/UCAM-CL-TR-696.pdf.

Worsley, P., Stokes, M. and Taylor, M. (2011). Predicted knee kinematics and kinetics during functional activities using motion capture and musculoskeletal modelling in healthy older people. *Gait & posture*, **33** (2): pp. 268–73. DOI:10.1016/j.gaitpost.2010.11.018. Available at: http://www.ncbi.nlm.nih.gov/pubmed/21169022.

Wu, T. (1971). Hydromechanics of swimming propulsion. Part 3. Swimming and optimum movements of slender fish with side fins. *Journal of Fluid Mechanics*, **46**: pp. 545–568. Available at: http://authors.library.caltech.edu/344/1/WUTjfm71c.pdfhttp://journals.cambridge.org/production/action/cjoGetFulltext?fulltextid=366563.

Xsens (2013). Xsesns Motion Technologies. Available at: www.xsens.com.

Zamparo, P., Capelli, C., Cautero, M. and di Nino, A. (2000). Energy cost of front-crawl swimming at supra-maximal speeds and underwater torque in young swimmers. *European Journal of Applied Physiology*, **83** (6): pp. 487–491. DOI:10.1007/s004210000318. Available at: http://www.springerlink.com/openurl.asp?genre=article&id=doi:10.1007/s004210000318.

Zamparo, P. and Swaine, I. L. (2012). Mechanical and propelling efficiency in swimming derived from exercise using a laboratory-based whole-body swimming ergometer. *Journal of applied physiology (Bethesda, Md. : 1985)*, **113** (4): pp. 584–94. DOI:10.1152/japplphysiol.00324.2012. Available at: http://www.ncbi.nlm.nih.gov/pubmed/22723633.